GaoFeng Wang

Magnetic and Calorimetric Study of the Magnetocaloric Effect in Intermetallics Exhibiting First-order Magnetostructural Transitions

Departamento

Física de la Materia Condensada

Director/es

Burriel, Ramón
Palacios, Elías

Universidad Zaragoza
1542

Tesis Doctoral

MAGNETIC AND CALORIMETRIC STUDY OF THE MAGNETOCALORIC EFFECT IN INTERMETALLICS EXHIBITING FIRST-ORDER MAGNETOSTRUCTURAL TRANSITIONS

Autor

GaoFeng Wang

Director/es

Burriel, Ramón
Palacios, Elías

UNIVERSIDAD DE ZARAGOZA

Física de la Materia Condensada

2012

Magnetic and Calorimetric Study of the Magnetocaloric Effect in Intermetallics Exhibiting First-order Magnetostructural Transitions

Colección de Estudios de Física
Vol. 99

Esta colección recoge las tesis presentadas en el Departamento de Física de la Materia Condensada de la Universidad de Zaragoza desde su constitución en 1987.

Magnetic and Calorimetric Study of the Magnetocaloric Effect in Intermetallics Exhibiting First-order Magnetostructural Transitions

GaoFeng Wang

To my parents,
my wife ZengRu Zhao,
my younger brother GuoFeng Wang,
and my daughter MiaoKe Wang.

Contents

Summary

The present work is aimed at characterizing the magnetocaloric effect (MCE), including isothermal entropy change ΔS_T and adiabatic temperature change ΔT_S, in some intermetallic compounds exhibiting first-order magnetostructural transitions. Direct and indirect methods have been used. The studied compounds displaying giant MCEs have been regarded as candidates having potential for application in magnetic refrigeration near room temperature. The occurrence of first-order transitions in these compounds is accompanied by thermal and magnetic hysteresis with important related effects. It is proven that $|\Delta S_T|$ could be overestimated for such materials when it is deduced from isothermal magnetization data, depending on the followed protocol. In most publications, only ΔS_T is characterized, however, which can be meaningless without a detailed explanation of the followed protocol. Moreover, ΔT_S is also crucial for practical applications and is related to the operating temperature span of the cooling systems. This Ph.D Thesis is devoted to optimize the methods for the determination of the MCE in materials exhibiting first-order transitions with hysteresis, and also to characterize accurately both parameters ΔS_T and ΔT_S in the studied compounds using several methods.

The Thesis contains nine chapters, as follows:

In chapter 1, a brief introduction to MCE and to room-temperature refrigeration, and a short review of near room-temperature MCE materials developed in recent years are presented.

Some theoretical aspects related to MCE are given in chapter 2. The Bean-Rodbell model is introduced. On the basis of this model, the irreversible behavior associated with first-order transitions and the effects of irreversibility on the determination of magnetocaloric parameters are discussed.

In chapter 3, the main experimental techniques used in this Thesis are described, including the sample preparation and characterization. Importantly, a detailed description of an adiabatic calorimeter which provides a great part of the data of this Thesis is presented. The fundamentals of heat capacity, thermograms, enthalpy runs, direct ΔS_T and ΔT_S measurements as well as their corresponding corrections are reported.

Chapter 4 is dedicated to the determination of the MCE from magnetization, heat-capacity and direct measurements. The "spike" effect (spurious peak) of ΔS_T in hysteretic materials is discussed with the help of the magnetic phase diagram. As typical examples, the heat capacity and magnetocaloric properties of two materials, pure Gd metal and $Mn_{1.1}Fe_{0.9}P_{0.82}Ge_{0.18}$ compound, are studied. The first sample exhibits a typical second-order phase transition and the latter shows a first-order transition with large hysteresis.

In the subsequent five chapters, the structural, magnetic, heat capacity and magnetocaloric properties of several series of materials exhibiting first-order transitions are investigated. The studied materials are derived from the following parent compounds by doping or small atomic substitution: $Gd_5Si_2Ge_2$-type (chapter 5), $La(Fe,Si)_{13}$-type (chapter 6), MnAs-type (chapter 7), $(Mn,Fe)_2$ (P,Ge)-type (chapter 8) and $MnCoGeB_x$-type (chapter 9) compounds.

In chapter 5, we show the suppression of first-order magnetostructural transitions in Cu- and Ga-doped $Gd_5Si_2Ge_2$ compounds by measuring X-ray diffraction and hot neutron diffraction patterns at different temperatures. The MCE of the parent $Gd_5Si_2Ge_2$ compound is determined anew by means of heat-capacity and direct measurements. Smaller but more correct ΔS_T values, compared to the literature, are obtained.

In chapter 6, we report on the properties of $La(Fe,Si)_{13}$-type compounds with low Si content which have been prepared by the melt-spinning technique. The Si concentration of the melt-spun ribbons is determined for each sample on the basis of XRD analysis. The MCEs of $La(Fe,Si)_{13}$ ribbons and their hydrides are characterized by means of direct and indirect methods.

Chapter 7 is devoted to study the influence produced on the properties of MnAs by a small substitution of Fe or Co on the Mn site. The MCE has been determined on these doped compounds. The existence of magnetostructural transitions in Fe-doped (up to 1.5 at.%) and Co-doped (up to 2 at.%) compounds, as well as in pure MnAs, are confirmed by means of temperature dependent XRD measurements. The magnetocaloric parameters ΔS_T and ΔT_S derived from magnetization and direct measurements, performed following different protocols, are compared with those obtained from heat capacity measured at constant magnetic fields in heating and cooling processes. The Bean-Rodbell model is introduced to semi-quantitatively illustrate the phase transitions and magnetocaloric properties of the doped compounds.

The Mn-rich Fe_2P-type compounds undergo first-order phase transitions, but showing very small hysteresis. The magnetocaloric properties of two selected compounds are investigated by means of direct and indirect methods in chapter 8.

A first-order structural transition and a second-order magnetic phase transition occur at different temperatures in the intermetallic compound MnCoGe. These temperatures can be adjusted to coincide by adding a small amount of B. In chapter 9, we report on the peculiar behavior of the coupled magnetic and structural transitions occurring in $MnCo_{0.98}Cu_{0.02}GeB_{0.02}$. It has been studied by means of XRD, magnetization and heat-capacity measurements. The MCE of this compound has also been determined from direct and indirect measurements.

Chapter 1

Introduction

1.1 Room-temperature refrigeration

In the current modern society, room-temperature refrigeration has become an indispensable technology in our daily life, such as the fridge for food storage in homes and supermarkets, the air-conditioning in private homes and public buildings. The cooling technology is also crucial to industrial fields, such as gaseous liquefaction, the operating capability of superconductive electronic coils at low temperature. To date, the gas compression/expansion refrigerators have been utilized ubiquitously since the first commercial refrigerator was successfully made more than a hundred years ago. However, the cooling efficiency of such initial refrigerators is very low [1]. In addition, the use of ozone-depleting chemicals (such as chlorofluorocarbons (CFCs) and hydrochlorofluorocarbons (HCFCs)), hazardous chemicals (such as ammonia) or greenhouse gases (such as hydrofluorocarbons (HFCs)) as working refrigerants has raised serious environmental concerns. The CFCs and HCFCs have been prohibited, and the HFCs will also be completely banned in the coming years according to the Montreal Protocol [2]. Therefore, it is a matter of great urgency to replace the conventional gaseous refrigeration by a new environmental-friendliness cooling technology, such as thermoelectric refrigeration, magnetic refrigeration and thermoacoustic refrigeration. Among these methods, the magnetic refrigeration could be the best way for room-temperature refrigeration due to its high cooling efficiency and feasibility [3].

Comparing to the conventional gaseous refrigeration, the magnetic refrigeration shows some superior points, such as environmental friendliness, high energy-efficiency, small volume, low noise and longevity [3]. The magnetic refrigeration uses magnetic materials (usually in a form of spheres or thin sheets) as refrigerants instead of gaseous or liquid refrigerants. The application of solid

refrigerants and common heat transfer fluids, such as air, helium gas, water or ethanol, avoids the ozone-depleting and global-warming effects, as well as the presence of a compressor. Simultaneously, the utilization of magnetic solid refrigerants and the absence of the compressor allow compacting the configuration and lowering the noise of the refrigerators. Another important advantage of the magnetic refrigerators compared with the gas compression/expansion refrigerators is the lower energy loss incurred in the cooling cycle. Up to date, the efficiency of the most efficient commercial gas-compression / expansion refrigerators is only about 40 % of the Carnot efficiency (according to the Second Law of Thermodynamics, the efficiency of a refrigeration unit is limited to the Carnot efficiency). Besides, a significant improvement of the efficiency of the traditional refrigerators is hardly expected in the future. Whereas, the cooling efficiency of a magnetic refrigerator operating with gadolinium (Gd) as the refrigerant has shown to reach 60 % of the Carnot efficiency [1]. In other words, the magnetic refrigerator could conserve about 20 % or even more energy than the gas compression/expansion refrigerators, drastically reducing the operating cost.

In short, it is expected that the magnetic refrigeration, an environment-friendly, high-efficient and green cooling technology, will replace the conventional gaseous refrigeration near room-temperature in the future.

1.2   Magnetocaloric effect

Magnetocaloric effect (MCE) is described as the thermal response (heating or cooling) of a magnetic substance when a magnetic field is applied or removed. The MCE is an intrinsic characteristic of magnetic solids, which was originally discovered experimentally in Fe by Warburg in 1881 [4].

A magnetic substance contains mainly two energy reservoirs, the usual phonon excitations linked to the lattice degrees of freedom and the magnetic excitations linked to the spin degrees of freedom. The spin-lattice coupling often exists in order to ensure the loss-free energy transfer within millisecond time scales. For a usual ferromagnetic (FM) or a paramagnetic (PM) substance, an external magnetic field can strongly affect the spin system, but make less influence on the lattice system, that results in the MCE. The MCE can be realized in two fundamental thermodynamic processes. As illustrated in figure 1.1, the initially disordered magnetic moments are aligned by applying a magnetic field isothermally, reducing the disorder of the spin system, thus substantially lowering the magnetic entropy. When the external magnetic field is applied in an adiabatic condition, the entropy of the lattice system must increase in order to compensate the magnetic entropy reduction, maintaining

the total entropy constant. The increase of the lattice entropy represents a rise of the temperature of the material. Therefore, the MCE of a substance is quantified by two parameters, isothermal entropy change, ΔS_T, and adiabatic temperature change, ΔT_S. The reduction of magnetic entropy and the rise of temperature greatly occur near absolute 0 K for a PM material, and near its spontaneous magnetic ordering temperature (the Curie temperature, T_C) for a FM material.
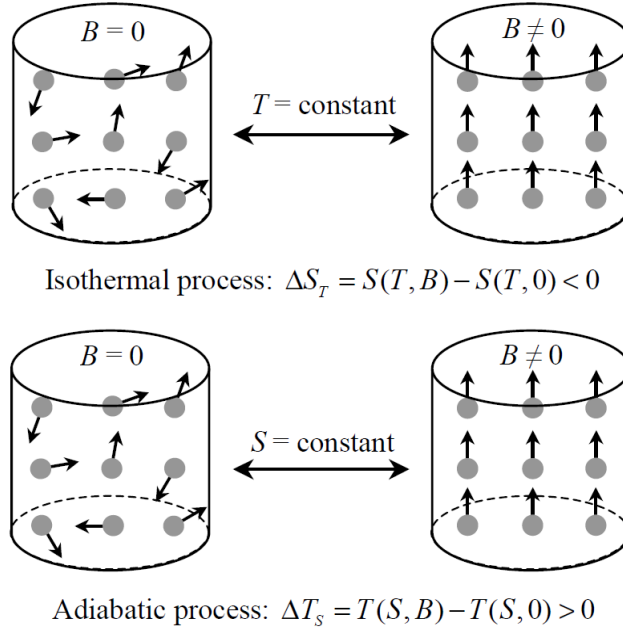
Figure 1.1: Schematic representation for application of magnetic field in two basic thermodynamic processes. Total entropy change is non-zero and negative in the isothermal process, and temperature change is non-zero and positive in the adiabatic process.

1.3 Room-temperature MCE materials

1.3.1 Gd and its solid solutions

The rare-earth metal Gd, with a quite high saturation magnetic moment of 7.63 μ_B, is the only ferromagnetic element having the Curie temperature near room temperature [5]. This lanthanide undergoes a purely magnetic second-

order phase transition (SOPT) at $T_C = 293$ K. It has been regarded as a prototype material for room-temperature refrigeration since Brown *et al.* [6] reported its MCE in 1976. The magnetocaloric parameters of Gd at T_C were found to be $-\Delta S_T = 13.2$ J/kg·K and $\Delta T_S = 14$ K for a field change of 7 T [6]. However, the large MCE in Gd is significantly reduced by the existence of impurities [5].

The solid solutions of Gd have been extensively studied, such as Gd_{1-x} RE_x compounds with RE = lanthanide (Tb, Ho, Er and Dy) [7–9], $Gd_{1-x}M_x$ compounds with M = other elements (Ni, Al, Pd, Rh, In, Zn and B) [10–16]. It was found that the MCEs of these solutions do not increase significantly or even decrease with respect to the pure Gd and their Curie temperatures show a considerably decrease, which are not desirable for the application of room-temperature refrigeration.

1.3.2   Other series of compounds

In the room-temperature range, the so-called giant magnetocaloric (GMCE) was first observed in binary intermetallic compounds $Fe_{1-x}Rh_x$ ($0.47 \leq x \leq 0.53$) [17]. The GMCE of these compounds is negative because they undergo first-order phase transitions (FOPTs) from antiferromagnetic (AFM) to FM state. The high magnetocaloric properties in the $Fe_{1-x}Rh_x$ compounds result from the strong coupling of electronic and lattice systems in magnetic-field conditions, accompanied by a large thermal expansion (≈ 0.27 %) at the transition (in this case, the magnetic entropy change is slight) [17]. Unfortunately, the GMCE in the $Fe_{1-x}Rh_x$ compounds is irreversible, it can only be observed upon the application of a magnetic field to a fresh sample [18]. On the other hand, the very high cost of Rh (\$ 80,000 per kilogram) makes this system unsuitable for practical applications.

It is a milestone for developing room-temperature magnetic refrigerants that GMCE was discovered in the ternary compound $Gd_5Ge_2Si_2$ in 1997 by Pecharsky and Gschneidner [19]. The most prominent feature of $Gd_5(Ge_{1-x}Si_x)_4$ ($0.3 \leq x \leq 0.5$, 195 K $\leq T_C \leq$ 276 K) compounds is that the GMCE originates from the occurrence of a field-induced FOPT accompanied by a structural change, that is, from the FM phase with the orthorhombic Gd_5Si_4-type structure to the PM phase with the monoclinic $Gd_5Ge_2Si_2$-type structure [20]. With a small amount of Fe or other elements (Cu, Co, Ge, Mn and Al) doping, the structural transition is suppressed in $Gd_5Ge_2Si_2$, leaving only a single orthorhombic phase over the transition range, meanwhile, the transition temperature is slightly shifted to higher temperatures. The elemental doping makes the transition be of second-order, which eliminates the large hysteresis

loss presenting in $Gd_5Ge_2Si_2$ [21, 22]. The substitution of Gd by other rare-earth elements (e.g. Nd, Tb, Dy, and Ho) results in a significant decrease of T_C, which departs from the room-temperature range [23–26].

Since the GMCE of $Gd_5Ge_2Si_2$ was reported, much attention has been paid to the materials undergoing FOPTs. MnAs is a well-known ferromagnet undergoing a magnetostructural FOPT. The FM NiAs-type hexagonal structure transforms to the PM MnP-type orthorhombic structure at $T_{C,h} = 317$ K in a heating process, and the inverse one occurs at $T_{C,c} = 306$ K in a cooling process [27]. GMCE with the same order of magnitude as in $Gd_5(Ge_{1-x}Si_x)_4$ compounds was observed in MnAs [28–30]. The partial substitution of Sb for As causes a decrease in both of the transition temperature and the thermal hysteresis. The nature of the transition in the $Mn(As_{1-x}Sb_x)$ compounds changes from first- to second-order when the Sb content is higher than 0.3, leading to a reduction of the MCE [29, 31]. Recently, the so-called "colossal" MCE was reported in the Fe-doped compounds $Mn_{1-x}Fe_xAs$, displaying a very high and sharp peak in ΔS_T vs. T curve [32]. However, the "colossal" MCE is merely a spurious spike, which is ubiquitous in materials showing FOPTs when ΔS_T is deduced from isothermal magnetization data. The details of the source and characteristics of the spurious spike, as well as how to avoid or weaken the "spike" effect will be discussed in chapter 4.

$LaFe_{13-x}Si_x$ intermetallic compounds, which crystallize in the cubic $NaZn_{13}$-type structure, are also a series of promising candidates as magnetic refrigerants for room-temperature refrigeration due to their low cost of row materials and GMCE originating from a field-induced first-order itinerant electron metamagnetic (IEM) transition [33–36]. Whereas there are still, at least, two main drawbacks in these materials to be practical refrigerants. One is the quite long annealing time (few weeks) in order to achieve a single-phase bulk [33–35]. Another one is that the transition temperatures of these compounds ($\sim$ 200 K) are too low away from room temperature. A great deal of effort has been done to overcome these problems, such as to shorten the annealing time by using melt-spinning technique in sample preparation, and to raise the transition temperature by increasing the concentration of Si, substituting Fe with Co, or adding interstitial H or C atoms [33–40]. It was found that the increase of the content of Si, Co or C results in the absence of the IEM transition. The nature of the transition becomes second order, reducing significantly the MCE. Although the first-order IEM transition and the GMCE are maintained in the H-interstitial compounds, the stability is not as good as expected. Moreover, a large volume change of 1.5 % is associated with the phase transition in these compounds [41]. This has to be taken into account in the practical application, because the material will definitely become very brittle and probably break into small grains when this volume change is performed very frequently.

In 2002, Tegus *et al.* pointed out that $MnFeP_{1-x}As_x$ compounds show promising MCE properties [42]. The magnitude of the MCE in the $MnFeP_{1-x}As_x$ compounds is higher than in Gd metal, and comparable to other compounds which undergo FOPTs, such as the famous $Gd_5(Ge_{1-x}Si_x)_4$ compounds. The GMCE in the $MnFeP_{1-x}As_x$ compounds originates from a field-induced metamagnetic FOPT. Unlike what happens in the $Gd_5(Ge_{1-x}Si_x)_4$ compounds, the hexagonal Fe_2P-type crystallographic structure does not change below and above the transition, but a sharp decrease of the *a*-axis lattice parameter and a sharp increase of the *c*-axis lattice parameter happen in going from FM to PM phase. The benefits of this family of compounds are: First, the transition temperature is tunable between 150 K and 350 K (covering the room-temperature range) by varying As content between 0.25 and 0.65 without losing the GMCE properties [43–45]. Second, the use of abundant transition metals Mn and Fe makes them more applicable than other rare elements (e.g. Gd) in magnetic refrigeration applications. However, the presence of the toxic element As could be hazardous for the use in a domestic kitchen. Recently, it has been found that As can be replaced completely by Si and / or Ge, simultaneously keeping the GMCE properties [46–52]. Unluckily, the introduction of Si and Ge results in an increase of thermal hysteresis, which gives rise to energy losses in a magnetic-field cycle. Anyhow, the excellent magnetocaloric features of MnFe(P,Si,Ge) compounds make them be attractive candidate materials for a commercial magnetic refrigerator.

For excellent reviews on magnetocaloric materials, see references [3, 53–57].

1.4   Magnetic refrigeration

Magnetic refrigeration is a cooling technology based on the MCE. It has a long history [58] and plays a very important role in cryogenic field. Its roots can be traced back to Warburg's discovery of the MCE of Fe in 1881. The originally fundamental principle of the magnetic refrigeration via adiabatic demagnetization was independently proposed by Debye [59] in 1926 and Giauque [60] in 1927. In 1933, Giauque and MacDougall first successfully achieved temperatures (from 3.5 K to 0.25 K) below the liquid helium temperature via adiabatic demagnetization refrigeration [61]. Between 1933 and 1976, a number of advances in the utilization of the MCE for magnetic refrigeration were reported [18, 62–64], but most were concerned with the refrigeration below 20 K. The true beginning of near room-temperature magnetic refrigeration was a published seminal paper and a designed reciprocating magnetic refrigerator operating with Gd plates in 1976 by Brown [6]. Following the work of Brown, many magnetic refrigerator prototypes have been built in laboratories over the

world, see reviews [65, 66].

Analogous to a gas-compression / expansion refrigerator, magnetic refrigerators have to operate with a cycle, e.g. the Carnot cycle, the Stirling cycle or the Ericsson cycle. A typical cycle for the gaseous refrigeration includes four processes, so the same for the magnetic refrigeration. The cycle is illustrated with the help of figure 1.2, as follows:

- Adiabatic magnetization a → b: When a magnetic refrigerant is placed in a thermal insulated environment, applying an external magnetic field causes an increase of temperature of the refrigerant because of its MCE.

- Isofield heat extraction b → c: Then this added heat (the MCE) is removed to its surroundings by a heat-transfer medium, such as, water and helium gas. The magnetic field is kept constant to prevent the magnetic spin system from reabsorbing the heat.

- Adiabatic demagnetization c → d: Once the magnetic refrigerant is cooled sufficiently by the coolants, the magnetic field is removed adiabatically. The temperature of the refrigerant reduces due to its MCE.

- Isofield heat absorption d → a: The magnetic field is held constant (0 T), preventing the magnetic refrigerant from heating back up. The refrigerant is in thermal contact with a heat load and absorbs heat. Once the refrigerant and the heat load reach a thermal equilibrium state, the cycle finishes, and a new one begins.

1.5 Motivation of this Thesis

The main motivation of this Thesis is to precisely characterize the MCE of materials exhibiting FOPTs by means of isofield magnetization, isothermal magnetization, heat capacity, and direct measurements, as well as to seek applicable materials as refrigerants for magnetic refrigeration near room temperature.

The isothermal entropy change of a magnetic material quantifies the heat transferred between the hot and cold sinks, and the adiabatic temperature change is related to the operating temperature span. Both of them are crucial to the achievement of magnetic refrigeration. Recently, the huge values of ΔS_T for some hysteretic materials derived from isothermal magnetization with the help of the Maxwell relation have been questioned, such as in La(Fe,Si)$_{13}$ [67], MnAs [68] and MnFe(P,Ge) [69]. All these materials have been regarded as promising candidates for refrigerants and could be employed as refrigerants
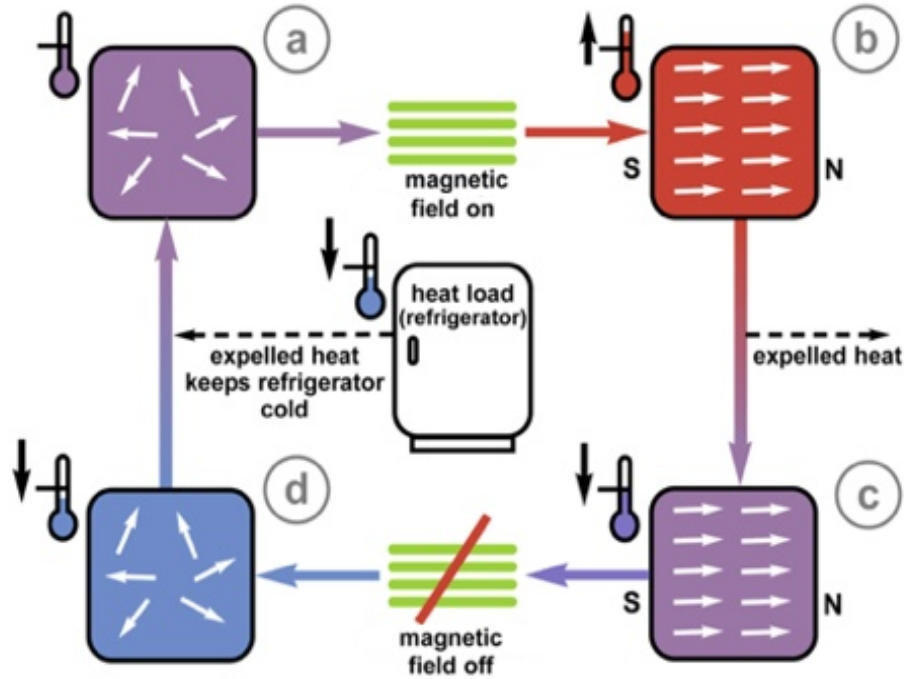
Figure 1.2: Schematic representation of a magnetic refrigeration cycle which transports heat from a heat load to its surroundings.

for magnetic refrigerators in the future. Therefore, from both the fundamental and the practical application points of view, it is meaningful to precisely determine the magnetocaloric parameters of the materials which show their advantages to be used as working refrigerants. To this end, the structural, magnetic, calorimetric and magnetocaloric properties for different types of materials, such as $Gd_5Si_2Ge_2$-type, $La(Fe,Si)_{13}$-type, MnAs-type, MnFe(P,Ge)-type and $MnCoGeB_x$-type compounds, were studied by means of X-ray diffraction, magnetization, heat capacity and direct measurements.

In order to get correct and precise MCE by different techniques, the magnetic and direct measurements have been performed following some special ways and the corrections of irreversibility were made. The discrepancies in the results determined by the different methods were explained with the help of magnetic phase diagrams.

Chapter 2

Theoretical aspects

2.1 Thermodynamic functions

Let us consider a thermodynamic function, the Gibbs free energy, which can fully describe the magnetocaloric properties of magnetic systems. When the system is at a magnetic field B at a temperature T under a pressure p, the Gibbs free energy G is given by:

$$G = U - TS + pV - MB \tag{2.1}$$

where U, S, V and M are the internal energy, total entropy, volume and magnetization of the system, respectively.

The total differential of G can be written as:

$$dG = V\,dp - S\,dT - M\,dB \tag{2.2}$$

Accordingly, the parameters S, V and M are given by the first derivatives of G, as follows:

$$S(T, B, p) = -\left(\frac{\partial G}{\partial T}\right)_{p,B} \tag{2.3}$$

$$V(T, B, p) = \left(\frac{\partial G}{\partial p}\right)_{T,B} \tag{2.4}$$

$$M(T, B, p) = -\left(\frac{\partial G}{\partial B}\right)_{T,p} \tag{2.5}$$

One of the so-called magnetic Maxwell relations can be obtained by making the derivative for equations (2.3) and (2.5):

$$\left(\frac{\partial S}{\partial B}\right)_{T,p} = \left(\frac{\partial M}{\partial T}\right)_{p,B} \tag{2.6}$$

The heat capacity C at constant external pressure and magnetic field is represented as the second derivative of G with respect to temperature:

$$C_{p,B} = -T \left(\frac{\partial^2 G}{\partial T^2} \right)_{p,B} \qquad (2.7)$$

Taking into account equation (2.3), equation (2.7) is written as:

$$C_{p,B} = T \left(\frac{\partial S}{\partial T} \right)_{p,B} \qquad (2.8)$$

The total differential of the total entropy of the magnetic system expressed as a function of T, B and p is written as:

$$dS = \left(\frac{\partial S}{\partial T} \right)_{p,B} dT + \left(\frac{\partial S}{\partial B} \right)_{T,p} dB + \left(\frac{\partial S}{\partial p} \right)_{T,B} dp \qquad (2.9)$$

One can see in equation (2.9), dS consists of three components, the first term is due to the change of temperature, the second one is induced by the change of magnetic field and the last one is related to the change of pressure. Here, it has to be noted that all the following cases are considered as reversible processes. Irreversible processes will be discussed in section 2.7 independently. For isothermal and isobaric processes (i.e. $dT = 0$ and $dp = 0$), only the second term is non-zero. Using the Maxwell relation (2.6), the differential of isothermal-isobaric entropy change induced by a change of magnetic field can be presented in the form:

$$dS = \left(\frac{\partial M}{\partial T} \right)_{p,B} dB \qquad (2.10)$$

The isothermal entropy change (ΔS_T) for a field change $\Delta B = B_f - B_i$ (from an initial field B_i to a final field B_f) can be calculated from the integral of equation (2.10):

$$\Delta S_T = \int_{B_i}^{B_f} \left(\frac{\partial M}{\partial T} \right)_{p,B} dB \qquad (2.11)$$

According to equation (2.11), the MCE of materials is proportional to $(\partial M / \partial T)_{p,B}$. Since magnetization changes rapidly at the temperature of a magnetic phase transition and slowly out of the transition region, a MCE peak located in the transition region is expected for simple ferromagnets [70].

Under adiabatic and isobaric conditions (i.e. $dS = 0$ and $dp = 0$), the left hand side and the pressure term in the right hand side of equation (2.9) are equal to zero. Using equations (2.6), (2.8) and (2.9), the differential of

an adiabatic-isobaric temperature change caused by a change of magnetic field can be expressed as:

$$dT = -\frac{T}{C_{p,B}} \left(\frac{\partial M}{\partial T}\right)_{p,B} dB \qquad (2.12)$$

Accordingly, the adiabatic temperature change (ΔT_S) for a magnetic field change ΔB can be determined from the integral of equation (2.12):

$$\Delta T_S = -\int_{B_i}^{B_f} \frac{T}{C_{p,B}} \left(\frac{\partial M}{\partial T}\right)_{p,B} dB \qquad (2.13)$$

2.2 Total entropy, isothermal entropy change and adiabatic temperature change

Generally speaking, the total entropy of a magnetic substance is usually assumed to consist of several independent contributions, from the crystalline lattice (S_l) and from the conduction electrons (S_e), besides, the magnetic contributions from the atomic magnetic moments (S_m) and from the atomic nucleus (S_n). Since S_n is only important at very low temperature (in mK), normally, it can be neglected. Thus the total entropy of the magnetic material at constant pressure is presented as:

$$S(T, B) = S_l(T, B) + S_m(T, B) + S_e(T, B) \qquad (2.14)$$

In the general case, the contributions S_l, S_m and S_e are supposed to depend on both temperature and magnetic field, and cannot be clearly separated. This is especially more obvious in the low temperature range (below 20 K), where the electronic contribution is much sensitive to the magnetic field. For the sake of simplicity, we assume in this section that S_l and S_e do not depend on the applied magnetic field but only on the temperature. Hence, the total entropy change induced by the magnetic field variation is attributed to the change of the magnetic entropy.

The lattice entropy is due to atomic motion. The simplest approximation to describe that is the Debye expression [53]:

$$S_l = N_a R \left[12 \left(\frac{T}{T_D}\right)^3 \int_0^{T_D/T} \frac{x^3}{e^x - 1} dx - 3\ln\left(1 - e^{T_D/T}\right)\right] \qquad (2.15)$$

where N_a is the number of atoms per formula unit in a material, R is the gas constant and T_D is the Debye temperature.

The electronic entropy is directly proportional to temperature with a slope given by the electronic heat-capacity coefficient γ_e :

$$S_e = \gamma_e T \tag{2.16}$$

From the statistical point of view, the magnetic entropy of a paramagnet consisting of N magnetic atoms with a quantum number J for the total angular momentum of an atom can be written as:

$$S_m(T, B) = N k_B \left[\ln \frac{\sinh\left(\frac{2J+1}{2J}x\right)}{\sinh\left(\frac{1}{2J}x\right)} - x B_J(x) \right] \tag{2.17}$$

where x is defined as:

$$x = \frac{gJ\mu_B B}{k_B T} \tag{2.18}$$

k_B is the Boltzmann constant; μ_B is the Bohr magneton; g is the spectroscopic splitting factor; and $B_J(x)$ is the Brillouin function which is in the form of:

$$B_J(x) = \frac{2J+1}{2J} \coth\left(\frac{2J+1}{2J}x\right) - \frac{1}{2J} \coth\left(\frac{x}{2J}\right) \tag{2.19}$$

In the case of high temperature and low field (i.e. $x \ll 1$), $B_J(x)$ can be expanded in a power series of x. Using the approximation $\sinh(x) \approx x$, the magnetic entropy of the paramagnet can be expressed as:

$$S_m(T, B) = N k_B \left[\ln(2J+1) - \frac{J+1}{3J}x^2 \right] \tag{2.20}$$

Magnetic entropy reaches the maximum in a completely disordered state, which may be realized for conditions $T \to \infty$ and $B = 0$. Consequently, neglecting the second term in the square bracket of equation (2.20), the maximum magnetic entropy is given by:

$$S_{m,\max} = N k_B \ln(2J+1) \tag{2.21}$$

According to equation (2.21), the limit of the magnetic entropy change for one mole of magnetic atoms is:

$$\Delta S_{m,\max} = N_A k_B \ln(2J+1) \equiv R \ln(2J+1) \tag{2.22}$$

where N_A is the Avogadro's constant.

Figure 2.1 shows schematically total entropy as a function of temperature for a simple ferromagnet near its Curie temperature at constant applied

magnetic fields, B_i and B_f. The total entropy increases with increasing temperature at a given magnetic field and decreases with increasing field at a given temperature. The change of a magnetic field from B_i to B_f can cause not only a finite decrease of entropy, but also a finite increase of temperature in the material.

Two relevant processes illustrating MCE are displayed in the entropy versus temperature diagram figure 2.1. According to the diagram, when the magnetic field is applied isothermally (i.e. from state A to B), the total entropy decreases from S to S' because of the reduction of magnetic contribution, therefore, the entropy change in the process is defined as:

$$\Delta S_T(T, \Delta B) = S' - S = S(T, B_f) - S(T, B_i) \tag{2.23}$$

Alternatively, when the magnetic field is applied adiabatically (i.e. from state A to C), the total entropy of the system keeps constant, whereas the magnetic part is reduced by applying the magnetic field, so the lattice entropy increases, resulting in a rise of temperature from T to T'. This temperature difference at the given temperature T is determined by:

$$\Delta T_S(T, \Delta B) = T' - T = T(S, B_f) - T(S, B_i) \tag{2.24}$$

And viceversa for the removal of the magnetic field in an isothermal condition and in an adiabatic condition.

Referring to equations (2.10) and (2.12), the differential of the temperature change can be written as:

$$dT = -\frac{T}{C_{p,B}} dS \tag{2.25}$$

In equation (2.25), it is straightforward to see that the differentials of the entropy change and the temperature change have opposite signs, namely, the magnetocaloric parameters ΔS_T and ΔT_S have opposite signs.

Assuming that $T/C_{p,B}$ is a constant, that is reasonable only in the region far away from a phase transition where heat capacity is less dependent on magnetic field, thus the integral of equation (2.25) (i.e. taking equation (2.11) into (2.13)) leads to:

$$\Delta T_S = -\frac{T}{C_{p,B}} \Delta S_T \tag{2.26}$$

In equation (2.26), it can be seen that the value of ΔT_S is proportional to $T/C_{p,B}$ (for the same ΔS_T) and a large ΔT_S is expected in materials with small total heat capacity. A large ΔT_S also corresponds to a large ΔS_T in a given material. It has to be noted that equation (2.26) does not hold strictly in the transition region for for both FOPT and SOPT.
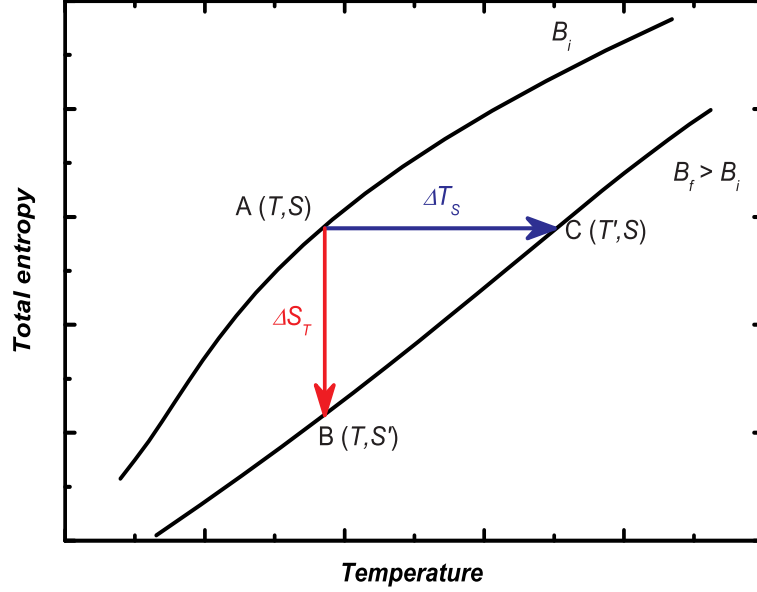
Figure 2.1: Temperature dependence of total entropy for a simple ferromagnet at constant magnetic fields B_i and B_f. Red arrowed line indicates an isothermal process from state A to B. The blue one represents an adiabatic process from state A to C.

According to figure 2.1, a true relationship between ΔS_T and ΔT_S is given by:

$$\Delta S_T(T) = -\int_{T}^{T+\Delta T_S} \frac{C_{p,B_f}(T)}{T} dT \tag{2.27}$$

or

$$\Delta S_T(T + \Delta T_S) = -\int_{T}^{T+\Delta T_S} \frac{C_{p,B_i}(T)}{T} dT \tag{2.28}$$

where C_{p,B_i} and C_{p,B_f} are heat capacities at the initial field B_i and the final field B_f, respectively. Equations (2.27) and (2.28) are simplified to equation (2.26) when $C_{p,B_i}/T = C_{p,B_f}/T = C_{p,B}/T$ is constant.

The negative ΔS_T or positive ΔT_S exhibited in magnetic materials is usually called normal MCE, and for the opposite it is called inverse MCE. The normal MCE is observed in materials undergoing phase transitions from a disordered state to an ordered one upon the application of a magnetic field, for example, in most simple ferromagnets and ferrimagnets at their Curie temperatures and in all paramagnets. The inverse MCE takes place in a material

which shows a stable FM phase with large net magnetization at high temperature and a stable AFM or PM phase with small net magnetization at low temperature. In this case, the application of a strong enough field produces the ferromagnetism. The total entropy variation at the transition upon increasing field is positive if the electronic entropy increases and overcomes the magnetic part. For example, the inverse MCE in Mn_3GaC compound originates from a transition from AFM to FM phase (order-order). The application of a magnetic field adiabatically causes a very small change of magnetic entropy, but a significant increase of the electronic entropy, leading to a decrease of the lattice entropy in order to keep the total entropy unchanged [71]. The negative lattice entropy change stands for a decrease of the temperature of the sample, namely, the inverse MCE.

2.3 Heat capacity

Heat capacity is a fundamental physical quantity of materials. It indicates how much thermal energy δQ a physical body can absorb for a change of temperature δT. The heat capacity of a substance at an arbitrary temperature T is defined as:

$$C = \lim_{\delta T \to 0} \frac{\delta Q}{\delta T} \tag{2.29}$$

When we consider a nonmagnetic material, whose heat capacity consists of the lattice and electronic contributions, there are two principal heat capacities, the isobaric heat capacity C_p (at constant pressure) and the isovolumetric heat capacity C_v (at constant volume). According to equation (2.8), C_p and C_v can be written as:

$$C_p = \left(\frac{dQ}{dT}\right)_p = T\left(\frac{\partial S}{\partial T}\right)_p \tag{2.30}$$

$$C_v = \left(\frac{dQ}{dT}\right)_v = T\left(\frac{\partial S}{\partial T}\right)_v \tag{2.31}$$

For most solids the difference between C_p and C_v is small (about 5 % at room temperature) and it rapidly decreases with decreasing temperature [53]. It should be noted that $C_p - C_v = R$ for ideal gases, where R is the gas constant.

In the case of magnetic materials, the total heat capacity at constant pressure C_p, includes three contributions, namely, the lattice heat capacity $C_{p,l}$, the electronic heat capacity $C_{p,e}$ and the magnetic heat capacity $C_{p,m}$:

$$C_p = C_{p,l} + C_{p,e} + C_{p,m} \tag{2.32}$$

Although the total heat capacity of a sample can be determined experimentally with high accuracy, the individual heat-capacity contributions from different physical sources are not easily estimated. In general, the lattice heat capacity at constant volume $C_{v,l}$, instead of $C_{p,l}$ (the difference between $C_{v,l}$ and $C_{p,l}$ is very small for a solid), is estimated with the Debye model [53]. In the framework of the Debye model, the vibrations of the atomic lattice are treated as phonons in a box, and the lattice heat capacity is expressed as:

$$C_{p,l} \approx C_{v,l} = 9N_a R \left[4 \left(\frac{T}{T_D} \right)^3 \int_0^{T_D/T} \frac{x^3}{e^x - 1} dx - \frac{T_D/T}{e^{T_D/T} - 1} \right] \qquad (2.33)$$

For the high temperature limit, $T \gg T_D$, using the approximation $e^x - 1 \approx x$ if $| x | \ll 1$, equation (2.33) leads to:

$$C_{p,l} \approx 3N_a R \qquad (2.34)$$

Equation (2.34) matches well the Dulong-Petit law which predicts that the limit of the heat capacities of solids with a relatively simple structure (containing one atom in a formula unit) is $3R$ at high temperatures. At low temperatures, $T \ll T_D$ equation (2.33) becomes:

$$C_{p,l} \approx \frac{12\pi^4}{5} N_a R \left(\frac{T}{T_D} \right)^3 \qquad (2.35)$$

Equation (2.35) describes the heat capacity going to zero as a T^3 power law, which agrees well with experimental observation. The Debye model predicts correctly the heat-capacity behavior of a solid at low and high temperatures, but due to the simple assumptions, its accuracy reduces at intermediate temperatures.

In metals, besides the lattice contribution to the internal energy, the electronic contribution of the conduction electron subsystem has to be considered. The electronic contribution to heat capacity is proportional to T at any temperature and may become a dominant term at very low temperatures. Taking into account the Fermi-Dirac statistics of electrons in metals and their band energetic structures, the electronic heat capacity is given by:

$$C_{v,e} = \frac{\pi^2}{3} k_B^2 D(E_F) T = \gamma_e T \qquad (2.36)$$

where $\gamma_e = \pi^2 k_B^2 D(E_F)/3$ is the electronic heat-capacity coefficient and $D(E_F)$ is the electron density of states at the Fermi energy E_F. It has to be noted that $C_{v,e}$ is a linear function of T in the whole temperature range, because the

free electron heat-capacity concept is assumed to be valid even at very high temperatures.

For nonmagnetic solids, the total heat capacity at constant pressure and constant magnetic field in the low temperature region ($T \ll T_D$) can be represented by:

$$C_{p,B} \approx C_{v,B} = \gamma_e T + \frac{12\pi^4}{5} N_a R \left(\frac{T}{T_D}\right)^3 \qquad (2.37)$$

In order to evaluate the value of γ_e, equation (2.37) is converted to the form:

$$C_{p,B}/T \approx \gamma_e + \alpha T^2 \qquad (2.38)$$

where $\alpha = 12\pi^4 N_a R/(5T_D^3)$. The coefficient γ_e and the Debye temperature T_D can be evaluated from the plot of $C_{p,B}/T$ versus T^2 at low temperature by taking the value of the intercept at $T = 0$ K and the slope of the straight line, respectively.

Once the total experimental heat capacity of a magnetic solid is measured, the magnetic contribution can be deduced using equations (2.32), (2.35) and (2.36). It is a general way to obtain the magnetic heat capacity by most scientists for studying the magnetic phase transition.

2.4 Enthalpy and entropy changes at a transition

If the total heat capacity of a system is known, the enthalpy H and entropy S of the system at arbitrary temperature T can be written as:

$$H = H(0) + \int_0^T C_p dT \qquad (2.39)$$

$$S = S(0) + \int_0^T \frac{C_p}{T} dT \qquad (2.40)$$

where $H(0)$ and $S(0)$ are the enthalpy and entropy at absolute 0 K, and both are equal to zero according to the Third Law of Thermodynamics.

As a matter of fact, the heat-capacity measurements are usually carried out starting from some temperatures above 0 K, depending on the experimental conditions. Therefore, equations (2.39) and (2.40) are written as:

$$H = H(T_0) + \int_{T_0}^T C_p dT \qquad (2.41)$$

$$S = S(T_0) + \int_{T_0}^T \frac{C_p}{T} dT \qquad (2.42)$$

where $H(T_0)$ and $S(T_0)$ are the enthalpy and entropy at temperature T_0, respectively. In this Thesis, $H(T_0)$ and $S(T_0)$ are evaluated on the basis of the Debye model. Although $H(T_0)$ and $S(T_0)$ are added without considering the magnetic and electronic contributions, it has no influence on the main results we obtain.

Since, both, enthalpy H and entropy S are state functions, the change of the enthalpy or entropy is more important than itself. The enthalpy change ΔH and the entropy change ΔS of a system in a temperature range from T_1 to T_2 are given by:

$$\Delta H(T_1 \to T_2) = \int_{T_1}^{T_2} C_p dT \tag{2.43}$$

$$\Delta S(T_1 \to T_2) = \int_{T_1}^{T_2} \frac{C_p}{T} dT \tag{2.44}$$

For a material undergoing a phase transition, the heat capacity shows an anomaly, leading to abnormal changes of the enthalpy and entropy at the transition temperature, no mater what the order of the transition is (FOPT or SOPT). The heat capacity is usually treated as composed of two parts, a continuous one called *normal* contribution corresponding to the degrees of freedom not involved in the ordering process, and another discontinuous one called *anomalous* contribution for the degrees of freedom associated to the ordering process. Thus the variations of the enthalpy and entropy, namely, the anomalous enthalpy and entropy changes at the transition can be obtained:

$$\Delta H_{an}(T_1 \to T_2) = \int_{T_1}^{T_2} (C_p - C_{nor}) dT \tag{2.45}$$

$$\Delta S_{an}(T_1 \to T_2) = \int_{T_1}^{T_2} \frac{C_p - C_{nor}}{T} dT \tag{2.46}$$

where T_1 and T_2 are two temperatures far below and above the transition, respectively. C_{nor} is the sum of lattice and electronic heat capacities. ΔH_{an} is a practical determination of the discontinuity of H and means the latent heat of a FOPT. Equations $(2.39) - (2.46)$ also fulfil the calculation of H, ΔH, ΔH_{an}, S, ΔS and ΔS_{an} from the heat capacity at constant applied magnetic fields.

As is known, SOPTs are defined as that, the first derivatives of the thermodynamic potential with respect to temperature are continuous functions and the second derivatives undergo a discontinuous change. For a practical material undergoing a SOPT, the enthalpy and entropy change continuously with temperature at zero field or constant magnetic field. Whereas, discontinuous

changes (jumps) of enthalpy and entropy at the transition temperature are observed at the point of a FOPT, in which there is a sharp heat-capacity peak at the transition temperature due to the accompanied latent heat. For materials exhibiting sharp FOPTs, the latent heat L can be regarded as equalling to the transition enthalpy, and are calculated using equation (2.45). In a real material, the normal contributions are hardly extracted from total heat capacity, because they are different for each phase. Generally, the FOPTs take place in a very narrow temperature range and a sigmoidal type of the normal heat capacity is expected at the transition. For the sake of simplicity, a line with one step at the temperature of the heat-capacity peak is used instead of the sigmoidal variation. This procedure makes a very small error when evaluating the integral.

Consequently, referring to equations (2.45) and (2.46), the enthalpy and entropy changes at a transition can be represented by:

$$\Delta H_{an}(T_1 \rightarrow T_2) = \int_{T_1}^{T_C} (C_p - C_{LP})dT + \int_{T_C}^{T_2} (C_p - C_{HP})dT \qquad (2.47)$$

$$\Delta S_{an}(T_1 \rightarrow T_2) = \int_{T_1}^{T_C} \frac{(C_p - C_{LP})}{T}dT + \int_{T_C}^{T_2} \frac{(C_p - C_{HP})}{T}dT \approx \frac{\Delta H_{an}}{T_C} \qquad (2.48)$$

where T_C is the transition temperature where the heat-capacity peaks. C_{LP} and C_{HP} are the normal heat capacities of the stable phases below and above T_C, respectively.

As an example, figure 2.2 shows the computation of the transition enthalpy for $Mn_{0.997}Co_{0.003}As$. In the calculation, C_{LP} and C_{HP} are assumed to be linearly dependent on temperature, denoted by two straight lines. In this case, the latent heat equals the transition enthalpy which is taken as the area enclosed by the heat-capacity anomaly and the two lines.

Moreover, the entropy change at a FOPT, when it takes place at the equilibrium point of two phases in a magnetizing or demagnetizing process, is also given by the magnetic Clausius-Clapeyron equation:

$$\Delta S = -\frac{dB}{dT_t}\Delta M \qquad (2.49)$$

where ΔS and ΔM are the differences of the entropy and magnetization between two magnetic phases at the transition temperature T_t. dB/dT_t can be deduced from the magnetic phase diagram.
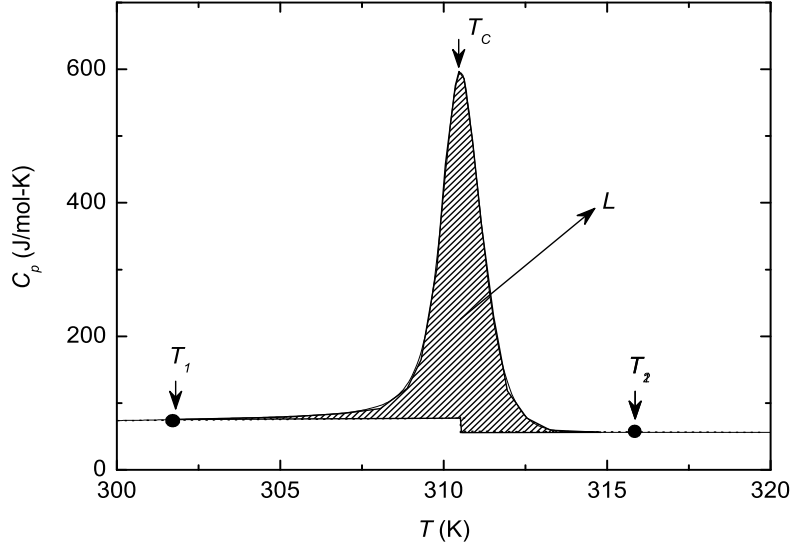
Figure 2.2: Temperature dependence of the heat capacity at zero field for $Mn_{0.997}Co_{0.003}As$. The value of shaded area indicates the latent heat associated to a FOPT. The stepped line represents the normal heat capacity.

2.5   Refrigeration capacity

Gschneidner *et al.* proposed refrigeration capacity for evaluating the cooling power of magnetic refrigerants for use in magnetic refrigeration [72]. The refrigeration capacity is defined as:

$$RC^S = \int_{T_1}^{T_2} \Delta S_T(T) dT \tag{2.50}$$

$$RC^T = \int_{T_1}^{T_2} \Delta T_S(T) dT \tag{2.51}$$

where T_1 and T_2 are temperatures of the hot and cold sinks, respectively. Thus, the quantity RC^S indicates how much heat can be transferred between the cold and hot sinks in one ideal refrigeration cycle. The value of RC^T has K^2 dimension, and may be useful for the numerical comparison of different magnetocaloric materials.

Later, Gschneidner *et al.* pointed out that refrigeration capacity can also be characterized by the MCE peak value and its full width at half maximum

(δT_{FWHM}) [63]. The so-called relative cooling power is expressed as:

$$RCP^S = \Delta S_{T,\max} \times \delta T_{FWHM} \tag{2.52}$$

$$RCP^T = \Delta T_{S,\max} \times \delta T_{FWHM} \tag{2.53}$$

In the case of ΔS_T, the value of RCP^S is found to be close to $4/3$ times RC^S. A large RC^S or RCP^S for the same field variation generally indicates a better magnetocaloric material.

For materials exhibiting hysteresis, the energy loss during one magnetic field loop must be taken into account when evaluating the usefulness of a magnetic refrigerant being subjected to the cyclic fields. The effective refrigeration capacity (RC_{eff}) can be obtained by subtracting the average hysteretic loss from RC [21]. The energy loss in a process on increasing or decreasing field is approximately taken as one half of the area enclosed by a magnetization loop, $Q_{loss} = -\frac{1}{2} \oint M dB$.

2.6 The Bean-Rodbell model

Bean and Rodbell have proposed a phenomenological model to describe the magnetostructural FOPT in MnAs [73]. The framework of the model was extended to explain the FOPTs occurring in $MnFeP_{1-x}As_x$ [74, 75], $Gd_5(Ge_{1-x}Si_x)_4$ [76] and $MnAs_{1-x}Sb_x$ [77] series of compounds. In this section, we introduce the Bean-Rodbell model.

The Bean-Rodbell model is based on the molecular mean field approximation. The central consideration of the model is that the exchange interaction parameter (or the Curie temperature) is a strong function of the lattice spacing. The volume change dependence of the Curie temperature is given by:

$$T_C = T_0[1 + \beta(V - V_0)/V_0] \tag{2.54}$$

where T_C is the Curie temperature, and T_0 would be the Curie temperature if the lattice were not compressible. V is the volume, and V_0 would be the volume in the absence of exchange interactions. β is the slope of the Curie temperature dependence on the lattice deformation, and may be positive or negative.

In the Bean-Rodbell model, for a magnetic system with an ion total angular momentum J, the Gibbs free energy for the system, in the absence of external pressure, is given by:

$$G(T, B) = -BM_s\sigma - \frac{3}{2}\left(\frac{J}{J+1}\right)Nk_BT_C\sigma^2 + \frac{1}{2K}\left(\frac{V-V_0}{V_0}\right)^2 - TS_m \tag{2.55}$$

where the first term on the right hand side is the Zeeman energy, the second is the exchange interaction on the basis of the molecular mean field approximation, the third is elastic energy due to the distortion of lattice, and the last is entropy term. N is the number of magnetic ions per unit volume, B is external magnetic field, $M_s = NgJ\mu_B$ is saturation magnetization (where g is the Landé factor, and μ_B is the Bohr magneton), the relative magnetization σ is normalized by M_s, k_B is the Boltzmann constant, $K = -V^{-1}(\partial V/\partial p)_{T,B}$ is the isothermal compressibility, assumed to be constant, T is temperature, and S_m is the entropy of the spin system. Here we neglect other terms, in particular the lattice entropy, since the main conclusions may be drawn from this simplified form and we do not expect to fit precisely the experimental results. Minimizing the Gibbs free energy G with respect to volume, we obtain the equilibrium volume equation for spin J to be:

$$\frac{V - V_0}{V_0} = \frac{3}{2}\left(\frac{J}{J+1}\right)Nk_BKT_0\beta\sigma^2 \qquad (2.56)$$

This equality shows that the volume change is due to the effect of magnetization.

By substitution of equations (2.54) and (2.56) into (2.55), we expand the entropy term into a power series of σ and after collecting the terms with the same power of σ (neglecting powers higher than σ^6), we have:

$$\frac{G(\sigma) - G(0)}{Nk_BT_0} = -\frac{BM_s\sigma}{Nk_BT_0} + a_J\left(\frac{T}{T_0} - 1\right)\sigma^2 + b_J\left(\frac{T}{T_0} - \eta_J\right)\sigma^4 + c_J\frac{T}{T_0}\sigma^6 \tag{2.57}$$

where

$$a_J = \frac{3}{2}\left(\frac{J}{J+1}\right) \qquad (2.58)$$

$$b_J = \frac{9}{20}\frac{[(2J+1)^4 - 1]}{[2(J+1)]^4} \qquad (2.59)$$

$$c_J = \frac{1}{2}\frac{J}{(J+1)^5}\left(\frac{99}{175}J^4 + \frac{198}{175}J^3 + \frac{63}{50}J^2 + \frac{243}{350}J + \frac{243}{1400}\right) \qquad (2.60)$$

$$\eta_J = \frac{5}{2}\frac{[4J(J+1)]^2}{[(2J+1)^4 - 1]}Nk_BKT_0\beta^2 \qquad (2.61)$$

Performing the derivative of equation (2.55) with respect to σ, the magnetic state equation is obtained:

$$\sigma = B_J\left(\frac{\langle y \rangle}{T}\right) = B_J\left\{\frac{1}{T}\left[\frac{NgJ\mu_B}{k_B}B + 2a_JT_0\sigma + 4b_J\eta_JT_0\sigma^3\right]\right\} \qquad (2.62)$$

where $B_J(\langle y \rangle / T)$ is the Brillouin function. The mean field $\langle y \rangle$, which would produce the same free energy for a system without interacting spins, is magnetization dependent.

In statistical mechanics, the entropy is a logarithmic measure of the density of states. Specifically, it is:

$$S = -R \sum_m P_m \ln(P_m) \tag{2.63}$$

where P_m is the occupation probability of the magnetic energy level E_m, and has the form:

$$P_m = \frac{1}{Z} \exp\left(-\frac{E_m}{k_B T}\right) \tag{2.64}$$

where Z is the partition function. Taking the energy levels as $E_m = -m_J g \mu_B \langle y \rangle$ ($m_J = J, J-1, \cdots, -J$), Z can be expressed as:

$$Z = \sum_{m=-J}^{J} \exp\left(-\frac{E_m}{k_B T}\right) = \sinh\left(\frac{2J+1}{2J}Y\right) \Big/ \sinh\left(\frac{1}{2J}Y\right) \tag{2.65}$$

where $Y = \langle y \rangle / T$. Substituting equations (2.64) and (2.65) into (2.63), the expression of the magnetic entropy is obtained:

$$S_m(T, B, T_0, \eta_J) = R \left[\ln Z - \frac{1}{Z} \sum_{m=-J}^{J} \left(\frac{m_J g \mu_B \langle y \rangle}{k_B T}\right) \exp\left(\frac{m_J g \mu_B \langle y \rangle}{k_B T}\right)\right] \tag{2.66}$$

According to the Landau theory of phase transitions, the magnetic system undergoes a FOPT when $\eta_J > 1$. Otherwise, if $\eta_J < 1$, a SOPT occurs. It is worth while to point out that $\eta_J = 0$ leads equation (2.62) to the molecular mean field approximation in which the Brillouin function contains only the linear term in σ.

2.7 Irreversibility of first-order transitions

Magnetization and entropy are the first derivatives on magnetic field and temperature of the thermodynamic potential G, respectively. For SOPTs, both are continuous functions of temperature and field, so the whole process is fully reversible. The transition occurs at the equilibrium point, where $\Delta G = 0$. However, for FOPTs, the transition could occur beyond the equilibrium point from a metastable state to a stable one, that means $\Delta G < 0$ and the process is irreversible. In the case of a magnetic material, the transition takes place

at a higher temperature on heating or a higher filed on increasing field than the equilibrium point, and the contrary on cooling and decreasing field, resulting in the existence of thermal and magnetic hysteresis. In this section, we shall quantitatively discuss the effects of irreversibility on the magnetocaloric parameters for FOPTs on the basis of the Bean-Rodbell model.

2.7.1 Irreversibility of isofield entropy determined from heat capacity

Referring to the description of the Bean-Rodbell model in the previous section, the thermodynamic functions, Gibbs free energy and entropy, of a spin system can be obtained using equations (2.57) and (2.66), respectively. Figure 2.3(a) shows entropy as a function of temperature predicted on the basis of the Bean-Rodbell model with the parameters $J = 1.5$, $g = 2.27$, $\eta = 2$, $T_0 = 285$ K and $B = 2$ T, as well as the Debye model $T_D = 305$ K and 2 atoms per formula unit (e.g. in the case of MnAs). Here, we assume that the electronic contribution is small and the lattice entropy is independent of magnetic field. To illustrate the irreversible process, the Gibbs free energy related to magnetic moment (the net Gibbs free energy) as a function of temperature is displayed in figure 2.3(b). In order to present a clear-cut graph, the other contributions are not included, while this omission does not influence the validity of discussions and conclusions in the following.

In figure 2.3(a), it is seen that $A' - M - B'$ are unstable states because $dS/dT < 0$. These are absent in a real system, because any small fluctuation in the real system would move the state away and bring it to a metastable one with a local minimum of the Gibbs free energy. Between T_A and T_B, the equilibrium coexistence of PM and FM phases occurs at some temperature T_E. The states E and E' are determined by the condition that the values of the Gibbs free energy in the FM and PM phases are equal, i.e. the shadows in figure 2.3(a) are equal, (see also figure 2.3(b), where the points E and E' overlap, $G_E = G_{E'}$), namely:

$$G_{E'} - G_E = - \int_E^{E'} S dT = 0 \tag{2.67}$$

Therefore, the temperature at the state E is called the equilibrium temperature T_E, at which the transition should occur. In the presence of nucleation processes, the magnetization σ_E will go to $\sigma_{E'}$ in a sufficient time via a fluctuation which is large enough to overcome the energy barrier. The transition does not occur at T_E in a real material, but at a higher temperature in a heating process and at a lower temperature in a cooling process. That may be attributed to the fact that the energy barrier at T_E in the material is so high,

due to impurities, defects, intrinsic nature, etc., that the fluctuation cannot go over it.

In figure 2.3(b), it is easily found that $A - E'$ and $B - E$ are stable states, since their Gibbs free energies are the absolute minima. The Gibbs free energies at states $E' - B'$ and $E - A'$ are local minima but not absolute minima, hence they are metastable states. As mentioned previously, the states of $A' - M - B'$ are unstable. We assume that a transition takes place when the phase becomes unstable and the energy barrier reaches zero. In other words, the transitions occur at T_A on heating and at T_B on cooling. The temperature difference between T_A and T_B is the upper limit of the thermal hysteresis of the system. In the hysteretic region, both FM and PM phases coexist and the fraction of each phase depends on the temperature and magnetic field histories.

In a heating process, the FM phase remains up to T_A, where the energy barrier becomes zero and the state of the system jumps from A' to A. The Gibbs free energy at A' is higher than that at A, the difference is given by:

$$G_A - G'_A = - \int_{A'}^{A} S dT = -A_{A'B'A} \qquad (2.68)$$

or

$$G_A - G_{A'} = (H_A - H_{A'}) - T_A(S_A - S_{A'}) = \Delta H^h - T_A \Delta S^h \qquad (2.69)$$

where $A_{A'B'A}$ is the area enclosed by the curve $\widehat{A'B'A}$ and the vertical line AA', being positive. H and S represent the enthalpy and entropy of the system, respectively. ΔH is the anomalous enthalpy or the latent heat of a transition, it can be determined via heat-capacity measurements (see section 2.4). ΔS is the entropy variation at the transition. To distinguish it from a cooling process, we put the superscript h, indicating the heating process. Using equations (2.68) and (2.69), we obtain:

$$\Delta S^h = \frac{\Delta H^h}{T_A} + \frac{A_{A'B'A}}{T_A} > \frac{\Delta H^h}{T_A} \qquad (2.70)$$

The inequality implies that the anomalous entropy of the transition cannot be correctly estimated as $\Delta H^h/T_A$, but is higher by the amount $A_{A'B'A}/T_A$ due to the irreversibility of FOPTs. The term $A_{A'B'A}/T_A$ can be ascribed to an entropy production of the system at the transition. We name $\Delta H^h/T_A = \Delta S'^h$ as transition pseudo-entropy which can be deduced from experimental heat-capacity data.

In order to evaluate the difference, $\Delta S^h - \Delta S'^h$, namely, $A_{A'B'A}/T_A$, the area $A_{A'B'A}$ is considered as a triangle. Then we have $A_{A'B'A} = \Delta S^h(T_A -$
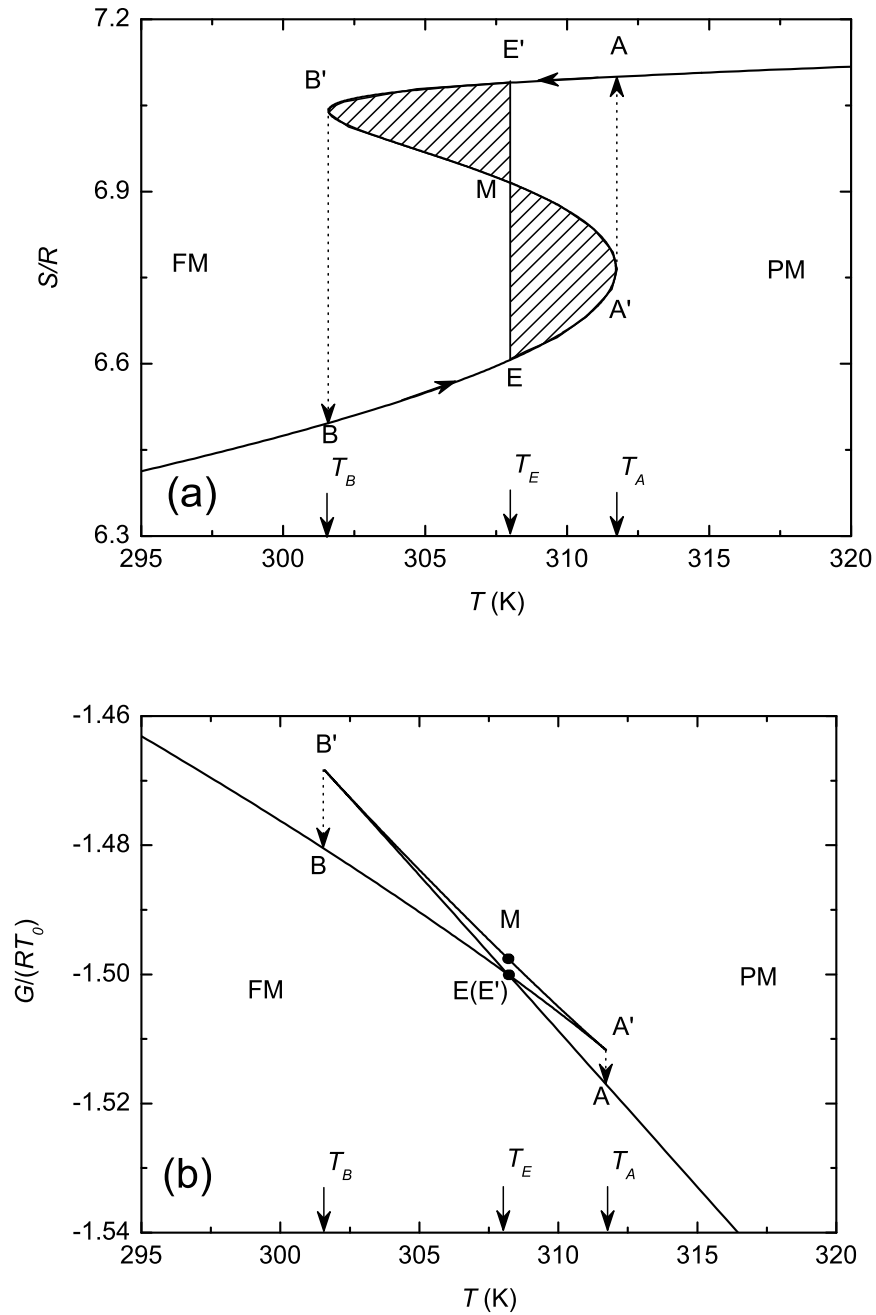
Figure 2.3: Theoretical prediction of the temperature dependence of the entropy (a) and the net Gibbs free energy (b) at a constant field $B = 2$ T obtained on the basis of the Bean-Rodbell model. $A - E'$ and $B - E$ represent stable states. $A' - M - B'$ represents unstable states. $E' - B'$ and $E - A'$ denote metastable states on cooling and heating, respectively.

$T_B)/2$. Substituting it into equation (2.70), we obtain:

$$\delta^h = \Delta S^h - \Delta S'^h = \Delta S'^h \left(\frac{T_A - T_B}{T_A + T_B} \right) \tag{2.71}$$

Similar analysis can be done when the system cools from high temperature. On cooling, the difference, $\Delta S^c - \Delta S'^c$ is given by:

$$\delta^c = \Delta S^c - \Delta S'^c = \Delta S'^c \left(\frac{T_B - T_A}{T_A + T_B} \right) \tag{2.72}$$

It should be noted that $\Delta H^h > 0$, $\Delta S^h > 0$, $\Delta S'^h > 0$ and $\delta^h > 0$ in heating processes, and $\Delta H^c < 0$, $\Delta S^c < 0$, $\Delta S'^c < 0$ and $\delta^c > 0$ in cooling processes. Accordingly, the absolute value of the transition entropy obtained from heat capacity is underestimated by the amount δ^h in heating processes, and overestimated by the amount δ^c in cooling processes. In other words, in a heating-cooling loop, the total difference of the pseudo entropy S' at the initial and final temperatures is $\delta^h + \delta^c$.

We define $T_{t,B}$ as the transition temperature at a magnetic field B, it is equal to the Curie temperature T_C when $B = 0$. Thus, the slopes of the transition temperatures shifted by the magnetic field are written as $k^h = dT_t^h/dB$ for heating processes and $k^c = dT_t^c/dB$ for cooling processes. Taking k^h and k^c as constants is reasonable, at least for most magnetic materials we know, such as MnFe(P,As), La(Fe,Si)$_{13}$ and Gd$_5$(Si,Ge)$_4$ series of compounds. Generally, k^c is greater than k^h, resulting in the coincidence of T_t^h and T_t^c at some temperature, T_{crit}, when the magnetic field reaches B_{crit} which corresponds to the critical point. Above the critical point, the nature of a FOPT disappears. Then we have:

$$\Delta T_{hys,0T} = T_{t,0T}^h - T_{t,0T}^c = B_{crit}(k^c - k^h) \tag{2.73}$$

where, $\Delta T_{hys,0T}$ is the hysteresis at zero field. $T_{t,0T}^h$ and $T_{t,0T}^c$ are the transition temperatures at zero field on heating and cooling, respectively.

The differences, δ^h and δ^c, also exist at magnetic fields. Both are field dependent due to the changes of the transition temperatures T_A and T_B as well as the transition pseudo-entropy $\Delta S'$ with field. We assume that both $\Delta S'^h$ and $\Delta S'^c$ decrease linearly with increasing field, being zero at the critical field. According to equations (2.71) − (2.73), the values of δ^h and δ^c at zero field and nonzero field B ($B \leq B_{crit}$) can be respectively written as:

$$\delta_{0T}^h = \Delta S_{0T}'^h \frac{\Delta T_{hys,0T}}{2T_{t,0T}^h - \Delta T_{hys,0T}} \tag{2.74}$$

$$\delta_B^h = \Delta S_{0T}'^h \left(1 - \frac{B}{B_{crit}}\right) \left(\frac{\Delta T_{hys,0T} - B(k^c - k^h)}{2T_{t,0T}^h - \Delta T_{hys,0T} + B(k^c + k^h)}\right) \qquad (2.75)$$

and

$$\delta_{0T}^c = -\Delta S_{0T}'^c \frac{\Delta T_{hys,0T}}{2T_{t,0T}^c + \Delta T_{hys,0T}} \qquad (2.76)$$

$$\delta_B^c = -\Delta S_{0T}'^c \left(1 - \frac{B}{B_{crit}}\right) \left(\frac{\Delta T_{hys,0T} - B(k^c - k^h)}{2T_{t,0T}^c + \Delta T_{hys,0T} + B(k^c + k^h)}\right) \qquad (2.77)$$

In a heating-cooling loop at constant field B, the total error of the irreversibility is:

$$\delta_B^h + \delta_B^c = \frac{(\Delta S_B'^h - \Delta S_B'^c)\Delta T_{hys,B}}{T_{t,B}^h + T_{t,B}^c} \approx \frac{2A_{loop}}{T_{t,B}^h + T_{t,B}^c} \qquad (2.78)$$

where $A_{loop} = -\oint S dT \approx (\Delta S_B'^h + |\Delta S_B'^c|)\Delta T_{hys,B}/2$ represents the net heat released to external sources (the adiabatic screen) in the heating-cooling loop.

Accordingly, when ΔS_T is calculated from pseudo entropy curves, there is an error due the irreversibility. In the calculation from heating curves, $|\Delta S_T'|$ underestimates the real entropy change by the amount δ_{0T}^h in the transition region, and by the amount $\delta_{0T}^h - \delta_B^h$ above the transition region, as seen in figure 2.4(a). On cooling, $|\Delta S_T'|$ overestimates the real entropy change by the amount δ_{0T}^c in the transition region, and by the amount $\delta_{0T}^c - \delta_B^c$ above the transition region. In this Thesis, the relative positions of pseudo entropy curves were determined using a correct value of ΔS_T or ΔT_S obtained from direct measurements in the PM phase, where the MCE is small, as displayed in figure 2.4(b) for cooling processes. As a result, $|\Delta S_T'|$ underestimates the real entropy change by the amount δ_B^h in the transition region, but overestimates it by the amount $\delta_{0T}^h - \delta_B^h$ below the transition region on heating; $|\Delta S_T'|$ overestimates the real entropy change by the amount δ_B^c in the transition region, but underestimates it by the amount $\delta_{0T}^c - \delta_B^c$ below the transition region on cooling. With this election, the effect of irreversibility on ΔS_T is smaller in the transition region because $\delta_B^h < \delta_{0T}^h$ and $\delta_B^c < \delta_{0T}^c$.

2.7.2 Irreversibility of isothermal magnetization

The existence of thermal hysteresis in a material is always accompanied by magnetic hysteresis, that is, a field-induced transition occurs at different fields
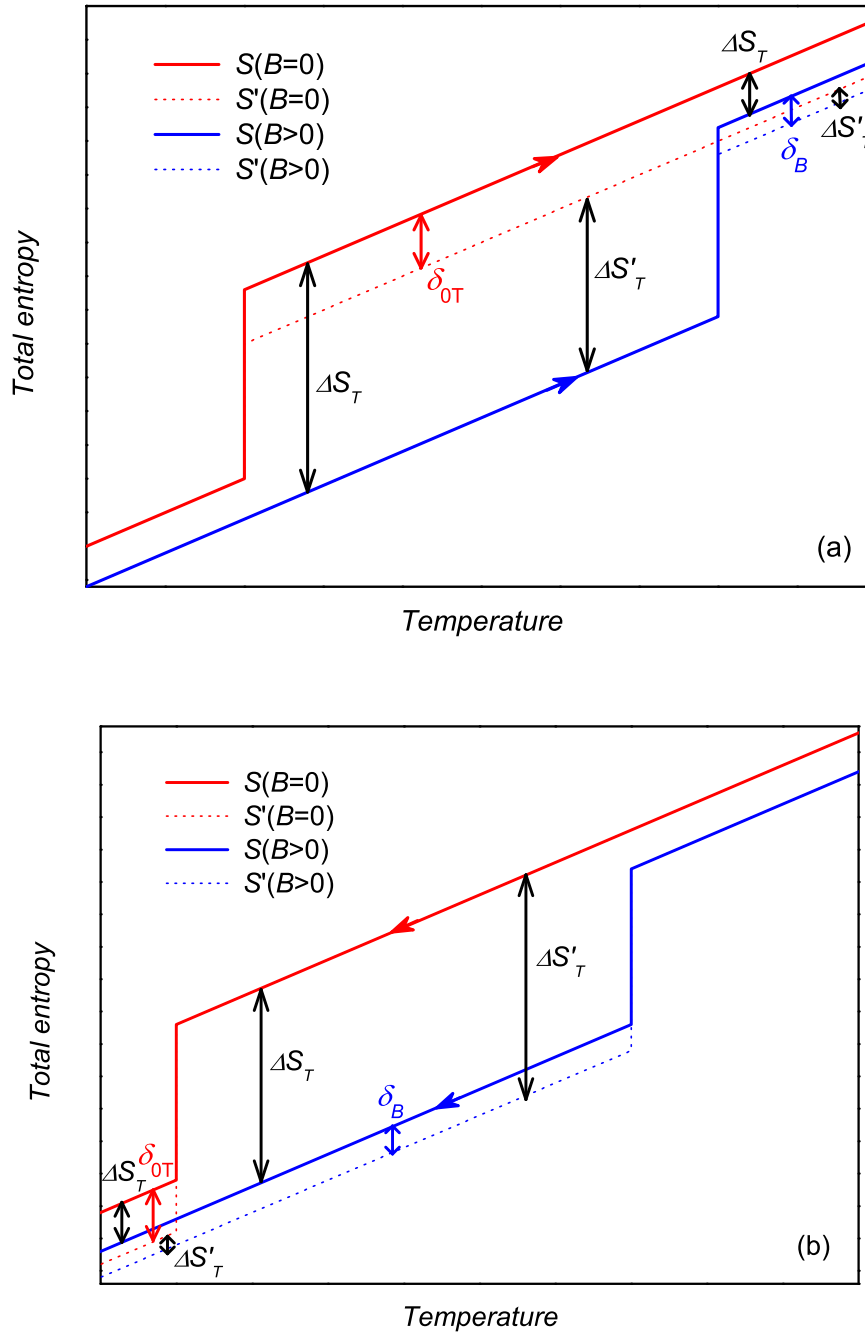
Figure 2.4: Schematic representation of real entropy S and pseudo entropy S' as functions of temperature at constant fields for a FOPT. The positions of the heating curves (a) and the cooling curves (b) are determined with correct values of ΔS_T or ΔT_S at temperatures in the FM and PM phases, respectively.

when the field is applied and removed. When the material is magnetized and then demagnetized, the energy loss caused by the hysteresis is the area surrounded by a magnetization loop. Such loss is normally released in the form of heat, thus the magnetic hysteresis is harmful to magnetic refrigeration applications. The magnetic hysteresis is explained by the stress model and doping theory in most magnetic textbooks. Here we discuss the transition entropy involved in FOPT based on the framework of the Bean-Rodbell model.

Figure 2.5 shows the theoretical prediction of isothermal magnetization curves simulated with the parameters $J = 1.5$, $g = 2.27$, $\eta = 2$ and $T_0 = 285$ K at temperatures $T/T_0 = 1.10$ and 1.12. A transition should occur at an equilibrium field where the values of the Gibbs free energy in FM and PM phases are equal. However, due to the existence of hysteresis, it happens at a higher field in a magnetizing process and at a lower field in a demagnetizing process. We assume that the transition occurs at state A on increasing field and at state C on decreasing field, where the states become unstable, since $(\partial M/\partial B)_T$ goes to infinite.

For increasing field or cooling processes, the states on curves $A - C$ and $A' - C'$ are unstable because $(\partial M/\partial B)_T < 0$, which cannot be measured experimentally in a real system. The value of the Gibbs free energy at state A is higher than that at state B, the difference is given by:

$$G_B - G_A = - \int_A^B M dB = -A_{ACB} < 0 \tag{2.79}$$

where A_{ACB} is the shaded area enclosed by the curve $\widehat{ACB}$ and the vertical line AB in figure 2.5.

To study the entropy change at a transition induced by a change of magnetic field, let us consider two isothermal magnetization curves at temperatures T_A and $T_{A'}$, where $T_{A'} - T_A = \delta T > 0$. In the magnetic phase diagram figure 2.6, States A and B are at the same point of a transition curve, but they correspond to different phases (A is a PM state and B is a FM state). Similarly for states A' and B'. The Gibbs free energy differences for the two phases are:

$$\Delta G_{PM} = G_{A'} - G_A = -S_{PM}\delta T - M_{PM}\delta B_t \tag{2.80}$$

$$\Delta G_{FM} = G_{B'} - G_B = -S_{FM}\delta T - M_{FM}\delta B_t \tag{2.81}$$

where δB_t is the change of the transition field from T_A to $T_{A'}$. Subtracting equation (2.80) from equation (2.81), we get:

$$\Delta G_{FM} - \Delta G_{PM} = -(S_{FM} - S_{PM})\delta T - (M_{FM} - M_{PM})\delta B_t \tag{2.82}$$
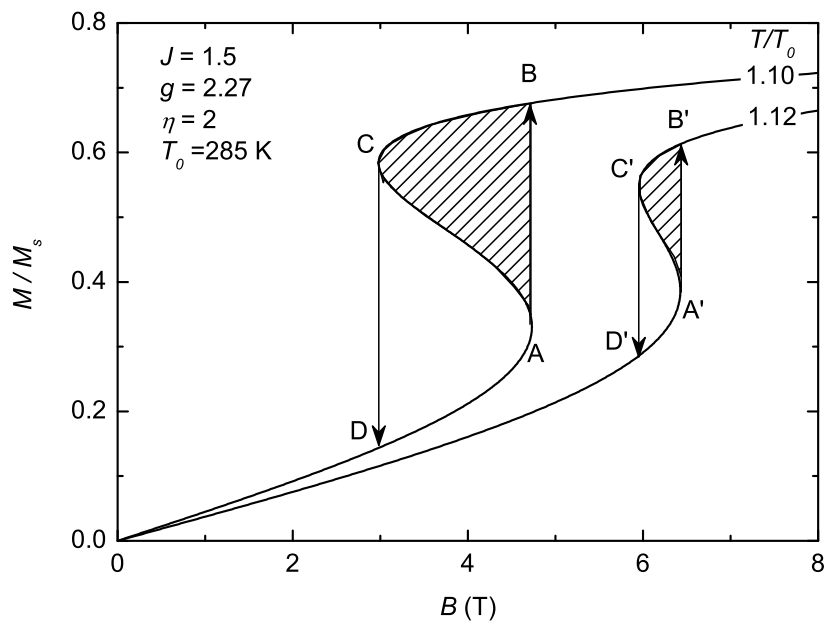
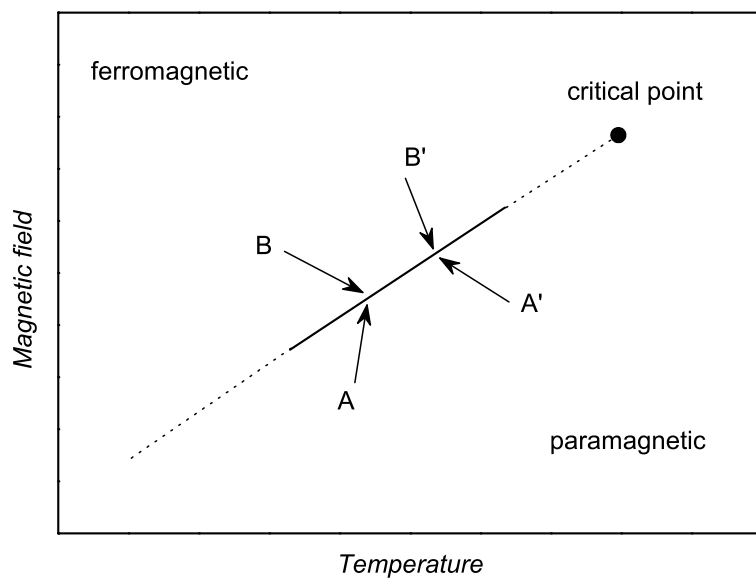Figure 2.5: Isothermal magnetization curves predicted with the help of the Bean-Rodbell model.

Figure 2.6: Representation of a magnetic phase diagram, in which the states A, B, A', and B' schematically correspond to those in figure 2.5.

In the case that a transition takes place at equilibrium point, i.e. $\Delta G_{FM} - \Delta G_{PM} = 0$, equation (2.82) turns into the magnetic Clausius-Clapeyron equation (2.49). Whereas in a hysteretic FOPT as described in figure 2.5, $\Delta G_{FM} - \Delta G_{PM} = A_{ACB} - A_{A'C'B'} > 0$, according to equation (2.79). The area A_{ACB} is larger than $A_{A'C'B'}$, because $T_{A'}$ is closer to the critical point than T_A. Thus the modified Clausius-Clapeyron is obtained for the hysteretic transition [29]:

$$\Delta S = -\Delta M \frac{dB_t}{dT} + \frac{A_{A'C'B'} - A_{ACB}}{dT} = -\Delta M \frac{dB_t}{dT} + \frac{dA}{dT} \qquad (2.83)$$

where dA/dT represents the variation of the area A_{ACB} with respect to temperature, $\Delta S < 0$, $\Delta M > 0$ and $dA/dT < 0$. For a real system, the area A can be evaluated as one half of the area of the magnetization loop at each temperature, i.e. $A = -\frac{1}{2} \oint M dB$. Equation (2.83) indicates that in an increasing field or cooling process, the original Clausius-Clapeyron equation underestimates the entropy change at a hysteretic transition, and it is corrected by adding a term dA/dT.

Equation (2.83) also holds for decreasing field or heating processes. In this case, dA/dT represents the variation of the area A_{CAD} with respect to temperature, $\Delta S > 0$, $\Delta M < 0$ and $dA/dT < 0$. Therefore, the original Clausius-Clapeyron equation overestimates the entropy change at the transition.

Chapter 3

Experimental techniques

In this chapter we report on the experimental techniques used in this Thesis, in both aspects of sample preparation and characterization. The procedures of three common synthesis methods of samples are described. A brief description of spectroscopy (XRD), microscopy (SEM), calorimetry (DSC) and magnetometry (SQUID) is given. We also present the details of the operating principles of a setup for studying the thermal and magnetocaloric properties of magnetic materials as functions of temperature and magnetic field.

3.1   Sample preparation

Three different methods used in this Thesis to synthesize samples are arc-melting, melt-spinning and ball-milling. Various synthesis routes can be used according to the properties of the raw materials. For example, the ball-milling method is needed when an evaporable element, like red phosphorus (P), is included in the initial components. In addition, the properties of a sample can be affected by the use of various synthesis methods. Therefore, the properties of samples could be optimized through changing the preparation method. Of course, in the commercial point of view, a low cost of the preparation method of the production is desired.

3.1.1   Arc-melting

Arc-melting is the most common way for alloy preparation, a simple but effective method. The procedure to synthesize a sample with the arc-melting is described as follows: Pure elements are mixed in near a stoichiometric proportion and melted under an Ar gas atmosphere. The casting is done in such a

way that allows rapid cooling of the melt in order to prevent oxidation as much as possible. The ingot is remelted several times with turning it over each time in order to ensure a good homogeneity of the elements in the alloy. The as-cast ingot is sealed in a quartz tube under high vacuum or high purity protection of Ar gas, and then treated at the annealing temperature for some hours to form the expected phase. The length of the annealing time depends on the rate of the phase formation of the alloys. Sometime, a quenching process from high temperature to low temperature, such as quenching into ice water or liquid nitrogen, is needed to obtain the high temperature phase. The samples described in chapter 5, chapter 7 and chapter 9 were prepared in this way.

3.1.2   Melt-spinning

Melt-spinning is a technique used for rapid cooling of liquids. An as-cast ingot obtained by the arc-melting is inserted into a quartz tube with a nozzle. The ingot is induction melted under an Ar gas atmosphere, and ejected through the nozzle using a differential pressure. A thin stream of liquid is then dripped on to a rotating wheel which is cooled internally by water, causing rapid solidification. This technique is used to develop materials which require extremely high cooling rates to be formed, such as metallic glasses. The cooling rates achievable by the melt-spinning are on the order of $10^4 - 10^7$ K/s [78]. The melt-spun production is present only in the shape of thin ribbons. To obtain the desired specimens, the melt-spun ribbons are sintered at a given annealing temperature for some hours and then quenched to low temperature if necessary. The specimens described in chapter 6 were prepared with this technique.

3.1.3   Ball-milling

The last method used to synthesize samples in this Thesis is ball-milling technique which is used to grind materials into extremely fine powder. Samples containing P are difficult to synthesize by means of the arc-melting due to the low boiling point of P. Instead of the arc-melting, the ball-milling technique is suitable to prepare the P-contained samples. The samples investigated in chapters 4 and 8 were prepared by means of the ball-milling method. The mixture of starting materials in powder or chips are ball-milled in a high vacuum condition ($<10^{-6}$ mbar) for a long time which is sufficient to grind the starting materials into amorphous phase. During milling, solid-state-reactions are initiated through the repeated deformation and fracture of the powder particles. The ball-milled powder is collected in a molybdenum crucible, and then treated in a quartz tube under an Ar gas atmosphere for a couple of hours at a temperature at which the solid-state-reaction takes place. To homogenize

the specimen, subsequent annealing needs to be performed at a lower temperature than the reaction temperature. Finally, the annealed powder is cooled naturally down to room temperature, or quenched into ice water.

3.2 Sample characterization

3.2.1 X-ray diffraction

Powder X-ray diffraction (XRD) patterns of the studied samples were collected by means of a RIGAKU D/max diffractometer 2500 with a rotating anode RU 300, operating at 40 kV and 80 mA using Cu K_α radiation. The equipment in the Service of X-Ray Diffraction and Fluorescence Analysis of Zaragoza University [79] can perform the powder diffraction at different temperatures (between 100 K and 500 K) by He or N_2 regulating flow. The patterns were recorded in a range of 2θ between 5° and 120° at a step of 0.03°. All the diffraction patterns collected at various temperatures were analyzed by a Rietveld refinement program FULLPROF [80]. The crystal structure and lattice parameters of each phase as well as the fraction of the impurity phases of the sample were determined.

3.2.2 Scanning electron microscopy

The microstructure of compounds was investigated by scanning electron microscopy (SEM) using a JEOL JSM 6400 instrument in the Service of Electron Microscopy of Zaragoza University [81]. The accelerating voltage determining the energy and wavelength of electrons in the electron beam can be varied between 0.2 kV and 40 kV. The resolution in the secondary electron mode at 35 kV is 3.5 nm at a working distance of 8 mm. Samples were examined in either polished or unpolished condition.

3.2.3 Energy dispersive spectroscopy

Energy dispersive spectroscopy (EDS) is an analytical technique, coupled with the SEM equipment. It is used predominantly for the elemental analysis or chemical characterization of a specimen. The SEM equipment we used was equipped with a 300 INCA model EDS Oxford Instruments, with a resolution of 133 eV to 5.39 keV.

3.2.4   Differential scanning calorimetry

Differential scanning calorimetry (DSC) is a common thermoanalytical technique to obtain heat flux as a function of temperature by measuring the amount of heat required to increase the temperature of the studied sample and the reference. Both temperatures of the sample and reference are maintained at the same throughout the experiment. The heat capacity of the studied sample can be derived from the heat flux, since the former is proportional to the latter.

The heat flux as a function of temperature for some samples was measured in a Q1000 model differential scanning calorimeter from TA Instruments in the Service of Thermal Analysis of the Materials Science Institute of Aragón [82]. The Q1000 DSC equipped with a liquid nitrogen cooling system accessory allows working in a temperature range from 90 K to 473 K. The mass of samples between 5 mg and 100 mg and the heating or cooling rate between 5 K/min and 20 K/min are acceptable in the experiments.

3.2.5   SQUID magnetometry

Three Quantum Design Superconducting Quantum Interference Device (SQUID) magnetometers are available in the Service of Scientific Instruments of Zaragoza University, Magnetic Property Measurement System (MPMS) of model 5S and model XL, and Physical Property Measurement System (PPMS) [83]. The MPMS provides the exceptional sensitivity of a SQUID-based magnetometer in a fully automated analytical instrument. It can measure DC magnetic moment and AC magnetic susceptibility on samples as small as a few milligrams. The specifications of the MPMS are given by [84]:

- Absolute sensitivity: 10^{-11} Am^2

- Applied DC field range: –5.0 T to 5.0 T

- Applied AC field range: 0 to 3×10^{-4} T (amplitude)

- Frequencies of AC field: 0.01 Hz to 1000 Hz

- Temperature range: 1.9 K to 400 K (extends to 800 K with an oven)

- Measurement magnetic moment range: 10^{-11} Am^2 to 0.1 Am^2

The PPMS is an upgraded MPMS. The key optional features of the MPMS have been greatly improved and expanded in the PPMS, which allows to measure heat capacity, thermal transport and thermoelectric effects. Moreover, the model P525 Vibrating Sample Magnetometer (VSM) option can be chosen

in the PPMS. The PPMS VSM linear motor is designed to operate at 40 Hz, with rapid slewing possible over a travel of 6.5 cm. The large range of the motion enables the PPMS to perform completely automated centering operations. The PPMS VSM is a fast DC magnetometer, whose sensitivity is not significantly affected by large magnetic fields. The expanded specifications of the PPMS VSM are given by [85]:

- Applied DC field range: –9.0 T to 9.0 T

- Temperature range: 1.9 K to 400 K (with the He^3 refrigerator option down to 0.5 K, and with the VSM oven option up to 1000 K)

- Thermal conductance accuracy: 5 %

- Heat capacity sample size: 1 mg to 200 mg

- Heat capacity resolution: 10 nJ/K at 2 K

The DC magnetization measurements (magnetization vs. temperature at constant fields and magnetization vs. field at constant temperatures) in this Thesis have been performed with the three SQUID magnetometers (the VSM option was used in the PPMS).

3.2.6   Adiabatic calorimetry

In our laboratory, two commercial adiabatic calorimeters from Termis Ltd can be used to determine the heat capacity of substances. One is named as D2 and the other is called DD2. D2 has been continuously working since 1996. D2 and DD2 are similar to a traditional adiabatic calorimeter but modified to be able to measure heat capacity at magnetic fields, as well as isothermal entropy change and adiabatic temperature change. The precision of D2 is higher than that of DD2, since the sample holder of D2 is bigger, that allows loading more amount of sample. Both calorimeters were employed to characterize the thermal properties of the studied samples. Here a detailed description and correction of D2 is made. The configuration of DD2 has been presented in the Ph.D Thesis of Tocado [29].

3.2.6.1   Description of the setup

The calorimeter D2 is a cryostat with a length of 127 cm and an overall outside diameter of 4.4 cm. It can be directly inserted into a Dewar with liquid helium or nitrogen. In order to perform measurements at magnetic fields, the calorimeter is inserted into a specially designed cryocooler from Cryogenic

Limited [86] which provides the conditions of low temperature (the minimum is ∼2 K) and magnetic field (the maximum is 9 T). The working temperature range of D2 is from 1.5 K to 350 K (a specific procedure with liquid helium is needed below 5 K). The typical accuracy is ± 3 % at 5 K and ± 0.5 % at 300 K [87].

A picture and a schematic view of the construction of D2 are shown in figures 3.1(a) and 3.1(b), respectively. The head of the cryostat contains a vacuum valve (1), a gas output valve (2) and an electronic connector (3). The chamber is evacuated by a rotatory-pump for few hours at room temperature after sealing. No vacuum pumping is required during experiments, because a high vacuum condition is provided by an efficient charcoal getter (4) which is placed at the bottom of vacuum jacket (5). Valve (2) controls the rate of the gas flow through capillary (6) to adjust the cooling speed of the system. Connector (3) is connected to a PC by a multi-wire cable. Data acquisition is in Pascal language, which runs in DOC system.

A calibrated rhodium-iron resistance thermometer RIRT-2 (9) is placed on the adiabatic screen (11). There is also a series of 10 iron-copper / chrome thermocouples (10) between heater sleeve (8) and adiabatic screen (11). The assembly of the screen and heater sleeve is supported by a stainless steel tube (12) with thermal anchoring (13). A cylindric sample container (7) (see figure 3.2(a)) is inserted tightly into heater sleeve (8) which is suspended inside of adiabatic screen (11) with nylon threads. Sample container (7) loading a sample can be heated by a resistance heater or by the thermal radiation of the adiabatic screen with a temperature higher than the sample temperature, and cooled by thermal radiation of the adiabatic screen with a temperature lower than the sample temperature. At low temperature, the thermal conduction through the wires (the nylon threads and the thermocouples) is also important.

The temperature of the system is controlled with a proportional-integral (PI) controller routine. When the average value of the thermocouples indicates zero, the temperature of the sample is equal to the temperature of the adiabatic screen, and the latter is measured by thermometer (9). Another outer shield (14) serves as a thermal intermedium between the vacuum wall and the adiabatic screen to obtain a good control of the temperature of the adiabatic screen. The temperature of outer shield (14) is controlled typically 15 K below the temperature of the adiabatic screen. A stainless steel shield (16) serves as a protection for the wires.

Since the sensitivity of the thermocouples decreases at low temperature (below 70 K), then the temperatures of sample container (7) and adiabatic screen (11) are measured directly with two carbon-glass resistance thermome-

(a)   (b)
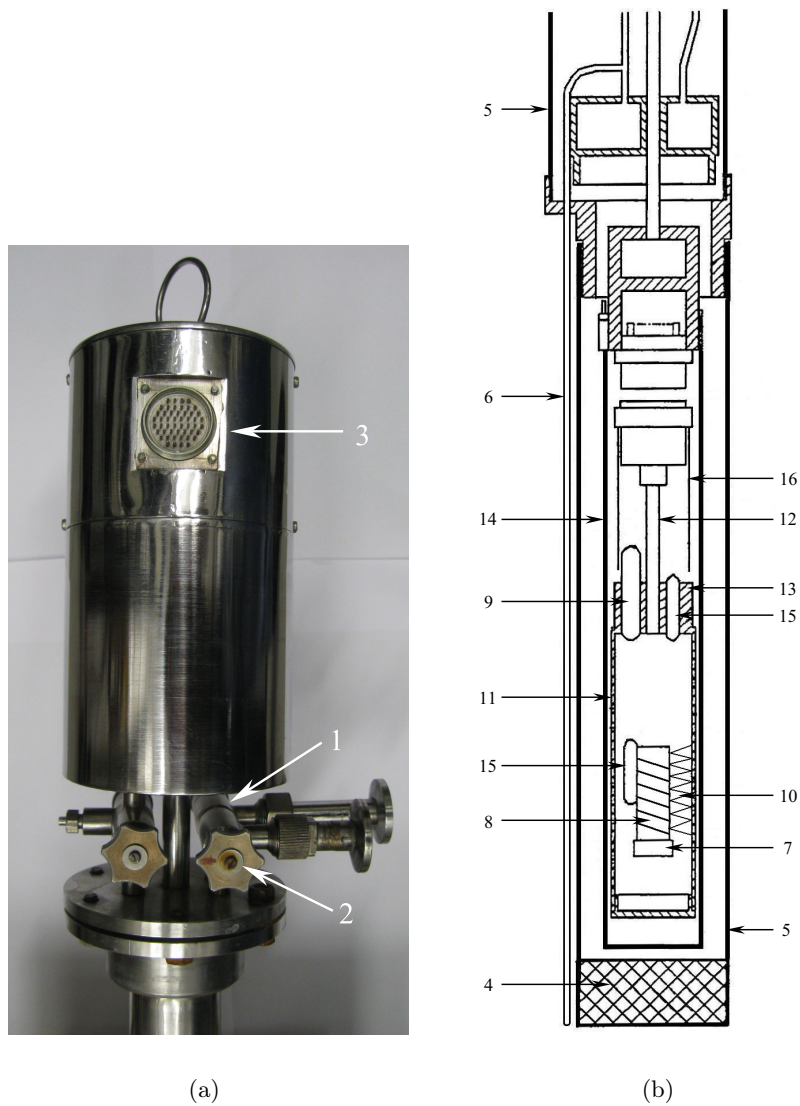
Figure 3.1: (a) Photograph of the head of the calorimeter. (b) Schematics of
the bottom part of the calorimeter. (1) vacuum valve; (2) cooling gas output
valve; (3) electronic connector; (4) charcoal getter; (5) vacuum jacket; (6)
cooling gas input capillary; (7) sample container; (8) heater sleeve (a copper
tube plus resistance wires); (9) RIRT-2 thermometer; (10) thermocouples. (11)
adiabatic screen; (12) stainless steel tube; (13) thermal anchoring; (14) outer
shield; (15) carbon-glass resistance thermometer; (16) stainless steel shield.

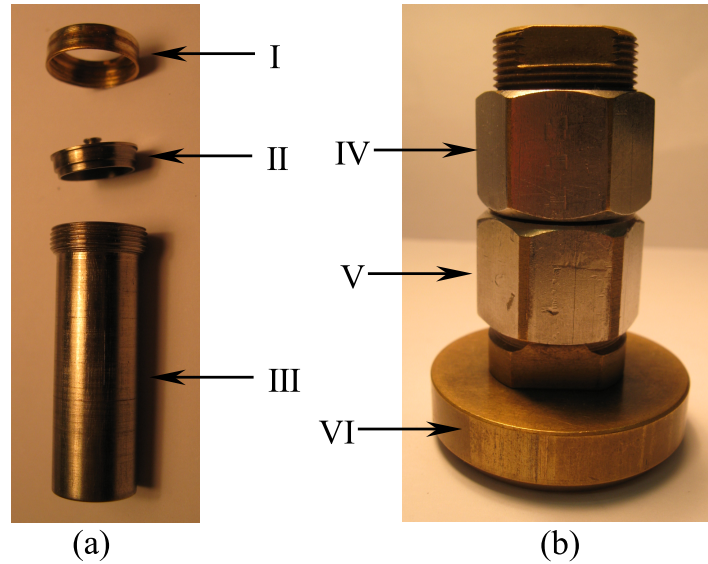Figure 3.2: (a) Photograph of the sample container. (b) Photograph of a device for sealing the sample container. (I) brass nut; (II) titanium lid; (III) titanium container; (IV) top piece of the sealing device; (V) bottom piece of the sealing device; (VI) pedestal of the sealing device.

ters (CGRT) (15) mounted on heater sleeve (8) and adiabatic screen (11), respectively. In this case, thermocouples (10) are not considered, the temperature difference between sample container (7) and adiabatic screen (11) is indicated by two thermometers (15).

Figure 3.2(a) presents a picture of sample container (III), its lid (II), and a nut (I). The sample container with a diameter of 8.0 mm, a length of 25.0 mm and a thickness of 0.1 mm, is made of titanium (≈ 1 cm^3 in volume), that allows a sample to be measured in either powder or bulk. The sample is sealed in the container by using a special device as shown in figure 3.2(b). Nut (I) and container (III) are clutched by top piece (IV) and bottom piece (V), respectively. The container and its lid with a tiny indium ring between them are tightened by screwing the nut. Generally, a small amount of He gas (~ 10 mbar) is filled to assure a better thermal exchange between the sample and container.

3.2.6.2 Principles of heat-capacity measurements

The heat-pulse technique is a standard method for determining heat capacities and widely used by many researchers. The details of the measurements principle of this technique can be found elsewhere [88]. In a heat-pulse experiment, heat capacity is thermodynamically given by $C \cong Q/\Delta T$, where Q is the amount of heat introduced into the calorimeter during a heat pulse, ΔT is the temperature increment of the sample between initial and final equilibrium states. The precision of the heat-capacity data basically depends on the accuracy of ΔT, because the error of the input heat Q is insignificantly small ($< 10^{-6}$ W). Virtually, ΔT is determined as the temperature rise at the median heating time by extrapolating the drifts before and after the heat pulse. Hence, ideal zero-slope drifts are expected to obtain an accurate ΔT. The present calorimeter provides a good adiabatic condition with a maximum slope of the drift being ± 0.1 mK/s in the absence of external heat supply and at zero field or constant nonzero fields. With the correction of a tiny temperature balance, smaller values (± 0.05 mK/s) are usually indicated in the measurements. Accordingly, for a typical experiment between 50 and 350 K, about 1 J/K of the total heat capacity of sample and container causes 0.05 mW heat gains or losses due to the lack of adiabaticity.

Although the heat-pulse technique is a well-known method for measuring the heat capacity and has been used widely by scientists, it has a problem for measuring a sample with a sharp heat-capacity peak due to the long relaxation time. After each pulse, the relaxation time τ can be expressed as: $\tau = C/K$, where C is the heat capacity and K is the effective thermal conductance between the sample and the container. It is necessary to wait several times of τ to assure that the final temperature of the sample is the actual indication of the thermometer which is attached on the adiabatic screen (normally, τ is about 30 s for alloys and the waiting time is 150 s in our measurements). The longer τ is, the worse extrapolation of the temperature relaxation is. A very high peak in the heat capacity for a FOPT (i.e. C value is quite large) leads to a long τ. Sometimes even worse, the long exponential relaxation is computed as a negative trend, which is considered as a slight depart from the thermal isolation provided by the adiabatic screen. Then this negative temperature trend is used to deduce the final temperature, and also it is taken as the initial temperature for next point. That produces a higher final temperature but a lower initial temperature, resulting in an overestimation of ΔT, i.e. the heat capacity is underestimated. Theoretically, the relaxation time is infinite at the heat-capacity anomaly especially for a FOPT. It means that the heat-pulse technique cannot give precise heat-capacity values in the transition region, where a FOPT happens. To overcome this problem and get more pre-

cise heat capacity, another technique called thermogram has been developed in our group.

The details of the thermogram are depicted as follows: a negative (or positive) constant temperature difference δT between the sample and the adiabatic shield is kept in a heating (or cooling) process. Then, the sample and the shield are heated (or cooled) via thermal radiation and conduction in a quasi-equilibrium condition. As a result, the heating (or cooling) rate of the sample as a function of temperature is obtained, from which the heat capacity can be determined. Alternatively, the heating thermogram can also be carried out by applying a constant power to the sample with an electrical heater.

The rate of temperature variation is inversely proportional to heat capacity and given by a heating (or cooling) power law with conduction and radiation terms:

$$\frac{dQ}{dt} = \frac{dQ}{dT}\frac{dT}{dt} = C_p\frac{dT}{dt} \tag{3.1}$$

and

$$\frac{dQ}{dt} = A\delta T + B'[(T + \delta T)^4 - T^4] \approx (A + BT^3)\delta T \tag{3.2}$$

Using equations (3.1) and (3.2), we get

$$C_p = \frac{(A + BT^3)\delta T}{dT/dt} \tag{3.3}$$

where dT/dt is the heating (or cooling) rate, calculated by straightly fitting a few points around each temperature from the experimental data of temperature time dependence $T(t)$. The constants A and B are evaluated from the C_p obtained by the heat-pulse method at two temperatures far from the transition region, where the dynamic and static values should match.

In order to assure a thermal quasi-equilibrium condition, a low rate of ± 1 mK/s is often used during the measurement. The temperature $T(t)$ is recorded for every Δt (the data in this Thesis were obtained with $\Delta t = 40$ s), the heating or cooling rate is taken as $dT(t)/dt = [T(t + \Delta t) - T(t)]/\Delta t$. In figures 3.3(a) and 3.3(b), we present temperature and the rate of temperature variation as functions of time obtained from a cooling thermogram of Gd metal from 298 K to 260 K and a heating thermogram of $Mn_{0.997}Co_{0.003}As$ from 273 K to 333 K, respectively. The cooling thermogram was done through thermal radiation and the heating thermogram was done through heating the sample by the electrical heater. When we compare the two thermograms qualitatively, some general characteristics are found. First, the kink in dT/dt curve in figure 3.3(a) and the split-type dT/dt curve in figure 3.3(b) correspond to the anomalies in the heat-capacity curves. Second, the change of dT/dt in figure 3.3(b) is much

more significant than that in figure 3.3(a) due to the sharper and higher heat-capacity peak of $Mn_{0.997}Co_{0.003}As$ than that of Gd. Finally, the heating and cooling rates become slower and slower with the temperature evolution. In the cooling thermogram, it is mainly due to that the cooling power (dominantly the radiation term) reduces with decreasing temperature in a cubic function (see equation (3.2)). In the heating thermogram, the heating power is constant, but the total heat capacity of the addenda plus sample increases with temperature, resulting in a decrease of the heating rate according to equation (3.1).

The heat-capacity curves for Gd and $Mn_{0.997}Co_{0.003}As$ derived from thermograms using equation (3.3) are displayed in the insets of figures 3.3(a) and 3.3(b), respectively. The heat-capacity curves are significantly smoothed when compared with the original dT/dt curves, since each value of dT/dt has been taken as an average of a few (about 30) points. The obtained heat capacity contains two contributions, addenda and sample, a correction is required to take away the contribution of the addenda.

Figures 3.4(a) and 3.4(b) display the corrected heat capacities (lines) of Gd and $Mn_{0.997}Co_{0.003}As$, derived from the raw data in figures 3.3(a) and 3.3(b), respectively. The results are in agreement with those measured with the heat-pulse technique (symbols). An excellent coincidence between the two sets of data is found in the case of Gd in the whole studied temperature range. However, the coincidence is only observed below and above the transition in $Mn_{0.997}Co_{0.003}As$. At the transition, the maximum of the thermogram data is about 50 % higher than that of the heat-pulse data. The heat-pulse method gives an average total heat capacity of the sample plus addenda between the initial and final temperatures. The resulting heat-capacity value of the sample could be larger than, smaller than or equal to the real one, depending on the profile of the real heat-capacity curve between the initial and final temperatures. The results determined from the heat-pulse method could be improved if a smaller temperature interval is used, but the smaller temperature increment produces a larger relative error due to the long relaxation time at the transition. The thermogram technique can provide precise heat-capacity data in the transition region, especially in the case of a FOPT.

As described above, the heat capacity can be obtained in a cooling process by means of the thermogram technique. Thus, the reliability of the thermograms can be examined with an integral:

$$\sigma_H = \int_{T_1}^{T_2} [C_{p,B}(heating) - C_{p,B}(cooling)]dT \qquad (3.4)$$

where $C_{p,B}(heating)$ and $C_{p,B}(cooling)$ are heat capacities obtained from heating and cooling thermograms at a constant field, respectively. T_1 and T_2 are two
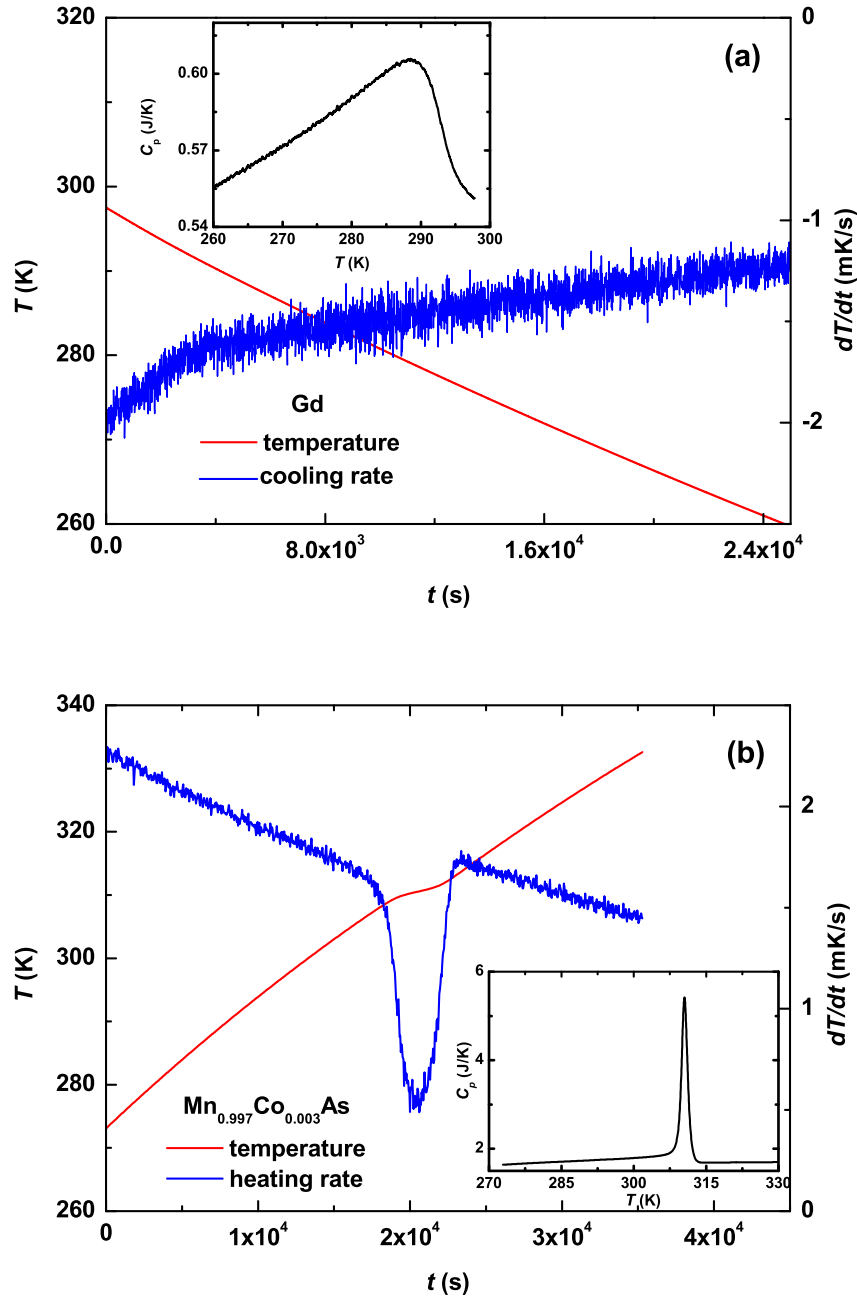
Figure 3.3: (a) Temperature and cooling rate as functions of time for Gd which undergoes a SOPT. (b) Temperature and heating rate as functions of time for $Mn_{0.997}Co_{0.003}As$ which undergoes a FOPT. Insets show smoothed heat-capacity curves.
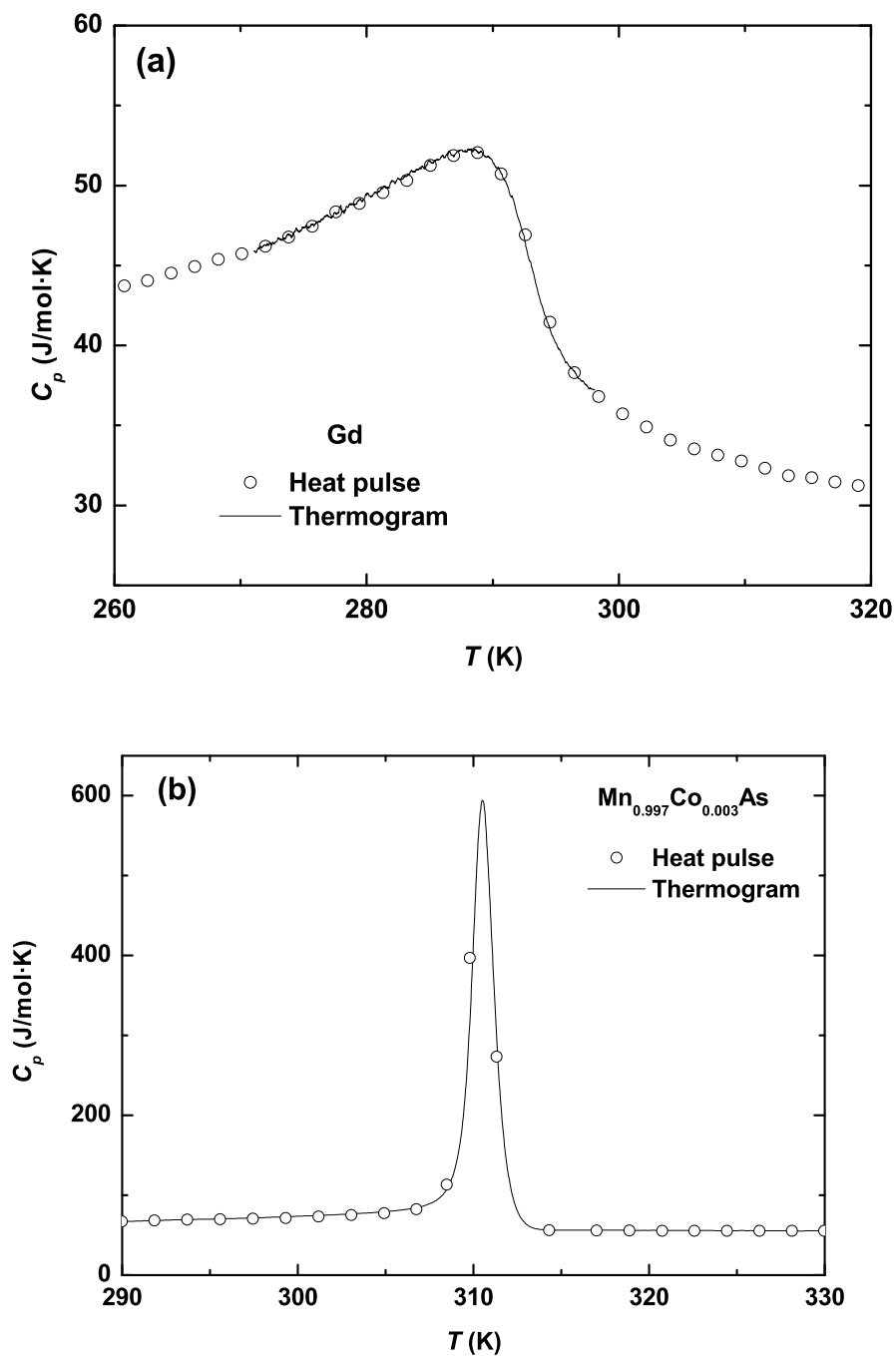
Figure 3.4: Heat capacity as a function of temperature for Gd (a) and Mn$_{0.997}$Co$_{0.003}$As (b). Open circles represent the heat-capacity data measured with the heat-pulse technique. Lines denote the heat-capacity data derived from the thermograms in figure 3.3(a) and 3.3(b).

temperatures well below and above the transition temperature, respectively. The integral means the enthalpy difference between the heating and cooling processes when the thermograms are performed between T_1 and T_2. The difference should be zero since enthalpy is a state function. Therefore, any nonzero difference is attributed to experimental errors. As an example, we did the integral for the data of $Mn_{0.997}Co_{0.003}As$. The plots of the heat capacity on heating and cooling obtained from the thermogram technique are shown in figure 3.5. $T_1 = 281.209$ K and $T_2 = 321.737$ K are taken as the initial and final temperatures of the integral. A nonzero difference $\sigma_H = 0.064$ J/g is found. The positive σ_H indicates that a net heat gain exists due to an imperfect control of the screen but is not computed. As the heat leak is always positive or negative (on heating and on cooling), an average error of the heat capacity in this temperature interval is given by $\sigma_H / \int_{T_1}^{T_2} [C_{p,B}(heating)dT + C_{p,B}(cooling)]dT \approx$ 0.2 %.

Let's summarize the advantages of the thermogram technique when comparing to the heat-pulse technique. First, it allows us to measure the heat capacity on cooling, while it is impossible to be carried out with the heat-pulse method. That is essential in the case of hysteretic transitions. Second, the precision of the heat capacity from the thermogram is similar to that from the heat-pulse technique in the case of SOPTs, but the former data are more precise in the transition region of a FOPT. Third, vary small temperature step used in the thermogram can provide more detailed results. This is very important in the determination of the enthalpy change or entropy change of a transition. Last, the cooling or heating rate of the thermogram is so slow that it assures that the temperature reading of thermometer corresponds to the actual temperature of the sample. Therefore, the thermogram is a very effective technique for the investigation of the thermal properties of materials. There is a shortcoming that the thermogram is a time-consuming technique.

Although a very slow cooling or heating speed is used in the thermograms, somehow, there is still a small difference in the transition temperature between heating and cooling heat-capacity curves even for a SOPT. This "apparent hysteresis" is attributed to the fact that the thermal quasi-equilibrium inside the container is not complete. The size of the "apparent hysteresis" depends on the heating and cooling rates used in the measurements.

Assuming C_s is the heat capacity of a sample, and K is the effective thermal conductance (it involves the contributions between the container and He gas, between the He gas and sample, between the sample grains and grains, and also the sample grain itself). Let $T(t)$ be the temperature of the container (directly measured temperature) and $T_s(t)$ be the average temperature of the sample. When the container is receiving some power from the heater by conduction
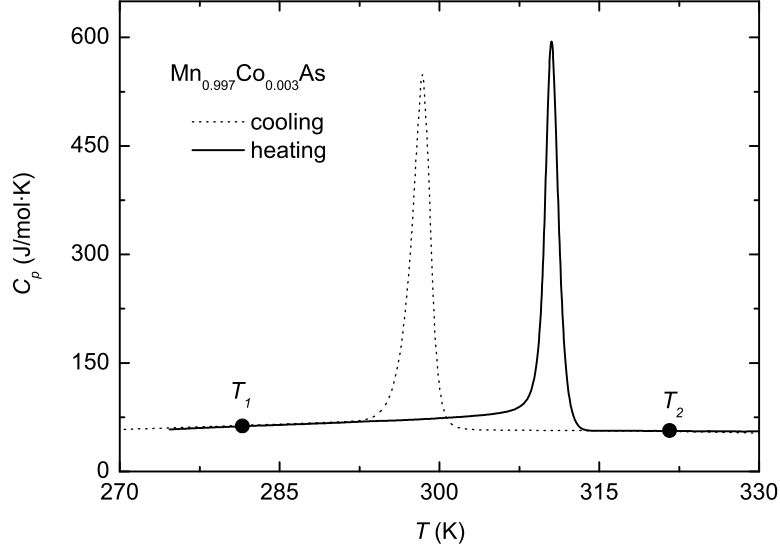
Figure 3.5: Temperature dependence of the heat capacity measured at zero field on heating and cooling for $Mn_{0.997}Co_{0.003}As$.

or from the adiabatic screen by radiation and conduction, both temperatures obey equation:

$$C_s \frac{dT}{dt} = K(T - T_s) \tag{3.5}$$

therefore, the apparent hysteresis is:

$$\Delta T_{app} = 2(T - T_s) = 2\frac{C_s}{K}\frac{dT}{dt} = 2\tau_s \frac{dT}{dt} \tag{3.6}$$

where $\tau_s = C_s/K$ is the relaxation time of the sample. By instance, taking values $\tau_s = 50$ s and $dT/dt = 1$ mK/s, it leads to $\Delta T_{app} = 0.1$ K, which means that the temperature of the sample is 50 mK lower (average over the sample) than the temperature indicated by the thermometer in a heating thermogram, but 50 mK higher than that in a cooling thermogram. That is the reason why the cooling and heating rates should be very slow in the thermograms.

3.2.6.3 Principles of enthalpy runs

The enthalpy change of a sample between T_1 (below T_t) and T_2 (above T_t) can be measured as the heat absorbed by the sample when heating from T_1 to T_2. It is called enthalpy run [89] which is a measurement like the usual heat-pulse technique for determining heat capacity, but covering the full transition

region during a single heat pulse. The enthalpy run is a more precise method for determining the total enthalpy change between T_1 and T_2 than both the heat-pulse method and the thermogram. Its error mainly results from the heat gained or lost (not considered in the calculation) due to an imperfect adiabatic control. Nevertheless, a better control of the adiabatic screen and a shorter time consumption (namely a lower gain / loss of heat) in the enthalpy run lead to a much smaller error than that in the heat-pulse or thermogram technique. Additionally, the enthalpy run is a useful technique to determine the enthalpy change of a transition, since it does not take care of the details of the transition. That is effective in particular for a FOPT, because the long relaxation time at the transition has no influence on the determination. Therefore, this technique can also be used as a reference for estimating the precision of the enthalpy and entropy at a transition obtained from other methods.

3.2.6.4   Principles of ΔS_T direct measurements

At a constant applied zero or nonzero field B, the temperature of a sample can be maintained at a set value by applying a constant power P_0, assuming that the surrounding temperature (the adiabatic screen) is kept at a constant value below that of the sample. When the magnetic field B varies from B_i to B_f, the power P will decrease or increase to make up for the heat Q_T released by the sample during a magnetizing process or absorbed during a demagnetizing process. By measuring $P(t)$, we can obtain the entropy change induced by the field variation, as follows:

$$\Delta S_T = S(T, B_f) - S(T, B_i) = \frac{Q_T}{T} = \frac{1}{T} \int_0^t (P - P_0) dt \qquad (3.7)$$

Usually, the magnetic field is set in a decreasing mode to have a positive heat input Q_T when the sample exhibits normal MCE, and viceversa when the sample shows inverse MCE. The magnetic field is varied in a sigmoidal way with a maximum slope lower than –1.5 T/min to improve the temperature control. The temperature of the sample is set 0.5 K lower than that of the adiabatic screen, in order to avoid losing the control of the temperature. The temperature of the sample is maintained at a desired value within ± 0.02 K during the measurement. About 30 s of temperature trends are recorded before and after the field variation to get the power baseline P_0 which is the power to compensate the heat leak induced by the difference, 0.5 K. As a typical example, the external magnetic field, heating power and temperature displacement as functions of time are shown in figure 3.6 for a single measurement.

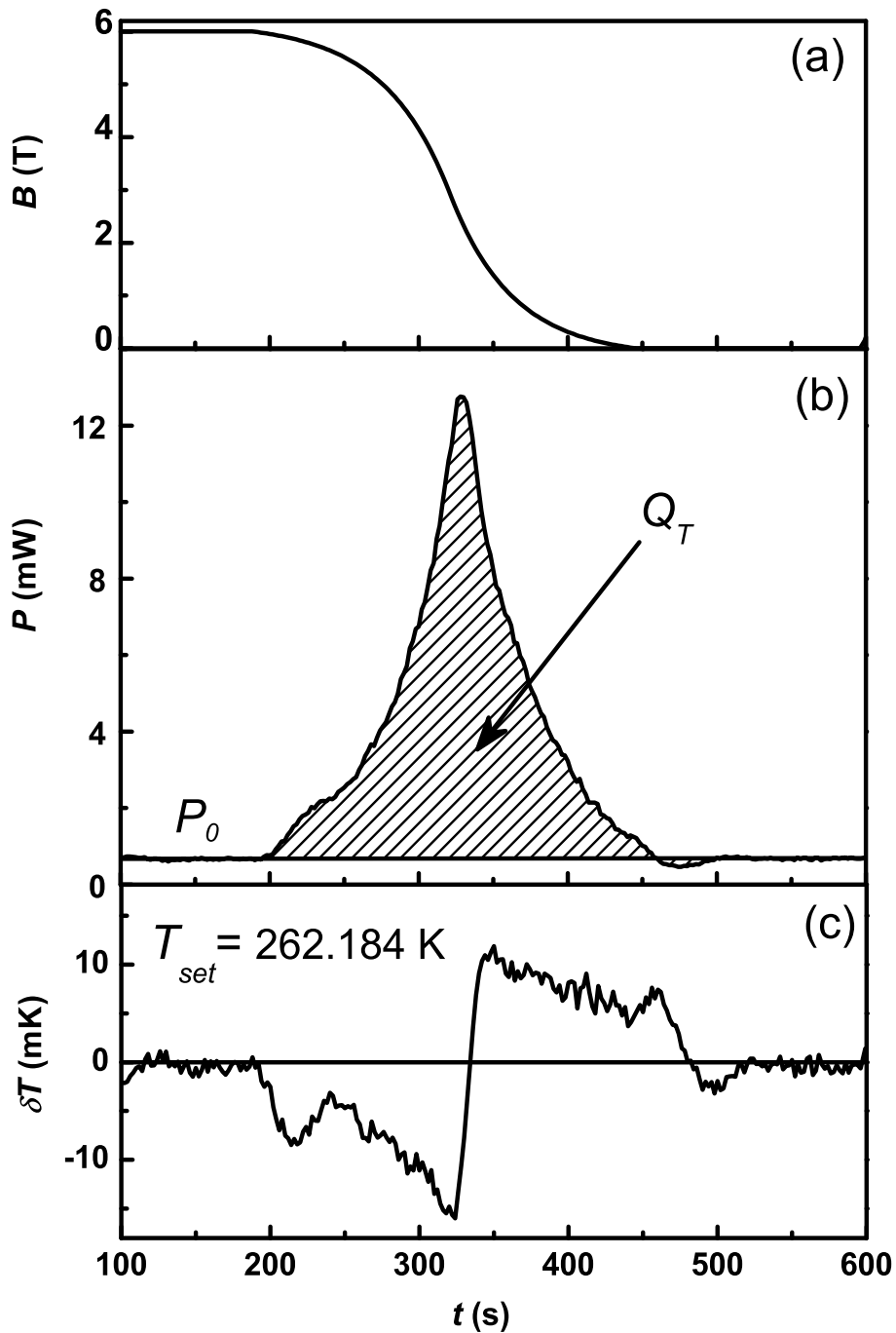The total entropy of a magnetic system can be expressed as a function of

Figure 3.6: (a) Magnetic field versus time, (b) power versus time, and (c) temperature displacement ($\delta T = T - T_{set}$) versus time for a typical direct measurement of entropy change. The heat Q_T absorbed by the sample when the magnetic field varies from B to 0 is denoted by the shadow.

B and T, so the differential of the entropy is:

$$dS = \left(\frac{\partial S}{\partial B}\right)_T dB + \left(\frac{\partial S}{\partial T}\right)_B dT \tag{3.8}$$

The first term at the right hand side is the entropy change induced by a variation of B, and the second one is the effect of a non-constant T. Integrating equation (3.8) leads to:

$$\Delta S = \int_{B_i}^{B_f} \left(\frac{\partial S}{\partial B}\right)_T dB + \int_{T_i}^{T_f} \left(\frac{\partial S}{\partial T}\right)_B dT = \frac{1}{T}\int (P - P_0)dt + \int \frac{C_{total}}{T}dT \tag{3.9}$$

In the first term of the right hand side, the error of power recording can be neglected because of its high accuracy (10^{-6} W). However, the determination of the baseline of P_0 could cause some errors. For instance, in figure 3.6 the baseline is located between $P_{down} = 6.3 \times 10^{-4}$ W and $P_{up} = 7.0 \times 10^{-4}$ W, whose difference multiplied by a time interval $\Delta t = 383$ s gives the maximum error $\delta Q_T = 26.8$ mJ. Taking $P_0 = (P_{up} + P_{down})/2$, the area of the peak is found to be $Q_T = 0.9893$ J. The resulting random error is $\sigma_1(\Delta S) = 2.7$ %. Indeed, the actual value of this error is much lower than the evaluated one, because the baseline is normally taken as an average of several points of the power at the initial and final fields.

The second term in the right hand side of equation (3.8) is the entropy change induced by a variation of temperature. It should be considered as an error when the isothermal entropy change measurement is performed. In our experiments, the temperature is maintained at $T_{set} = 262.18$ K within 20 mK, while the difference between the final and initial temperatures is about 3 mK. The temperature displacement δT exhibits negative and subsequently positive variations, as seen in figure 3.6. The difference between the enclosed areas of δT below and above the T_{set} line is quite small. Taking the value of the total heat capacity $C_{total} = 0.562$ J/K for the sample and addenda (the total mass is about 1 g) at 262 K, the entropy change due to the temperature variation is estimated to be $0.003 C_{total}/T_{set} = 6.4 \times 10^{-6}$ J/K which results in a relative error of $\sigma_2(\Delta S) = 0.2$ %. This error is one order of magnitude smaller than $\sigma_1(\Delta S)$. However, $\sigma_2(\Delta S)$ could be comparable to $\sigma_1(\Delta S)$ in practice, since the practical $\sigma_1(\Delta S)$ is much smaller than the evaluated one.

Accordingly, the entropy change is obtained at 262 K with a combined relative error lower than 3 %. Nevertheless, the combined relative error in our experiment is much smaller than those evaluated in the magnetization measurement for Gd sample [90], that are 20 % $\sim$ 30 % above T_C and even higher below T_C.

3.2.6.5 Principles of ΔT_S direct measurements

Adiabatic temperature change, ΔT_S, is directly measured by applying a magnetic field quasi-statically. The adiabatic condition in the measurements is maintained by keeping the temperature of the adiabatic screen the same as that of the sample. The procedure is very similar to the heat-pulse heat-capacity measurement, in which power is supplied as heat by an electrical resistance. But instead of that, power is supplied as magnetic work by external superconductor coils in the direct measurement of ΔT_S.

The magnetic field is normally applied at a rate of about 0.5 T/min which is slow enough to avoid the temperature going out of control. The temperature difference between the adiabatic screen and the sample is kept lower than 0.1 K during the application of magnetic field. Then, a thermal insulation condition within a drift of ±0.1 mK/s (the same as in the heat-capacity measurement) is maintained for 150 s before and after the field change to get the initial and final temperatures which are determined by linear extrapolations of the temperature evolutions at the initial and final fields, respectively. The temperature change is derived from the difference between the final and initial temperatures for each field variation.

The field step, field rate, waiting time for temperature relaxation, and temperature step are settable parameters in the configuration file that can be changed before running the program. Figure 3.7 shows the magnetic field and temperature as functions of time for a direct measurement of ΔT_S, as an example of the results obtained with several magnetic field steps. The temperature evolution is controlled with an average slope of –0.07 mK/s during the measurement. Only a few mK difference is observed between the temperatures at initial field and final zero field. As in precision in heat-capacity measurements, the experimental temperature change ΔT_{exp} can be obtained accurately within 0.01 K which is 1 % in the case of $\Delta T_{exp} = 1$ K.

3.2.6.6 Magnetoresistance of the thermometers

It is known that temperature can be determined by measuring the resistance of an electric wire whose value has been calibrated at standard fixed points (or against another calibrated thermometer) and fitted by a polynomial. In this way, the temperature is determined within a standard error (in mK) which depends on the type of the thermometer and the range of the measuring temperature. In the present device, RIRT-2 and CGRT thermometers, which have been calibrated previously at fixed points, are used to characterize the temperature in different temperature ranges. Nevertheless, most resistance thermometers change their resistance values in the presence of a magnetic field
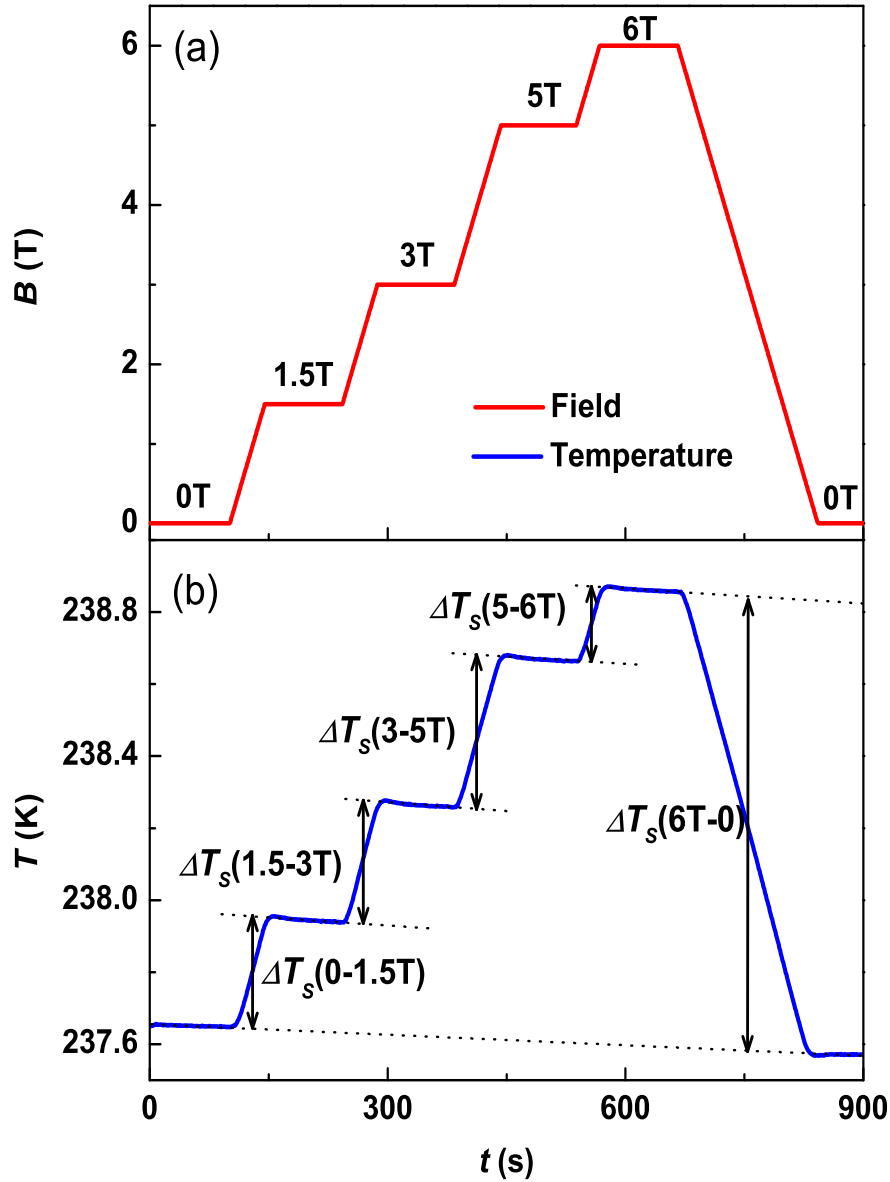
Figure 3.7: (a) Magnetic field as a function of time, (b) temperature as a function of time for a direct measurement of ΔT_S. Dotted lines denote the linear fits of $T(t)$ before switching the field on and after switching it off. Arrowed lines represent the temperature changes for the corresponding magnetic field variations. The magnitudes of the arrowed lines are determined as the distance between two dotted lines in the middle time of the field variation.

due to the magnetoresistive effect. The use of a resistance thermometer under magnetic fields would result in an erroneous temperature determination when the same polynomial fitting is applied. Therefore, the indication of a thermometer should be corrected when it is measured under a magnetic field.

In order to check the magnetoresistive effect of the present RIRT used in the calorimeter, a direct measurement of ΔT_S for the empty calorimeter (addenda) has been carried out following a field sequence $0 - 1\,\text{T} - 2\,\text{T} - 3\,\text{T} - 4\,\text{T} - 5\,\text{T} - 6\,\text{T} - 0$. The resulting temperature increments of the RIRT for increasing-field changes are displayed in figure 3.8(a). The experimental data were fitted with an exponential function $\Delta T_{MR} = (a_2 - a_4 B^2)B^2 \exp(-T/T_0)$, where B is the magnetic field. The fitting parameters are $a_2 = 0.02693$ K/T^2, $a_4 = 5.36885 \times 10^{-5}$ K/T^4 and $T_0 = 200$ K. It can be seen that the magnetoresistive effect is more significant at low temperatures and at high magnetic fields. As an alternative check, we also measured the heat absorbed by the empty calorimeter in a direct measurement of ΔS_T, the results are plotted in figure 3.8(b). The amount of heat Q_{MR} is necessary to increase the actual temperature of the calorimeter from $T_{set} - \Delta T_{MR}$ at an initial field B to T_{set} at the final field 0 T, however, both temperatures are indicated as being equal by the RIRT during the measurement. Therefore, we have:

$$Q_{MR} = \int_{T_{set}-\Delta T_{MR}}^{T_{set}} C_p(T)dT \tag{3.10}$$

where C_p is the total heat capacity of the addenda which is field independent. In the case of measurement with a sample, C_p amounts to the total heat capacity of the addenda plus the sample and is a function of temperature and field. It change from $C_{p,B}(T_{set} - \Delta T_{MR})$ to $C_{p,0}(T_{set})$ when the magnetic field decreases from B to 0.

Using the fitting data of ΔT_{MR} displayed in figure 3.8(a) and the heat capacity of the addenda, the resulting values of $Q_{MR} \approx C_p(T_{set} + \Delta T_{MR}/2) \cdot \Delta T_{MR}$ (the lines of figure 3.8(b)) are in agreement with those obtained from the direct measurement of ΔS_T. Taking into account the sample contribution, Q_{MR} is estimated by $Q_{MR} \approx [C_{p,0}(T_{set}) + C_{p,B}(T_{set} - \Delta T_{MR})]\Delta T_{MR}/2$.

In addition, the calorimeter was designed to be able to change the working thermometers during a measurement. Generally, the RIRT operates at high temperatures, the CGRTs are used below 70 K. According to the specifications provided by Lakeshore Ltd, at magnetic fields of 2.5 T and 8 T, the errors $(\Delta T_{MR}/T)$ of the CGRT decrease from 2.9 % and 3.8 % at 4.2 K to < 0.1 % at 78 K, respectively [91].
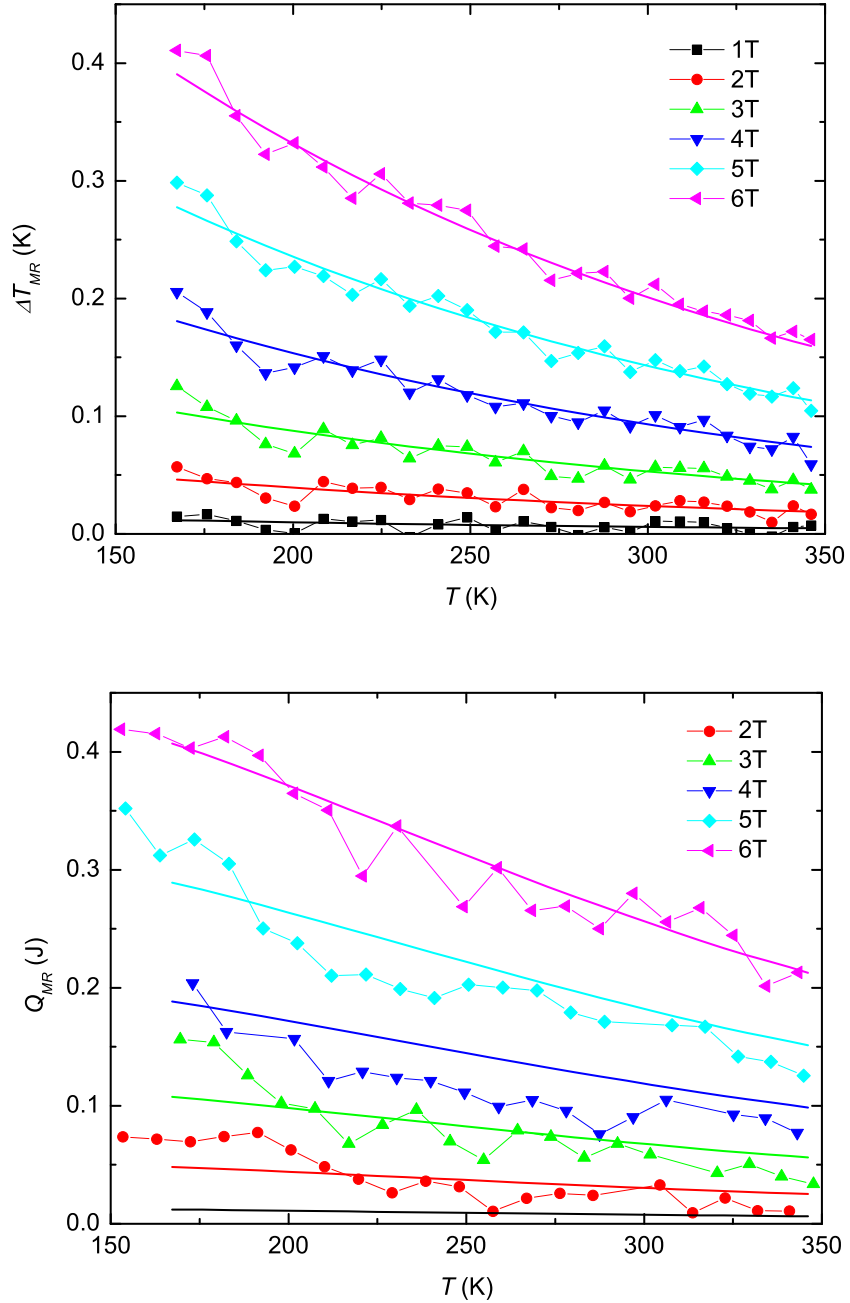
Figure 3.8: (a) Field-induced temperature rise ΔT_{MR} as a function of temperature for a rhodium-iron resistance thermometer (RIRT) measured in adiabatic conditions upon several field changes. (b) Temperature dependence of the heat required to increase the temperature of the addenda by the amount ΔT_{MR} obtained from direct measurements of ΔS_T (symbols). Lines represent the calculated data using the approximation $Q_{MR} \approx C_p \Delta T_{MR}$.

3.2.6.7 Eddy currents

When a hollow conductor cylinder with an inner radius a, outer radius b and length L is subjected to a variable magnetic field, according to the Faraday's law, an electric field is induced, that produces circular eddy currents. It is easy to calculate the power dissipated by these currents, that is given by:

$$P_{eddy} = \frac{\pi L}{8\rho} \left(\frac{dB}{dt} \right)^2 (b^4 - a^4) \tag{3.11}$$

where ρ is the electrical resistivity. This expression indicates that the dissipated power is proportional to the thickness and length of the cylinder wall. For a field variation from 0 to B, the total dissipated heat is expressed as:

$$Q_{eddy} = \frac{\pi L}{8\rho} \left(\frac{dB}{dt} \right) B(b^4 - a^4) \tag{3.12}$$

Taking $(dB/dt)_{\max} = 1.5$ T/min, $B_{\max} = 6$ T and $\rho = 4 \times 10^{-9}$ Ω·m (for titanium at 20 °C) for the present calorimeter, the eddy-current heat of the sample container is calculated to be 7×10^{-5} J. It is negligible comparing to a few Joule of the heat supplied by the electrical heater in ΔS_T measurements. This amount of heat would result in about 0.1 mK temperature increment assuming that the total heat capacity of sample and addenda is 1 J/K. This effect is even much smaller than the experimental errors in ΔT_S measurements. It may become significant at low temperature because the total heat capacity is small.

The eddy-current heat does not only exist in the sample container, but also in the sample. In most cases, we do measurements using samples in the form of powder or ground grains instead of a bulk. Anyway, the eddy-current heat in bulk samples still can be estimated by taking $a = 0$ in equation (3.12). It is about 3×10^{-3} J when the same other parameters as above are used.

3.2.6.8 Corrections

Heat capacity and thermogram

Both, raw heat-pulse and thermogram data include the contributions of sample and addenda. So they need to be corrected by subtracting the contribution of the addenda which has been measured in an independent experiment previously. As mentioned above, about 0.1 K "apparent hysteresis" exists between heating and cooling thermograms. The magnitude of the "apparent hysteresis" is related to the heating and cooling rates of the thermograms. In a usual heat-capacity measurement, this temperature shift is irrelevant and is somehow

corrected when adjusting the radiation and conduction coefficients. Therefore, this kind of correction can be neglected.

The magnetoresistive effect of the thermometer has influence on the results of heat capacity when a heat-pulse or thermogram measurement is carried out under magnetic field. There are two kinds of corrections to be made, that is, on the temperature and on the heat capacity. In the heat-pulse method, the true heat capacity of a sample measured at a field B is determined by:

$$C_{p,B}\left(\frac{T_1 + T_2}{2}\right) = \frac{1}{N}\frac{Q - \Delta H_0}{T_2 - T_1} \tag{3.13}$$

where Q is the total heat supplied between the initial temperature T_1 and final temperature T_2. ΔH_0 is the enthalpy increment of the addenda. N is the number of molars in the sample.

In the actual calculation, the initial and final temperatures are $T_1' = T_1 + \Delta T_{MR1}$ and $T_2' = T_2 + \Delta T_{MR2}$, respectively. Accordingly, the measured heat capacity is:

$$C_{p,B}'\left(\frac{T_1' + T_2'}{2}\right) = \frac{1}{N}\frac{Q - \Delta H_0'}{T_2' - T_1'} \tag{3.14}$$

Using $\Delta T_{MR2} - \Delta T_{MR1} = \frac{d\Delta T_{MR}}{dT}(T_2 - T_1)$, therefore:

$$C_{p,B}'\left(\frac{T_1' + T_2'}{2}\right) = \frac{C_{p,B}}{1 + d\Delta T_{MR}/dT} - \frac{C_0}{N(1 + d\Delta T_{MR})}\frac{d\Delta T_{MR}}{dT}$$

$$\cong \frac{C_{p,B}}{1 + d\Delta T_{MR}/dT} - \frac{C_0}{N}\frac{d\Delta T_{MR}}{dT} \tag{3.15}$$

where C_0 is the heat capacity of the addenda at $(T_1 + T_2)/2$. The approximation can be made because the bracket in the denominator is a second-order correction.

Taking the derivative of the analytical fitting function of ΔT_{MR}, $d\Delta T_{MR}/dT = -\Delta T_{MR}/T_0$, the true heat capacity can be written as:

$$C_{p,B}\left(\frac{T_1 + T_2}{2}\right) = C_{p,B}'\left(\frac{T_1' + T_2'}{2}\right) - \left[C_{p,B}'\left(\frac{T_1' + T_2'}{2}\right) + \frac{C_0}{N}\right]\frac{\Delta T_{MR}}{T_0}$$

$$= C_{p,B}' - \Delta C_{p,B} \tag{3.16}$$

where

$$\Delta C_{p,B} = \left[C_{p,B}'\left(\frac{T_1' + T_2'}{2}\right) + \frac{C_0}{N}\right]\frac{\Delta T_{MR}}{T_0} \tag{3.17}$$

Therefore, the temperature indicated by the thermometer should be corrected by $T = T' - \Delta T_{MR}$, and the heat capacity should be corrected by $C_{p,B} = C'_{p,B} - \Delta C_{p,B}$. In the case of $B = 6$ T, the corrections around 300 K are found to be $\Delta T_{MR} = 0.2$ K which is 0.07 %, and $\Delta C_{p,B}$ is at most 0.2 %. These corrections were not made on the data of this Thesis, since they are small and comparable to the experimental errors above 150 K.

Isothermal entropy change

Due to the fact that the isothermal entropy changes of the addenda (primarily comprised of titanium, brass and indium) induced by a change of external magnetic field is insignificantly weak, it is too small to be taken into account. In a direct measurement of ΔS_T, we measure the additional power which compensates the temperature change of the sample induced by the magnetic field change. This additional power includes three contributions, the main part related to the MCE of the sample, the extra parts due to the magnetoresistive effect of the RIRT and the eddy-current effect. The last two contributions should be subtracted from the total computed heat in the calculation of ΔS_T of the sample, namely, $\Delta S_{corr} = Q_{exp}/T - Q_{MR}/T - Q_{eddy}/T$. The effect of eddy currents could be significant only when the measurements are performed at very low temperatures and / or with a very fast change of magnetic field, none of which is the case of our measurements. According to the Q_{MR} data of figure 3.8(b), the correction at 300 K is $Q_{MR}/T = 0.3/300 = 1$ J/kg·K (the mass of the sample is taken to be 1 g). The magnetoresistive effect of the RIRT were not taken into account in this Thesis, because it is much smaller than the ΔS_T values in the transition region. But it could be a significant error source out of the transition region.

Adiabatic temperature change

In the direct measurement of ΔT_S, the magnetoresistive effect of the thermometers and the eddy-current heat of the empty container should be considered. The experimental value ΔT_{exp} is corrected by $\Delta T_{corr} = \Delta T_{exp} - \Delta T_{MR} - \Delta T_{eddy}$, where $\Delta T_{eddy} = Q_{eddy}/C_{total}$. Most measurements have been carried out near 300 K with a maximum magnetic field of 6 T in the present Thesis, thus, ΔT_{eddy} is negligible. The maximum of ΔT_{MR} is about 0.2 K which is much smaller than ΔT_S of the studied samples in the transition region for a field change of 6 T. Although ΔT_{MR} could be comparable to ΔT_S out of the transition region, we are not interested in the values of ΔT_S in pure FM and PM phases. Therefore, the magnetoresistive and eddy-current effects were not taken into account in the data processing.

The most important correction in the direct measurement of ΔT_S is the enthalpy gained by the addenda, since ΔT_{corr} is the temperature change of the sample and addenda when a magnetic field changes adiabatically. Most

often, the relationship of the correction is approximately given by: $\Delta T_S \cong \Delta T_{corr}(1 + C_0/C_{p,B})$, where C_0 is the heat capacity of the addenda and is magnetic field independent. $C_{p,B}$ is the heat capacity of the sample at the magnetic field B. But more precise correction can be made as detailed in the Thesis of Tocado [29]. The correction can be done in two ways, depending on which state is close to a transition temperature, the initial or the final one. The correction of ΔT_S in this Thesis has been made using the second method.

Chapter 4

Methods of magnetocaloric effect determination

The methods of MCE determination are divided into direct and indirect measurements. Generally speaking, in the direct measurements, the temperature change of a sample is directly characterized by using a thermometer when the sample is subjected to a magnetic field in adiabatic conditions. The definition of entropy for reversible processes $dS = \delta Q/T$ introduces the direct measurement of entropy change, i.e. the isothermal entropy change can be directly determined by measuring the heat released or absorbed by the sample when the magnetic field varies isothermally. On the other hand, the MCE parameters can be derived from heat-capacity and / or magnetization data, the so called indirect methods. In this chapter, both of the direct and indirect methods are reported. The application of these methods is illustrated in two different magnetocaloric materials, Gd metal and Fe$_2$P-type Mn$_{1.1}$Fe$_{0.9}$P$_{0.82}$Ge$_{0.18}$ compound which undergo a SOPT and a FOPT, respectively.

4.1 Determination of MCE from magnetization

Integrating equation (2.6), we have:

$$\Delta S = \int_{B_i}^{B_f} \left(\frac{\partial M}{\partial T} \right)_B dB \tag{4.1}$$

So, the entropy change can be calculated from the numerical integration of equation (4.1) on the basis of experimental magnetization data measured as a function of temperature and magnetic field. Considering the discrete data we can obtain in the experiment, the integral of equation (4.1) is approximately replaced with summation. The summation can be made in two different

forms. One of the calculations is to use the magnetization data obtained from isothermal magnetization measurements. In the case of small discrete field and temperature intervals, ΔS_T can be expressed as:

$$\Delta S_T = \sum_i \left[\frac{(M_{m+1} - M_m)_{B_i}}{T_{m+1} - T_m} \right] \Delta B_i \tag{4.2}$$

where M_m and M_{m+1} are the experimental magnetization data at T_m and T_{m+1}, respectively, under a magnetic field B_i. Another calculation is to use the magnetization data obtained from isofield magnetization measurements. In the case of small discrete field and temperature intervals, ΔS_T can be expressed as:

$$\Delta S_T = \sum_i \frac{1}{2} \left[\left(\frac{\partial M}{\partial T} \right)_{B_i} + \left(\frac{\partial M}{\partial T} \right)_{B_{i+1}} \right] \Delta B_i \tag{4.3}$$

where $(\partial M/\partial T)_{B_i}$ and $(\partial M/\partial T)_{B_{i+1}}$ are the experimental values obtained from $M - T$ curves at constant applied fields B_i and B_{i+1}, respectively.

As we know from equation (2.83), the Clausius-Clapeyron equation underestimates entropy change in magnetizing and cooling processes or overestimates it in demagnetizing and heating processes due to the irreversibility of FOPTs. Although the original Clausius-Clapeyron equation is only a specific limit of the Maxwell relation, the underestimation and overestimation also hold for the latter. Namely, on increasing field and cooling, the absolute value of the entropy change ($\Delta S_T < 0$) is underestimated by the amount $|dA/dT|$ when using equations (4.2) and (4.3); and in decreasing field and heating processes, the entropy change ($\Delta S_T > 0$) is overestimated by the amount $|dA/dT|$ when using equations (4.2) and (4.3), where A is the dissipated energy in each process due to the irreversibility. In real materials, A can be estimated from isothermal magnetization measurements, that is, taken as one half of the area enclosed by the loop at each temperature:

$$A = -\frac{1}{2} \oint M dB \tag{4.4}$$

Moreover, one has to be cautious when using equation (4.2) for FOPTs, because in most cases the obtained maximum values of $|\Delta S_T|$ are overestimated due to the "spike" effect. The use of equation (4.3) for isofield magnetization data does not meet this problem, therefore, it is worth popularizing this method in the calculation of ΔS_T for FOPTs. To the best of our knowledge, only few researchers have used equation (4.3) to derive ΔS_T in their publications [92, 93].

It has to be noted that the overestimation of the spurious spike in ΔS_T is completely different from that due to irreversibility. The "spike" effect is due

to an inadequate application of equation (4.2) to the path dependent isothermal magnetization data. Detailed discussions about the "spike" effect will be shown below. The "spike" effect only occurs in the isothermal magnetization measurements and can be reduced or avoided by using a modified measurement process. However, the overestimation and underestimation induced by the irreversibility exist in both of the isothermal and isofield magnetization measurements. They are unavoidable but can be corrected.

It is worth to point out that only the isothermal entropy change ΔS_T can be obtained through these kinds of magnetization measurements. It has been proven that the attempts to simplify the basic thermodynamic relation to allow the calculation of the adiabatic temperature change ΔT_S from the magnetization data using equation (2.26) fail because the assumption that heat capacity is magnetic field independent is erroneous in the transition region [94]. But it is feasible to derive another entropy curve from the combined heat capacity and ΔS_T data, then use two entropy curves to obtain ΔT_S.

4.2   Determination of MCE from heat capacity

Both magnetocaloric parameters ΔS_T and ΔT_S can be determined from heat capacity temperature dependence measured at different constant magnetic fields. In this case, total entropy curves at different fields are necessary to be derived from the heat-capacity data.

According to equation (2.40), the total entropy at a magnetic field B is calculated as:

$$S(T, B) = \int_{T_0}^{T} \frac{C_p(T, B)}{T} dT + S(T_0, B) \tag{4.5}$$

where $S(T_0, B)$ is the entropy at T_0. In this Thesis, the $S(T_0, B)$ at zero field has been evaluated by using equation (2.33) (the Debye model). The electronic and magnetic contributions are not taken into account, since T_0 usually is far below the transition temperature. The relative positions of the entropy curves at different fields are determined by using the value of ΔS_T or ΔT_S with respect to the zero-field entropy, where ΔS_T and ΔT_S are obtained from direct measurements performed at a temperature well above or below the transition temperature.

Once the total entropy curves $S(T, B)$ are obtained, the magnetocaloric parameters ΔS_T and ΔT_S can be determined using equations (2.23) and (2.24), respectively. For FOPTs, the resultant $|\Delta S_T|$ is overestimated by the amount δ_{0T}^h in heating processes, or underestimated by the amount δ_{0T}^c in cooling processes due to irreversibility (see section 2.7).

When the relative positions of the entropy curves at different fields are adjusted by using a value of ΔS_T or ΔT_S measured directly at a high temperature in PM phase, ΔS_T and ΔT_S determined from the entropy curves have the same values as those from the direct measurement in the PM phase but not in the FM phase, the latter method provides precise results in both the FM and PM phases. The errors of ΔS_T and ΔT_S determined from the entropy curves in FM phase are not only due to a systematic error but also due to irreversibility. It is the opposite if the entropy curves are adjusted using the direct ΔS_T or ΔT_S in FM phase. Therefore, the discrepancies of ΔS_T and ΔT_S obtained from the heat-capacity and direct measurements are unavoidable, existing either in FM phase or in PM phase. Anyhow, the relative errors of ΔS_T and ΔT_S in FM and PM phases are much higher than those in a transition temperature region, since the small ΔS_T and ΔT_S are calculated from the subtraction of two large and similar quantities. Nevertheless, the small and erroneous ΔS_T and ΔT_S in FM and PM phases are irrelevant to ours discussions and conclusions.

4.3   Determination of MCE from direct measurement

In chapter 3, we have introduced the experimental methods for direct determinations of ΔS_T and ΔT_S using the calorimeter. Basically, both of the ΔS_T and ΔT_S can be well determined from direct measurements, but some considerations should be done when performing the measurements on materials exhibiting FOPTs.

In the direct measurement of ΔS_T, the entropy change is determined on the basis of the Second Law of Thermodynamics $\Delta S_T \geq Q/T$, where ΔS_T is the entropy variation of a system in an isothermal process. The equality holds only in reversible processes. Namely, equation (3.7) can be exactly employed for materials exhibiting SOPTs. In an irreversible process (FOPT), equation (3.7) gives smaller ΔS_T than the real one. Therefore, equation (3.7) is modified as:

$$\Delta S_T = Q/T + \Delta S_{prod} \tag{4.6}$$

where ΔS_{prod} is the irreversible entropy produced in the material. The inequality $\Delta S_T > Q/T$ holds in both magnetizing and demagnetizing processes, since ΔS_{prod} is always strictly positive.

When a magnetic field cycle is performed in a soft magnet, the final state of the sample returns back to the initial one. That is, in the case of an isothermal magnetization loop, $\Delta U_{loop} = Q_{loop} + \oint BdM = 0$, therefore:

$$\Delta S_{prod,loop} = -\frac{Q_{loop}}{T} = \frac{1}{T}\oint BdM \tag{4.7}$$

where Q_{loop} is the heat released in the magnetization loop and is negative. In the direct measurement of ΔS_T, the magnetic field is changed in a monotonic way, i.e. only a magnetizing or demagnetizing process. The simplest assumption is to take the value of ΔS_{prod} as one half of the entropy production in a loop, that is:

$$\Delta S_{prod} = \frac{1}{2T} \oint B dM = -\frac{1}{2T} \oint M dB \qquad (4.8)$$

The integral $\oint -MdB$ represents the area enclosed by a magnetization loop, and can be easily estimated by performing isothermal magnetization measurements. The entropy production is proportional to the hysteresis of a sample but inversely proportional to the temperature of the sample. Indeed, the entropy production is not so significant even in a sample with strong hysteresis when its transition occurs near room temperature. For example, the compound $Mn_{0.99}Co_{0.01}As$ shows a large thermal hysteresis of 17 K at zero field, the estimated ΔS_{prod} is about 0.43 J/kg·K at 302 K, which is only 1.7 % of $\Delta S_T = Q/T = 25$ J/kg·K obtained from the direct measurement performed at the same temperature with a field change from 6 T to 0.

In the direct measurements of ΔT_S, there is no difference in the measuring principles for both SOPT and FOPT. However, for FOPTs, the resultant values of ΔT_S in a hysteretic region are influenced by the thermal and magnetic history of the sample.

4.4 Bypassing the "spike" effect in first-order transitions

So far we have introduced three methods (direct and indirect) to determine the magnetocaloric parameters. The values of ΔS_T can be obtained from magnetization, heat-capacity and direct measurements independently. While the values of ΔT_S can be directly measured and also may be calculated from heat capacity. Theoretically, the results should be coincident with each other within the experimental errors of each technique for both SOPT and FOPT. However, this is only practically true in materials undergoing SOPTs. Significant discrepancies have been found between the values of ΔS_T obtained from magnetization and heat-capacity data in materials exhibiting FOPTs. It is proven that the values of $|\Delta S_T|$ have been incorrectly overestimated in isothermal magnetization measurements. The origin of the overestimated $|\Delta S_T|$ and the solution to overcome this problem will be discussed below.

Recently, very large values of MCE with the maxima $-\Delta S_{T,\max} = 78$ J/kg·K for a field change of 3 T in $La_{0.8}Ce_{0.2}Fe_{11.4}Si_{1.6}$ [95] and $-\Delta S_{T,\max}$

= 75 J/kg·K for a field change of 5 T in $Mn_{1.1}Fe_{0.9}P_{0.8}Ge_{0.2}$ [96] were reported. Later, the so-called "colossal" MCE with $-\Delta S_{T,\max} = 300$ J/kg·K for a field change of 5 T was reported in MnAs under a hydrostatic pressure of 2.23 kbar [97]. A similar magnitude of $-\Delta S_{T,\max}$ was also observed in $Mn_{1-x}Fe_xAs$ (0.003 < x < 0.0175) [32] and $Mn_{1-x}Cu_xAs$ (0.003 < x < 0.020) [98] at ambient pressure. The curves of the entropy change showing a very high spike followed by a plateau with a moderate value is a common characteristic of these giant and "colossal" magnetocaloric materials.

Regarding the origin of the "spike" effect, several interpretations have been proposed. Wada *et al.* [28] considered that the spurious spike is probably an artifact, because the summation of the Maxwell relation with a finite field interval, rather than integration, is employed to evaluate ΔS_T. Liu *et al.* [67] thought that the spurious spike is caused by an inadequate use the Maxwell relation in the vicinity of the Curie temperature where PM and FM phases coexist. Zhang *et al.* [99] said that the spurious spike could be attributed to the superheat of the FM state when the Maxwell relation or the Clausius-Clapeyron equation is employed to obtain ΔS_T. All these interpretations are incorrect.

Recently, Tocado *et al.* [68] have discussed the spurious spike quantitatively on the basis of fundamental thermodynamics. The spurious spike is explained as an artifact due to an inadequate application of the Maxwell relation to path dependent isothermal magnetization data. The additional contribution to ΔS_T was obtained through calculating the real fractions of PM and FM phases using calorimetric data, giving a good agreement with the result obtained from the magnetization measurement. The extra contribution given by the spurious spike for a magnetic field change from 0 to B (0 < $B \leq B_{\max}$, B_{max} is the maximum field applied in the isothermal magnetization measurement) was obtained by Tocado *et al.* [68], as follows:

$$|\Delta S_{extra}| = \frac{\Delta x}{\Delta T}(M_{FM} - M_{PM})B \qquad B \leq B_{th,in} \qquad (4.9)$$

$$|\Delta S_{extra}| = \frac{\Delta x}{\Delta T}(M_{FM} - M_{PM})B_{th,in} \qquad B > B_{th,in} \qquad (4.10)$$

where x is the molar faction of PM phase. ΔT is the temperature step used in the isothermal magnetization measurements. Δx is the variation of x when the temperature of sample changes from T to $T+\Delta T$. The threshold for increasing field, $B_{th,in}$, is the lowest magnetic field inducing a transition from PM to FM phase in the magnetization measurement (see figure 4.1 below).

The case of decreasing field was not given in Ref. [68], but can be discussed in a similar way. For a magnetic field change from B to 0 (0 < $B \leq B_{\max}$),

the extra entropy change is expressed as:

$$\Delta S_{extra} = -\frac{\Delta x'}{\Delta T}(M_{FM} - M_{PM})(B - B_{th,de}) \qquad\qquad B < B_{th,de} \qquad (4.11)$$

$$\Delta S_{extra} = 0 \qquad\qquad B \geq B_{th,de} \qquad (4.12)$$

where x' is the molar faction of the FM phase at the initial state for each decreasing magnetization curve. $\Delta x'$ is the difference of x' between two adjacent curves at temperatures T and $T + \Delta T$. The threshold field $B_{th,de}$ is the highest magnetic field to induce a transition from FM to PM phase in the measurement (see figure 4.1 below).

One finds in equations $(4.9) - (4.11)$ that the size of the spurious spike is proportional to Δx or $\Delta x'$ and inversely proportional to ΔT. In isothermal magnetization measurements, the sample state at the beginning of each magnetizing or demagnetizing curve is defined by T, B, and x. On increasing field from $B = 0$, when the phase fraction x as a function of T has the same evolution as that in a heat-capacity measurement performed on heating at zero field, the ratio of Δx to ΔT can be expressed as:

$$\frac{\Delta x(T)}{\Delta T} = \frac{C_{an,0T}(T) - C_{nor,0T}(T)}{\Delta H_{0T}} \qquad (4.13)$$

where $C_{an,0T}$ and $C_{nor,0T}$ are the heat-capacity anomaly and the normal heat capacity, respectively, on heating at zero field. The integral $\int(C_{an,0T} - C_{nor,0T})dT$ gives the value of ΔH_{0T}, being the transition enthalpy. On decreasing field from $B = B_{max}$, when the phase fraction x' as a function of T has the same evolution as that in a heat-capacity measurement performed on cooling at constant field B_{max}, the ratio of $\Delta x'$ to ΔT can be expressed as:

$$-\frac{\Delta x'}{\Delta T} = \frac{C_{an,B_{max}}(T) - C_{nor,B_{max}}(T)}{\Delta H_{B_{max}}} \qquad (4.14)$$

where $C_{an,B_{max}}$ and $C_{nor,B_{max}}$ are the heat-capacity anomaly and the normal heat capacity, respectively, on cooling at a constant field B_{max}. The integral $\int(C_{an,B_{max}} - C_{nor,B_{max}})dT$ gives the value of $\Delta H_{B_{max}}$.

In equations (4.13) and (4.14), $\Delta x/\Delta T$ and $|\Delta x'/\Delta T|$ reach their maxima for $\Delta T \to 0$ and $T = T_t$, where T_t is the temperature of the maximum $C_{an,0T}$ or $C_{an,B_{max}}$. Therefore, under the limit conditions, on increasing field, the maximum value of the spurious spike is proportional to the magnetic field B until it reaches a threshold value $B_{th,in}$, above which it no longer increases; on decreasing field, the magnitude of the spurious spike is proportional to $B - B_{th,de}$ for fields greater than $B_{th,de}$, below which no "spike" effect shows.

Some efforts have been done to eliminate the "spike" effect displayed in ΔS_T calculated from isothermal magnetization data. Liu *et al.* [67] proposed an elaborate procedure based on the Clausius-Clapeyron equation to remove the spurious spike from their results. Das *et al.* [100] and Cui *et al.* [101] put forward similar approaches to remove the "spike" effect near the transition temperature, based on the estimation of phase fraction from the isothermal magnetization data measured in a mixed-phase state. Actually, these approaches are essentially the same as that proposed by Liu *et al.* [67], but quantitative. Caron *et al.* [69] performed the isothermal magnetization measurements with temperature and / or magnetic field cycles. They found that the spurious spike disappears when the isothermal magnetization is measured after the sample is cooled from a PM state to a measuring temperature in the hysteretic region. We will see that among these approaches, the last one is the most advisable method to avoid the "spike" effect, but time-consuming, and the "spike" effect still exists to some extent (see below).

Moreover, some scientists have proposed that ΔS_T can be correctly obtained using the Clausius-Clapeyron equation for FOPTs [102, 103]. However, some issues have to be considered when one uses the Clausius-Clapeyron equation. First, the magnetization change ΔM is not so easily and precisely determined, especially in the case that the magnetization does not change sharply with magnetic field. Second, the Clausius-Clapeyron equation gives only the entropy change at the transition which is certainly smaller than total ΔS_T (including the normal MCEs in pure PM and FM phases). Last but not least, as discussed in section 2.7, the original Clausius-Clapeyron equation underestimates $|\Delta S_T|$ in magnetizing processes and overestimates $|\Delta S_T|$ in demagnetizing processes due to the irreversibility of FOPTs. In the case of MnAs, Tocado *et al.* [29] estimated that $|\Delta S_T|$ should be decreased / increased by the amount 15 % for the results obtained from demagnetization / magnetization data.

Figure 4.1 shows a typical magnetic phase diagram for magnetic materials which undergo FOPTs. The FOPT is associated with a hysteretic behavior. Normally, the hysteresis reduces with an increase of magnetic field and finally disappears when the field is strong enough, i.e. two transitions joint at the critical point at some temperature and field, where the transition becomes second order. The corresponding temperature and magnetic field are named critical temperature T_{crit} and critical field B_{crit}, respectively. Above the critical point, mixed phases cannot be distinguished. In figure 4.1, the region above the upper transition line (PM-FM transition line) is FM and below the lower one (FM-PM transition line) is PM. In the region between the two lines, the state of the sample depends on the temperature and external magnetic field history. It is worth to note that a reproducible FM or PM phase can be formed
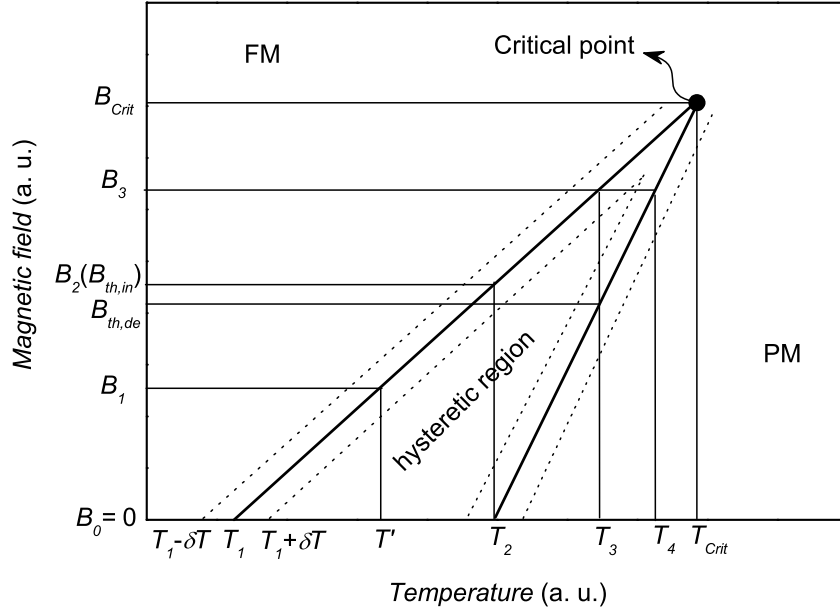
Figure 4.1: Magnetic phase diagram of a magnetic material showing a FOPT associated with hysteresis.

in the hysteretic region through a specific cycling of the temperature and the external magnetic field in the sample. A phase transition does not happen until the temperature or the magnetic field crosses the FM-PM transition line in a heating or demagnetizing process, and until it crosses the PM-FM transition line in a cooling or magnetizing process. Moreover, it should be noted that sharp transition lines are only true for an ideal case. In a real material, the occurrence of a FOPT is not concentrated at a single temperature or magnetic field, but in a narrow band (transition band) as illustrated by the dotted lines in figure 4.1. The width of the transition band, which depends on the properties of the sample, is assumed to be $2\delta T$. In the transition bands, the percentages of the FM and PM phases of the sample also depend on the thermal and magnetic history.

As discussed in the previous section, in order to estimate the MCE of magnetic materials, nothing more than magnetization versus temperature $M_B(T)$, magnetization versus magnetic field $M_T(B)$, heat capacity versus temperature at constant magnetic fields $C_{p,B}$, and direct measurements need to be performed. So, in the following, discussions will be made on the detailed processes of these measurements.

In the present Thesis, four different protocols have been employed in the

magnetization and direct measurements, described as follows:

Protocol 1: A measurement is performed with the magnetic field changing from 0 to B and then back to 0 at a starting temperature T_l, at which the sample is in fully FM phase. Then the sample is heated to the next measuring temperature T_i at zero field and then a measurement is performed following the same field sequence as used at T_l. The procedure is repeated until the temperature reaches T_h, at which the sample is in fully PM phase.

Protocol 2: The sample is first heated up to T_h at zero field, then cooled down to a measuring temperature T_i, at which a measurement is performed with the magnetic field changing from 0 to B and then back to 0. After that, the sample is heated up to T_h again, and then cooled down to the next measuring temperature T_{i+1} ($T_i < T_{i+1}$). Perform a measurement at T_{i+1} following the same field sequence as used at T_i. The procedure is repeated until the temperature reaches T_h.

Protocol 3: The sample is first cooled down to T_l, then a magnetic field B is applied. Then the sample is heated up to a measuring temperature T_i at a constant magnetic field B. A measurement is performed when the magnetic field is brought back to 0 at T_i. After that, the sample is cooled down to T_l again, and then heated up to the next measuring temperature T_{i+1} ($T_i < T_{i+1}$) at a constant magnetic field B. A measurement is performed at T_{i+1} following the same field sequence as used at T_i. The procedure is repeated until the temperature reaches T_h.

Protocol 4: A magnetic field B is applied at T_l, then a measurement is performed with the magnetic field changing from B to 0 and then back to B. After that, the sample is heated to the next measuring temperature T_i at a constant magnetic field B, and then a measurement is performed following the same field sequence as used at T_l. The procedure is repeated until the temperature reaches T_h.

In most publications, the entropy change is determined from isothermal magnetization data which are measured following protocol 1. As a result, an unphysical spike appears in the case of FOPT. Tocado *et al.* [68] explained the cause of the "spike" effect based on the magnetic phase diagram (figure 4.2). When one calculates the entropy change between the states A and A'' on the basis of isothermal magnetization measurement performed following protocol 1, the "spike" effect appears. The temperatures corresponding to the states A and A'' are just in the two-phase-coexistence (TPC) region. In the measurements, the sample is not brought from state A to A'' directly on heating at constant field, but following a path $A - O - O' - A''$, as shown in figure 4.2. The changes of phase fraction are quite small in the processes $A - O$ and $O' - A''$, but there could be a large portion of the sample suffering a transition from FM to PM
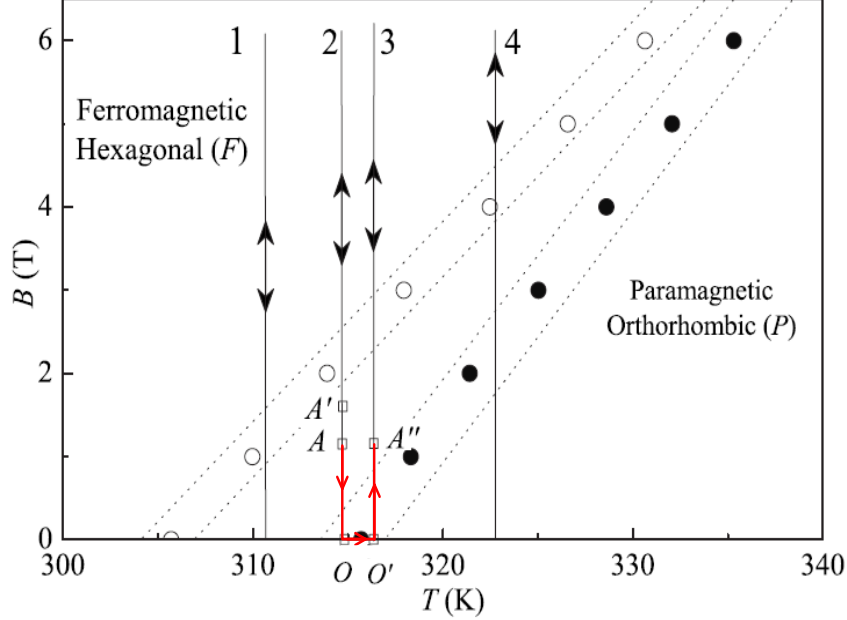
Figure 4.2: Magnetic phase diagram of MnAs (after Ref. [68]). Full and empty circles represent FM to PM and PM to FM phase transitions, respectively. Discontinuous lines show the finite width of the phase transition bands. Vertical arrows and lines (1-4) show the paths of magnetization measurements. Red arrowed curve indicates the path of the sample state, changing from A to A''.

phase during the heating process $O - O'$, which leads to a large drop of the magnetization in the sample. The large change of the magnetization between A and A'' translates into an entropy change induced by the field variation between A and A', but it is not real. On increasing field, the large phase-fraction-induced magnetization difference keeps up to a threshold field $B_{th,in}$ in the magnetization curves, resulting in a huge value of ΔS_T, namely, the "spike" effect. Similar discussions can be made for decreasing fields. Therefore, we can conclude that the "spike" effect appears in the results obtained from isothermal magnetization data for a FOPT when the threshold fields $B_{th,in}$ and $B_{th,de}$ are not close to zero and B_{max} on magnetizing and demagnetizing, respectively. That takes only place in the TPC region. In other words, the "spike" effect exists when the isothermal magnetization curves are measured starting in the high temperature transition band for increasing field or in the low temperature transition band for decreasing field.

Referring to equations (4.10) and (4.11), the size of the "spikes" is pro-

portional to the converted phase fraction Δx and the threshold field $B_{th,in}$ for increasing field, or to $\Delta x'$ and $B_{\max} - B_{th,de}$ for decreasing field, if the temperature step ΔT is fixed in the measurements.

With the help of the magnetic phase diagram of figure 4.1, the discussions about the "spike" effect are made when applying different maximum magnetic fields in various temperature ranges due to the fact that the state of a sample with FOPT is history dependent on both of the external magnetic field and the temperature. In figure 4.1, T_1 and T_2 are transition temperatures on cooling and heating at zero field ($B_0 = 0$), respectively. T_3 is an arbitrary temperature between T_2 and T_{crit}. B_2 and B_3 are the transition magnetic fields when the sample is magnetized at constant temperatures T_2 and T_3, respectively. B_1 is an arbitrary field below B_2. T' is the transition temperature when the sample is cooled at a constant field B_1. T_4 is the transition temperature when the sample is heated at a constant field B_3. Nevertheless, we have to bear in mind that the transition does not take place at a single temperature or field in a real material, but in a transition band ($T - \delta T < T < T + \delta T$).

Generally speaking, GMCE comes from a field-induced phase transition in a transition temperature region, out of which the MCE is weak. In the absence of the field-induced phase transition, the observed MCE is normal even in the transition temperature region for a material exhibiting FOPT. When the measurement is performed following protocol 1, the threshold field of a phase transition is $B_{th,in}$ on increasing field, and $B_{th,de}$ on decreasing field, as indicated in figure 4.1. Defining $B_{\max}$ as the maximum magnetic field applied in an isothermal magnetization measurement, the "spike" effect can be discussed on the basis of equations $(4.9) - (4.12)$ as follows:

1. When $B_{\max} = B_1 < B_2$, there is no field-induced transition in the whole temperature range. Therefore, no GMCE would be observed in the results. The sample keeps in FM phase below $T_2 - \delta T$, and in PM phase above $T_2 + \delta T$. The phase components of the sample can be quite different when the measurement is performed in the transition band $T_2 - \delta T < T < T_2 + \delta T$ (TPC region), resulting in the "spike" effect on both increasing and decreasing fields. According to equation (4.9), the magnitude of the "spike" is proportional to B and, is large because of $B_{\max} < B_{th,in}$. In this case, the isothermal magnetization curves on increasing and decreasing fields overlap and the resultant spurious spikes locate at the same position at T_2. This effect is clearly observed in $MnCo_{0.98}Cu_{0.02}GeB_{0.02}$ (see chapter 9), where the applied maximum field 5 T is much lower than the threshold field $B_{th,in} = B_2 = 9.5$ T.

2. When $B_2 < B_{\max} = B_3 < B_{crit}$, similarly, no field-induced transition happens below $T_2 - \delta T$, while a transition from PM to FM phase

and a transition from FM to PM phase can be triggered in the temperature range $T_2 - \delta T < T < T_3 + \delta T$ on increasing and decreasing fields, respectively. The measurements started at the transition bands $T_2 - \delta T < T < T_2 + \delta T$ and $T_3 - \delta T < T < T_3 + \delta T$ result in spurious spikes on increasing and decreasing fields, respectively. For increasing field, according to equations (4.9) and (4.10), the "spike" effect is large, and its magnitude is proportional to B below $B_{th,in}$ and reach a maximum above $B_{th,in}$; for decreasing field, according to equations (4.11) and (4.12), the "spike" effect is large and its magnitude is proportional to $B - B_{th,de}$ above $B_{th,de}$ but there is no spike below $B_{th,de}$. As a result, one can obtain reliable values of ΔS_T above $T_2 + \delta T$ but with a spurious spike at T_2 for a field change from 0 to B_{max}, and also reliable below $T_3 - \delta T$ but with a spurious spike at T_3 for a field change from B_{max} to 0. Figure 2(a) in Ref. [104] for $Gd_5Si_{0.33}Ge_{3.67}$ belongs exactly to this situation, where two separated spurious spikes are observed on increasing and decreasing fields, as shown in figure 4.3.

3. When $B > B_{crit}$, above the critical temperature, the nature of the transition becomes second-order or there is no transition at all. Therefore, only measurements performed in the TPC region $T_2 - \delta T < T < T_2 + \delta T$ on increasing field produce the "spike" effect whose magnitude is proportional to B below $B_{th,in}$, and reaches a maximum above $B_{th,in}$. For decreasing field, there is no "spike" effect for all the field changes.

When an isothermal magnetization measurement is carried out following protocol 2, the threshold on increasing field happens in the $T_1 - \delta T < T < T_1 + \delta T$ range and is reduced close to zero, while $B_{th,de}$ is the same as that with protocol 1. The discussions are also divided in three steps:

1. When $B_{max} = B_1 < B_2$, below $T_1 - \delta T$ no field-induced transition happens since the state of the sample keeps in FM phase. Therefore, the MCE is weak. Transitions take place between $T_1 - \delta T$ and T' because the sample maintains the PM phase in this temperature range when it cools from T_h at zero field. Applying an external magnetic field B_{max} leads to the occurrence of a field-transition from PM to FM phase. It is different from the measurement following protocol 1, in which no transition takes place in this temperature range. However, the measurement performed in the TPC region $T_1 - \delta T < T < T_1 + \delta T$ still results in the "spike" effect. In this case, the spurious spike happens at T_1 and its magnitude is much smaller than that obtained using protocol 1, because the threshold field $B_{th,in}$ is reduced close to zero by using protocol 2. The decreasing field does not trigger any transition since each magnetization

curve initiates from the FM state below $T' - \delta T$ and from the PM state above $T' + \delta T$. That leads to a large spurious spike at T' on decreasing field. Consequently, reliable values of ΔS_T can be obtained only from magnetization on increasing field, though a small spurious spike exists to some extent. For decreasing field, the values of ΔS_T around T' are attributed to the "spike" effect.

2. When $B_2 < B_{\max} = B_3 < B_{crit}$, the increasing field magnetization data give reliable values of ΔS_T but with a small spurious spike at T_1, which is similar to the previous case. For decreasing field, a field-induced transition from FM to PM phase occurs between $T_2 - \delta T$ and $T_3 + \delta T$, because the sample has been brought to a FM state by applying a magnetic field $B_{\max}$ in this temperature range. Nevertheless, for decreasing field, the use of protocol 2 still makes the sample state be FM below T_3 and PM above T_3, resulting in a large spurious spike of ΔS_T at T_3.

3. When $B_{\max} > B_{crit}$, ΔS_T shows a small spurious spike at T_1 on increasing field, and no "spike" effect is present on decreasing field.

When protocol 3 is employed in an isothermal magnetization measurement, the magnetization is measured only on decreasing field. Because $B_{th,de}$ is close to $B_{\max}$ by the use of protocol 3, the "spike" effect is reduced according to equation (4.11). For $B_{\max} = B_3 < B_{crit}$, a small spurious spike shows at T_4 for a field change from $B_{\max}$ to 0 and no "spike" effect is present for other field changes from B lower than $B_{\max}$, according to equation (4.12). The "spike" effect is absent for $B \geq B_{crit}$.

Accordingly, the large spurious spikes of the entropy change on increasing and decreasing fields obtained using protocol 1 can be significantly reduced by employing protocols 2 and 3, respectively. Because on increasing field, $B_{th,in}$ is close to zero in the region where Δx is different than zero, the "spike" effect is small according to equations (4.9) and (4.10). Similarly, $B_{th,de}$ is close to $B_{\max}$ in the region where $\Delta x'$ is different than zero, equation (4.11) gives a small value of $|\Delta S_T|$. The "spike" effect can be completely avoided only when the applied maximum magnetic field exceeds the critical field and the isothermal magnetization measurements are performed on decreasing field, no matter which protocol is used. Otherwise, the "spike" effect always appears, but the magnitude and position of the "spike" depend on the maximum applied field and the type of protocol used. Spurious spikes with different magnitudes exist at T_2 and T_1 on increasing field when the isothermal magnetization data are measured following protocols 1 and 2, respectively, no matter how strong is the field applied. The "spike" effect depending on the protocols and the maximum of the applied field is summarized in table 4.1.

Table 4.1: Spurious spikes for a field change of $B_{\max}$ in the case of different protocols and various applied maximum magnetic fields.

Isothermal measurement			Spike	Position	Magnitude
Protocol 1	Increasing field	$B = B_1 < B_2$	Yes	T_2	Large
		$B_2 < B = B_3 < B_{crit}$	Yes	T_2	Large
		$B > B_{crit}$	Yes	T_2	Large
	Decreasing field	$B = B_1 < B_2$	Yes	T_2	Large
		$B_2 < B = B_3 < B_{crit}$	Yes	T_3	Large
		$B > B_{crit}$	No	-----	-----
Protocol 2	Increasing field	$B = B_1 < B_2$	Yes	T_1	Small
		$B_2 < B = B_3 < B_{crit}$	Yes	T_1	Small
		$B > B_{crit}$	Yes	T_1	Small
	Decreasing field	$B = B_1 < B_2$	Yes	T'	Large
		$B_2 < B = B_3 < B_{crit}$	Yes	T_3	Large
		$B > B_{crit}$	No	-----	-----
Protocol 3	Increasing field	-----	-----	-----	-----
		-----	-----	-----	-----
	Decreasing field	$B < B_{crit}$	Yes	T_4	Small
		$B > B_{crit}$	No	-----	-----
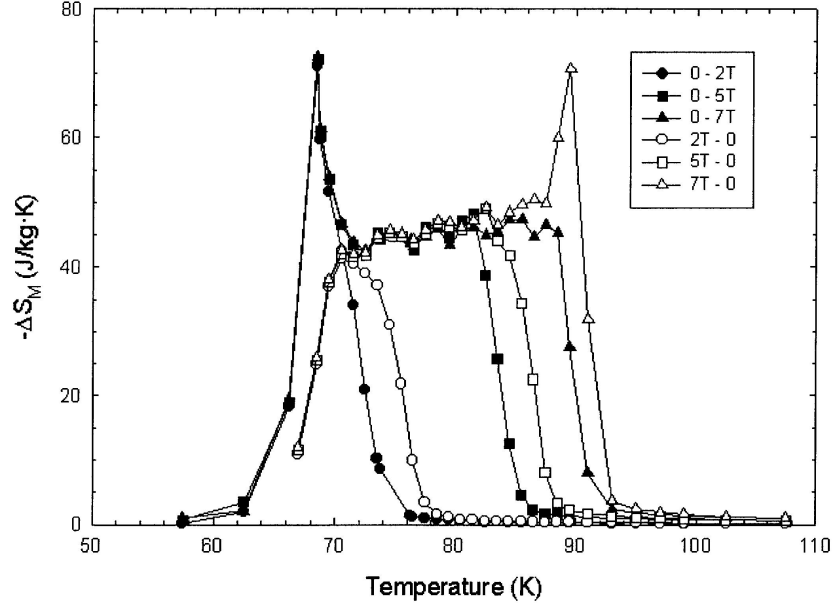
Figure 4.3: Temperature dependence of the isothermal entropy change for $Gd_5Si_{0.33}Ge_{3.67}$. The data were calculated from magnetization data recorded on increasing and decreasing magnetic fields. Taken from Ref. [104].

According to equation (4.2), for every two adjacent isothermal magnetization curves at T_m and T_{m+1} ($T_m < T_{m+1}$), one has:

$$(T_{m+1} - T_m)\Delta S \left(\frac{T_{m+1} + T_m}{2} \right) = \sum_i (M_{m+1,i} - M_{m,i})\Delta B_i = A_m \quad (4.15)$$

where the term in the left hand side stands for the area below the entropy change curve from T_m to T_{m+1}, and the term in the right hand side represents the area between the isothermal magnetization curves at T_m and T_{m+1}.

In figure 4.4, we present a schematic representation of the isothermal magnetization curves (a) and the entropy change resulted from the magnetization data (b). According to equation (4.15), the shaded areas in figures 4.4(a) and 4.4(b) should be equal. By summating equation (4.15), the total area below the entropy change curve from T_l to T_h (it is related to the refrigeration capacity) is equal to that between the isothermal magnetization curves at T_l and T_h. T_l and T_h are two temperatures far below and above the transition temperature, respectively.

As the sample is fully in FM phase at T_l and fully in PM phase at T_h, at these states the magnetization of the sample only depends on the temperature and field, is independent of the trajectory followed by the state point. There-
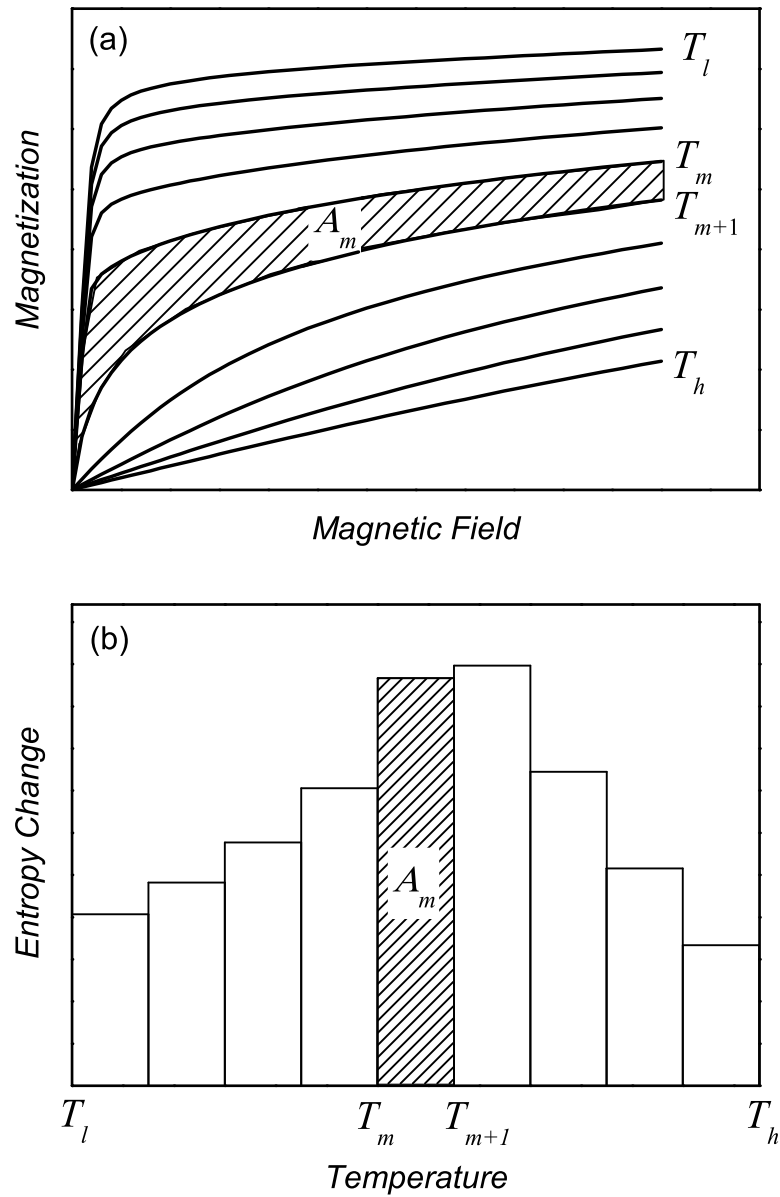
Figure 4.4: (a) Schematic representations of the isothermal magnetization curves. (b) The resultant isothermal entropy change as a function of temperature. The shaded area of (a) corresponds to that of (b).
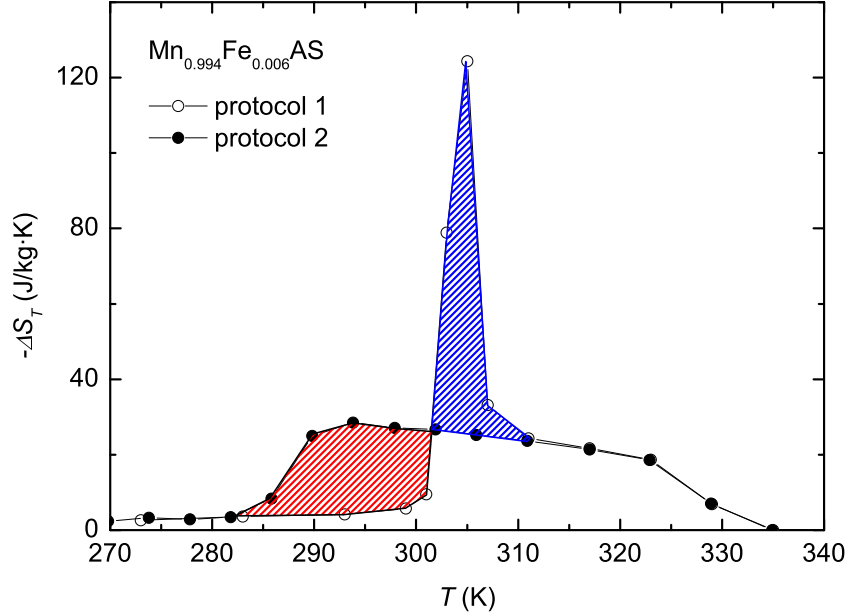
Figure 4.5: Temperature dependence of the entropy change for a field change from 0 to 9 T for $Mn_{0.994}Fe_{0.006}As$. Open and solid circles represent ΔS_T determined from isothermal magnetization data measured following protocols 1 and 2, respectively.

fore, the area between the two isothermal magnetization curves at T_l and T_h is well defined, namely, the area is always the same no mater which protocol is followed in the measurements. Thus, the areas below the entropy change curves obtained from the measurements following protocols 1 and 2 are the same. As a result, the area below the spurious spike (from the plateau to the top of the peak) obtained from the measurement following protocol 1 should be equal to the area below the entropy change curve from T_1 to T_2 obtained from the measurement following protocol 2. For example, the size of the green shadow (~ 317 J/kg) is equal to that of the red shadow (~ 314 J/kg) in figure 4.5 for the results of $Mn_{0.994}Fe_{0.006}As$.

According to equations (4.10) and (4.13), the area below the spurious spike for increasing magnetic field can be expressed as:

$$A_{spike} = \int \frac{C_{an,0T}(T) - C_{nor,0T}(T)}{\Delta H_{0T}}(M_{FM} - M_{PM})B_t(T_2)dT \qquad (4.16)$$

where $B_t(T_2)$ is the transition field when it crosses the PM-FM transition line at T_2. It is reasonable to assume $(M_{FM} - M_{PM})$ approximately to be a

constant in a narrow temperature range ($T - \delta$ to $T + \delta$). Therefore, $(M_{FM} - M_{PM})B_t/\Delta H_{0T}$ can be taken out of the integral, leaving the integral being just ΔH_{0T}. So we have:

$$A_{spike} = (M_{FM} - M_{PM})B_t(T_2) \tag{4.17}$$

On the other hand, the area below the entropy change curve between T_1 and T_2 is given by:

$$A_{T_1,T_2} = -\int_{T_1}^{T_2} \Delta S_T dT \tag{4.18}$$

where ΔS_T is the entropy change determined using protocol 2, and it is approximately equal to the results predicted by the Clausius-Clapeyron equation, assuming that entropy increments in PM and FM phases are small. Then equation (4.18) can be written as:

$$A_{T_1,T_2} \approx \int_{T_1}^{T_2} (M_{FM} - M_{PM})\frac{dB_t}{dT}dT = (M_{FM} - M_{PM})[B_t(T_2) - B_t(T_1)] \tag{4.19}$$

where $B_t(T_1) = 0$ makes A_{spike} to be equal to A_{T_1,T_2}.

Alternatively, both isofield magnetization $M_B(T)$ and isofield heat capacity $C_{p.B}$ can be used to bypass the spurious spike of ΔS_T in materials exhibiting FOPTs. In the isofield magnetization measurement, the magnetization data are recorded from low temperature to high temperature or the opposite direction at a constant magnetic field. A transition does not occur until temperature passes the FM-PM transition line in a heating process or the PM-FM transition line in a cooling process. In other words, the occurrence of the transition agrees with the phase diagram. Therefore, no "spike" effect shows in the resulting ΔS_T. However, the value of $(\partial M/\partial T)_B$ could be underestimated in practical measurements, where magnetization data are measured at discrete temperatures, because the magnetization changes sharply with temperature for FOPTs. The underestimated $(\partial M/\partial T)_B$ results in an underestimation of $|\Delta S_T|$ according to equation (4.1). On the other hand, small interval of magnetic fields is also needed to make equation (4.3) hold accurate enough.

A heat-capacity measurement is performed with the same temperature evolution as the $M_B(T)$ measurement, i.e. from FM to PM on heating and from PM to FM on cooling. In this case, both magnetocaloric parameters, ΔS_T and ΔT_S, can be correctly determined.

Regarding the direct measurements of ΔS_T, the large ΔS_T of a material exhibiting a FOPT mainly originates from the heat Q related to the field-induced phase transition which also leads to a large ΔT_S. In the absence of the field-induced phase transition, only normal ΔS_T and ΔT_S for pure PM and FM

phases can be observed. The occurrence of the field-induced transition requires using protocol 2 when performing direct measurements on increasing magnetic field between T_1 and T_2, and following protocol 3 on decreasing magnetic field between T_3 and T_4. Otherwise, with protocol 1 or 4, the normal ΔS_T and ΔT_S of the FM phase are obtained in the range T_1 to T_2 on increasing field and the normal ΔS_T and ΔT_S of the PM phase are obtained in the range T_3 to T_4 on decreasing field. The normal ΔS_T and ΔT_S obtained from the direct measurements are smaller than those obtained from heat capacity in the respective temperature ranges. These small ΔS_T and ΔT_S are correct, and are mainly due to a lower FM or PM phase fraction in the sample when the measurement starts. Therefore, different results can be obtained in the direct measurements of ΔS_T and ΔT_S when following different protocols which lead to different initial states of the sample. Throughout this Thesis, the direct measurements of ΔS_T were carried out on decreasing field, and the direct measurements of ΔT_S were done on increasing field. Therefore, in order to obtain coinciding results with those from heat capacity, protocols 2 and 3 were employed in the direct measurements of ΔT_S and ΔS_T, respectively.

4.5 A case of study of MCE in Gd

The magnetocaloric properties of rare-earth metals have been intensively investigated in the past years due to their high values of total angular momentum number, i.e. high magnetic moments [53]. Unfortunately, only Gd exhibits a SOPT from PM to FM phase near room temperature among the whole series of the rare-earth metals. Previous studies showed that Gd is a simple ferromagnet from liquid helium temperature up to its Curie temperature $T_C = 293$ K [105]. The MCE of Gd was firstly reported by Brown [6] in 1976. Since then Gd has been regarded as a prototype of magnetocaloric materials for room-temperature magnetic refrigeration, and the MCEs of other materials are often compared with it. As an example for studying a material with SOPT using the calorimeter described in chapter 3, we examined the heat capacity and MCE of a polycrystal Gd sample. The results were compared with those determined from magnetization and literature values. Besides, the demagnetization effect on the MCE was taken into account.

4.5.1 Experimental

Four platelets of commercial Gd with dimensions of $a = 2.45, 3.30, 2.75, 3.55$ mm, $b = 1.10, 1.10, 1.05, 1.05$ mm, and $c = 5.70, 7.80, 9.80, 4.50$ mm, called platelet 1, platelet 2, platelet 3, and platelet 4, respectively, were used in

calorimetric measurements. The platelets were put into a sample container, arranged one by one with the c direction along the vertical axis. Magnetic field was applied parallel to the c axis of the platelet. The heat capacities of Gd were determined with the heat-pulse and thermogram techniques under magnetic fields of 0, 1.5 T and 6 T. A temperature step of 2 K was used in the heat-pulse measurement and a rate about 2 mK/s was set in the thermogram measurement. The direct measurements of ΔS_T were carried out upon magnetic field changes from 1.5 T and 6 T to 0 with maximum slopes of –2.2 T/min and –4.4 T/min, respectively. A constant slope of 2.2 T/min was used during the direct measurement of ΔT_S, following the magnetic field sequence $0 - 1.5\text{ T} - 3\text{ T} - 5\text{ T} - 6\text{ T}$. Magnetization measurements were performed on platelet 4 using a commercial SQUID magnetometer (PPMS), applying a magnetic field parallel to the c axis. Isothermal magnetization curves were measured from 220 K to 360 K with an interval of 5 K upon applying a field from 0 to 6 T with a step of 0.2 T.

4.5.2 Heat capacity

Figure 4.6 shows the temperature dependence of the heat capacity for the studied Gd together with that reported by Dan'kov *et al.* [5] at zero field. As can be seen, the two sets of zero-field heat capacity data show λ-type anomalies. The maximum of the λ-type anomaly of our sample is not so large as that of a single crystal reported by Dan'kov *et al.* [5] within the graphic resolution. The heat-capacity anomaly and the MCE of Gd are reduced by the existence of impurities. Therefore, our data and the reported data match well below and above the peak, where the impurities affect weakly to the heat capacity. As a result, any small difference of the heat capacity can be attributed to both, the different qualities of the samples and the experimental errors.

Cooling and heating thermograms coincide better than 0.1 K at the drop of the anomaly ($T = 293.5$ K). This "apparent hysteresis" is expected for a heating (cooling) rate of $\sim$2 mK/s and a relaxation time of 24 s at this temperature (according to equation (3.6), $2(T - T_s) = 0.096$ K). The heat-capacity data obtained from the thermogram show a maximum difference of 0.8 % at 288.3 K with respect to the heat-pulse data. All these very small differences serve as a calibration of the typical experimental errors of the thermograms, since the magnetic transition of Gd is of second order.

Heat capacities at magnetic fields of 1.5 T and 6 T determined from the thermograms are also presented in figure 4.6. The λ-type anomaly at zero field is considerably broadened and shifts to high temperature as the magnetic field increases, which is the typical behavior of a simple FM material,
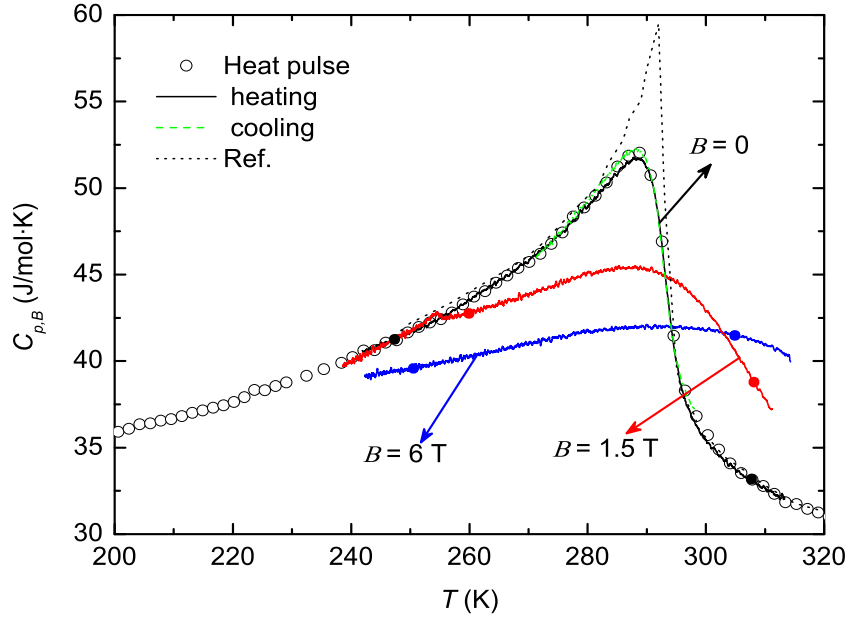
Figure 4.6: Heat capacity as a function of temperature at applied fields of 0, 1.5 T and 6 T for the Gd platelets. Colored solid circles denote the chosen equilibrium points for the fitting of thermograms. Dotted line represents the heat capacity measured at zero field, taken from figure 7 of Ref. [5].

4.5.3   Isothermal entropy change

The values of ΔS_T of the Gd platelets have been determined from direct and indirect measurements. First we compare ΔS_T of our polycrystal Gd platelet with that of a single crystal Gd reported in the literature [5], both sets of data were determined from isothermal magnetization data for the same magnetic field variation, as shown in figure 4.7(a). It is seen that the ΔS_T peaks locate at nearly the same temperature 294 K for both a small magnetic field change of 2 T and a large magnetic field change of 5 T. Near the transition temperature, the values of ΔS_T reported by Dan'kov *et al* are slightly larger than those of our sample for the same field variation. The difference should be mainly due to the lower purity of the Gd sample we used, since the MCE is less dependent on the crystal orientation at magnetic fields stronger than 2 T [5]. The difference becomes negligible far away from the transition region, which is consistent with the comparison of the heat-capacity data.

Figure 4.7(b) displays the entropy changes for field changes of 1.5 T and 6 T obtained from the direct measurements (solid triangles) and from the heat
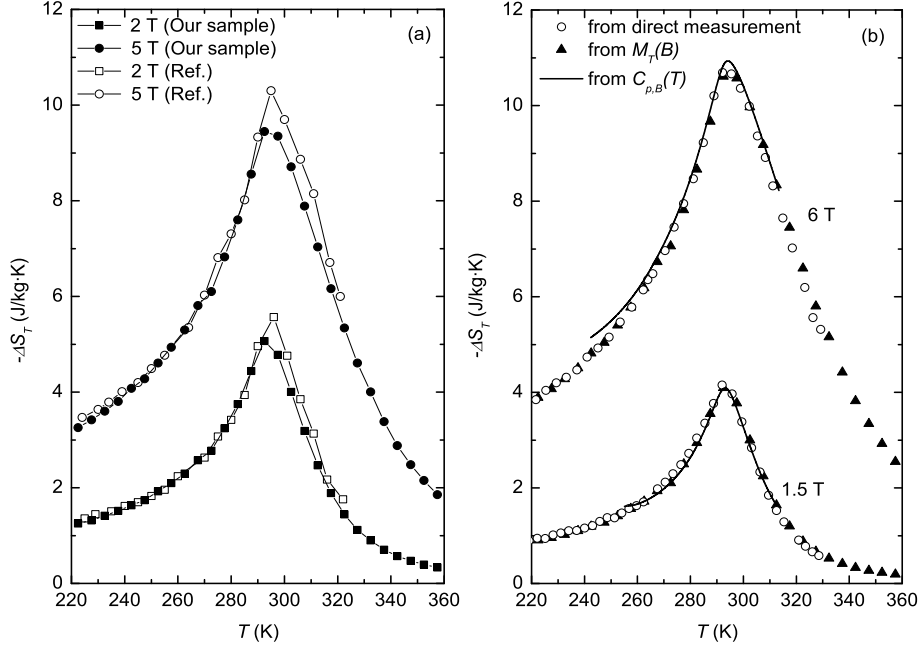
Figure 4.7: (a) Comparison of ΔS_T, obtained from isothermal magnetization data by using the Maxwell relation, between a single crystal Gd (taken from figure 14 of Ref. [5]) and our sample. (b) Comparison of ΔS_T of our Gd sample determined by three techniques, i.e. isothermal magnetization, heat capacity and direct measurements. All the results are shown without any correction of the demagnetization effect.

capacity at constant magnetic fields (solid lines) as well as from the isothermal magnetization data (open circles). Taking ΔS_T determined from the direct measurements as a standard because of its high accuracy, the maximum differences between ΔS_T obtained from the direct and heat-capacity measurements are 0.07 J/kg·K (1.7 %) and 0.23 J/kg·K (2.1 %) for field changes of 1.5 T and 6 T, respectively. They are 0.06 J/kg·K (1.4 %) and 0.09 J/kg·K (0.8 %) between the ΔS_T obtained from direct and magnetization measurements for the same field variations. One can see that the results are well consistent with each other, with a discrepancy lower than 2 %.

4.5.4 Adiabatic temperature change

Adiabatic temperature change determined from direct measurement (solid symbols) and from heat-capacity data (lines) for field changes of 1.5 T and 6 T are displayed in figure 4.8. A good agreement between the results obtained from

both methods is observed. The maximum differences between ΔT_S obtained from the direct and heat-capacity measurements are 0.08 K (1.8 %) and 0.07 K (0.6 %) for field changes of 1.5 T and 6 T, respectively. At the Curie temperature, the maxima $\Delta T_{S,\mathrm{max}} = 4.4$ K and 12.3 K for our sample are slightly smaller than 4.8 K and 12.9 K reported by Dan'kov *et al.* [5, 106] for magnetic field changes from 0 to 1.5 T and 6 T, respectively. The difference could be still mainly caused by the higher impurity of our sample.
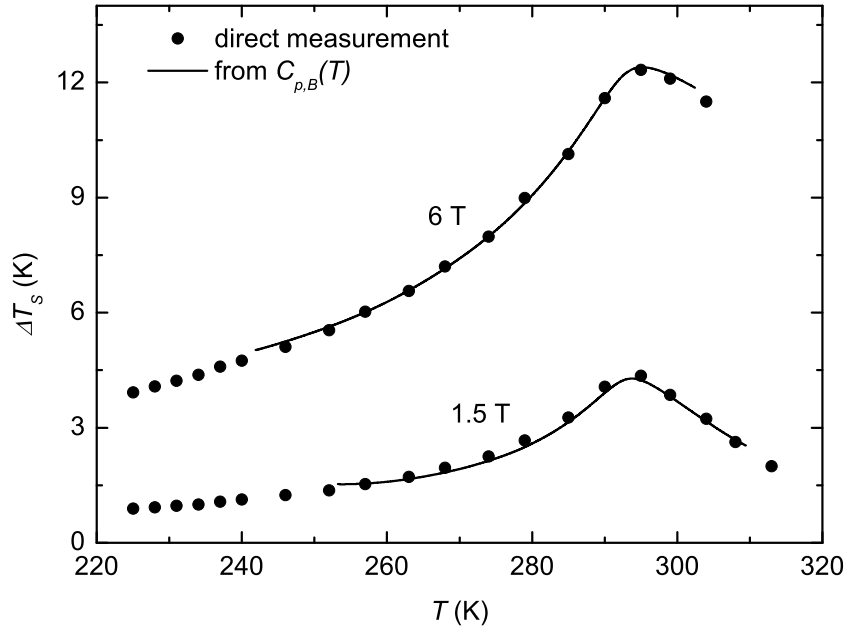
Figure 4.8: Adiabatic temperature change as a function of temperature of Gd obtained from heat-capacity and direct measurements with magnetic field changes of 1.5 T and 6 T, respectively.

4.5.5 Demagnetization effect on MCE

In a homogeneously magnetized magnetic system, a relevant intensive parameter is the external magnetic field B_{ext} (i.e the field in the absence of sample) and a corresponding extensive parameter is the magnetic moment I. The external field B_{ext} can be easily measured, because it is proportional to the applied current in the exciting coils, and the magnetic moment I also can be measured [107]. There is no problem choosing these parameters to denote the magnetic work except that magnetization $M(B,T)$ depends not only on the nature of a sample but also on its shape. The magnetization of a magnet de-
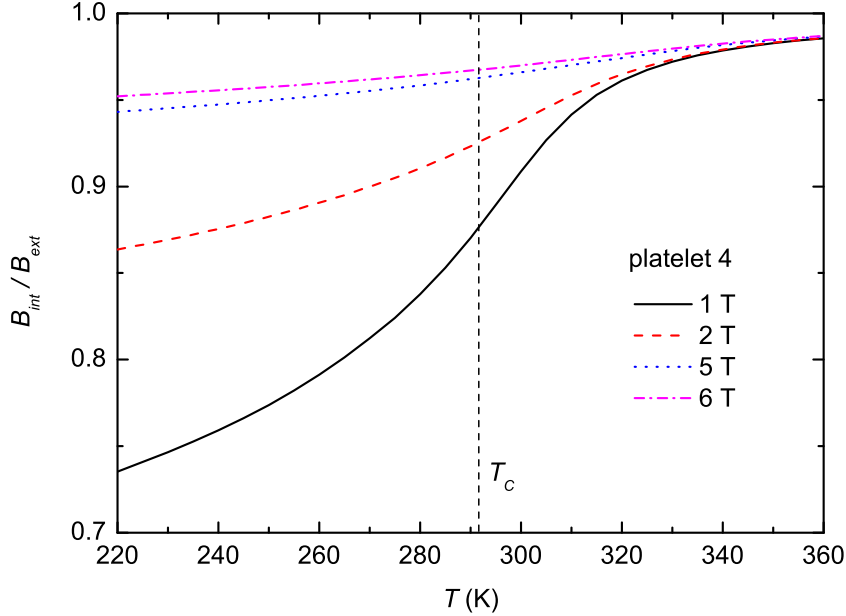
Figure 4.9: Normalized internal field as a function of temperature at different external fields for platelet 4.

pends on the total field, including the external field and the field produced by the magnet, the latter is called demagnetizing field. The demagnetizing field is proportional to the magnetization by the so-called demagnetization factor, N_D, that is, $B_{int} = B_{ext} - N_D M$. It is uniform over the whole sample and antiparallel to the external field only in the case of an ellipsoid under an external uniform field. For other shaped samples, the simplest approximation is to take its average over the magnet.

In materials showing GMCEs, usually a FOPT takes place between PM and FM phases. In the PM phase, the magnetization and the demagnetizing field are small; and in the FM phase, the magnetization of the material is nearly saturated, namely, the magnetization is close to its maximum and does not depend strongly on the external field. Therefore, there would not be a large difference if we take the external field or the internal field. In both phases, the demagnetizing field plays a secondary role for a FOPT. But in the case of a SOPT, like in Gd, near the Curie point this effect may be significant.

The demagnetization factor N_D of platelet 4 has been calculated approximately by a relatively simple analytical expression for a rectangular prism [108]. Taking the dimensions of the platelet $a = 3.55$ mm, $b = 1.05$ mm and c

= 4.50 mm, the resultant N_D is 0.158. In the calorimetric measurements, there are four platelets with different dimensions placed parallel to each other, the internal field on each platelet includes five contributions: the external field and the field produced by each of the four pieces. The calculation of the effective N_D is complex. We will only take into account the demagnetization effect in the magnetization measurements.

Figure 4.9 shows the normalized internal magnetic field as a function of temperature at different applied external fields for the Gd platelet 4. It is seen that the internal field decreases smoothly with a reduction of temperature due to that the magnetization changes from a low value in the PM phase to a high value in the FM phase. That is, the demagnetization effect in the FM phase is larger than in the PM phase. The demagnetization effect is significantly reduced by applying a higher external field due to the fact that the change of magnetization becomes much gradual at high fields.

In order to obtain the magnetocaloric parameters under constant internal field changes over the studied temperature range, we assume that the MCE modified by the demagnetizing field is estimated by the Maxwell relation $(\partial S/\partial B)_T = (\partial M/\partial T)_B$, that is, $\Delta S'_T = \Delta S_T + (\partial M/\partial T)_{B_{ext}} \cdot (B_{ext} - B_{int})$, where $\Delta S'_T$ represents the entropy change induced by an internal field change with the same value as the external field change, and is independent of the shape of the sample. The plots of ΔS_T, $\Delta S'_T$ and $\Delta S_T/\Delta S'_T$ as functions of temperature for different fields are shown in figure 4.10. The demagnetization effect on the MCE decrease with both increasing temperature and external field, which is similar to the variation of the internal fields. In other words, the demagnetization effect is more significant below T_C than above it. At a low field of 1 T, the value of ΔS_T is ~25 % smaller than that of $\Delta S'_T$ at 220 K, reducing gradually to ~3 % at 360 K. In the case of high fields, 5 T and 6 T, the demagnetization effect keeps lower than 5 % in the whole studied temperature range from 220 K to 360 K. Moreover, it is expected that the demagnetizing field has similar effects on ΔT_S as those on ΔS_T.

4.6   A case of study of MCE in $Mn_{1.1}Fe_{0.9}P_{0.82}Ge_{0.18}$

Fe_2P-type materials have attracted much interest to be used as working refrigerants for magnetic refrigeration near room temperature since the GMCE of $MnFeP_{0.45}As_{0.55}$ was reported by Tegus *et al.* in 2002 [42]. The GMCE in the MnFe(P,As) system results from a FOPT accompanied by a sharp change of lattice parameters. However, the existence of the toxic element As restricts its application to domestic refrigeration. Recent studies showed that the toxic As can be replaced completely by Ge without losing the characteristic of GMCE
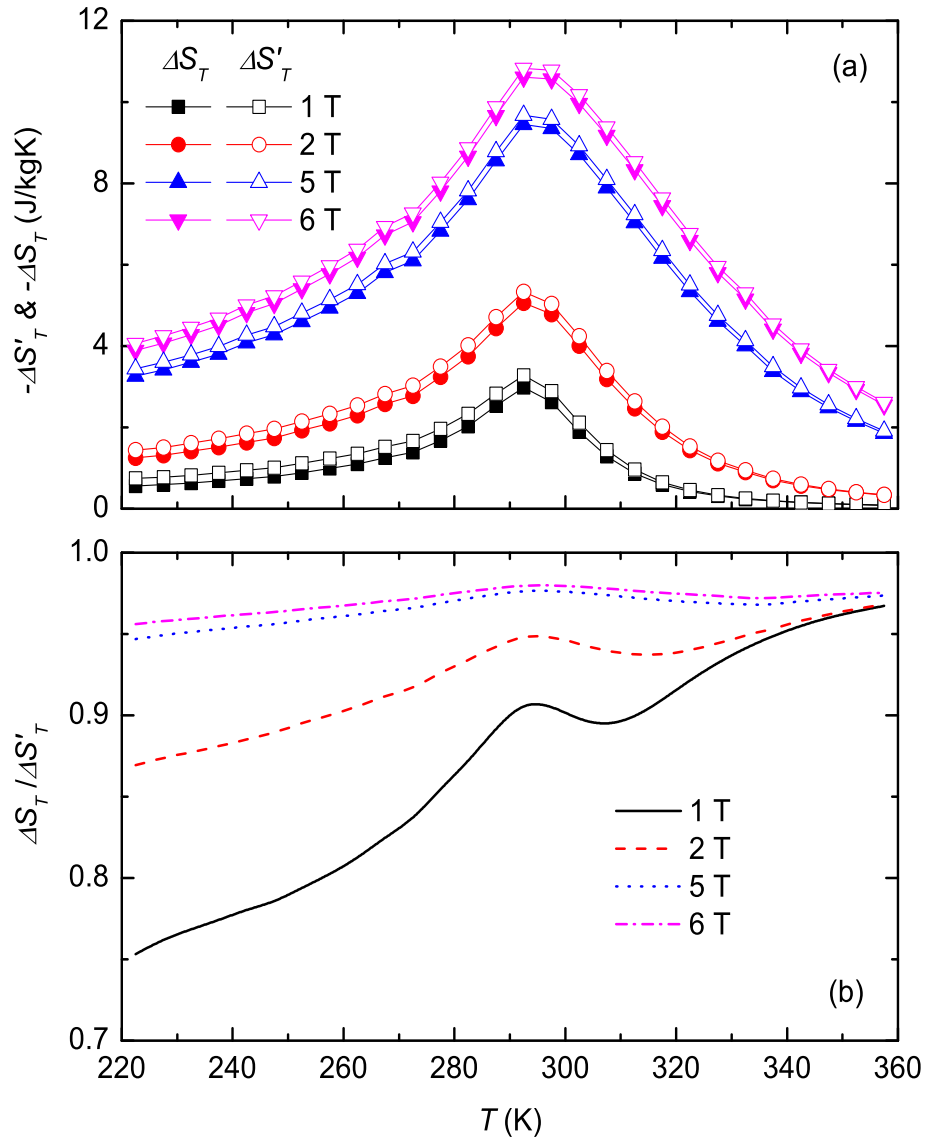
Figure 4.10: (a) Isothermal entropy change as a function of temperature of platelet 4 for the same change of the external and internal fields. (b) The normalized ΔS_T as a function of temperature for different fields.

[46–48, 109]. The introduction of Ge causes a broadening of the hysteresis [109]. As we discussed previously, one has to be careful to determine the MCE in materials exhibiting large hysteresis. In this section, as an example for the determination of MCE in hysteretic materials, we determined the MCE of $Mn_{1.1}Fe_{0.9}P_{0.82}Ge_{0.18}$ which undergoes a FOPT and exhibits a large thermal hysteresis of 19 K, by means of magnetic, calorimetric and direct measurements. The resultant values were compared.

4.6.1   Sample preparation

A polycrystalline sample with nominal composition $Mn_{1.1}Fe_{0.9}P_{0.82}Ge_{0.18}$ (provided by O.Tegus) was synthesized by means of high-energy ball-milling. The preparation details can be found in the literature [42]. The binary compound Fe_2P was mixed in the appropriate proportions with Mn chips, Ge fragments and P powder, and ground by ball-milling under a protective atmosphere. The obtained powders were sealed in a molybdenum tube under an Ar atmosphere, heated at $1000°$ for 120 h, followed by a homogenizing process at $650°$ for 120 h and finally slowly cooled down to ambient conditions.

4.6.2   X-ray diffraction

The analysis of powder XRD pattern indicates that the sample crystallizes mainly in the Fe_2P-type hexagonal structure ($a = 6.0651$Å, $c = 3.4597$ Å), with a small amount of a second phase MnO, as shown in figure 4.11.

4.6.3   Heat capacity

Figure 4.12 shows the temperature dependence of the heat capacity measured at zero field for the $Mn_{1.1}Fe_{0.9}P_{0.82}Ge_{0.18}$ compound. The measurement was performed starting from 6 K to 350 K. A sharp peak concentrates at 245 K, corresponding to its Curie temperature. Another small anomaly, as shown in inset (b), reveals the existence of a small amount of MnO impurity, which agrees with the XRD analysis. The electronic heat-capacity coefficient $\gamma_e = 7$ mJ/K^2·mole has been obtained by a linear extrapolation down to 0 K of the experimental C_p/T vs T^2 plot at low temperature, where the magnetic contribution is assumed to be negligible, as shown in inset (a). The resulting value of γ_e is lower than 24 mJ/K^2·mole reported for Fe_2P [110].

The lattice contribution to the total heat capacity has been estimated on the basis of the Debye model with the Debye temperature $T_D = 420$ K of Fe_2P [110], indicated by a red line shown in figure 4.12. The predicted lattice con-
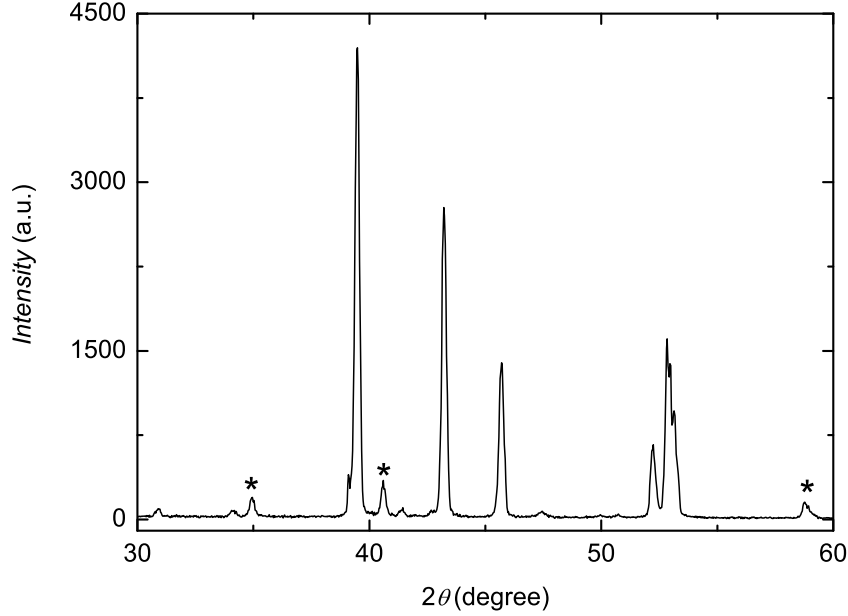
Figure 4.11: XRD pattern collected at room temperature for the $Mn_{1.1}Fe_{0.9}P_{0.82}Ge_{0.18}$ compound. The reflections of the secondary phase MnO are denoted by star symbols.

tribution fits well the experimental data below 150 K where the magnetic and electronic contributions are small. According to equation (2.32), the magnetic heat capacity has been obtained by subtracting the electronic and lattice contributions from the total heat capacity. The calculated magnetic entropy values at 223.86 K and 259.99 K, which are just below and above the heat-capacity peak, are $S_m(223.86$ K$) = 9.4$ J/kg·K and $S_m(259.99$ K$) = 47.0$ J/kg·K. It indicates that a large magnetic entropy change of 37.6 J/kg·K is associated with the transition from FM to PM phase.

We have measured the heat capacity of the $Mn_{1.1}Fe_{0.9}P_{0.82}Ge_{0.18}$ compound at constant magnetic fields of 0, 1 T, 3 T and 6 T in cooling and heating processes, displayed in figure 4.13. A large thermal hysteresis of 18.5 K is observed at zero field, reducing slightly to 15.9 K at 6 T. The transition temperature increases with increasing magnetic field at an average rate of 3.2 K/T on cooling, and 2.7 K/T on heating. The shape of the anomaly is hardly changed by the magnetic fields below 6 T.
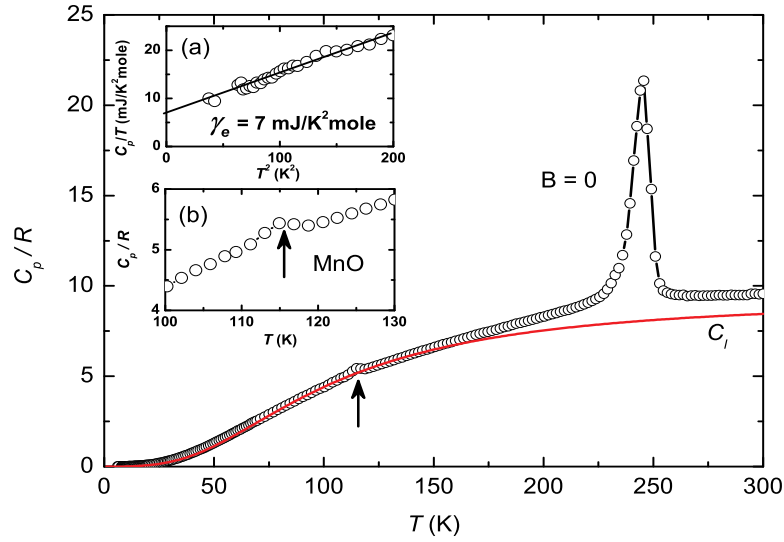
Figure 4.12: Heat capacity as a function of temperature for the $Mn_{1.1}Fe_{0.9}P_{0.82}Ge_{0.18}$ compound. The red solid line represents the lattice heat capacity estimated with $T_D = 420$ K. Inset (a) shows C_p/T vs T^2 plot at low temperature, and the black solid line is a linear fit of the data. Inset (b) indicates the anomaly of MnO phase.
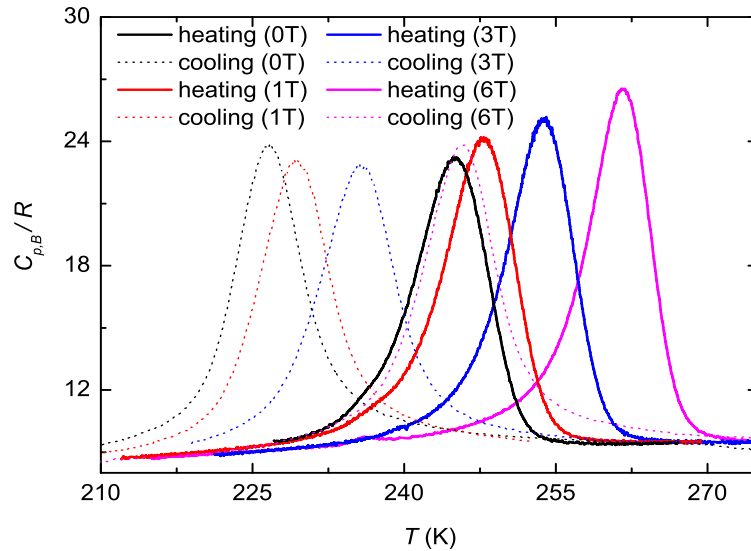
Figure 4.13: Heat capacity as a function of temperature measured at constant magnetic fields of 0, 1 T, 3 T and 6 T on heating and cooling for the $Mn_{1.1}Fe_{0.9}P_{0.82}Ge_{0.18}$ compound.

4.6.4 Magnetization

The measurement of magnetization as a function of temperature at constant magnetic fields between 1 T and 9 T has been carried out in heating and cooling processes for the $Mn_{1.1}Fe_{0.9}P_{0.82}Ge_{0.18}$ compound. The results are displayed in figure 4.14. A sharp magnetization drop is observed in each curve due to the occurrence of a temperature-induced FOPT. By taking the temperature where the first derivative of magnetization with respect to temperature reaches a minimum as the transition temperature for each curve in figure 4.14, the magnetic phase diagram of the studied compound has been constructed, as shown in figure 4.15. In this case, we found that the transition temperature increases with magnetic field at an average rate of 3.6 K/T on cooling and 2.9 K/T on heating, which agrees with that found in the heat-capacity measurements. The observed hysteresis 19.3 K at zero field is coincident with that obtained from the heat capacity. By taking linear extrapolations for the transition lines, the critical point would be at $T_{crit} = 325$ K and $B_{crit} = 27$ T.

We have carried out two types of isothermal magnetization measurements, one with a maximum field of 5 T and another with a maximum field of 9 T. By comparing the magnetic phase diagram of figure 4.15 with that of figure 4.1, $B_2 = 5.5$ T is the transition field (the threshold field $B_{th,in}$) on magnetizing process at $T_2 = 246$ K, and $B_3 = 9$ T is a field between B_2 and the critical field. Moreover, $T_1 = 227$ K is the transition temperature on cooling at zero field; $T_3 = 259$ K and $T_4 = 272$ K are the transition temperatures at 9 T on cooling and heating, respectively. The transition field (the threshold field $B_{th,de}$) at T_3 on demagnetizing process is about 4.3 T.

Figure 4.16 shows the isothermal magnetization curves measured with increasing magnetic field to 5 T and subsequent decreasing field following protocol 1. One can see that no complete field-induced metamagnetic transition happens at 244 K, 246 K, 248 K, 250 K, which are temperatures around $T_C = 246$ K. The presence of bent curves near 5 T on increasing field indicates the beginning of the transitions. The curves below 250 K exhibit a FM behavior on both increasing field and decreasing field. The decrease of magnetization with increasing temperature is mainly due to an increase of PM fraction in the sample during the heating period from one magnetization isotherm to the next one.

Figure 4.17 shows the isothermal magnetization curves measured also with a maximum magnetic field of 5 T, but following protocol 2. In this case, completely different magnetization curves from the curves of figure 4.16 are observed for increasing field. Field-induced metamagnetic transitions take place at temperatures just above $T_1 = 227$ K on increasing field, but only simple
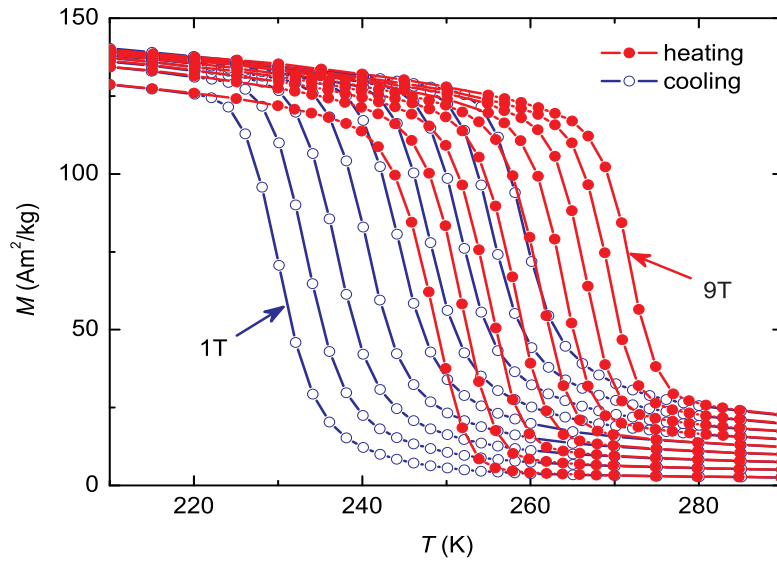
Figure 4.14: Magnetization as a function of temperature measured at constant magnetic fields of 1 T, 2 T, 3 T, 4 T, 5 T, 6 T, 7 T, 8 T and 9 T on heating and cooling for the $Mn_{1.1}Fe_{0.9}P_{0.82}Ge_{0.18}$ compound.
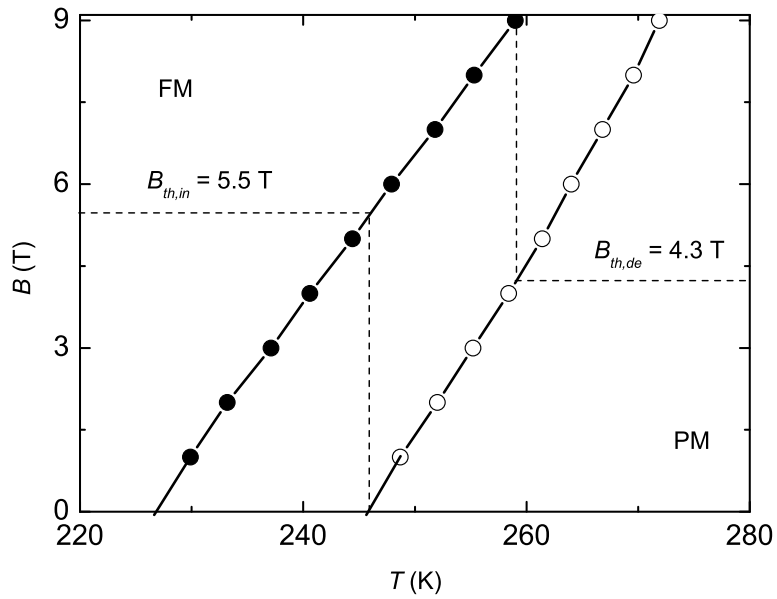

Figure 4.15: Magnetic phase diagram built from the isofield magnetization data for the $Mn_{1.1}Fe_{0.9}P_{0.82}Ge_{0.18}$ compound.

FM behavior is found in figure 4.16 at these temperatures. The magnetization curves on decreasing field exhibit a similar shape to those in figure 4.16 but with different magnitudes, because different initial sample states of the magnetization curves were caused by using protocols 1 and 2.

Figures 4.18 and 4.19 display the field dependence of the isothermal magnetization for the $Mn_{1.1}Fe_{0.9}P_{0.82}Ge_{0.18}$ compound obtained following the same procedure as those shown in figures 4.16 and 4.17, respectively, but with a maximum field of 9 T. One can see that field-induced metamagnetic transitions are observed in figure 4.18 for increasing field above 5 T and also for decreasing field below 5 T. A maximum field of 9 T can trigger the transitions between $T_2 = 246$ K and $T_3 = 259$ K on both increasing field and decreasing field. It is found that the magnetization curves (0 to 5 T and 5 T to 0) extracted from the data measured with the maximum field 9 T are significantly different from those obtained with the maximum field 5 T at the same temperatures. This happens because the magnetization curves correspond to different initial sample states that are obtained by applying different maximum fields, though the same protocol is employed.

Exactly identical magnetization curves are found in figures 4.18 and 4.19 on decreasing field but not on increasing field. Between $T_1 - \delta T$ and $T_2 + \delta T$, the initial sample states of the magnetization curves on increasing field are different in the two measurements, but they are the same for decreasing field because a maximum field of 9 T can complete the transitions at those temperatures in magnetizing processes. But that is not true in figures 4.16 and 4.17, because the transition at T_2 cannot be completed by a maximum field of 5 T in a magnetizing process.

Figure 4.20 shows the isothermal magnetization as a function of field measured following protocol 3 for the $Mn_{1.1}Fe_{0.9}P_{0.82}$ $Ge_{0.18}$ compound. In this case, the magnetization was only recorded on decreasing field. It can be seen in figure 4.20 that field-induced transition happens at each temperature between $T_2 = 246$ K and $T_4 = 272$ K. It is very different from those in figures 4.18 and 4.19, where the transitions only occur at temperatures between T_2 and T_3.

4.6.5 Magnetocaloric effect

Figures 4.21(a) and 4.21(b) display the isothermal entropy change as a function of temperature and magnetic field for the $Mn_{1.1}Fe_{0.9}P_{0.82}Ge_{0.18}$ compound obtained by using different techniques. In the direct measurements of ΔS_T, in order to obtain ΔS_T coinciding with that derived from heat capacity on heating, each point has been measured following protocol 3. For a field change of 6 T, the observed maximum of $-\Delta S_T$ from the heat capacity is 31.2 J/kg·K
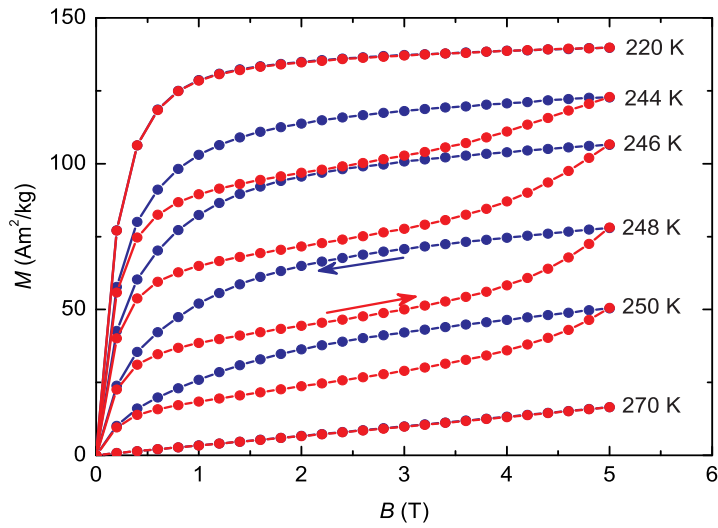
Figure 4.16: Magnetization as a function of magnetic field measured in the vicinity of its Curie temperature with a maximum field of 5 T for the $Mn_{1.1}Fe_{0.9}P_{0.82}Ge_{0.18}$ compound. The measurements were performed following protocol 1.
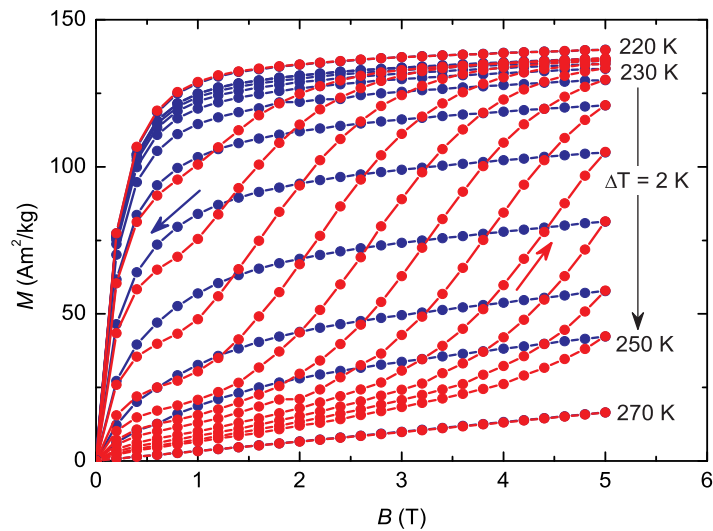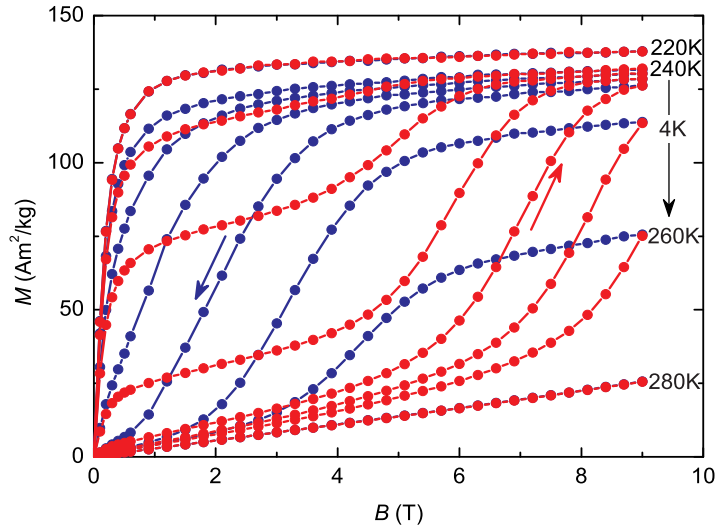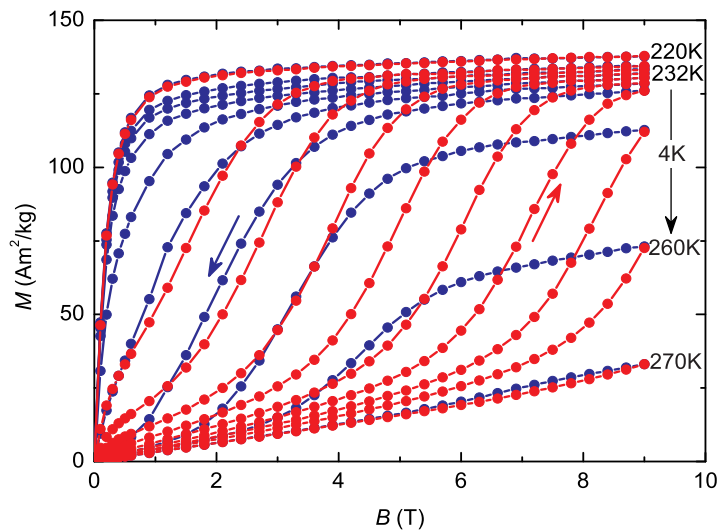

Figure 4.17: Magnetization as a function of magnetic field measured with a maximum field of 5 T for the $Mn_{1.1}Fe_{0.9}P_{0.82}Ge_{0.18}$ compound. The measurements were performed following protocol 2.
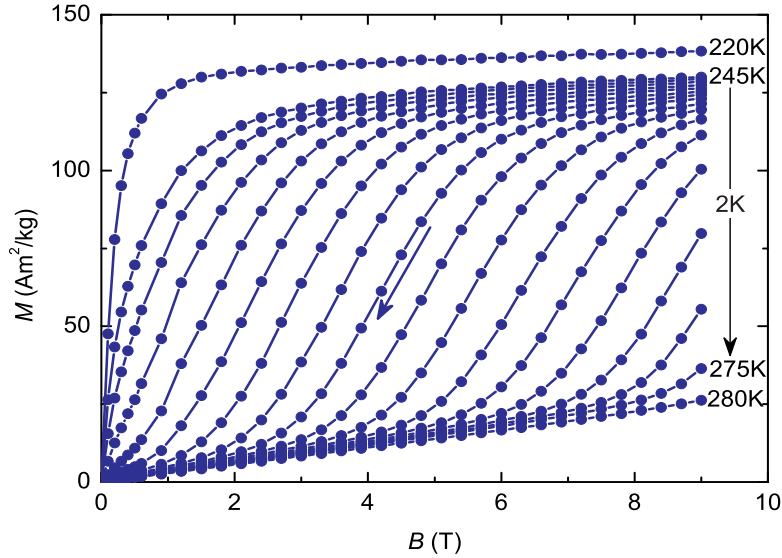
Figure 4.18: Magnetization as a function of magnetic field measured in the vicinity of its Curie temperature with a maximum field of 9 T for the $Mn_{1.1}Fe_{0.9}P_{0.82}Ge_{0.18}$ compound. The measurements were performed following protocol 1.

Figure 4.19: Magnetization as a function of magnetic field measured with a maximum field of 9 T for the $Mn_{1.1}Fe_{0.9}P_{0.82}Ge_{0.18}$ compound. The measurements were performed following protocol 2.

Figure 4.20: Magnetization as a function of magnetic field measured following protocol 3 for the $Mn_{1.1}Fe_{0.9}P_{0.82}Ge_{0.18}$ compound.

on cooling, and 29.8 J/kg·K on heating, and it is 30.7 J/kg·K from the direct measurements on decreasing field. According to the discussion in section 2.7, the value of $|\Delta S_T|$ derived from the heat capacity is about 2 % (or 0.6 J/kg·K) higher than the real one on heating but 2 % lower on cooling due to the irreversibility. Anyhow, this overestimation / underestimation is small, even lower than the experimental errors. A difference of 1.5 J/kg·K between the $\Delta S_{T,\mathrm{max}}$ from the heat capacity on heating and the direct measurement can be attributed to the experimental errors of both.

Figure 4.21(b) shows the temperature dependence of the isothermal entropy change derived from isofield magnetization data displayed in figure 4.14 using equation (4.3). In this case, $|\Delta S_T|$ is overestimated/underestimated by the amount $|dA/dT|$ on heating / cooling. For a field change of 9 T, the maxima of $|\Delta S_T|$ are found to be 36.4 J/kg·K and 32.4 J/kg·K on heating and cooling, respectively. Taking the areas enclosed by the magnetization loops (approximately equal to $2A$) at 248 and 252 K in figure 4.19, the value of $|dA/dT|$ is found to be 2.5 J/kg·K. The resulting maxima of $|\Delta S_T|$ are 33.9 J/kg·K and 34.9 J/kg·K on heating and cooling, respectively. Of course, these values are slightly higher than those obtained from the heat-capacity and direct measurements. The difference should be attributed to the entropy variation from 6 T to 9 T in the FM phase. The values of ΔS_T obtained from the three methods are coincident with each other by taking into account the effect of

irreversibility in each technique.

Additionally, we found that ΔS_T almost saturates for a field change of 5 T, and a further application of field does not improve the maximum value but broadens the width of ΔS_T, that is often observed in materials exhibiting field-induced metamagnetic transitions, such as in the La(Fe,Si)$_{13}$ system [34].

Figures 4.22(a) and 4.22(b) show the plots of $-\Delta S_T$ versus T derived from the magnetization data displayed in figures 4.16 and 4.17, respectively. One can see in figure 4.22(a) that the height of the ΔS_T peak is much higher than that observed in figure 4.21 for the same field variation. The maximum value of $-\Delta S_T$ almost linearly increases with field, being 76 J/kg·K for a field change from 5 T to 0 and 66 J/kg·K for a field change from 0 to 5 T. Both values are consistent with those reported in Ref. [96] for a similar compound. These values are merely due to the "spike" effect, but not a real MCE. According to the discussion we made previously, a maximum field of 5 T is approximately equal to the threshold field B_2, therefore, the plots of $-\Delta S_T$ versus T on increasing and decreasing fields overlap and center at $T_2 = 246$ K.

The isothermal measurements carried out following protocol 2 improve the results on increasing field but not on decreasing field. One can see in figure 4.22(b) that the maximum values of $-\Delta S_T$ on increasing field are comparable to those in figure 4.21, but much lower than those in figure 4.22(a). On decreasing field, the plots of $-\Delta S_T$ versus T with almost the same size and position as those in figure 4.22(a) are observed in figure 4.22(b), but differing from those in figure 4.21. The common center of the ΔS_T peaks on increasing field in figure 4.22(b) is at a temperature close to T_1, lower than that of the curves in figure 4.22(a), close to T_2.

The results of ΔS_T calculated from the magnetization data of figures 4.18 and 4.19 are shown in figures 4.23(a) and 4.23(b), respectively. Overall, it is found that the shape of the plots in figure 4.23 is similar to that in figure 4.22. However, the spurious spikes on increasing and decreasing fields in figure 4.23(a) are separated, and the separation becomes more obvious with an increase of the field, which is different from that shown in figure 4.22(a). According to table 4.1, these two spurious spikes locate at $T_2 = 246$ K and $T_3 = 259$ K for increasing and decreasing fields, respectively. Taking into account the amount 2.5 J/kg·K which is underestimated by the Maxwell relation due to irreversibility, the maximum is found to be $-\Delta S_{T,\text{max}} = 35.6$ J/kg·K for a field change from 0 to 9 T in figure 4.23(b). This value agrees well with 34.9 J/kg·K obtained from the isofield magnetization data on cooling.

Besides, we found that the maximum of the spurious spike on increasing field saturates above 6 T. The maxima of the spurious spikes can be evaluated by using equations (4.9) − (4.11). For instance, in figure 4.13, the maximum
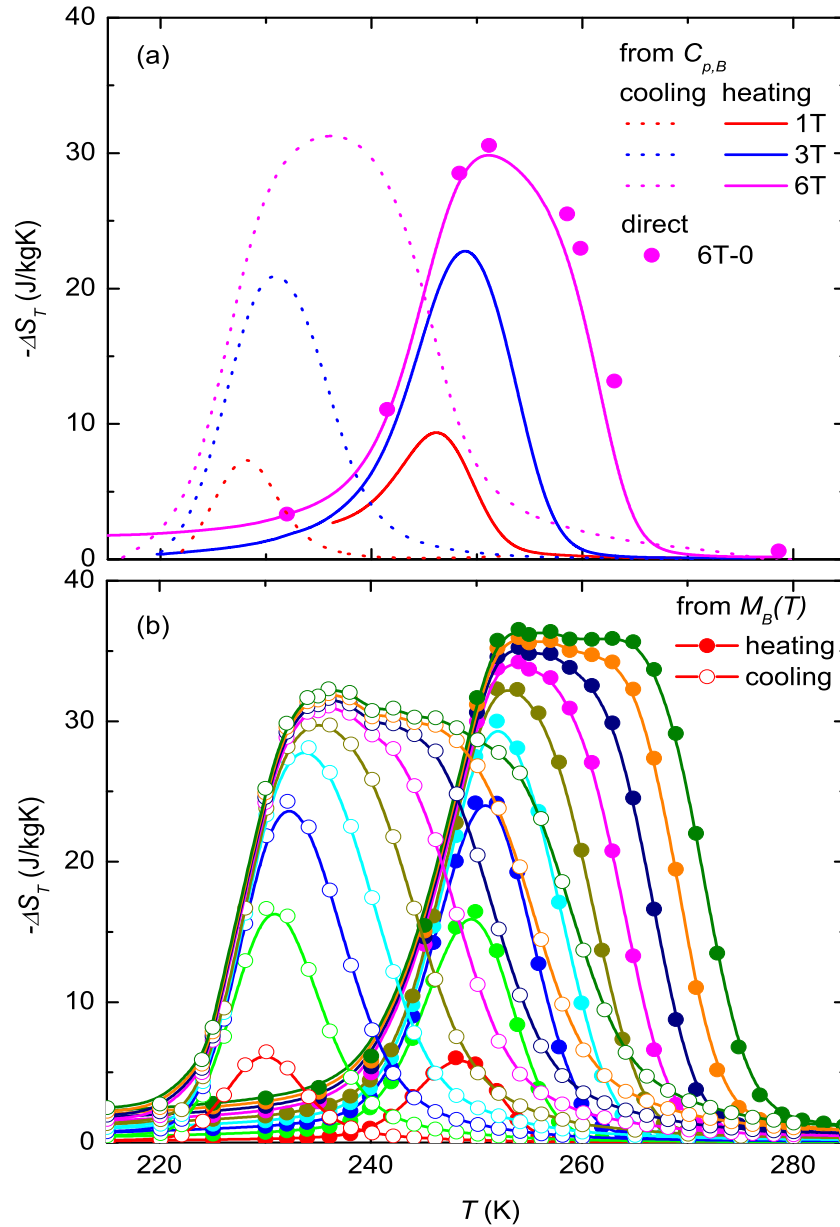
Figure 4.21: Isothermal entropy change as a function of temperature and magnetic field for the $Mn_{1.1}Fe_{0.9}P_{0.82}Ge_{0.18}$ compound. (a) Solid and dotted lines represent ΔS_T derived from heat capacity on heating and cooling for field changes of 1 T, 3 T and 6 T, respectively. Symbols denote ΔS_T obtained from direct measurement performed following protocol 3 for a field change from 6 T to 0. (b) Open and solid symbols stand for the results calculated from isofield magnetization on cooling and heating for field changes of 1 T, 2 T, 3 T, 4 T, 5 T, 6 T, 7 T, 8 T and 9 T, respectively.
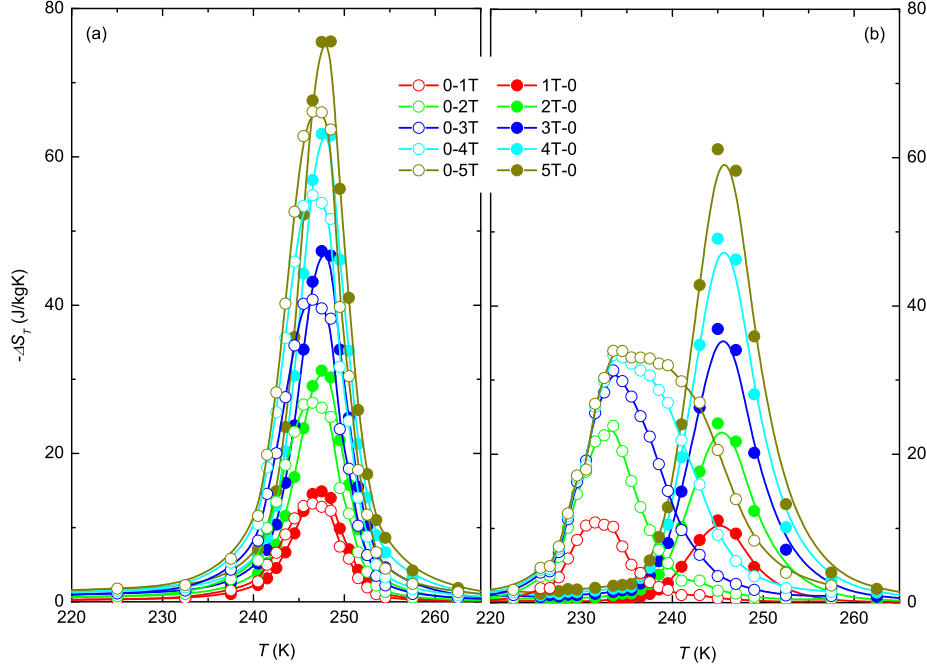
Figure 4.22: Temperature dependence of the isothermal entropy change for magnetic field changes of 1 T, 2 T, 3 T, 4 T and 5 T for the $Mn_{1.1}Fe_{0.9}P_{0.82}Ge_{0.18}$ compound. (a) calculated from isothermal magnetization data measured following protocol 1. (b) calculated from isothermal magnetization data measured following protocol 2.

heat-capacity at 245 K and zero field minus the normal contribution is $13.8R$, the transition enthalpy (the latent heat) at zero field on heating is $\Delta H_{0T} = 7.19$ J/g, the threshold field $B_{th,in} = 5.5$ T, and $M_{FM} - M_{PM} = 100$ Am^{2}kg. The resulting value $-\Delta S_{extra} = 59$ J/kg·K is slightly larger than the value obtained from isothermal magnetization measurements ~ 50 J/kg·K, that is, the maximum value ~ 80 J/kg·K minus the real entropy change ~ 30 J/kg·K, as seen in figure 4.23. The calculated limit can be realized with a smaller temperature step used in the isothermal magnetization measurement. For instance, in the $Mn_{0.99}Cu_{0.01}As$ compound of Ref. [69], a temperature step of 2 K leads to a maximum value $-\Delta S_{T,max} = 78$ J/kg·K for a field change of 5 T, but 178 J/kg·K with a temperature step of 1 K.

For the case of decreasing field in figures 4.23(a) and 4.23(b), the maximum of $-\Delta S_T$ increases almost linearly with an increase of field change. Correct data on decreasing field are obtained below a field of $B_{th,de} = 4.3$ T, resulting in correct values of ΔS_T (see equation (4.12)). The maximum of $-\Delta S_T$ is
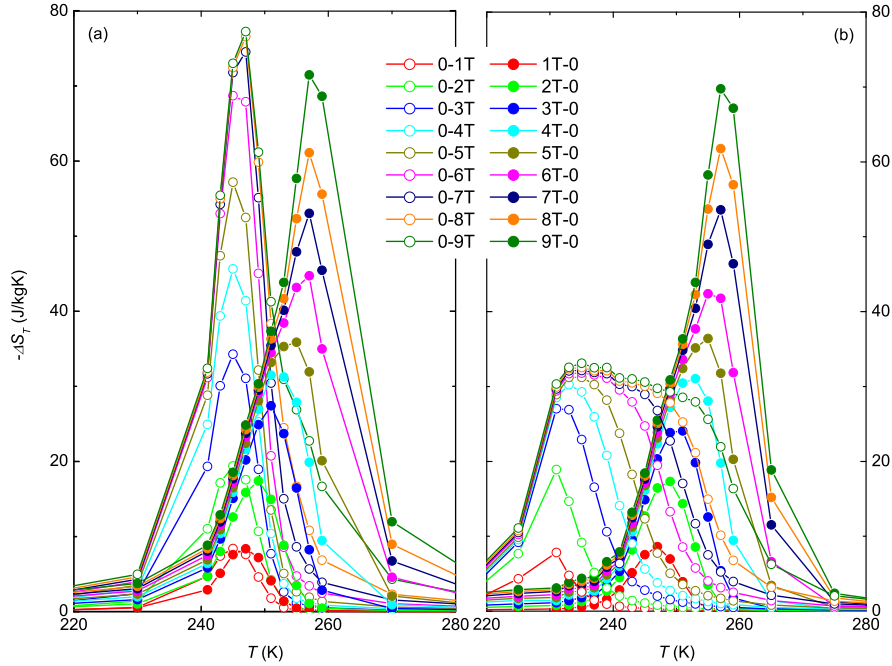
Figure 4.23: Temperature dependence of the isothermal entropy change with several magnetic field changes for the $Mn_{1.1}Fe_{0.9}P_{0.82}Ge_{0.18}$ compound. (a) calculated from isothermal magnetization measured following protocol 1. (b) calculated from isothermal magnetization measured following protocol 2.

about 30 J/kg·K for a field change from 4 T to 0. Above 4 T a linear increase of $-\Delta S_{T,\max}$ with increasing field is attributed to the "spike" effect according to equation (4.11).

Figure 4.24 shows the temperature dependence of the isothermal entropy change obtained from the magnetization measured following protocol 3 for the compound $Mn_{1.1}Fe_{0.9}P_{0.82}Ge_{0.18}$. For a field change from 9 T to 0, the maximum, $-\Delta S_{T,\max} = 35.0$ J/kg·K is obtained when the irreversible contribution (2.5 J/kg·K) is subtracted. It agrees with the value 33.9 J/kg·K determined from isofield magnetization data on heating. In figure 4.24, the values of ΔS_T for all the field changes are in agreement with those calculated from both isofield magnetization and heat capacity, but are completely different from those obtained from isothermal magnetization measured following the other two protocols represented in figures 4.23(a) and 4.23(b).
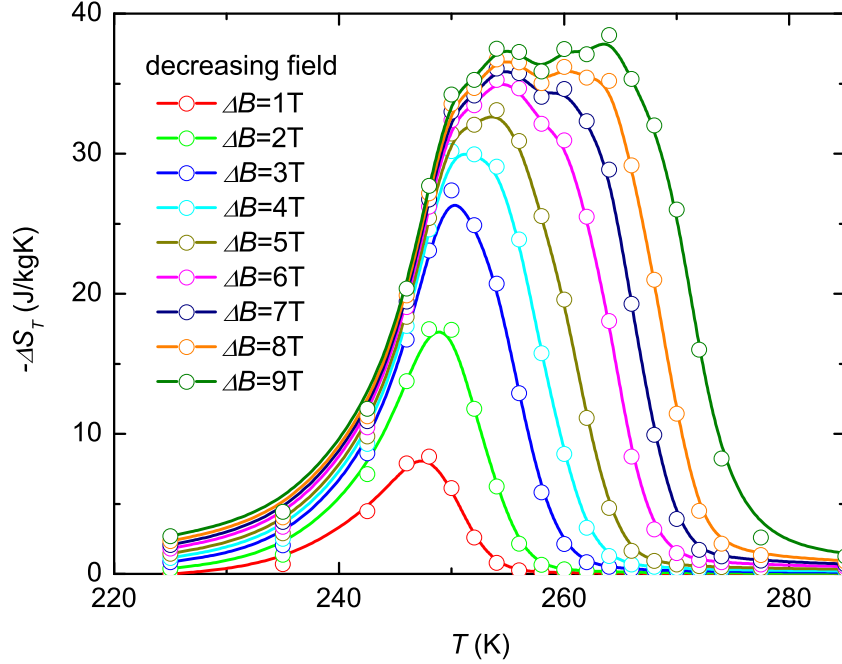
Figure 4.24: Temperature dependence of the isothermal entropy change calculated from isothermal magnetization measured following protocol 3 for the $Mn_{1.1}Fe_{0.9}P_{0.82}Ge_{0.18}$ compound.

4.7 Conclusions

In summary, we reported on the direct and indirect determinations of ΔS_T, as well as a discussion about the "spike" effect exhibited in ΔS_T derived from isothermal magnetization measurements. Four different protocols can be employed in the magnetization and direct measurements, which produce different results in the transition region of a FOPT. As examples, ΔS_T and ΔT_S have been characterized by using different methods following the four protocols in Gd and $Mn_{1.1}Fe_{0.9}P_{0.82}Ge_{0.18}$. The former metal undergoes a pure magnetic SOPT, while the latter compound undergoes a FOPT accompanied by large hysteresis (19 K). Consequently, we conclude:

- The values of ΔS_T of a sample can be determined by means of three different methods, i.e. magnetization, heat-capacity, and direct measurements. In principle, all the methods should give the same results for a given sample when correctly applied. However, this happens in practice only for samples exhibiting second-order transitions, and it does not hold in many published works for samples exhibiting first-order transi-

tions with hysteresis.

- The application of the Maxwell relation to the isothermal magnetization data measured following protocol 1 results in the "spike" effect on increasing and decreasing fields. The "spike" effect on increasing field can be reduced by performing the measurement following protocol 2. On decreasing field it can be reduced by performing the measurement following protocol 3 or can be avoided by applying a maximum field higher than the critical field.

- The application of the Maxwell relation to the isofield magnetization data does not produce the "spike" effect. In addition, the Maxwell relation and the Clausius-Clapeyron equation, both underestimate $|\Delta S_T|$ in magnetizing or cooling processes, while they overestimate $|\Delta S_T|$ in demagnetizing or heating processes due to the irreversibility in first-order transitions. The value of $|\Delta S_T|$ derived from the heat capacity is underestimated in heating processes and overestimated in cooling processes due to the irreversibility. The effect of irreversibility in heat-capacity measurements is smaller than in magnetization measurement, since the former is related to A/T, and the latter is denoted by the derivative dA/dT.

- The direct measurement following protocol 4 gives small $|\Delta S_T|$ values in the hysteretic region, where the phase fraction of the sample is temperature and field dependent. In order to get coinciding values with those from heat capacity, the direct measurements have to be performed following protocol 2 on increasing field and following protocol 3 on decreasing field. Moreover, the entropy production $\Delta S_{prod} \approx -\frac{1}{2T} \oint MdB$ due to irreversibility needs to be taken into account.

- The values of ΔT_S can be determined by means of heat-capacity and direct measurements. Both methods result in coinciding results for second-order transitions, but not for first-order ones. In the case of first-order transitions, the disagreement of ΔT_S caused by the irreversibility is insignificant small. It is mainly due to the thermal and magnetic history dependent phase fractions of the sample. Thus, the values of ΔT_S coinciding with those from heat capacity can be obtained by performing the direct measurement following protocol 2 on increasing field and following protocol 3 on decreasing field.

- As an example for studying the materials exhibiting second-order transitions, we have characterized the heat capacity and MCE of a Gd sample. It is found that the heat capacity of Gd determined in our calorimeter shows a good agreement with the literature results. The magnetocaloric

parameters obtained from the indirect (magnetization and heat capacity) measurements agree well with those from direct measurements. The demagnetization effect on the MCE is small for the studied Gd sample. It is more important below the Curie temperature than above it, and at low field than at high field.

- The compound $Mn_{1.1}Fe_{0.9}P_{0.82}Ge_{0.18}$ has been taken as an example for studying materials exhibiting first-order transitions with large hysteresis. Two independent isothermal magnetization measurements have been performed by applying maximum magnetic fields of 5 T and 9 T, respectively. The isothermal magnetization was measured following three different protocols, namely, protocols 1, 2 and 3. At the transition region, the direct measurements of ΔS_T were performed following protocol 3. The results indicate that ΔS_T determined from isofield magnetization is consistent with that obtained from heat capacity, being considered this last the most accurate result. The ΔS_T results derived from the isothermal magnetization measured following protocol 1 show the "spike" effect on both increasing and decreasing fields. Reasonable values of ΔS_T on increasing and decreasing fields can be determined from the isothermal magnetization measurements by employing protocols 2 and 3, respectively. In the direct measurement of ΔS_T, protocol 3 is also required in order to obtain the ΔS_T values coinciding with the results deduced from heat capacity, since the measurement has been carried out on decreasing field. This study gives a guide for determining the MCE in materials exhibiting first-order phase transition with large hysteresis.

Chapter 5

Series of $Gd_5Si_2Ge_{1.9}X_{0.1}$ with X = Ge, Cu and Ga

5.1 Introduction

Since 1997, when the so-called GMCE was discovered in $Gd_5Si_2Ge_2$ [19], a great deal of attention has been focused on $Gd_5(Si_xGe_{1-x})_4$-type compounds due to their potential as magnetic refrigerants of magnetic cooling near room temperature. The compound $Gd_5Si_2Ge_2$ undergoes a first-order magnetostructural phase transition from the Sm_5Ge_4-type orthorhombic (space group $Pnma$) FM phase to the $Gd_5Si_2Ge_2$-type monoclinic (space group $P2_1/a$) PM one, which leads to the GMCE near its $T_C = 276$ K. The transition temperature is tunable from 30 K to 276 K by adjusting the Si:Ge ratio without losing the GMCE [111]. However, the presence of hysteresis and the use of the expensive rare-earth element Gd in $Gd_5Si_2Ge_2$ restrict its utilization for magnetic refrigeration. More importantly, the presence of hysteresis could lead to an overestimation of $|\Delta S_T|$ (the "spike" effect) when determined from isothermal magnetization, as described in chapter 4. Therefore, it is meaningful to determine the correct ΔS_T of $Gd_5Si_2Ge_2$ via other techniques, such as heat-capacity and direct measurements.

Recently, it has been reported that the large hysteresis in $Gd_5Si_2Ge_2$ can be significantly reduced by a few percent doping with iron [21]. The Fe-doping suppresses the formation of the monoclinic structure in $Gd_5Si_2Ge_2$, resulting in a change of the order of the transition, i.e. from a FOPT to a SOPT. Simultaneously, the Fe-doping lowers the magnitude of the MCE and broadens the width of the MCE peak, leading to an enhancement of effective refrigeration capacity when comparing to that of the undoped compound [21]. Similar results were also reported in Cu, Co, Ga, Mn and Al-doped compounds [22].

In this chapter, we present a detailed study of the structural and calorimetric properties as well as a redetermination of the MCE in $Gd_5Si_2Ge_{1.9}X_{0.1}$ (X = Ge, Cu and Ga) compounds. The phase transformation was investigated by means of X-ray diffraction (XRD) and neutron diffraction (ND) techniques. Heat capacity and magnetocaloric parameters ΔS_T and ΔT_S have been characterized with the calorimeter. The resulting MCEs from the direct and indirect measurements were compared to literature values.

5.2   Experimental

Samples with nominal compositions $Gd_5Si_2Ge_{1.9}X_{0.1}$ with X = Ge, Cu and Ga (provided by V. Provenzano's group) were prepared by the arc-melting technique using a water-cooled copper hearth in an Ar atmosphere under ambient pressure starting with the appropriate amounts of component elements. The melted ingots were homogenized at 1300 °C for 1 h in vacuum [22]. The XRD patterns of all compounds were measured at different temperatures (below and above transition temperature). ND experiment was carried out on the D4 diffractometer [112] at Institut Laue-Langevin, Grenoble (France). This instrument uses a hot neutron source and a Cu-(220) monochromator providing neutrons with wavelength $\lambda = 0.4964$ Å. Heat capacities were measured at constant magnetic fields $B = 0$ and $B \neq 0$ with the heat-pulse and thermogram techniques. The average rate of the thermograms was set around 1 mK/s. The direct measurements of ΔS_T and ΔT_S were carried out on decreasing and increasing magnetic fields, respectively.

5.3   XRD and ND

The XRD patterns for $Gd_5Si_2Ge_{1.9}X_{0.1}$ (X = Ge, Cu and Ga) compounds measured at different temperatures are displayed in figure 5.1. For $Gd_5Si_2Ge_2$, a structural change from an orthorhombic type to a monoclinic type is observed in the XRD patterns measured at 200 K and 300 K which are below and above the transition temperature 276 K. The Rietveld analysis of the patterns indicates that the doped compounds crystallize in the orthorhombic structure as the main phase below 350 K. It means that the structural transition of $Gd_5Si_2Ge_2$ is suppressed already by 5 % atomic substitution of Cu or Ga for Ge. In the Cu-doped compound, the only difference between the patterns at 250 K and 350 K is the appearance of two small peaks at $2\theta = 31.1$ ° and 32.6 ° in the latter pattern (indicated by two arrows in figure 5.1). That could reveal some inhomogeneity in composition, the proportion of Cu being too low to avoid the first-order orthorhombic $\leftrightarrow$ monoclinic transition and / or the
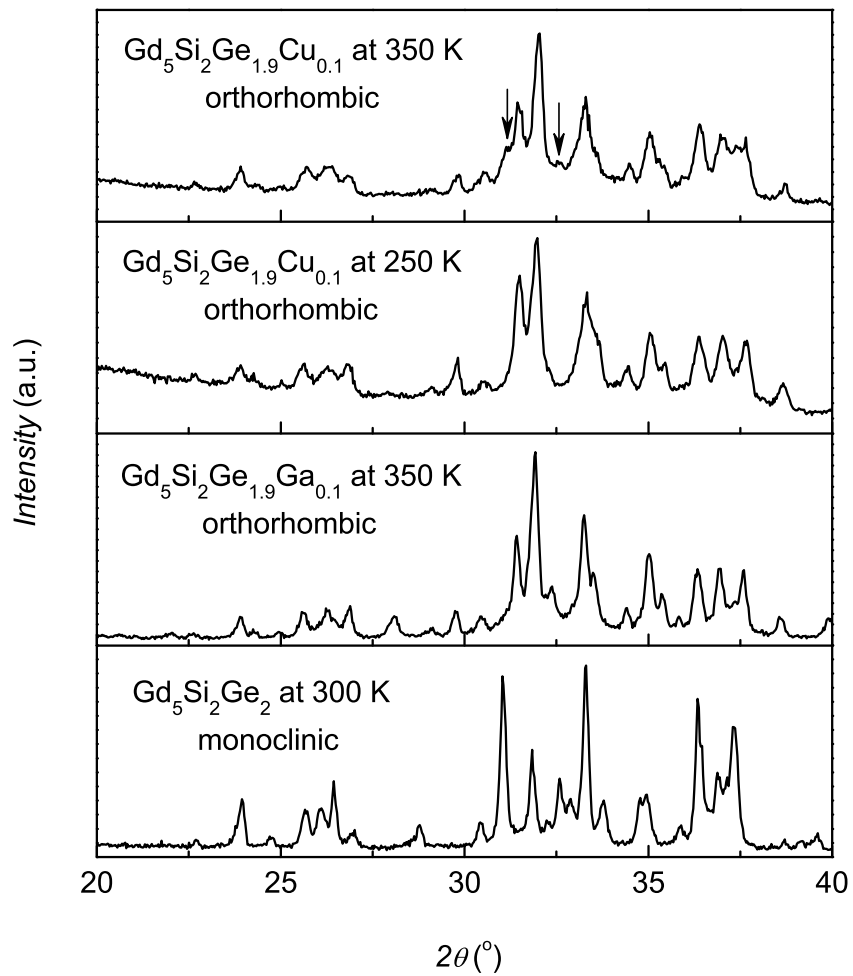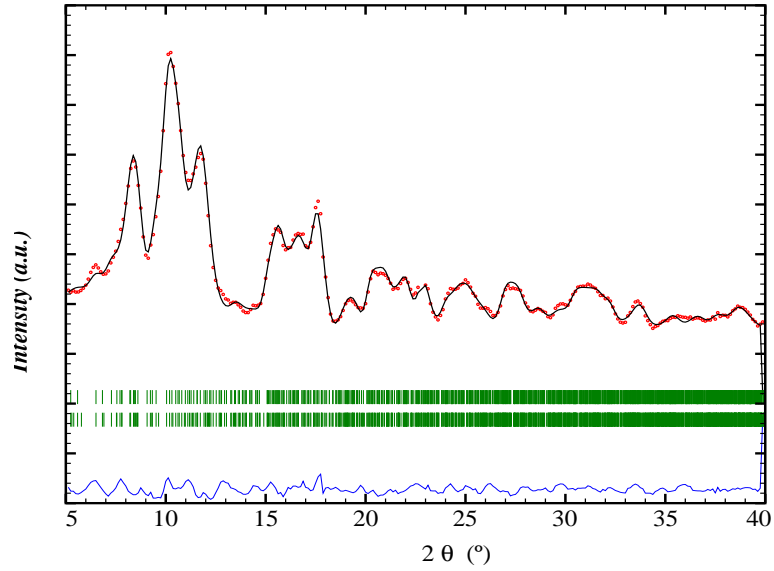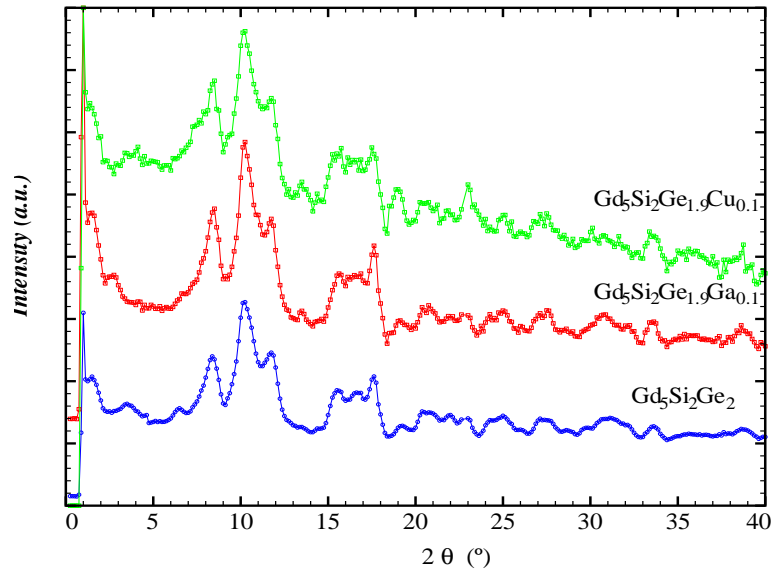
Figure 5.1: X-ray diffraction patterns measured at different temperatures for $Gd_5Si_2Ge_{1.9}X_{0.1}$ (X = Ge, Cu and Ga). Arrows mark the differences between the patterns at 250 K and 350 K for the Cu-doped compound.

(a)

(b)

Figure 5.2: (a) Observed ND pattern of $Gd_5Si_2Ge_2$ at 20 K. Lines: calculated after a Rietveld refinement with parameters given in table 5.1 (black), and difference (blue). Ticks: position of the Bragg peaks for the nuclear and magnetic scattering. (b) Observed ND patterns of $Gd_5Si_2Ge_2$ and the doped compounds at 20 K.

Table 5.1: Parameters of the Rietveld refinement of the ND patterns at 20 K for $Gd_5Si_2Ge_{1.9}X_{0.1}$ (X = Ge, Cu and Ga). Standard deviations in brackets, in units of the last digit. Tn = Si, Ge, Ga or Cu. Magnetic moments are in Bohr magnetons. For X = Cu the coordinates were not refined. N_{par} is the number of refined parameters.

		$Gd_5Si_2Ge_2$	$Gd_5Si_2Ge_{1.9}Ga_{0.1}$	$Gd_5Si_2Ge_{1.9}Cu_{0.1}$
Gd1(4c)	x	0.355(3)	0.380(3)	0.380
	y	1/4	1/4	1/4
	z	-0.018(2)	-0.002(4)	-0.002
Gd2(8d)	x	0.0301(14)	0.024(2)	0.024
	y	0.0920(6)	0.0963(10)	0.0963
	z	0.8129(14)	0.809(2)	0.809
Gd3(8d)	x	0.01781(16)	0.171(2)	0.171
	y	0.1198(8)	0.1217(12)	0.1217
	z	0.3231(13)	0.324(2)	0.324
T1(4c)	x	0.983(5)	0.991(7)	0.991
	y	1/4	1/4	1/4
	z	0.099(5)	0.067(7)	0.067
T2(4c)	x	0.265(5)	0.269(9)	0.269
	y	1/4	1/4	1/4
	z	0.663(4)	0.728(6)	0.728
T3(8d)	x	0.185(2)	0.228(5)	0.228
	y	0.9487(12)	0.928(3)	0.928
	z	0.537(3)	0.544(5)	0.544
μ(Gd1)		5.8(4)	6.4(2)	7.3(4)
μ(Gd2)		6.4(3)	6.4(2)	7.3(4)
μ(Gd3)		6.9(2)	6.4(2)	7.3(4)
a(Å)		7.586(6)	7.572(9)	7.64(2)
b(Å)		14.873(14)	14.822(20)	14.77(5)
c(Å)		7.874(6)	7.839(10)	7.87(2)
V(Å^3)		888.4(13)	880.0(20)	887(4)
R_p/R_{wp}(%)		1.7/2.1	3.2/4.1	2.2/2.9
R_{Bragg}/R_{mag} (%)		2.2/3.2	4.9/5.4	11/8.7
χ^2		1.5	2.1	1.4
N_{par}		34	28	10

Ge proportion being higher than the nominal value in some small parts of the sample. In addition to the main phase, a small amount of impurity phases, $Gd(Si,Ge)$ (1:1) and $Gd_5(Si,Ge)_3$ (5:3), are observed in the patterns.

The high-temperature (in PM phase) ND patterns are consistent with the structure derived from XRD, i.e. the monoclinic-type structure for $Gd_5Si_2Ge_2$ and the orthorhombic-type structure for the doped compounds. The magnetic structure in FM phase corresponds to the representation Γ_4 (table 2 in Ref. [113]) of the crystallographic group $Pnma$, corresponding to the magnetic group $Pn'ma'$. The observed and refined ND patterns of $Gd_5Si_2Ge_2$ at 20 K are shown in figure 5.2(a). The best Rietveld refinement corresponds to a non-canted structure within the standard deviation. If there is some canting, it should be very slight and below the experimental sensitivity. Therefore, most probably the magnetic structure is simply collinear ferromagnetic. The patterns of all the compounds at 20 K are shown in figure 5.2(b). The refined analysis shows that the doped compounds have the same magnetic structure as $Gd_5Si_2Ge_2$ with slightly different parameters, see table 5.1 [114].

5.4 Saturation magnetization

Figure 5.3 shows the magnetization as a function of magnetic field measured at 5 K with a maximum field of 5 T for $Gd_5Si_2Ge_{1.9}X_{0.1}$ (X = Ge, Cu and Ga). It can be seen that the magnetization of $Gd_5Si_2Ge_2$ is nearly saturated by applying a magnetic field of 5 T due to the easily field-aligned domains. A field of 2 T is necessary to overcome the energy barrier caused by impurities which act as the anchor points of the domain walls. In the doped compounds, besides the impurities effect, the conduction electrons of Cu or Ga are polarized by the field produced by the inner $4f$ electrons and also by the external field. As a result, the magnetization never reaches a true maximum on increasing field. As seen in figure 5.3, the magnetization values of the doped compounds are not saturated at 5 T. It means that the Ga or Cu doping has influence not only on the structure but also on the magnetic properties of $Gd_5Si_2Ge_2$. In addition, due to the different quantities of electrons in Cu and Ga, the resulting magnetic moments are not exactly the same. By using the law of approach to saturation, as shown in the inset of figure 5.3, the values of saturation magnetization are found to be 7.7 μ_B, 7.6 μ_B and 7.5 μ_B per Gd atom for the undoped, Ga-doped and Cu-doped compounds, respectively. These values are slightly higher than the theoretical value 7 μ_B for a Gd atom due to the magnetic polarization of the conduction electrons.
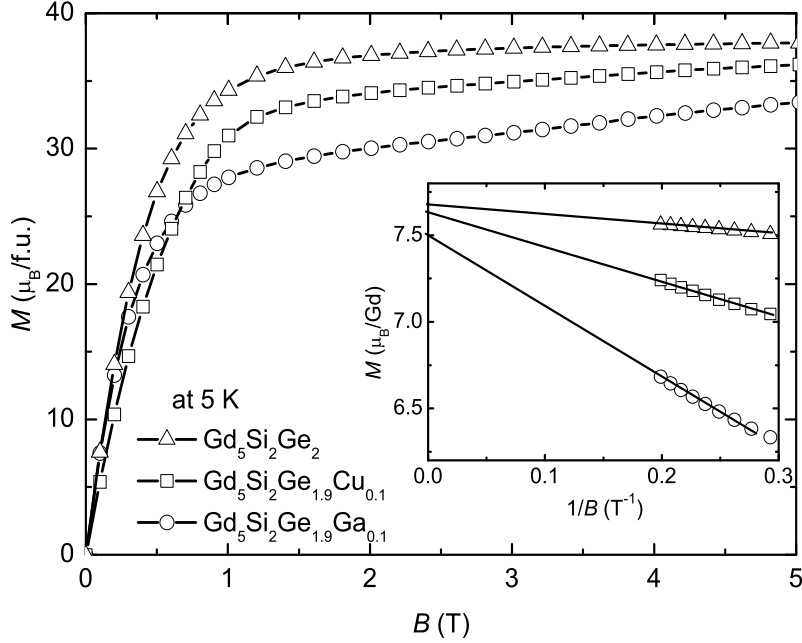
Figure 5.3: Magnetic field dependence of the magnetization measured at 5 K for $Gd_5Si_2Ge_{1.9}X_{0.1}$ (X = Ge, Cu and Ga). Inset shows the magnetic moment of Gd atom in each sample as a function of $1/B$. Lines represent the linear fits of the data.

5.5 Heat capacity

In figure 5.4, we present the temperature dependence of the heat capacity measured at zero field on heating for $Gd_5Si_2Ge_2$ and the Ga-doped compound. For the sake of comparison, the data reported by Pecharsky *et al.* (figure 1 in Ref.[19]) are plotted together. In our experiments, the heat capacity was measured starting from 187 K for $Gd_5Si_2Ge_2$ and from 123 K for the doped compound. Below those temperatures, the literature data will be used in the computation below. The heat capacity of our $Gd_5Si_2Ge_2$ agrees with the literature data below and above the transition. In the transition region, on one hand, although quite similar heat-capacity anomalies are present in both sets of data, the position of the peak in our sample is about 6 K lower than in the literature. It could be ascribed to a slight deviation of Si:Ge ratio due to the existence of impurities in our sample. On the other hand, a weak anomaly at 299 K showed in the literature data, which has been explained as a purely
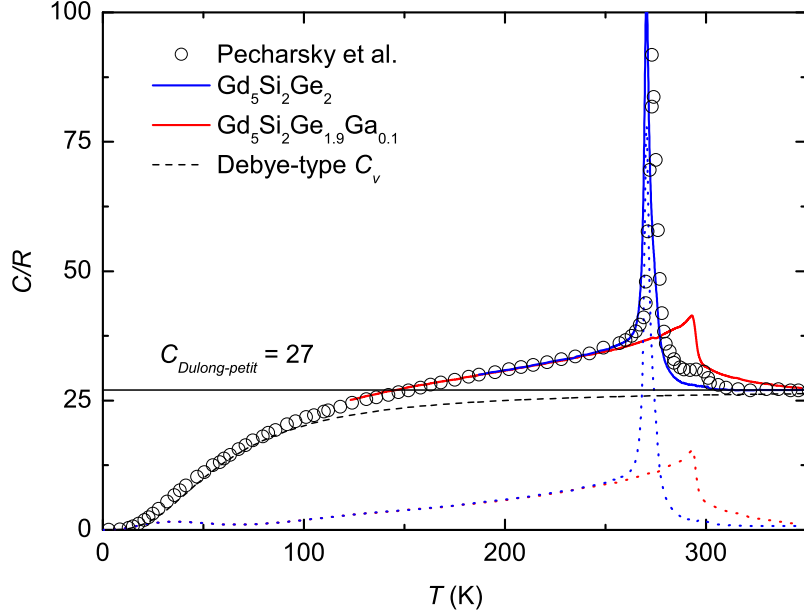
Figure 5.4: Heat capacity as a function of temperature at 0 T for $Gd_5Si_2Ge_2$ and $Gd_5Si_2Ge_{1.9}Ga_{0.1}$. Dotted lines represent the contributions after subtracting C_v from the total heat capacity. Open circles were taken from Ref. [19].

magnetic SOPT of $Gd_5Si_2Ge_2$ by Pecharsky *et al.* [19], is absent in our data. Actually, the weak anomaly should be attributed to some parts of the sample having a Si-rich deviation or even the appearance of the neighboring phase when the Si content is close to 2. Later, Pecharsky *et al.* [115] claimed that the anomaly can be removed by a brief ($\sim$1 h) heat treatment at 1300 °C. The sharp and narrow heat-capacity anomaly at 270.4 K (the temperature of the maximum of heat capacity) for $Gd_5Si_2Ge_2$ and the λ-type anomaly at 294.3 K (the temperature of the maximum drop of the heat capacity) for the Ga-doped compound indicate the nature of the transition changing from a first-order magnetostructural transition to a second-order magnetic transition. That is, the structural transition is suppressed in the Ga-doped compound, which agrees with the XRD and ND results.

It is evident that the doped compounds exhibit a single orthorhombic structure below and above the transition. It is interesting to compare the contributions of magnetic moments and electrons to the transition entropy between the monoclinic and orthorhombic structures. The lattice contribution was evaluated with the Debye model, with a Debye temperature $T_D = 250$ K which has been deduced from the ultrasonic elastic waves speed for $Gd_5Si_2Ge_2$ [116]. It

is seen that the heat capacities in the PM phase are tending to coincide with the Dulong-Petit Law ($27R$) at high temperatures for all the compounds. The anomalous contributions (including the electronic and magnetic parts) were obtained by subtracting the lattice part from the total heat capacity if $C_p - C_v$ is negligible, as denoted by the dotted curves in figure 5.4. The anomalous heat capacity of the Ga-doped compound shows a very similar behavior to that of pure Gd which undergoes a pure magnetic SOPT. In addition to that, the Ga-doping does not introduce any change to the heat capacity of $Gd_5Si_2Ge_2$ well below and above the transition temperature. Therefore, the electronic contribution to the transition entropy in $Gd_5Si_2Ge_2$ should be very small. The values of $C_p - C_v$ at 350 K are $0.74R$ and $0.99R$ for $Gd_5Si_2Ge_2$ and the Ga-doped compound, respectively. The larger value in the Ga-doped compound is probably ascribed to the magnetic contribution of a small amount of remaining FM phase due to the inhomogeneous composition and / or the existence of short-range order.

The magnetism of the studied compounds mainly originates from the $4f$ localized electrons of Gd, the distinction between electronic and magnetic terms has a very clear physical sense. If the electronic portion amounts to $0.74R$ at 350 K, the resulting electronic coefficient would be $\gamma_e = 17.6$ J/mol·K^2. By subtracting the electronic portion from the $C_p - C_v$, the magnetic enthalpy and entropy at 350 K are found to be $H_m = 1417R$ and $S_m = 8.7R$ for $Gd_5Si_2Ge_2$, and $H_m = 1393R$ and $S_m = 8.5R$ for the Ga-doped compound. It implies that the magnetic entropy (or the total entropy) is almost unchanged by the Ga-doping. The observed magnetic entropy is slightly lower than the theoretical limit $NR\ln(2J+1) = 10.4R$ (with $N = 5$, $J = 7/2$). The difference could be attribute to two aspects, the unprecise estimation of the lattice contribution predicted by the Debye approximation at intermediate temperatures, and the magnetic contribution above 350 K if any.

Heat-capacity data at different constant magnetic fields were determined for $Gd_5Si_2Ge_2$ and the Ga-doped compound. Because previous crystallographic and magnetic studies have indicated that the Cu-doped and Ga-doped compounds have quite similar properties, the calorimetric measurements were only carried out in the Ga-doped sample. Figures 5.5(a) and 5.5(b) show the heat capacity as a function of temperature measured at constant fields of 0, 2 T and 5 T for $Gd_5Si_2Ge_2$ and at 0, 1 T, 3 T and 6 T for the Ga-doped compound, respectively. As one can see in figure 5.5(a), sharp heat-capacity peaks appear at 265.5 K and 270.4 K on cooling and on heating, respectively. The resultant thermal hysteresis 4.9 K is large than ~2 K derived from DSC measurements by Pecharsky *et al.* [19]. However, a thermal hysteresis of 5.2 K, which agrees well with ours, has been derived from the isothermal magnetization data given by the same authors. The application of magnetic fields shifts the transition
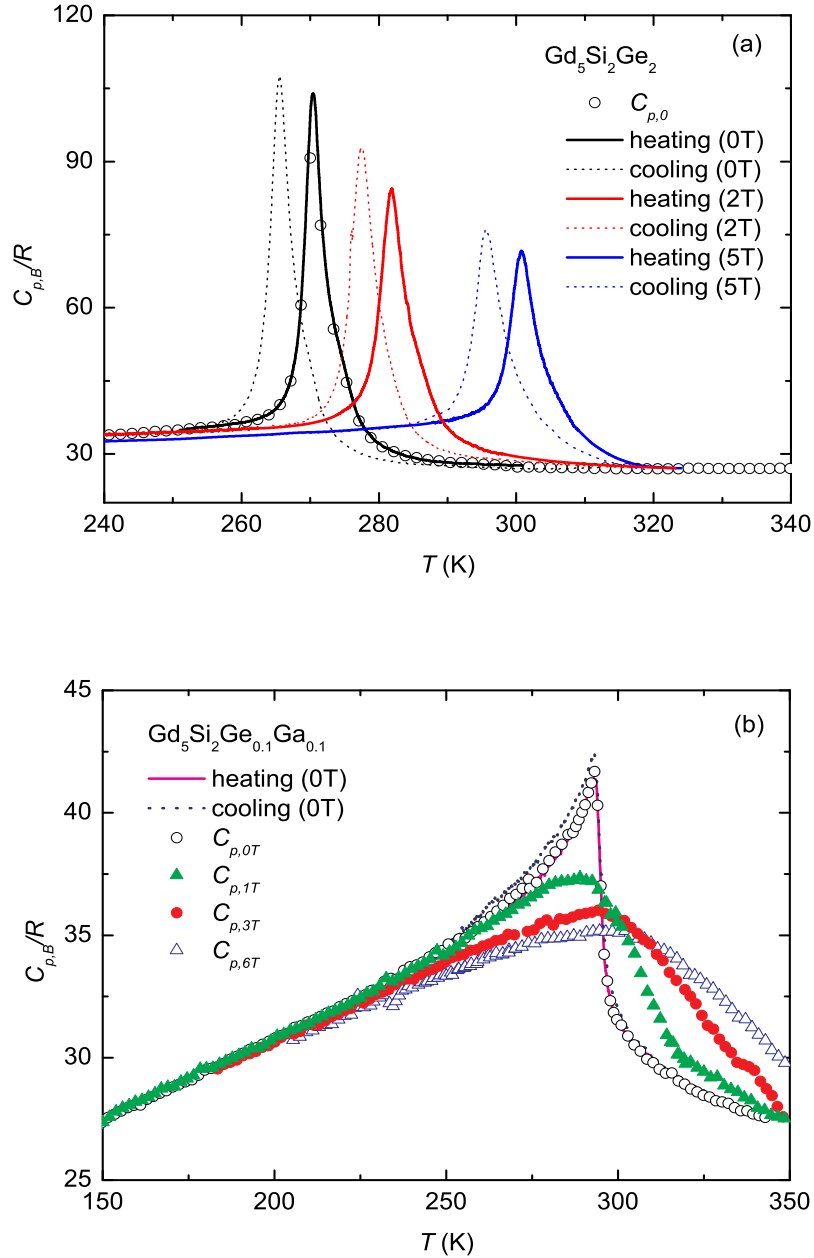
Figure 5.5: Heat capacity as a function of temperature measured at constant magnetic fields for $Gd_5Si_2Ge_2$ (a) and $Gd_5Si_2Ge_{1.9}Ga_{0.1}$ (b). Symbols denote the data obtained with the heat-pulse method. Solid and dotted lines denote the data obtained with the thermogram technique.

temperatures to higher temperatures with nearly the same rate $dT_t/dB = 6.1$ K/T in heating and cooling processes, maintaining the hysteresis almost unchanged for fields between 0 and 5 T. The heat-capacity peaks on heating and cooling are slightly lowered and broadened by the field.

For the Ga-doped compound, the λ-shape heat capacity at zero field is a typical characteristic of a SOPT. The λ-type heat-capacity peak is considerably broadened and shifted to higher temperatures by applying magnetic fields, even for low applied fields. That also corresponds to a normal ferromagnet exhibiting a SOPT at its Curie temperature. To be more convinced, we have measured heat capacity in heating and cooling processes at zero field. The results show a difference of 0.1 K between the cooling and heating curves at the transition temperature, where the heat capacity has a sharp drop. The difference should be attributed to the "apparent hysteresis", caused by the finite cooling and heating rates. Therefore, no thermal hysteresis exists, indicating also that the transition is of second order.

5.6 Magnetocaloric effect

The magnetocaloric parameters of $Gd_5Si_2Ge_2$ and the Ga-doped compound have been determined by using direct and indirect measurements. The temperature dependence of the isothermal entropy change with field changes of 2 T and 5 T for the two compounds are displayed in figures 5.6(a) and 5.6(b), respectively. According to equations (2.71) and (2.72), the underestimation and overestimation of $|\Delta S_T|$ due to irreversibility in the heat-capacity measurements are negligible for $Gd_5Si_2Ge_2$, since the hysteresis ($\sim$5 K) is not so large and is field independent below 5 T. Taking the maximum hysteresis loss obtained from the isothermal magnetization loop (0 – 5 T – 0) at 280 K of Ref. [21], the entropy production in the direct measurements estimated with equation (4.8) is 0.14 J/kg·K. The entropy production is only $\sim$1 % of $-\Delta S_T$ = 13.8 J/kg·K at 280 K, what is lower than the experimental errors. As a result, one can see that a good agreement between the values of ΔS_T determined from heat capacity on heating and direct measurements is observed in figure 5.6(a), except for few points at both sides of the peak. At the low-temperature side (in FM phase), the discrepancy is mainly due to the experimental errors, because, in the case of a FOPT, the sharp jump of entropy at zero field can lead to a large difference of ΔS_T near the transition temperature. At the high-temperature side (in PM phase), the sample is in the hysteretic region when the direct measurements are carried out following protocol 4 at these temperatures. A portion of the sample maintains the PM state due to the temperature and field history. This portion does not contribute to the large MCE when the

measurement is carried out from a field B to 0. That results in lower values of ΔS_T from direct measurements than from heat capacity because of the smaller portion of sample having the transition in the direct process. For instance, the discrepancies of ΔS_T are large at 280.2 K for a field change of 2 T and at 301.2 K for a field change of 5 T.

When comparing ΔS_T taken from Ref. [19] (derived from magnetization on increasing field) with that obtained from heat capacity, the "spike" effect is observed in the former plot. For a field change of 5 T, the maxima $-\Delta S_{T,\text{max}}$ = 18.5 J/kg·K, 15.4 J/kg·K and 13.9 J/kg·K are found in the plots obtained from magnetization, heat capacity on cooling and heat capacity on heating, respectively. The value of ΔS_T determined in a magnetizing process should match that in a cooling process, therefore, the resulting height of the spurious entropy (the "spike" effect) is found to be 3.1 J/kg·K.

Taking the hysteresis loss values for field cycles 0 – 5 T – 0 at 280 K and 290 K from Ref. [21] for $Gd_5Si_2Ge_2$, the $|\Delta S_T|$ values in the transition region are underestimated by the amount $\sim$0.8 J/kg·K by the application of the Maxwell relation. Taking into account this underestimation, all the data are coincident between 280 K and 294 K, where a field of 5 T can complete the transitions on both increasing field and decreasing field. Moreover, Giguère *et al.* calculated the entropy change using the original Clausius-Clapeyron equation, giving $-\Delta S_T$ = 12.5 J/kg·K at 280 K and 10.0 J/kg·K at 310 K with a linear variation between these two temperatures [102]. Their results agree with our data if the irreversibility effect is considered.

For the Ga-doped compound, the results of ΔS_T show an excellent agreement in the whole temperature range between direct and heat-capacity measurements, as the sample undergoes a SOPT. The maximum $-\Delta S_{T,\text{max}}$ = 6.9 J/kg·K upon a field change from 0 to 5 T at 296.8 K we obtained is comparable to the value, $-\Delta S_{T,\text{max}}$ = 6.5 J/kg·K, obtained from isothermal magnetization in a compound with similar composition [117]. The maximum of ΔS_T in the Ga-doped compound is much lower than that in $Gd_5Si_2Ge_2$ for the same field variation. Indeed, it is also lower than $-\Delta S_{T,\text{max}}$ = 10.6 J/kg·K for a field change of 6 T for pure Gd, as seen in figure 5.6(b). When they are normalized per gram-atom of Gd, we obtain $-\Delta S_{T,\text{max}}$ = 1.68 J/K·Gd-gram-atom for the Ga-doped compound, where the experimental phase percentage has been taken into account [118]. This values perfectly agrees with $-\Delta S_{T,\text{max}}$ = 1.67 J/K·Gd-gram-atom for Gd metal.

Figures 5.7(a) and 5.7(b) show the adiabatic temperature change obtained by means of direct and indirect methods for $Gd_5Si_2Ge_2$ and $Gd_5Si_2Ge_{1.9}Ga_{0.1}$, respectively. For $Gd_5Si_2Ge_2$, upon a field change from 0 to 5 T, the maximum $\Delta T_{S,\text{max}}$ = 12.4 K is observed at 278.5 K in the direct measurement. A higher
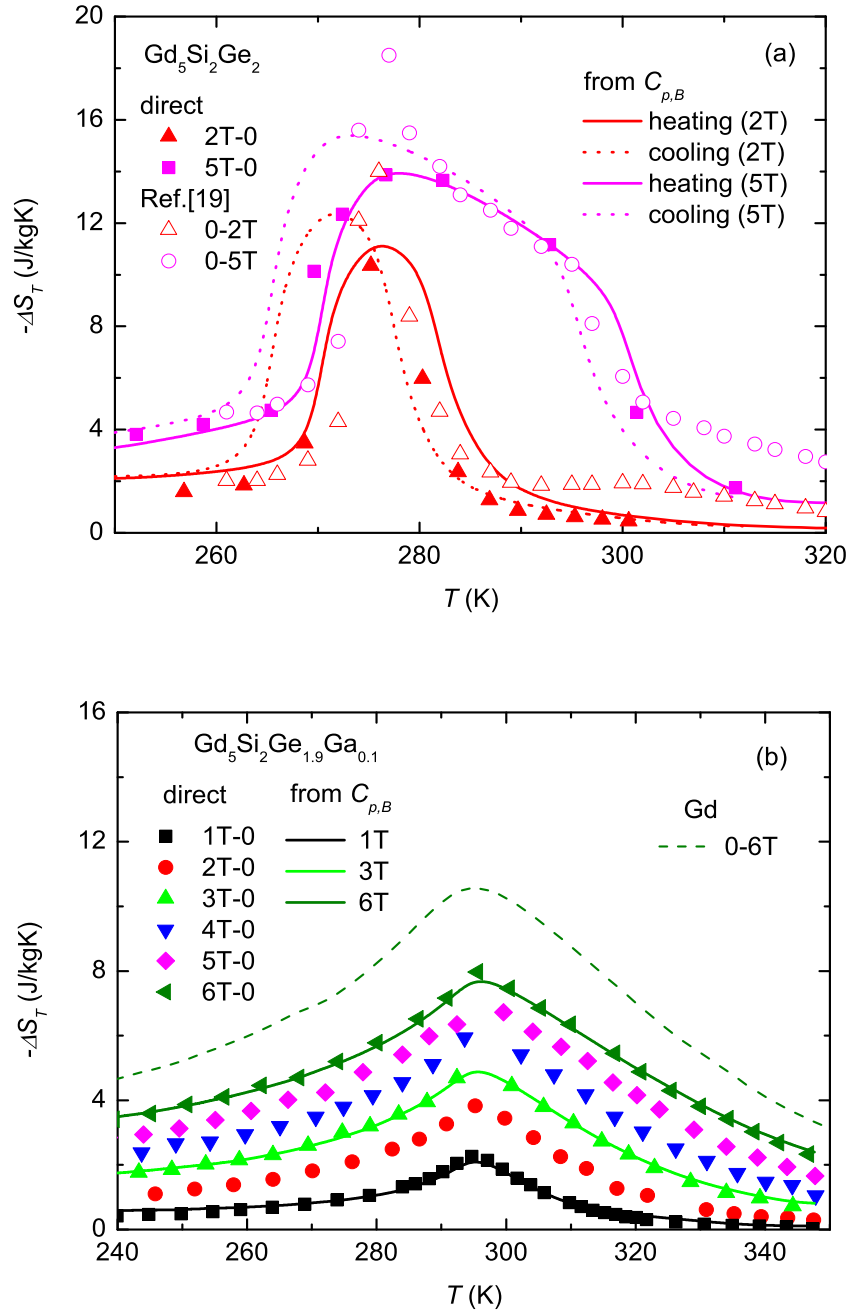
Figure 5.6: Isothermal entropy change as a function of temperature for Gd$_5$Si$_2$Ge$_2$ (a) and Gd$_5$Si$_2$Ge$_{1.9}$Ga$_{0.1}$ (b). Solid and dotted lines denote the data calculated from heat capacity in heating and cooling processes, respectively. Solid symbols denote the data determined from direct measurements. Open symbols were taken from Ref. [19].

maximum 14.5 K at 272.9 K is derived from the heat capacity on cooling, due to the hysteretic effect. The direct measurements were performed on increasing field following protocol 1, therefore, the phase fraction of the sample has the same evolution as in a heat-capacity measurement on heating at zero field. As a result, the direct ΔT_S values agree well with the heating curve at temperatures below $T_{h,0T}$ and with the cooling curve at temperature above $T_{c,5T}$, where $T_{h,0T}$ and $T_{c,5T}$ are the terminal temperatures of the hysteresis region at zero field on heating and at 5 T on cooling, respectively. In the present sample, $T_{h,0T} \approx T_{c,5T} = 283$ K, as seen in figure 5.5(a). By using protocol 2, the evolution of the phase fraction can be modified to be the same as that in a heat-capacity measurement on cooling at zero field. Thus, a good agreement between the direct ΔT_S values and the cooling curve can be obtained in the whole temperature range. For example, the value $\Delta T_S = 10.4$ K at 271.9 K (the arrow-marked point in figure 5.7(a)) would be significantly improved if following protocol 2.

It has been shown that the MCE of Gd$_5$Si$_2$Ge$_2$ is sample dependent [119]. For a field change $\Delta B = 5$ T, the maximum $\Delta T_{S,\mathrm{max}} = 14.5$ K determined from heat-capacity measurement in the present sample is slightly lower than 15.2 K reported by Pecharsky *et al.* [19], where ΔT_S was determined from heat capacity at zero field combined with ΔS_T calculated from magnetization measurements. However, in direct measurements, the maximum $\Delta T_{S,\mathrm{max}} = 12.4$ K we obtained is much higher than 8.5 K reported by Giguère *et al.* [102]. The latter value could be underestimated because Giguère *et al.* [102] measured ΔT_S by moving the sample into a high magnetic field in a matter of a few seconds, rather than under near equilibrium conditions, which may affect the MCE of a material exhibiting a first-order metamagnetic transition due to kinetic effects [119]. Nevertheless, our data agree well with the value 12.2 K, which was also determined from direct measurement, for the sample #1 in Ref. [119]. Anyhow, the present results are reliable, because when taking away the data in the hysteretic region, the ΔT_S data obtained from heat-capacity and direct measurements coincide well with each other. For a field change of 2 T, the maximum values of ΔT_S are found to be 7.4 K and 8.1 K in heating and cooling processes, respectively, that is of interest to magnetic refrigeration with permanent magnets.

The ΔT_S data of the Ga-doped compound determined with both techniques match well to each other in the whole studied temperature range. The value of ΔT_S increases linearly with increasing field. The maximum $\Delta T_{S,\mathrm{max}} = 7.0$ K occurs at 294.1 K for a field change of 5 T. It is only about one half of that of Gd$_5$Si$_2$Ge$_2$, and about 30 % lower than that of pure Gd due to the dilution effect caused by the presence of non-magnetic elements.
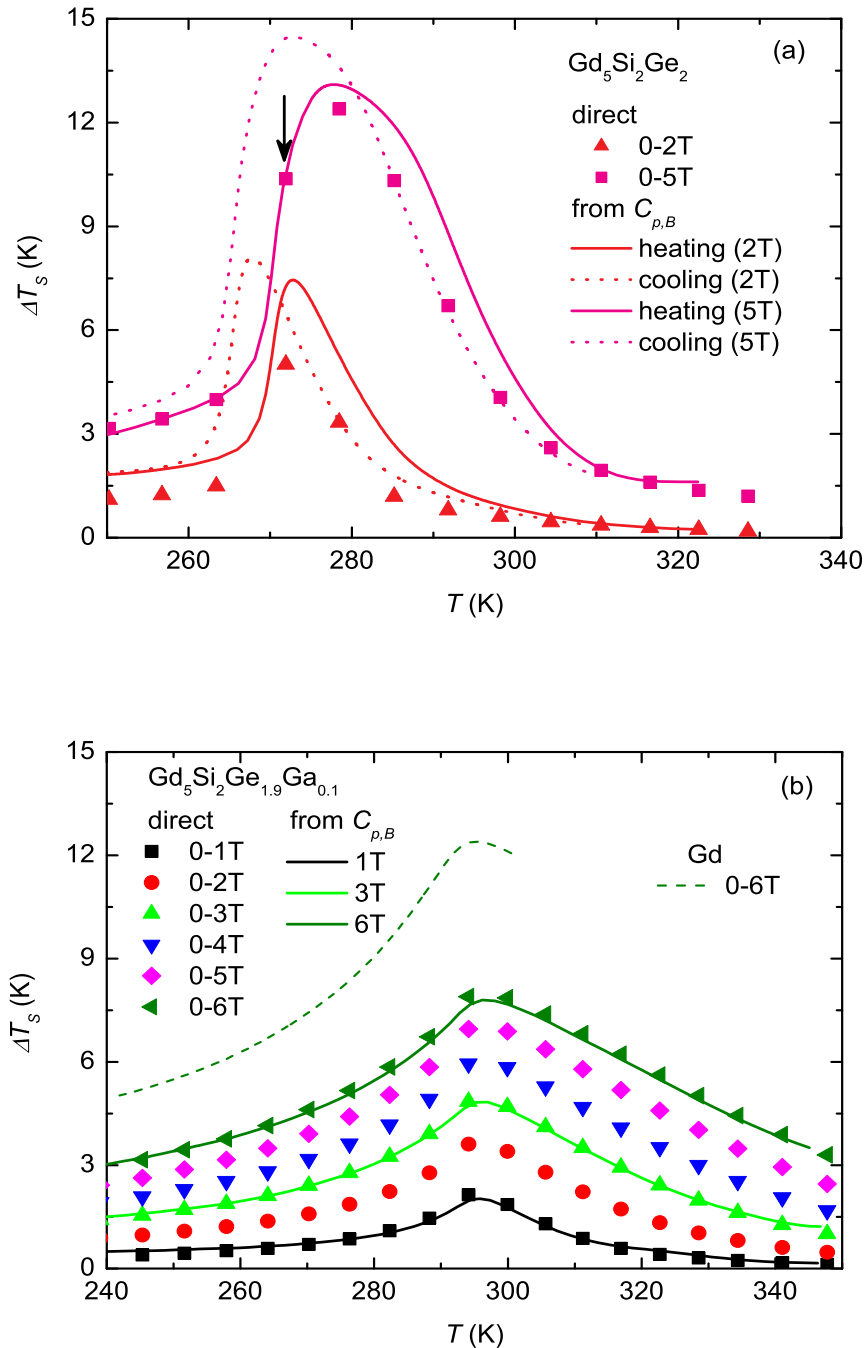
Figure 5.7: Adiabatic temperature change as a function of temperature for $Gd_5Si_2Ge_2$ (a) and $Gd_5Si_2Ge_{1.9}Ga_{0.1}$ (b). Symbols denote the data determined from direct measurements. Solid and dotted lines represent the data calculated from heat capacity.

The width of ΔS_T versus T and ΔT_S versus T curves of $Gd_5Si_2Ge_{1.9}Ga_{0.1}$ is much broader than that of $Gd_5Si_2Ge_2$. The broadening of the MCE peak and the absence of hysteresis in the former compound could lead to an enhancement of the effective refrigeration capacity [21]. Using equation (2.50), $RC^S = \int_{T_1}^{T_2} \Delta S_T dT$, the refrigeration capacities for a field change from 5 T to 0 are found to be 367 J/kg, 356 J/kg and 513 J/kg for $Gd_5Si_2Ge_2$, the Ga-doped compound and pure Gd, respectively. Taking into account the average hysteresis loss 33 J/kg (one half of the value obtained from the magnetization loops of Ref. [21]) on increasing field for $Gd_5Si_2Ge_2$, the resulting effective refrigeration capacity $RC_{eff} = 334$ J/kg is even slightly lower than that of the Ga-doped compound. Nevertheless, the RC_{eff} values of both are much smaller than that of pure Gd. The MCE and RC_{eff} of the Cu-doped compound are expected to be similar to that of the Ga-doped one. Finally, it has to be pointed out that in the computation of RC, T_1 and T_2 were taken as the temperatures corresponding to the full width at half maximum of the ΔS_T peaks. That makes the comparison of RC between materials with FOPT and SOPT be meaningless, because a low, but broad, ΔS_T peak can produce a large value of RC due to the wide integrating range. However, such a broad temperature range is probably not used completely in a real cooling system.

5.7   Conclusions

In summary, we have studied the structural, magnetic and magnetocaloric properties of $Gd_5Si_2Ge_{1.9}X_{0.1}$ with X = Ge, Cu and Ga. The analysis of the X-ray diffraction patterns obtained at different temperatures indicates that the structural transition occurring in $Gd_5Si_2Ge_2$ is suppressed by substituting Ge with about 5 % of Ga or Cu. The analysis of the neutron diffraction patterns reveals that the doped compounds exhibit a simple collinear ferromagnetism, which is the same as in the undoped compound. The observation of a λ-shape anomaly in heat capacity at zero field and its broadening by applying a magnetic field as well as zero hysteresis in $Gd_5Si_2Ge_{1.9}Ga_{0.1}$ indicates that the transition is of second order. The evaluation of magnetic entropy at 350 K indicates that the electronic contribution to the transition entropy in $Gd_5Si_2Ge_2$ is small.

For the famous compound $Gd_5Si_2Ge_2$, lower but more correct magnetocaloric parameters than those reported by Pecharsky *et al.* (being frequently cited) [19] were obtained from both direct and indirect measurements. The maxima $-\Delta S_{T,\max} = 13.9$ J/kg·K on decreasing field (heating) and $-\Delta S_{T,\max} = 15.4$ J/kg·K on increasing field (cooling) are observed for $\Delta B = 5$ T. Although the MCE of the Ga-doped compound is much lower than that of $Gd_5Si_2Ge_2$,

their effective refrigeration capacities are similar. The refrigeration capacity of the doped compound is much smaller than that of Gd metal, which is not favorable to be used in magnetic refrigeration.

Chapter 6

Series of melt-spun LaFe$_{13-x}$Si$_x$(H$_y$) ribbons

6.1 Introduction

In the past few years, LaFe$_{13-x}$Si$_x$ compounds have attracted much attention due to their potentials as magnetic refrigerants, such as large MCE, low cost of raw materials and small thermal hysteresis. The LaFe$_{13-x}$Si$_x$ compounds crystalize in the cubic NaZn$_{13}$-type structure (space group $Fm\bar{3}c$), the La atom occupies the $8a$ ($^1/_4$, $^1/_4$, $^1/_4$) site, and the Fe atoms occupy two different sites: Fe$^{\text{I}}$ occupies the $8b$ (0, 0, 0) site and Fe$^{\text{II}}$ occupies the $96i$ (0, $y \simeq 0.17$, $z \simeq 0.12$) site, in a ratio of 1:12. Neutron diffraction indicated that the Si atom occupies preferentially the $96i$ site rather than the $8b$ site [120]. The Si atoms situate near the La atoms for stabilizing the NaZn$_{13}$-type structure, which avoids the known aversion of Fe to La (the pure binary intermetallic LaFe$_{13}$ compound does not exist). Therefore, the Si atoms have crucial influences on the properties of the LaFe$_{13-x}$Si$_x$ compounds. It has been reported that by varying the concentration of Si in the LaFe$_{13-x}$Si$_x$ compounds, the order of the phase transition, the transition temperature, and even the crystal structure can be changed [34, 121, 122].

On the other hand, it was found that the LaFe$_{13-x}$Si$_x$ ($1.3 \leq x \leq 1.6$) intermetallic compounds exhibit GMCE around their transition temperatures due to the occurrence of a field-induced IEM FOPT accompanied by a negative volume expansion [34, 36, 120]. Further studies revealed that the transition temperature can be turned from 100 K to 350 K by elemental substitutions, such as transition metals for Fe [37, 123, 124] and rare-earth elements for La [125–128], or by incorporating interstitial atoms, such as H [39] and C [40].

It was proposed that the melt-spinning technique can considerably shorten the annealing time in a heat treatment to develop the NaZn$_{13}$-type phase [129–131] which is quite long (10 days – 30 days) for bulk samples [34, 122]. The MCEs of LaFe$_{13-x}$Si$_x$ ribbons were found to be comparable with those in bulk samples [129–131]. However, a small amount of remaining α-Fe is unavoidable in the samples with low Si concentration prepared by both the arc-melting and melt-spinning methods [129, 132]. The existence of free α-Fe results in a discrepancy between the real and nominal compositions, that is, the ratio of Si:Fe in the actual composition is higher than that in the nominal one. The free α-Fe results from trying to make compounds with a higher content of Fe than allowed. Gutfleisch *et al.* [129] have pointed out that the minimum Si concentration for stabilizing the NaZn$_{13}$-type phase in the LaFe$_{13-x}$Si$_x$ ribbons is $x = 1.2$ which is lower than $x = 1.3$ in the bulk compounds reported in Refs. [34, 121].

In this chapter, we report on the properties of the melt-spun LaFe$_{13-x}$Si$_x$ samples with low Si concentrations ($x = 1$ and 1.2). The composition of the studied compounds has been determined from the analysis of the XRD patterns. Although the LaFe$_{13-x}$Si$_x$ compounds present small hysteresis, the "spike" effect was still observed when ΔS_T was derived from isothermal magnetization measurement performed following protocol 1 [67, 95, 99]. We correctly characterized the values of ΔS_T of the LaFe$_{13-x}$Si$_x$ compounds with nominal compositions $x = 1$ and 1.2 by means of heat-capacity and direct measurements. The resulting values of ΔS_T were compared with those obtained from magnetization measurements. ΔT_S has also been determined from direct and indirect measurements. In addition to that, similar investigations were also done in a compound with higher Si concentration $x = 1.43$ and also in its hydride.

6.2   Sample preparation

As-cast LaFe$_{13-x}$Si$_x$ alloys with nominal compositions $x =$1, 1.2 and 1.43 (provided by O. Gutfleisch's group) were prepared by the arc-melting method in an Ar gas atmosphere. The ingot was then inserted into a quartz tube with a nozzle. The chamber was evacuated to a vacuum of 10^{-2} Pa and then filled with high-purity Ar. The ingot was induction melted and ejected through the nozzle on a cold wheel using a differential pressure. The surface speed of the Cu wheel was 40 m/s. The as-spun ribbons were subsequently annealed at 1050 °C for 2 h and then quenched to room temperature [129]. The DSC studies of LaFe$_{11.57}$Si$_{1.43}$ in the presence of hydrogen at a pressure of 5 bar and its hydride in a vacuum condition upon heating indicated that the temperature of

the formation of the hydride and the temperature of the maximum release of hydrogen are more or less the same, being about 200 °C [133]. Therefore, the LaFe$_{11.57}$Si$_{1.43}$ ribbons were annealed at 400 °C in the presence of 5 bar hydrogen for 60 min to incorporate hydrogen as interstitial atoms within the crystal structure [134]. The release of hydrogen from the sample was performed in a vacuum condition (less than 10^{-5} mbar, kept by a turbo molecular pump and a rotary pump) and at 400 °C for 15 min.

6.3 LaFe$_{12}$Si$_1$ and LaFe$_{11.8}$Si$_{1.2}$ ribbons

6.3.1 X-ray diffraction

Figures 6.1(a) and 6.1(b) display the powder XRD patterns of the LaFe$_{13-x}$Si$_x$ ribbons with nominal compositions of $x = 1$ and 1.2 collected at room temperature (not controlled). XRD analysis shows that both samples crystallize mainly in the NaZn$_{13}$-type structure with amounts of α-Fe (cubic with space group *Im-3m*) and LaFeSi (tetragonal with space group *P4/nmm*) as impurity phases. The fraction of the impurity phases is reduced with increasing Si content from 20.9 wt.% α-Fe and 1.1 wt.% LaFeSi in the $x = 1$ ribbons to 9.4 wt.% α-Fe and 1.3 wt.% LaFeSi in the $x = 1.2$ ribbons. By subtracting the free α-Fe from the nominal composition, the resulting compositions are found to be $x \approx 1.32$ for LaFe$_{12}$Si$_1$ and $x \approx 1.34$ for LaFe$_{11.8}$Si$_{1.2}$. That agrees well with the lowest Si concentration $x = 1.3$ concluded from single-crystal XRD patterns [121]. Although the real composition of the main phase is different from the nominal one, we shall keep the nominal formula for identifying the samples.

The composition of a specimen can be determined precisely by examining its lattice parameters, especially for the present samples which crystallize in the simple cubic structure. Aberrations and other instrumental effects have been corrected by measuring the XRD pattern of a standard Si sample, whose unit cell constant was known within 10^{-5} Å [135], in the same experimental conditions as for the studied samples. After that, the refined unit cell constants are found to be $a = 11.4715(10)$ Å and 11.4724(10) Å for $x = 1$ and 1.2, respectively. In the compositional diagram of Ref. [121], these values correspond to a composition close to LaFe$_{11.7(1)}$Si$_{1.3(1)}$ whose composition has been determined from the single crystal XRD measured at 293 K [121].

Besides, the observed Curie temperatures (from heat capacity seen below), $T_C = 184.5$ K for the $x = 1$ ribbons and $T_C = 184.6$ K for the $x = 1.2$ ribbons, are essentially coincident with $T_C = 184$ K obtained from magnetization for $x = 1.3$ in bulk samples [34, 39]. Accordingly, we conclude that the real
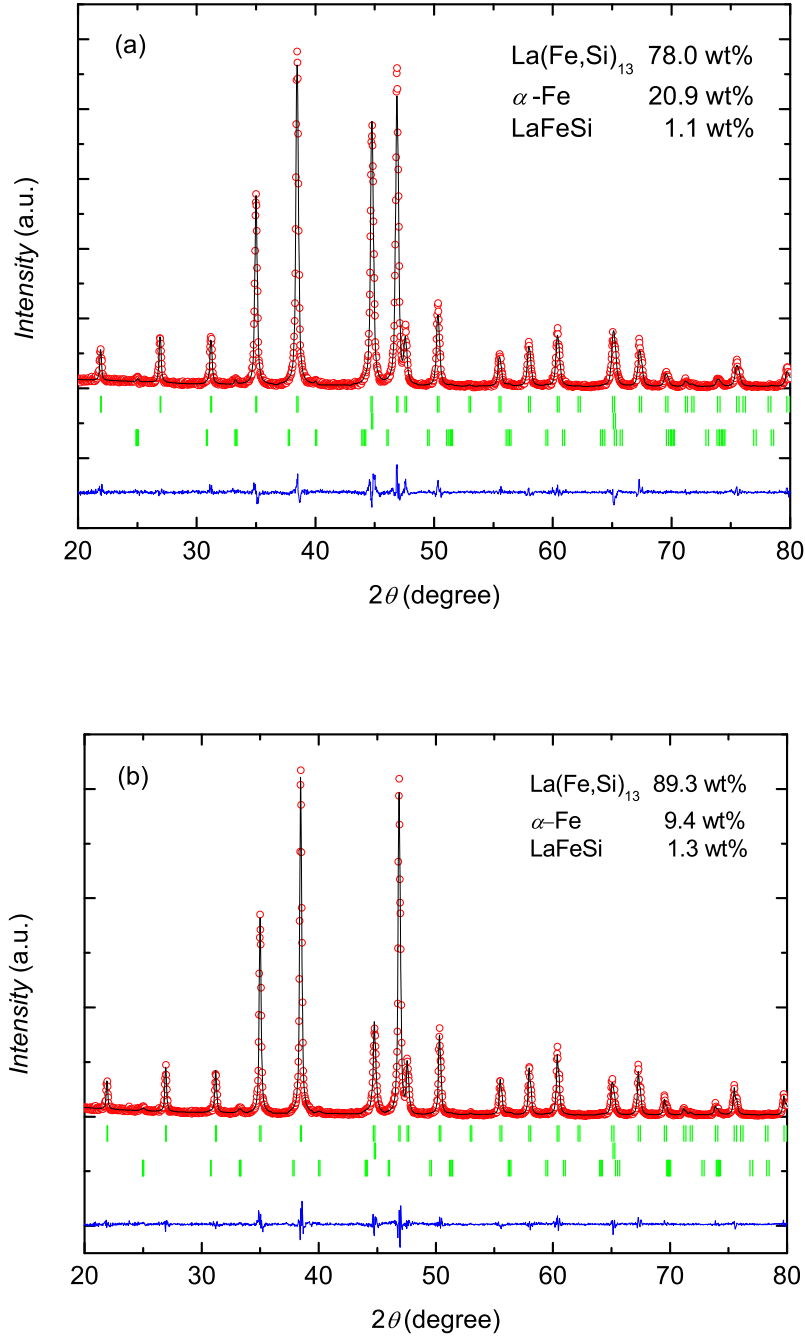
Figure 6.1: Experimental and calculated XRD patterns of the LaFe$_{13-x}$Si$_x$ ribbons, (a) for $x = 1$ and (b) for $x = 1.2$. Circles: experimental patterns. Line: calculated patterns. Ticks: positions of the Bragg reflections for the main phase, α-Fe and LaFeSi. Line below: difference between the experimental and calculated patterns.

compositions of the main phases in both samples are supposed to be the same, being LaFe$_{11.7}$Si$_{1.3}$, though their nominal compositions are different. It is reasonable that the real composition contains more Si atoms than the nominal one because of the presence of α-Fe in the samples. Moreover, it has to be pointed out that, although a certain amount of α-Fe exists, it does not affect the MCE determination in the parent samples because the MCEs in both α-Fe and LaFeSi are insignificantly small below 300 K. Anyway, the contributions of these extra phases will be subtracted as addenda.

In short, the concentration of Si $x = 1.3$ in both samples determined from the unit cell and from the transition temperature agrees with that estimated from the nominal composition by considering the fraction of α-Fe and LaFeSi phases. It is also coincident with the lowest x reported in the literature [34, 121].

6.3.2 Scanning electron microscopy
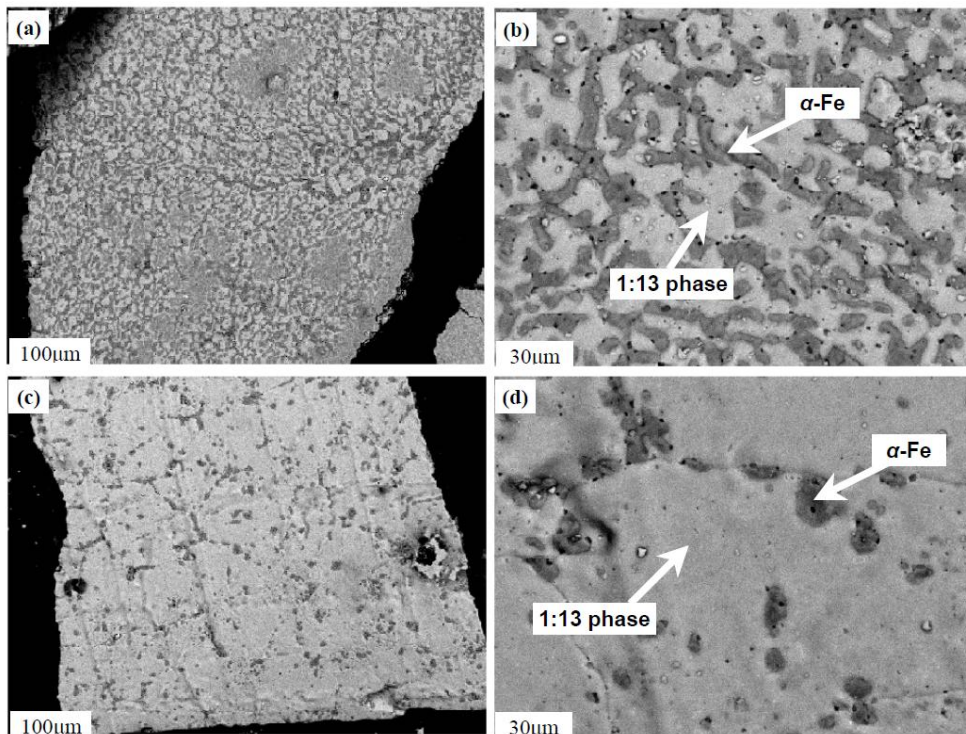
Figure 6.2: SEM images (a) and (b) taken for a piece of the $x = 1$ ribbon, and (c) and (d) taken for a piece of the $x = 1.2$ ribbon.

SEM measurement has been carried out on a randomly chosen piece of

ribbon for each sample. It can be seen in figures 6.2(a) and 6.2(c) that the ribbons exhibit a good global homogeneity. The samples mainly consist of two phases: the grey phase and the dark phase, as shown in figures 6.2(b) and 6.2(d). EDS analysis demonstrates that the grey phase: 7.26 at.% La, 84.12 at.% Fe and 8.26 at.% Si (La$_{1.07}$Fe$_{11.84}$Si$_{1.16}$), and the dark phase: 1.62 at.% La, 95.90 at.% Fe and 2.48 at.% Si (La$_{0.02}$FeSi$_{0.03}$) in figure 6.2(b), and the grey phase: 8.10 at.% La, 85.85 at.% Fe and 6.05 at.% Si (La$_{1.15}$Fe$_{12.14}$Si$_{0.86}$), and the dark phase: 1.09 at.% La, 97.95 at.% Fe and 0.96 at.% Si (La$_{0.01}$FeSi$_{0.01}$) in figure 6.2(d), correspond to the main phase and the α-Fe phase, respectively. White and black dots are the reflections of convex and concave defects in the ribbon plane. About 1 wt.% LaFeSi given by the XRD analysis could be undistinguishable in the SEM micrographs due to its negligible amount compared to the others. The fraction of the dark phase in figures 6.2(c) and 6.2(d) is much lower than that in figures 6.2(a) and 6.2(b), i.e. the α-Fe impurity is significantly reduced in the sample with higher Si content, which is in agreement with that observed in the XRD patterns. The determined compositions of the main phase by the EDS, La$_{1.07}$Fe$_{11.84}$Si$_{1.16}$ for figure 6.2(b) and La$_{1.15}$Fe$_{12.14}$Si$_{0.86}$ for figure 6.2(d), contain less Si atoms than that ($x = 1.3$) derived from the other methods. It is probably attributed to the poor precision of the EDS method when unpolished ribbons are studied.

6.3.3 Heat capacity

Figure 6.3 shows the plots of heat capacity versus temperature for the $x = 1$ and 1.2 ribbons measured on heating and cooling at zero field. We found that heat-capacity anomalies occur at nearly the same position on heating for both samples, but at different temperatures on cooling. The anomaly for the $x = 1$ ribbons locates at a higher temperature than that for the $x = 1.2$ ribbons on cooling. The equal transition temperature on heating reveals that the two compounds have close compositions, which agrees with the conclusion from the XRD analysis. The difference of the transition temperatures on cooling indicates that the sizes of thermal hysteresis in the two samples are different. The existence of defects in a material lowers the energy barriers of the FOPT. A larger content of the impurity phases in the $x = 1$ ribbons, which act as defects, implies a smaller hysteresis.

Taking the temperature where heat capacity reaches its maximum as the transition temperature, the resulting transition temperatures are $T_{t,h} = 184.5$ K and 184.6 K on heating, and $T_{t,c} = 182.8$ K and 181.7 K on cooling, for $x = 1$ and 1.2, respectively. The resulting values of thermal hysteresis are 1.7 K and 2.9 K. The presence of sharp heat-capacity peaks and the existence of hysteresis indicate the occurrence of FOPTs from the low-temperature FM
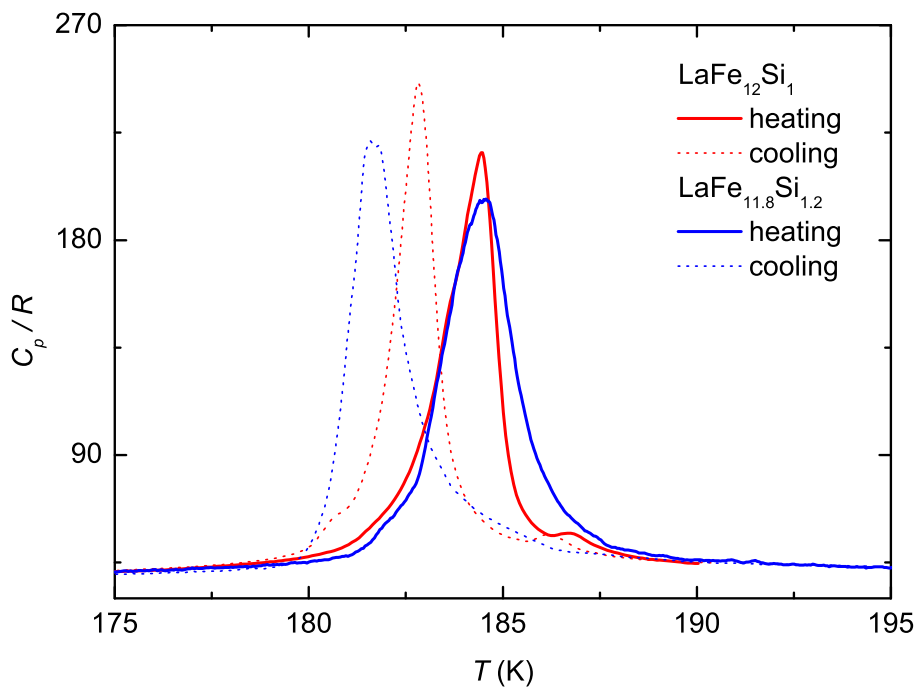
Figure 6.3: Temperature dependence of the heat capacity of the $x = 1$ and 1.2 ribbons measured on heating and cooling at zero field.

phase to the high-temperature PM phase in the samples. Moreover, very small anomalies are observed at 186.7 K on heating and at 186.2 K on cooling in the heat capacity of the $x = 1$ ribbons but not in the $x = 1.2$ ribbons. A further study shows that the anomalies shift to higher temperatures with increasing magnetic field, disappearing for fields above 2 T (see below). These small anomalies are probably attributed to a small amount of the same phase but with a higher Si concentration, since no more impurity phases were observed in the XRD pattern other than α-Fe and LaFeSi, the last one being a Pauli paramagnet [136]. The $T_{t,h}$ of the studied samples is about 10 K lower than 195 K determined from magnetization measurement for the ribbons with the same nominal composition in Ref. [129]. The higher transition temperature corresponds to higher contents of Si and free α-Fe in the ribbons.

An enthalpy run from $T_1 = 177.19$ K to $T_2 = 190.73$ K for the $x = 1$ ribbons at zero field gives an enthalpy increment of 9.67 J/g. It agrees well with the values, 9.46 J/g and 9.45 J/g, obtained from the integral of heating and cooling thermograms over the same temperature range. All these values are slightly higher than 9.38 J/g derived from the heat-pulse data, because

the heat-capacity values in the transition region are underestimated with the heat-pulse method. Similar results were also obtained in the $x = 1.2$ ribbons. That is, the enthalpy increments between 178.08 K and 192.82 K determined from the enthalpy run, cooling thermogram, heating thermogram and heat-pulse methods are 10.67 J/g, 10.26 J/g, 10.51 J/g and 10.39 J/g, respectively. It means that the thermogram is a more adequate technique than the heat-pulse method for studying phase transitions, in particular for FOPTs. A small difference (∼2 %) of the transition enthalpy obtained from the enthalpy run and thermograms can be ascribed to the heat actually gained by the sample but not computed as an enthalpy increment in the thermograms.

Heating and cooling thermograms of the $x = 1$ and 1.2 ribbons have been measured with an average rate of 1.5 mK/s at various constant magnetic fields between 0 and 5 T. The results are displayed in figures 6.4(a) and 6.4(b). Some common and uncommon features are observed between them. The common features: (i) the heat capacity obtained from the heating thermogram at zero field is coincident with that measured with the heat-pulse technique; (ii) the transition temperatures on heating and cooling, both, move to higher temperatures with increasing magnetic field; (iii) the rate of transition temperature field dependence, dT_t/dB, on cooling is larger than that on heating; (iv) the thermal hysteresis decreases gradually with increasing field; (v) a small hysteresis remains at a magnetic field of 5 T; (vi) the magnitude of the heat-capacity anomalies on cooling is slightly higher than that on heating, the difference becomes small with increasing field. The differences: (i) the heat-capacity anomaly becomes broader and lower with increasing field in the $x = 1$ ribbons, but becomes narrower and higher with increasing field in the $x = 1.2$ ribbons; (ii) the transition temperature increases from 182.8 K at 0 T to 205.1 K at 5 T with an average rate of $dT_{t,c}/dB = 4.46$ K/T on cooling and from 184.5 K at 0 T to 205.8 K at 5 T with $dT_{t,h}/dB = 4.26$ K/T on heating in the $x = 1$ ribbons, but from 181.7 K at 0 T to 203.5 K with $dT_{t,c}/dB = 4.36$ K/T on cooling and from 184.6 K at 0 T to 204.1 K at 5 T with $dT_{t,h}/dB = 3.90$ K/T on heating in the $x = 1.2$ ribbons.

The calculated enthalpy change ΔH and entropy change ΔS of the transition at different fields for the $x = 1$ and 1.2 ribbons are listed in table 6.1. The magnitudes of ΔH and ΔS are hardly changed by applying magnetic field below 5 T. The values of ΔH and ΔS are comparable in both samples. The large ΔS indicates the presence of GMCEs in these samples.

By integrating $C_{p,B}/T$, total entropy as a function of temperature at constant field has been obtained for each field. The heat capacity at low temperature (below 80 K) at zero field was estimated by using the Debye approximation, without taking into account the electronic and spin contributions. The
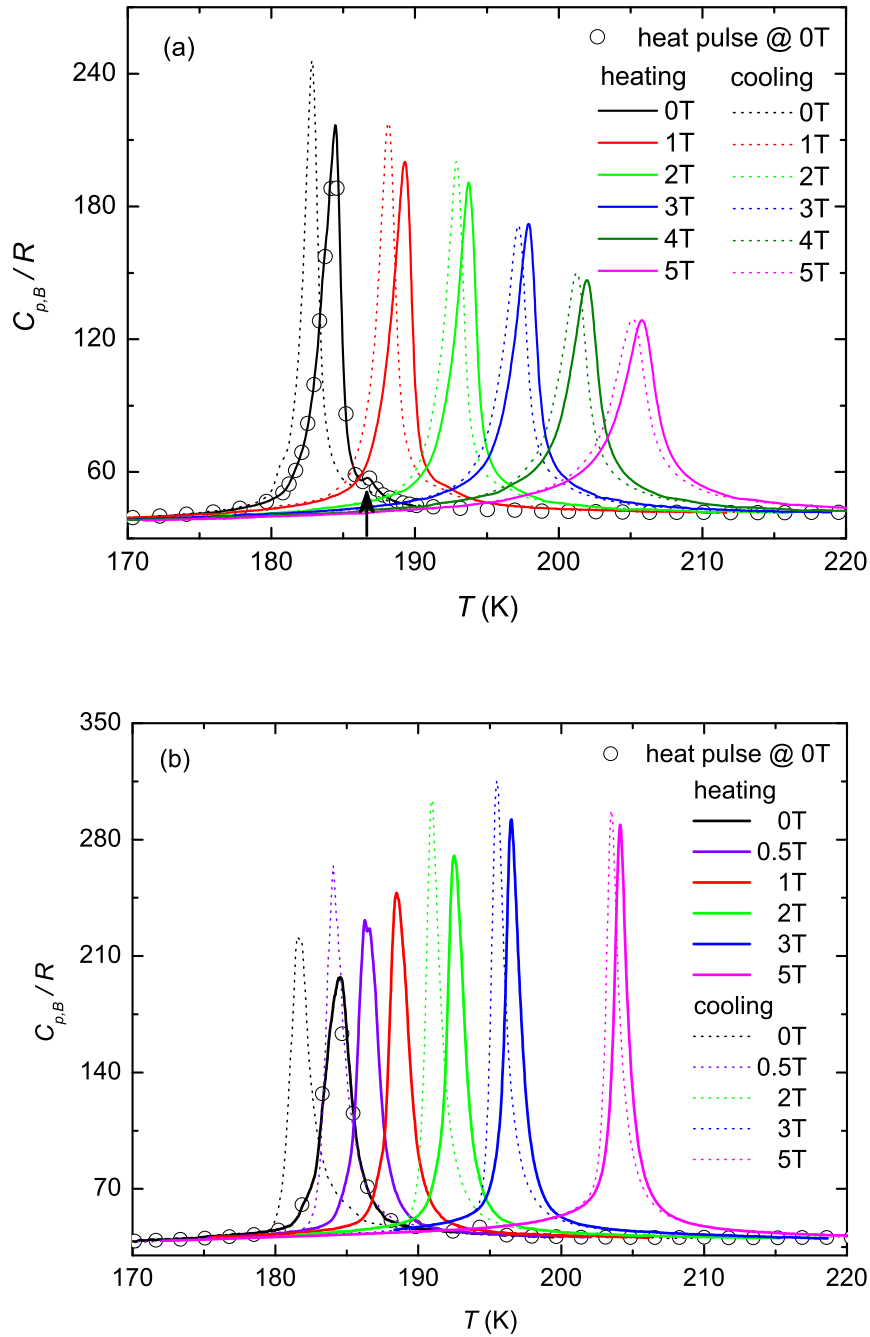
Figure 6.4: Heat capacity as a function of temperature measured on heating and cooling at various constant magnetic fields, (a) for the $x = 1$ ribbons and (b) for the $x = 1.2$ ribbons. The arrow denotes the position of a small anomaly.

Table 6.1: Transition temperature T_t, transition enthalpy ΔH, transition entropy ΔS, maximum isothermal entropy change $\Delta S_{T,\mathrm{max}}$ and maximum adiabatic temperature change $\Delta T_{S,\mathrm{max}}$ for various magnetic fields. The units are normalized with the mass of the main 1:13 phase.

B (T)	T_t (K)	ΔH (J/g)	ΔS (J/kg·K)	$-\Delta S_{T,\mathrm{max}}$ (J/kg·K)
		$x = 1$ on heating		
0	184.4^a	4.30^a	23.3^a	
0	184.5	4.37	23.7	
1	189.3	4.45	23.6	15.3^b
2	193.7	4.37	23.6	19.6^b
3	197.9	4.50	22.8	22.0^b
4	202.0	4.45	22.1	22.8^b
5	205.8	4.58	22.3	23.4^b
		$x = 1.2$ on heating		
0	184.5^a	4.18^a	22.7^a	
0	184.6	4.43	24.0	
0.5	186.4	4.31	23.1	15.2^c
1	188.6	4.36	23.1	19.8^c
2	192.5	4.52	23.5	22.1^b
3	196.5	4.84	24.6	26.0^c
5	204.1	4.77	23.4	27.2^b
		$x = 1$ on cooling		$\Delta T_{S,\mathrm{max}}$ (K)
0	182.8	4.38	24.0	
1	188.2	4.56	24.2	4.2^b
2	192.9	4.39	22.7	6.4^b
3	197.2	4.41	22.3	8.0^b
4	201.3	4.48	22.2	9.0^b
5	205.1	4.56	22.2	9.9^b
		$x = 1.2$ on cooling		$\Delta T_{S,\mathrm{max}}$ (K)
0	181.7	4.20	23.1	
0.5	184.0	4.34	23.6	2.1^c
2	190.9	4.55	23.8	7.0^b
3	195.5	4.81	24.6	9.0^b
4				10.6^b
5	203.5	4.65	22.9	11.6^b

^{a} obtained from heat-pulse $C_{p,0}$ data.
^{b} obtained from direct measurements.
^{c} obtained from $C_{p,B}$ data.
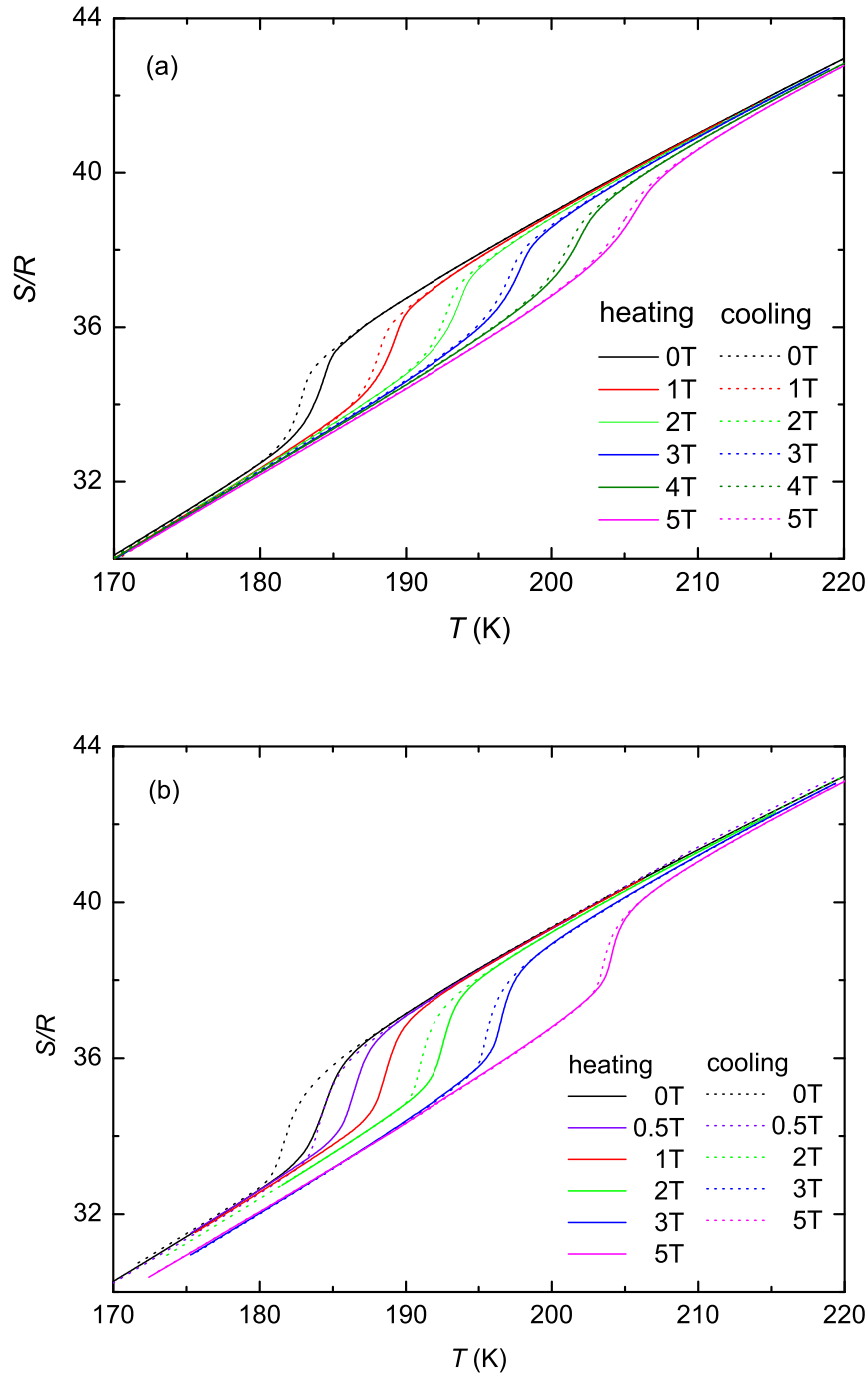
Figure 6.5: Total entropy as a function of temperature calculated from $C_{p,B}$ on heating and cooling, (a) for the $x = 1$ ribbons and (b) for the $x = 1.2$ ribbons.

estimation of $C_{p,0}$ is not so precise, but it has an insignificant effect on the results we shall derive. The total entropy curves at constant magnetic fields calculated from the $C_{p,B}$ data of figures 6.4(a) and 6.4(b) for the $x = 1$ and 1.2 ribbons are displayed in figures 6.5(a) and 6.5(b), respectively. The positions of the entropy curves at different fields were adjusted using the entropy curve at zero field and the values of ΔS_T determined from direct measurements at a temperature well above T_t. For each field, no obvious differences are found between the entropy curves on heating and cooling below and above the transition, since the thermal hysteresis is very small. According to equations (2.71) and (2.72), the errors $\delta^h + \delta^c$ caused by irreversibility are found to be 0.9 % and 1.6 % of ΔS for the $x = 1$ and 1.2 ribbons, respectively. These errors are even smaller than the experimental ones. Entropy jumps are observed at the transition temperatures in both heating and cooling curves, originating from thermal-induced FOPTs. The jumps shift to higher temperatures with increasing field, corresponding to the movement of the heat-capacity anomalies. Besides, the entropy jump is reduced by applying magnetic field, which is more obvious in the $x = 1$ ribbons than in the $x = 1.2$ ribbons.

6.3.4   Magnetization

Figures 6.6(a) and 6.6(b) show the isothermal magnetization curves measured on increasing and decreasing fields for the $x = 1$ and 1.2 ribbons, respectively. The presence of S-shaped curves associated with magnetic hysteresis just above the transition temperature T_t proves the occurrence of field-induced IEM transitions. The IEM transition is accompanied by a large discontinuous magnetization change, implying a large MCE in these compounds. It is obvious that the magnetic hysteresis observed in figure 6.6(b) is larger than that in figure 6.6(a). Taking the inflection points of the magnetizing and demagnetizing curves as the transition fields $B_{t,a}$ and $B_{t,d}$, the magnetic hysteresis is defined as $\Delta B_{hys} = B_{t,a} - B_{t,d}$. It is found that the thermal hysteresis deduced from the magnetic hysteresis is well consistent with that derived from the heat-capacity data.

Above T_t, the linear extrapolation of the experimental magnetization curves to $B = 0$ is non-zero because of the large magnetic moment of α-Fe at these temperatures. The percentages 20.9 wt.% and 9.4 wt.% α-Fe amount to M_{Fe} = 45 A·m^2/kg and 21 A·m^2/kg when considering a magnetic moment of 2.2 μ_B/f.u. for pure α-Fe. Those quantities agree well with the experimental values M_{Fe} = 48 A·m^2/kg in figure 6.6(a) and 20 A·m^2/kg in figure 6.6(b) at temperatures in PM phase obtained via a linear extrapolation to $B = 0$. Taking the magnetization jumps at $T = 189$ K, $\Delta M = 99$ A·m^2/kg and 101 A·m^2/kg (after taking into account the secondary phases) for the $x = 1$ and 1.2
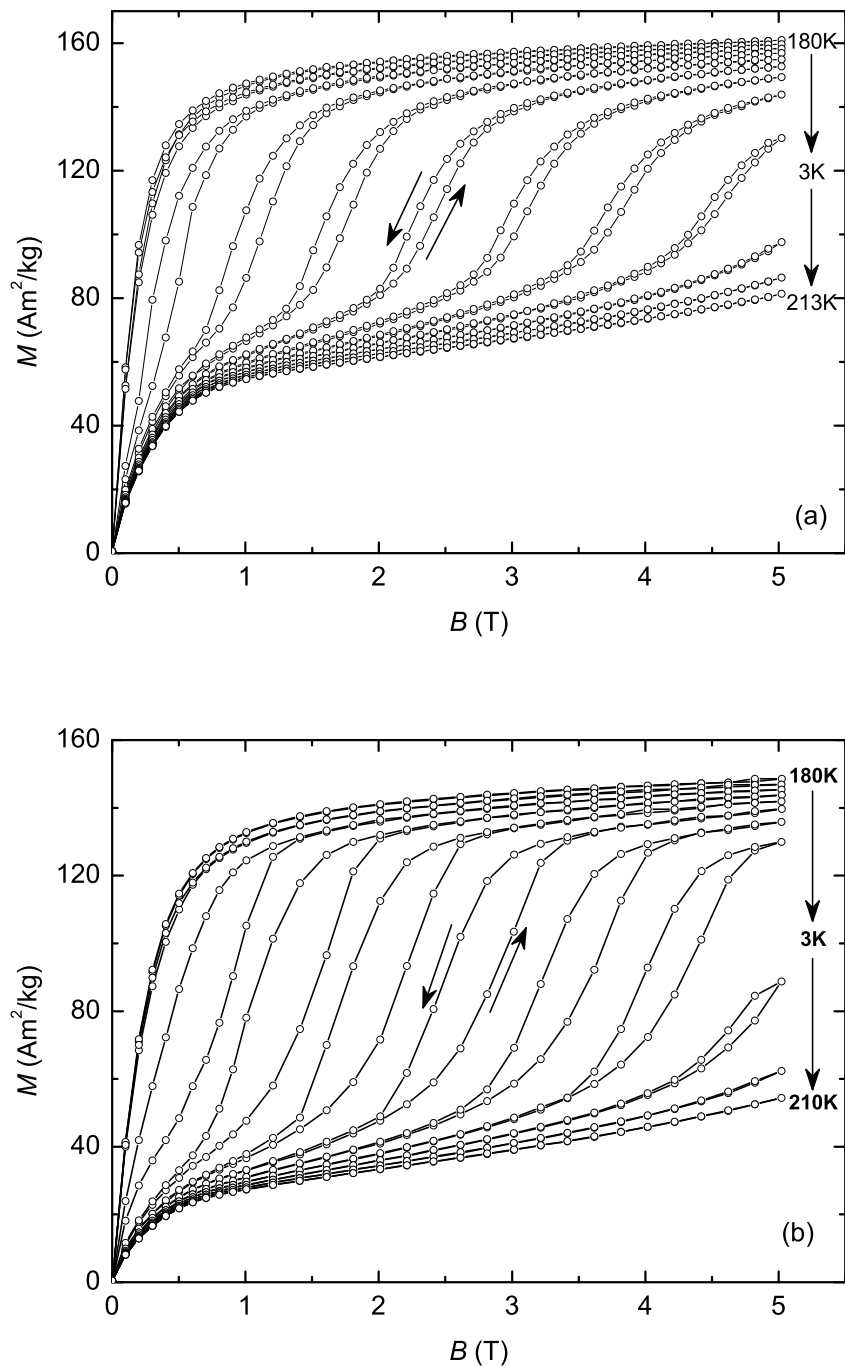
Figure 6.6: Magnetic field dependence of the isothermal magnetization measured on increasing and subsequent decreasing fields, (a) for the $x = 1$ ribbons and (b) for the $x = 1.2$ ribbons.

ribbons, the entropy changes of the field-induced transition calculated using the Clausius-Clapeyron equation are 22 J/kg·K and 23 J/kg·K, respectively. These values agree with those obtained from the heat-capacity data (see table 6.1).

6.3.5 Magnetocaloric effect

The plots of ΔS_T calculated from magnetization data on the basis of the Maxwell relation are displayed in figures 6.7(a) and 6.7(b) for the $x = 1$ and 1.2 ribbons, respectively. The "spike" effects are observed at 187 K on increasing field and at 202 K on decreasing field for the $x = 1.2$ ribbons, but very small. For the $x = 1$ ribbons, the "spike" effect is so weak that it is hardly realized in the results. For increasing field, using the values $C_{an,0T}(T_t) - C_{nor,0T}(T_t) = 1.75$ J/g·K and 1.55 J/g·K, $M_{FM} - M_{PM} = 99$ A·m^2/kg and 101 A·m^2/kg, ΔH_{0T} = 4.37 J/g and 4.43 J/g, $B_{th,in} = 0.4$ T and 0.7 T for $x = 1$ and 1.2 ribbons, the resulting values of $|\Delta S_{extra}|$ are 16 J/kg·K and 25 J/g·K, respectively.

The "spike" effect on decreasing field is weaker than on increasing field, since the maximum field 5 T is quite close to the critical point. Indeed, the "spike" effect is insignificantly small in our results, because the isothermal magnetization measurements were carried out with a temperature interval of 3 K. Referring to the discussions in section 4.4, the "spike" effect is inversely proportional to the temperature interval. The interval we used is larger than the thermal hysteresis, thus it is possible that the hysteretic region was overlapped when the sample was heated from one measuring temperature to the next one. It is due to the fact that the hysteresis in the studied ribbons is small, a maximum field of 5 T is enough to trigger the transition completely in both magnetizing process and demagnetizing process. So, an initial state defined by T, B, x (x is the phase fraction) can be well reached back when a loop of magnetic field is performed isothermally. The entropy change in the loop is zero, since entropy is a state function. Namely, the values of ΔS_T on magnetizing and demagnetizing processes should be equal. However, as one can see in figures 6.7(a) and 6.7(b) that the value of $|\Delta S_T|$ on increasing field is larger than on decreasing field in the transition region. The underestimation / overestimation of the Maxwell relation due to irreversibility should be responsible for the differences. As described in chapter 4, the Maxwell relation underestimates (overestimates) $|\Delta S_T|$ in magnetizing (demagnetizing) processes by the amount $|dA/dT|$, where $A \cong -\frac{1}{2} \oint M dB$. We did the estimation of $|dA/dT|$ using the isothermal magnetization loops shown in figures 6.6(a) and 6.6(b), as presented in the insets of figures 6.7(a) and 6.7(b). The resulting values, $2|dA/dT| = 0.6$ J/kg·K and 1.4 J/kg·K, are in good agreement with the observed differences, 0.9 J/kg·K and 1.5 J/kg·K, between the ΔS_T values on
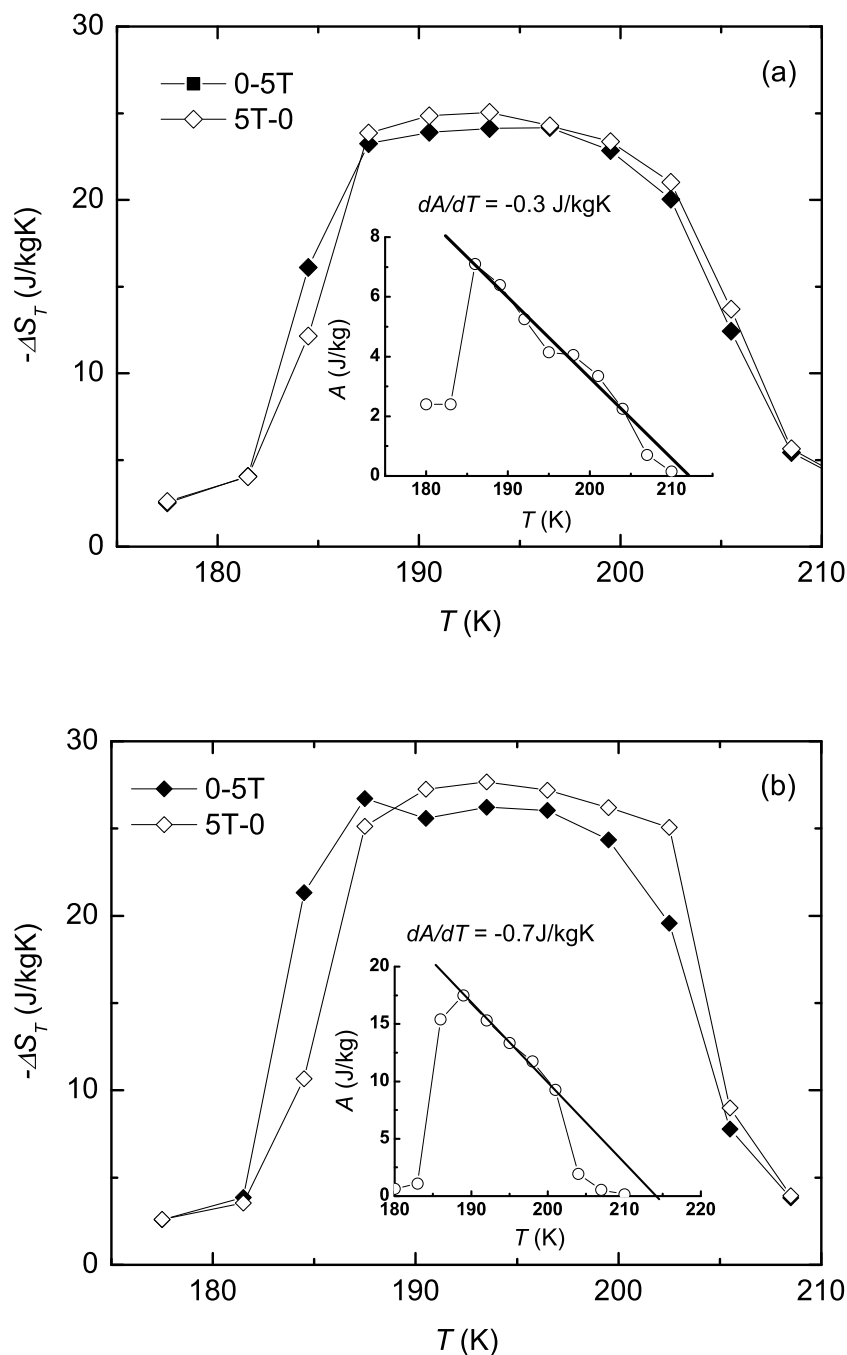
Figure 6.7: Isothermal entropy change as a function of temperature upon magnetic field changes $0 - 5$ T and 5 T $- 0$, (a) for the $x = 1$ ribbons and (b) for the $x = 1.2$ ribbons. Insets show one half of the area inclosed by an isothermal magnetization loop as a function of temperature. Solid lines are linear fits of the data in the transition region.

increasing and decreasing fields for the $x = 1$ and 1.2 ribbons, respectively.

In figures 6.8(a) and 6.8(b), the isothermal entropy change derived from heat-capacity, magnetization and direct measurements for the $x = 1$ and 1.2 ribbons are presented, respectively. It can be seen that comparable values of ΔS_T were obtained via different techniques. The heating curves are found at higher temperatures than the cooling curves due to the existence of a small thermal hysteresis, which is more clear for the $x = 1.2$ ribbons with a larger hysteresis.

It is found that the MCE of the $x = 1.2$ ribbons is slightly larger than that of the $x = 1$ ribbons. The maximum values, $-\Delta S_{T,\mathrm{max}} = 23.4$ J/kg·K for the $x = 1$ ribbons and $-\Delta S_{T,\mathrm{max}} = 27.1$ J/kg·K for the $x = 1.2$ ribbons, were obtained at 194 K from the direct measurements with a field change from 5 T to 0. The differences among the magnitudes of $-\Delta S_{T,\mathrm{max}}$ obtained from the three methods for a field change of 5 T is within 6 %. The values of $-\Delta S_{T,\mathrm{max}}$ for the $x = 1$ and 1.2 ribbons for other field changes are listed in table 6.1. With a field change of 2 T, $-\Delta S_{T,\mathrm{max}} = 22.1$ J/kg·K for the $x = 1.2$ ribbons is lower than 28 J/kg·K reported in a bulk sample LaFe$_{11.7}$Si$_{1.3}$ [34].

Figure 6.9 shows the magnetic phase diagram constructed by taking the transition temperatures from heat-capacity data for the $x = 1.2$ ribbons. Two magnetic field loops have been performed under adiabatic conditions. Cycle 1 was carried out starting at a temperature above the hysteretic region with a rate of 0.5 T/min and a maximum field of 5 T. After cooling the sample from a PM state, cycle 2 was carried out starting from a temperature in the hysteretic region with a rate of 0.3 T/min and a maximum field of 2 T. For the increasing field process of cycle 1, the temperature of the sample increases slightly in the regions below and above the PM-FM transition line due to the normal MCEs in PM and FM phases, and it rises significantly along the PM-FM transition line due to the GMCE resulting from a field-induced IEM transition from PM to FM phase. When the magnetic field decreases, the process is completely reversible up to the state just above the FM-PM transition line, and then a temperature drop occurs due to the GMCE resulting from a field-induced transition from FM to PM phase. The temperature should go back to the initial value if the process was reversible. We found in cycle 1 that the temperature of the sample starts at 190.2 K and ends at 190.3 K when the field varies from 0 to 5 T to 0. A difference of 0.1 K could be ascribed to a combination of the experimental error and the dissipated energy due to magnetic hysteresis.

For cycle 2, an open process is observed. The temperature of the sample starts at 184.0 K but ends at 184.5 K when the field changes from 0 to 2 T to 0. Cycle 2 starts in a fully PM phase, as it was performed following protocol 2. The field converts the whole sample from PM to FM phase when it
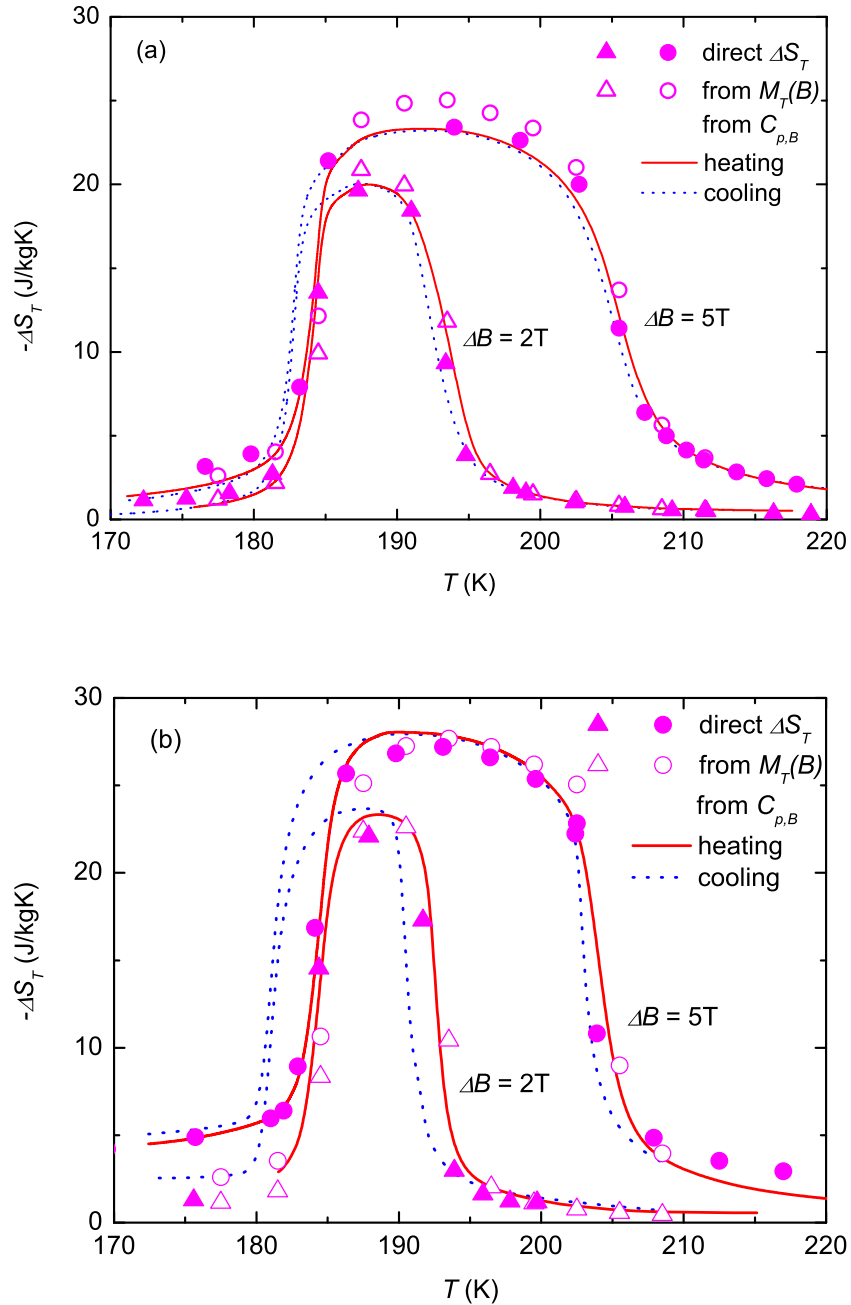
Figure 6.8: Isothermal entropy change as a function of temperature upon magnetic field changes of 2 T and 5 T, (a) for the $x = 1$ ribbons and (b) for the $x = 1.2$ ribbons. Solid lines: calculated from heat capacity on heating. Dotted lines: calculated from heat capacity on cooling. Solid symbols: determined from direct measurements on decreasing field. Open symbols: obtained from isothermal magnetization on decreasing field.
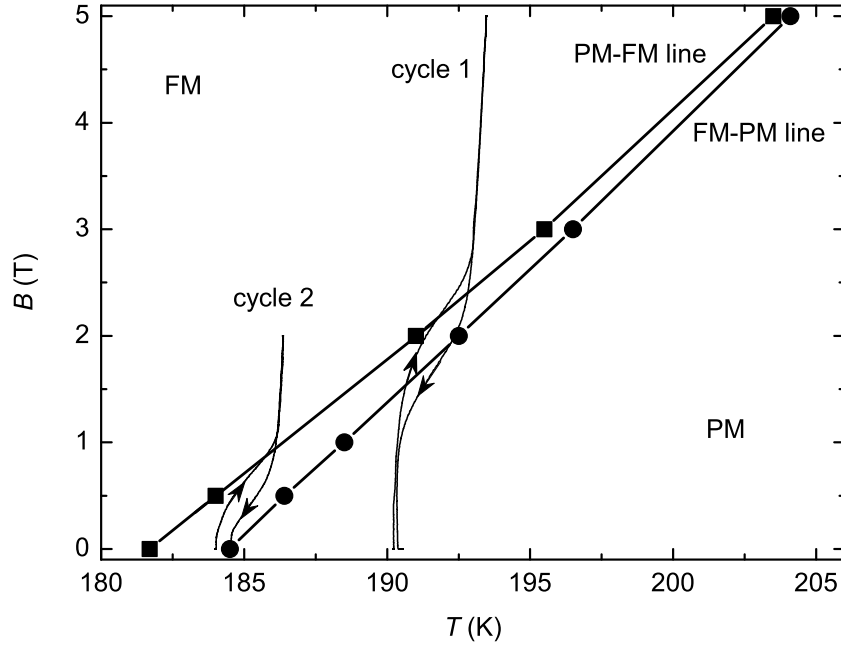
Figure 6.9: Magnetic phase diagram of the $x = 1.2$ ribbons. Square and circle symbols denote the transition temperatures determined from heat capacity on cooling and heating, respectively. Cycles 1 and 2 represent two magnetic field loops performed in adiabatic conditions.

goes through the PM-FM transition line in the magnetizing process. However, then only a part of the sample is brought back to the PM phase when the field is reduced to 0. In other words, the transition is not complete in the demagnetizing process due to the termination of the FM-PM transition line. It leads to a larger temperature variation on increasing field than on decreasing field.

The temperature evolution in the closed cycle 1 does not follow the transition lines because of the finite width of the transition. The points below the transition lines correspond to a higher fraction of PM phase than FM phase and those above the transition lines correspond to a higher fraction of FM phase than PM phase. In addition to that, the use of raw experimental data (the average temperature of the sample plus addenda) also contributes to a discrepancy in ΔT_S, that is, the temperature variation in the raw data is smaller than that exhibited by the sample for a given field change.

Figures 6.10(a) and 6.10(b) show the adiabatic temperature change as a function of temperature with field changes of 2 T and 5 T for the $x = 1$
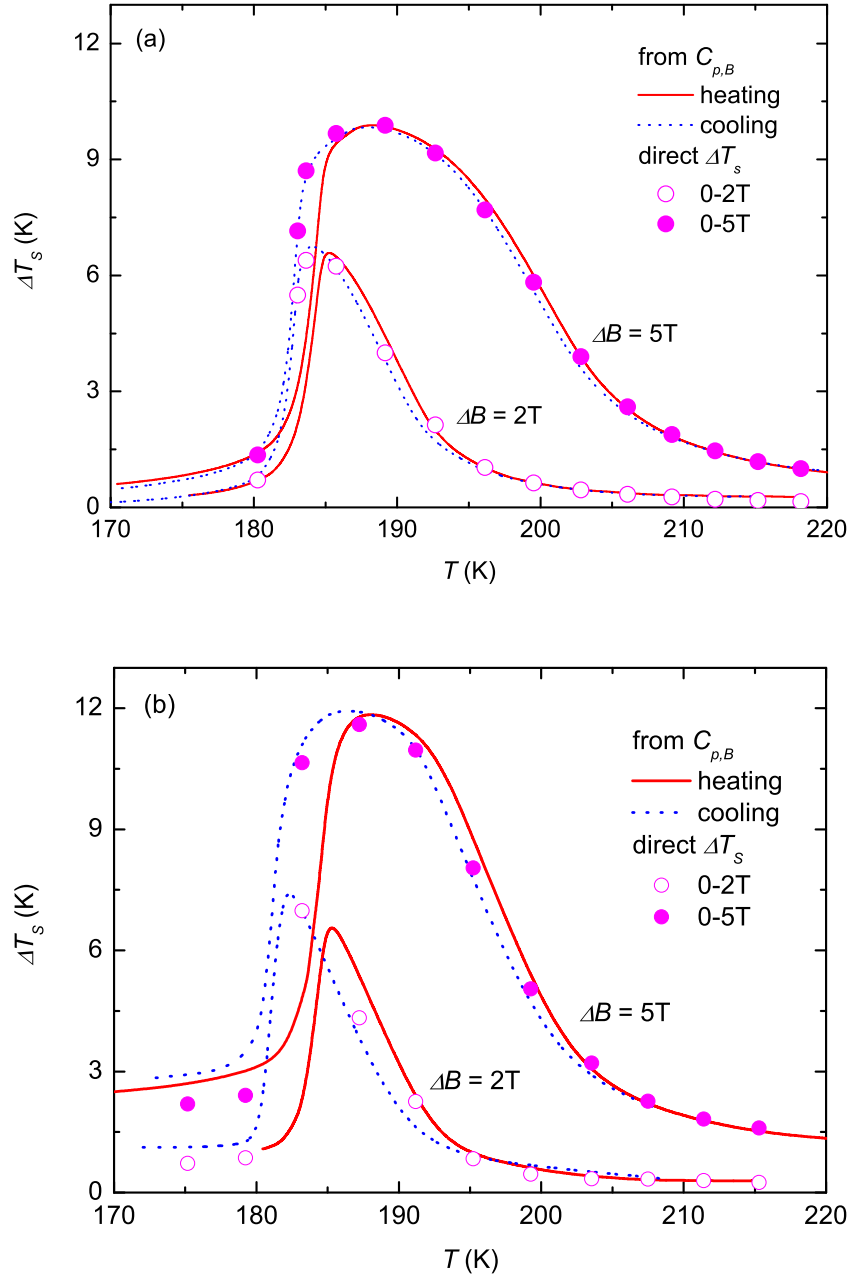
Figure 6.10: Adiabatic temperature change as a function of temperature, (a) for the $x = 1$ ribbons and (b) for the $x = 1.2$ ribbons. Solid lines: calculated from heat capacity on heating. Dotted lines: calculated from heat capacity on cooling. Solid symbols: determined from direct measurements on increasing magnetic field.
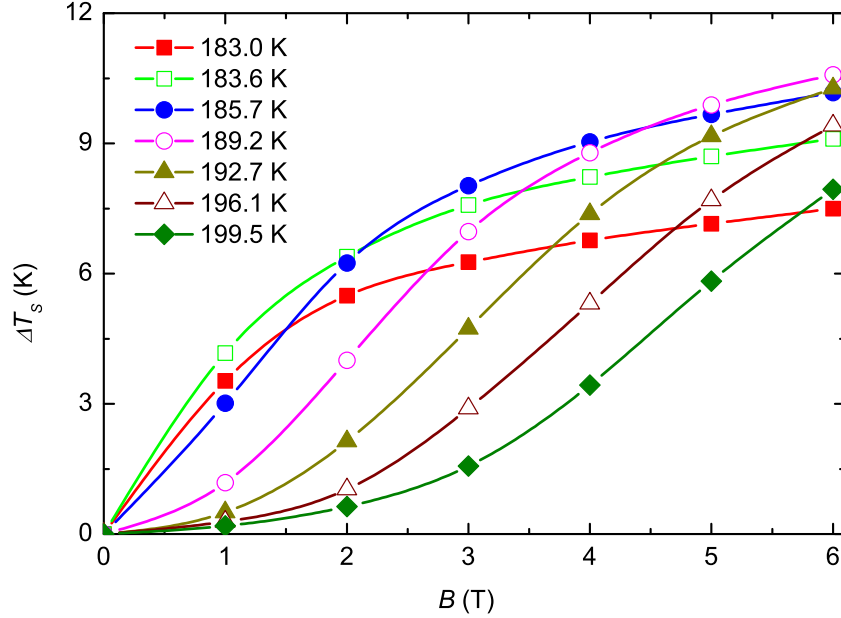
Figure 6.11: Adiabatic temperature change as a function of magnetic field at some given temperatures near the transition temperature for the $x = 1$ ribbons.

and $x = 1.2$ ribbons, respectively. When comparing ΔT_S obtained from heat capacity on heating (solid lines) and cooling (dotted lines), like ΔS_T, it shows a temperature shift between the heating and cooling curves due to hysteresis. The values of ΔT_S (symbols) obtained from direct measurement performed on increasing field show a good coincidence with those calculated from heat capacity on cooling. Large MCEs are observed in both samples. The maximum values of ΔT_S for the $x = 1$ and 1.2 ribbons for various field changes are listed in table 6.1. The values of $\Delta T_{S,\max}$ of the $x = 1.2$ ribbons are slightly higher than those of the $x = 1$ ribbons for the same field variation, which agrees with that observed in the results of ΔS_T. For a field change from 0 to 1 T, $\Delta T_{S,\max}$ = 4.2 K determined from the direct measurement in the $x = 1$ ribbons is much higher than ~ 2.3 K reported by Hu *et al.* in a bulk compound LaFe$_{11.7}$Si$_{1.3}$ [137].

Figure 6.11 shows ΔT_S as a function of magnetic field at different starting temperatures above the transition temperature $T_{t,c} = 182.8$ K for the $x = 1$ ribbons. Just below $T_{t,h} = 184.5$ K, ΔT_S initially changes fast with increasing field, leading to a high value of ΔT_S at a relative low field, e.g. at 183.6 K, $\Delta T_S = 6.4$ K when the field reaches 2 T, which is much favorable to a practical refrigerator working with a permanent magnet. The ΔT_S curve tends

to saturate with a further increase of the field. This phenomena is attributed to the easy occurrence of the IEM transition when applying a magnetic field. Above 184.5 K, S-shaped ΔT_S curves occur due to the increase of the transition field. In each S-shaped ΔT_S curve, the initial and final sections correspond to the normal MCEs in PM and FM phases, respectively, displaying smooth changes of temperature, and the middle part with a higher slope corresponds to the GMCE due to the field-induced IEM transition from PM to FM phase.

One can see in figures 6.8(a), 6.8(b), 6.10(a) and 6.10(b) that the ΔS_T and ΔT_S curves for the $x = 1.2$ ribbons exhibit higher but narrower peaks than those for the $x = 1$ ribbons. Using equations (2.50) and (2.51), for a field change of 5 T, the values of RC^S and RC^T are found to be 460 J/kg and 144 K^2 for the $x = 1$ ribbons, and 519 J/kg and 147 K^2 for the $x = 1.2$ ribbons, respectively. When taking into account the energy loss due to hysteresis, the resulting values of RC^S_{eff} are 453 J/kg and 501 J/kg for the $x = 1$ and 1.2 ribbons, respectively. Consequently, the sample with $x = 1.2$ exhibits a larger MCE and a higher effective RC than the one with $x = 1$ does, through the former sample has a larger hysteresis.

6.4 LaFe$_{11.57}$Si$_{1.43}$ and its hydrided ribbons

The concentration of hydrogen in a hydride LaFe$_{11.57}$Si$_{1.43}$H$_y$ was determined by weighing its mass before (518.63 mg) and after (517.64 mg) the hydrogen desorption. The resulting values $y = 1.72$ is reasonable when comparing the lattice parameter obtained from XRD pattern and the Curie temperature obtained from heat capacity with those of bulk compounds having similar composition in literature (see below). Moreover, the annealing temperature 400 °C used in the hydrogen absorption measurement is much higher than the reaction temperature 200 °C [133]. In the present ribbons, $y = 1.72$ could be close to the limit of the hydrogen content, since the experimental conditions employed are expected to be enough to overcome the energy barrier of hydrogen occupation in the lattice.

6.4.1 X-ray diffraction

Figure 6.12 shows the XRD patterns of LaFe$_{11.57}$Si$_{1.43}$ and its hydrided ribbons measured at room temperature. The XRD patterns confirm that the ribbons crystalize in the NaZn$_{13}$-type structure with the same amount of α-Fe (about 9 wt.%) before and after the hydrogen desorption. The introduction of hydrogen in the LaFe$_{11.57}$Si$_{1.43}$ ribbons changes neither the crystal symmetry of the main phase nor the fraction of the phases, but the lattice parameters. This results
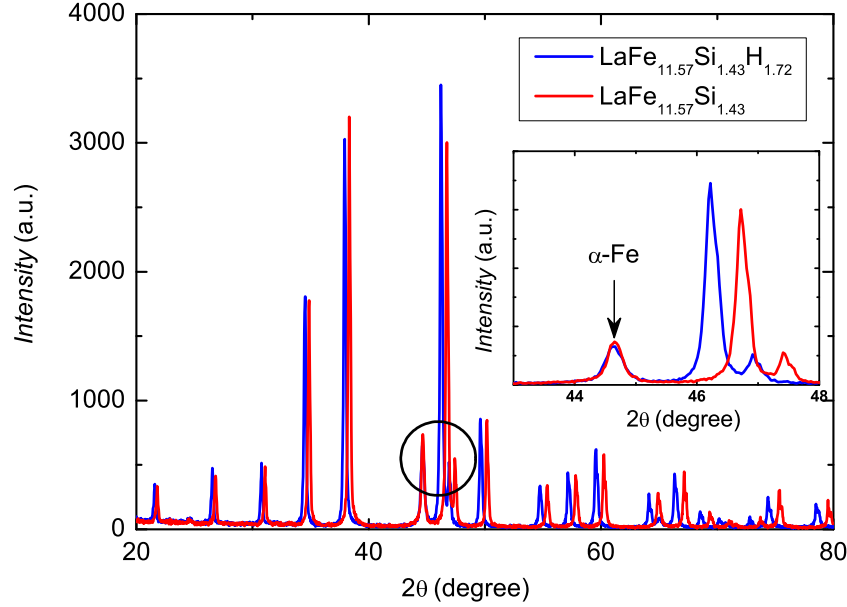
Figure 6.12: Room temperature XRD patterns of LaFe$_{11.57}$Si$_{1.43}$ and its hydrided ribbons. Inset shows the reflections in 2θ range 43 $^\circ$ − 48 $^\circ$.

in a significant expansion of the unit volume. As one can see in the inset of figure 6.12, the reflection (110) of α-Fe at 44.66 $^\circ$ keeps the same shape in both patterns. However, all the reflections of the main phase move to higher angles in the hydrided ribbons. The displacement becomes more and more important with an increase of the angle. It means that the hydrogen atoms enter into the interstices of the LaFe$_{11.57}$Si$_{1.43}$ ribbons, leading to an expansion of the unit cell and an increase of the Curie temperature [138].

Due to the presence of α-Fe in the sample, the real composition could not be equal to the nominal one. By considering 9 wt.% α-Fe determined from the XRD analysis, the composition La$_{1.09}$Fe$_{11.45}$Si$_{1.55}$ was obtained. The refined lattice parameters a = 11.4703(6) Å for the LaFe$_{11.57}$Si$_{1.43}$ ribbons and a = 11.5991(6) Å for the hydrided ribbons are consistent with the values a = 11.469 Å for the LaFe$_{11.44}$Si$_{1.56}$ bulk and a = 11.591 Å for its hydride with y = 1.60 [138]. Besides, the Curie temperature T_C = 194 K of the LaFe$_{11.57}$Si$_{1.43}$ ribbons determined from heat capacity at zero field (see below) is in good agreement with 195 K from magnetization [35] and 194 K from heat capacity [139] for the LaFe$_{11.44}$Si$_{1.56}$ bulk. In the hydrided ribbons, T_C = 334 K is the same as that reported by Podgornykh *et al.* in the LaFe$_{11.44}$Si$_{1.56}$H$_{1.50}$ bulk [139], but higher than 323 K reported by Fujita *et al.* in the same compound [39]. We

shall use the nominal compositions in the subsequent text.

6.4.2 Scanning electron microscopy

SEM images have been taken for a randomly chosen piece of the LaFe$_{11.57}$Si$_{1.43}$ ribbons. As one can see in figure 6.13(a), the ribbon exhibits a good homogeneity. The ribbon is mainly constructed by two phases, the gray one and the dark one, as seen figure 6.13(b). The EDS analysis in each phase indicates that the gray phase: 7.06 at.% La, 84.47 at.% Fe and 8.47 at.% Si (La$_{1.16}$Fe$_{11.60}$Si$_{1.40}$) and the dark phase: 0.74 at.% La, 97.34 at.% Fe and 1.92 at.% Si (La$_{0.01}$FeSi$_{0.02}$), which correspond to the main phase and the secondary phase α-Fe, respectively. The sum area of the dark surface is about 8 % of the total area in figure 6.13(b), relating to the volumetric fraction of α-Fe. It agrees well with 9 % in mass evaluated from the XRD patterns.
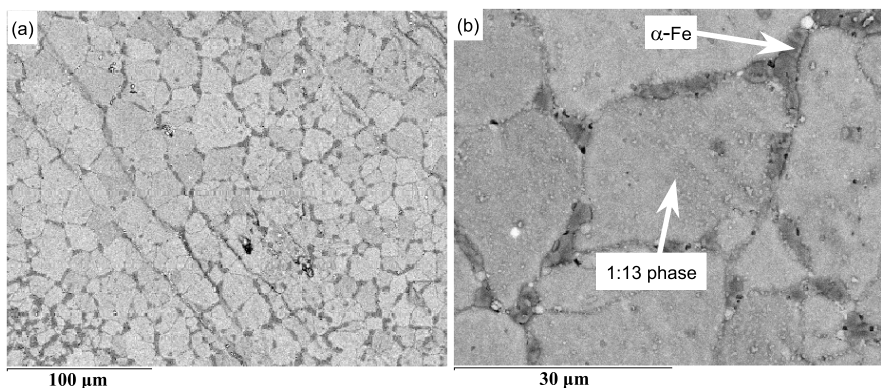
Figure 6.13: SEM images of the LaFe$_{11.57}$Si$_{1.43}$ ribbons.

6.4.3 Heat capacity

Figure 6.14 shows the temperature dependence of the heat capacity measured at zero field for LaFe$_{11.57}$Si$_{1.43}$ and its hydrided ribbons. The observation of sharp heat-capacity peaks confirms that the characteristic of FOPT in the LaFe$_{11.57}$Si$_{1.43}$ ribbons is unchanged by the hydrogenation. But the hydrogenation shifts the heat-capacity anomaly from 194 K to 334 K. The increase of the transition temperature with H concentration is about 81 K per H atom in a formula unit, practically coinciding with the value for bulk compounds, 85 K per H atom [39]. Additionally, the symmetric heat-capacity anomaly observed in the LaFe$_{11.57}$Si$_{1.43}$ ribbons is modified by the hydrogenation. For
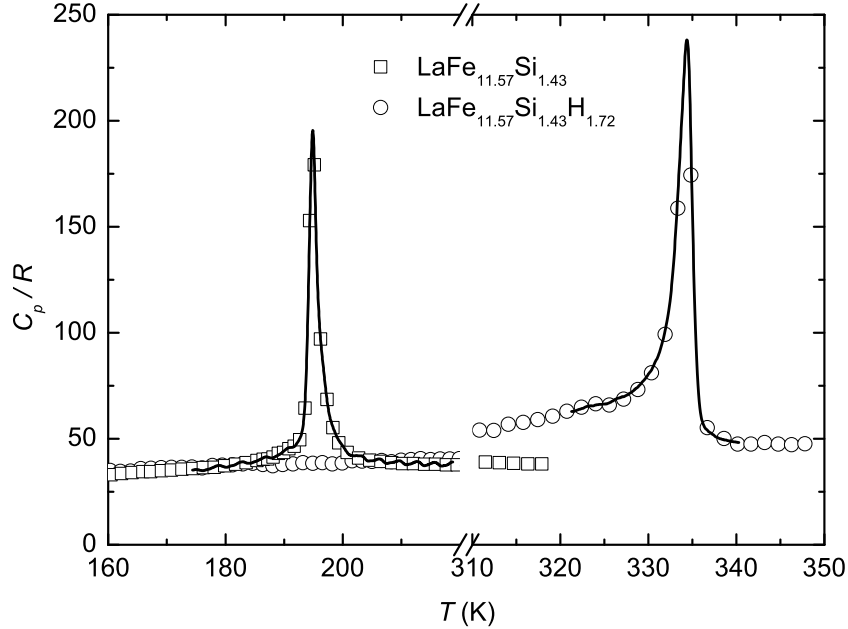
Figure 6.14: Heat capacity as a function of temperature for LaFe$_{11.57}$Si$_{1.43}$ and its hydrided ribbons measured at zero field. Symbols represent the heat-capacity data measured with the heat-pulse method. Lines stand for the heat-capacity data obtained from heating thermograms.

the hydrided ribbons, the anomaly is more like a λ-type peak, that is, the heat capacity increases smoothly to the maximum and then drops suddenly.

The heat capacities of LaFe$_{11.57}$Si$_{1.43}$ and its hydrided ribbons have been measured in heating and cooling processes at constant magnetic fields, as given in figure 6.15(a) and 6.15(b), respectively. Due to the fact that the upper temperature of our calorimeter is limited to 350 K, while the heat-capacity anomaly of the hydrided ribbons at 5 T is around (or just above) 350 K, we estimated the heat capacity at 5 T with the help of the Bean-Rodbell model which has been described in section 2.6. The nonmagnetic heat capacity was assumed to be a constant in the studied temperature range, amounting to the heat capacity value at 350 K at zero field ($C_{non} \cong 45R$), because above the transition region, the total heat capacity at zero field is almost unchanged and the magnetic contribution is very small (see figure 6.15(b)). The fitting parameters $J = 1$, $g = 2.2$, $\eta = 1.32$ and $T_0 = 335.6$ K were used in the model to achieve a good agreement between the experimental and theoretical heat-capacity curves at 3 T. Then the same parameters were employed to derive the heat capacity at 5 T.
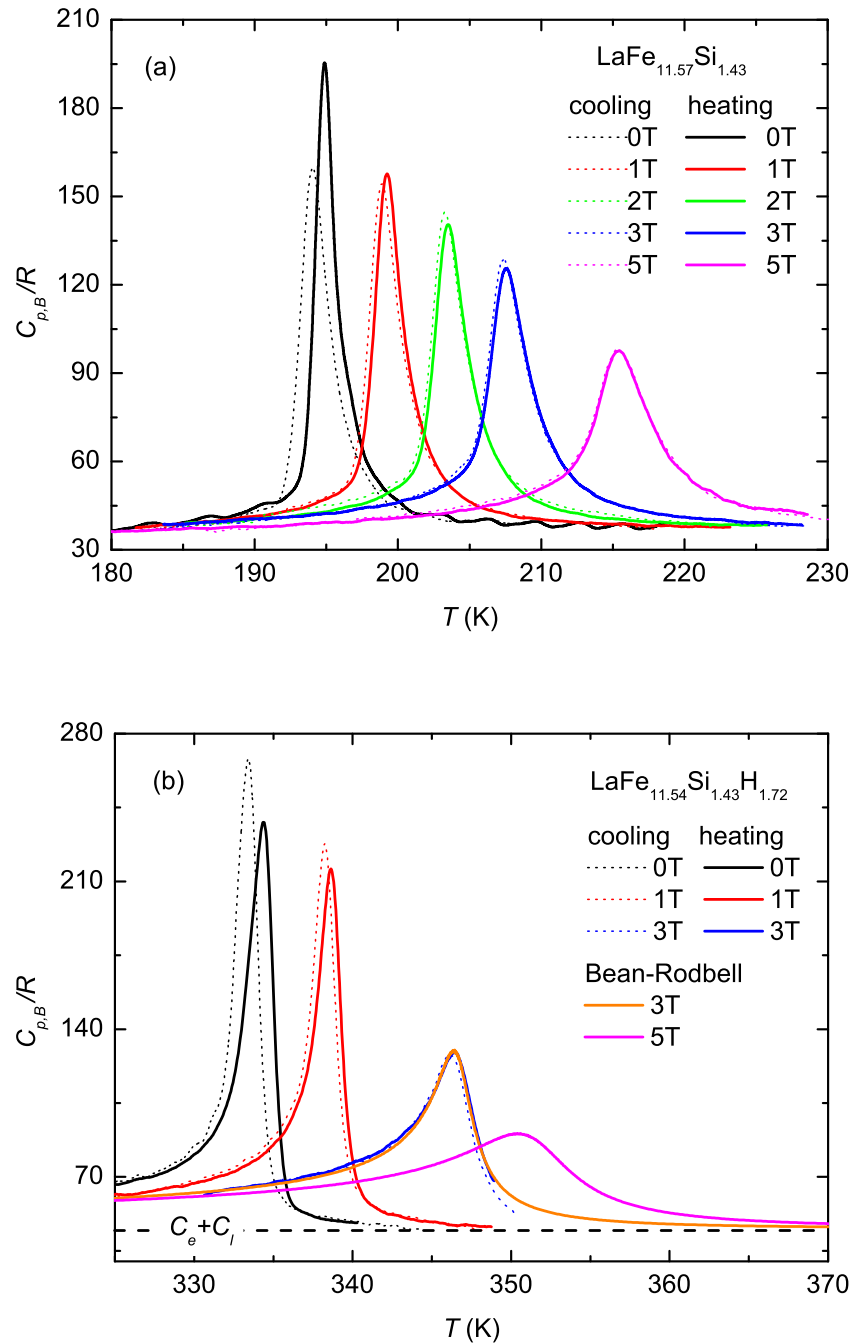
Figure 6.15: Heat capacity as a function of temperature measured at several constant fields, (a) for the LaFe$_{11.57}$Si$_{1.43}$ ribbons and (b) for the hydrided ribbons. Solid lines represent heating thermograms. Dotted lines represent cooling thermograms. Dashed line denotes the nonmagnetic heat capacity of the hydrided ribbons.
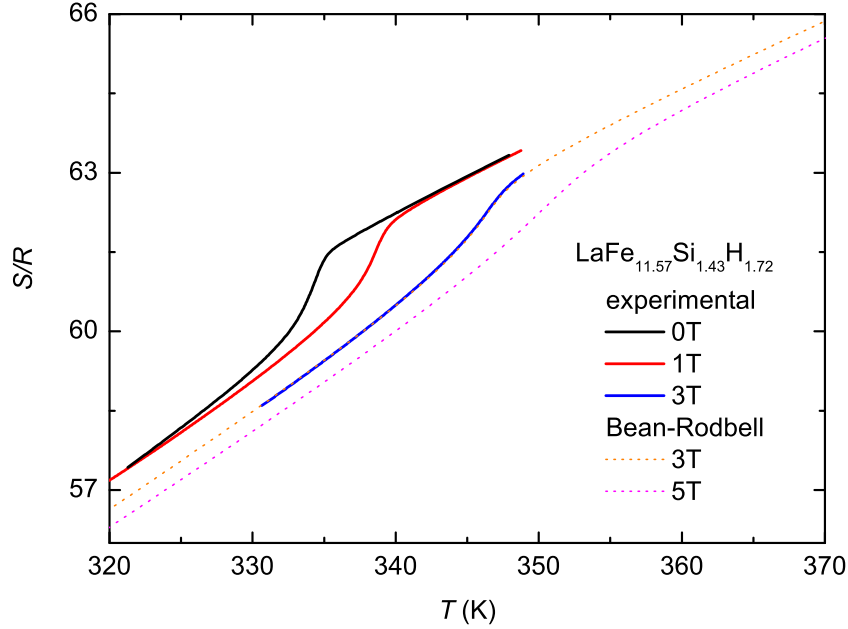
Figure 6.16: Temperature dependence of the total entropy at constant magnetic fields of 0, 1 T, 3 T and 5 T for the LaFe$_{11.57}$Si$_{1.43}$H$_{1.72}$ ribbons. Solid lines represent the entropy calculated from experimental heat-capacity data. Dotted lines represent the theoretical entropy curve on the basis of the Bean-Rodbell model.

In the heat capacities at zero field, the magnitudes of the thermal hysteresis are found to be 0.9 K and 1.0 K for LaFe$_{11.57}$Si$_{1.43}$ and its hydrided ribbons, respectively. The hysteresis is hardly influenced by the hydrogenation in the present ribbons, the difference 0.1 K may be ascribed to experimental errors (such as the "apparent hysteresis"). It is contrary to literature reports, where the thermal hysteresis reduces from a value around 2 K to 0 when the hydrogen concentration is $y = 1.6$ for the La$_{0.5}$Pr$_{0.5}$Fe$_{11.4}$Si$_{1.6}$H$_y$ bulk compound in Ref. [140] and $y = 2.3$ for the LaFe$_{11.57}$Si$_{1.43}$H$_y$ powder compound in Ref. [133]. Moreover, we found that the magnitude of the heat-capacity anomaly at zero field on cooling is broader and lower than that on heating in the LaFe$_{11.57}$Si$_{1.43}$ ribbons, but just the opposite is observed in the hydrided ribbons. The heat-capacity anomaly is broadened and lowered by applying magnetic fields. The hysteresis decreases with increasing field, disappearing at 3 T in both.

Figure 6.16 displays the total entropy as a function of temperature at constant fields of 0, 1 T, 3 T and 5 T for LaFe$_{11.57}$Si$_{1.43}$H$_{1.72}$ ribbons, calculated from the heat capacity on heating of figure 6.15(b). It can be seen that the

theoretical entropy curve at 3 T matches quite well with the experimental one. An entropy jump takes place at the transition temperature at zero field due to the occurrence of temperature-induced FOPT. The entropy jump is reduced significantly by applying magnetic fields. For a field of 3 T, a smooth entropy curve is observed, revealing that the FOPT occurring at zero field has been eliminated by the magnetic field.

6.4.4 Magnetocaloric effect

The isothermal entropy changes determined from heat-capacity, magnetization and direct measurements with magnetic field changes between 1 T and 5 T are shown in figure 6.17(a) for the LaFe$_{11.57}$Si$_{1.43}$ ribbons and in figure 6.17(b) for the hydrided ribbons. All methods give coinciding values of ΔS_T within the experimental errors. It is found that the MCE of the LaFe$_{11.57}$Si$_{1.43}$ ribbons is slightly reduced by the hydrogenation. The maximum values of $-\Delta S_T$ are seen to be 26.6 J/kg·K for the LaFe$_{11.57}$Si$_{1.43}$ ribbons and 23.0 J/kg·K for the hydrided ribbons upon a field change of 5 T. The former value is slightly higher than 23.0 J/kg·K for the bulk compound LaFe$_{11.44}$Si$_{1.56}$ reported by Fujita *et al.* [39], as well as 21.2 J/kg·K for the ribbons with the same nominal composition reported by Yan *et al.* [130], but much higher than 17.8 J/kg·K for the ribbons also with the same nominal composition reported by Gutfleisch *et al.* [129]. It could be attributed to the different real compositions of the samples prepared by different groups, because more Si atoms can be introduced in the main phase due to a higher cooling rate in the preparation of ribbons [130]. For the hydrided ribbons, $-\Delta S_{T,\mathrm{max}} = 23.0$ J/kg·K is equal to that for the LaFe$_{11.44}$Si$_{1.56}$H$_{1.5}$ bulk compound [39], but it is superior to 16.9 J/kg·K and 17.8 J/kg·K in the reactively-milled compounds LaFe$_{11.57}$Si$_{1.43}$H$_y$ ($y = 1.2$ and 2.3) [133].

Figures 6.18(a) and 6.18(b) show the temperature dependence of the adiabatic temperature change for LaFe$_{11.57}$Si$_{1.43}$ and its hydrided ribbons. The directly determined ΔT_S agrees well with that derived from heat capacity for both samples (the small discrepancy at 5 T for the hydrided ribbons can be attributed to the difference between the real and theoretical heat capacities). The maximum values of ΔT_S are found to be 12.0 K and 11.7 K with a field change of 5 T for LaFe$_{11.57}$Si$_{1.43}$ and its hydrided ribbons, respectively. The former maximum, $\Delta T_{S,\mathrm{max}} = 12.0$ K, is higher than 8.6 K reported by Fujita *et al.* in the bulk compound LaFe$_{11.44}$Si$_{1.56}$ [39], but the latter one, $\Delta T_{S,\mathrm{max}} = 11.7$ K, coincides with 10.7 K, 11.1 K and 12.6 K for the hydrided bulks LaFe$_{11.44}$ Si$_{1.56}$H$_y$ ($y = 0.5$, 1 and 1.5) reported by the same authors.

Collected data in table 6.2 are the transition temperatures, and the max-

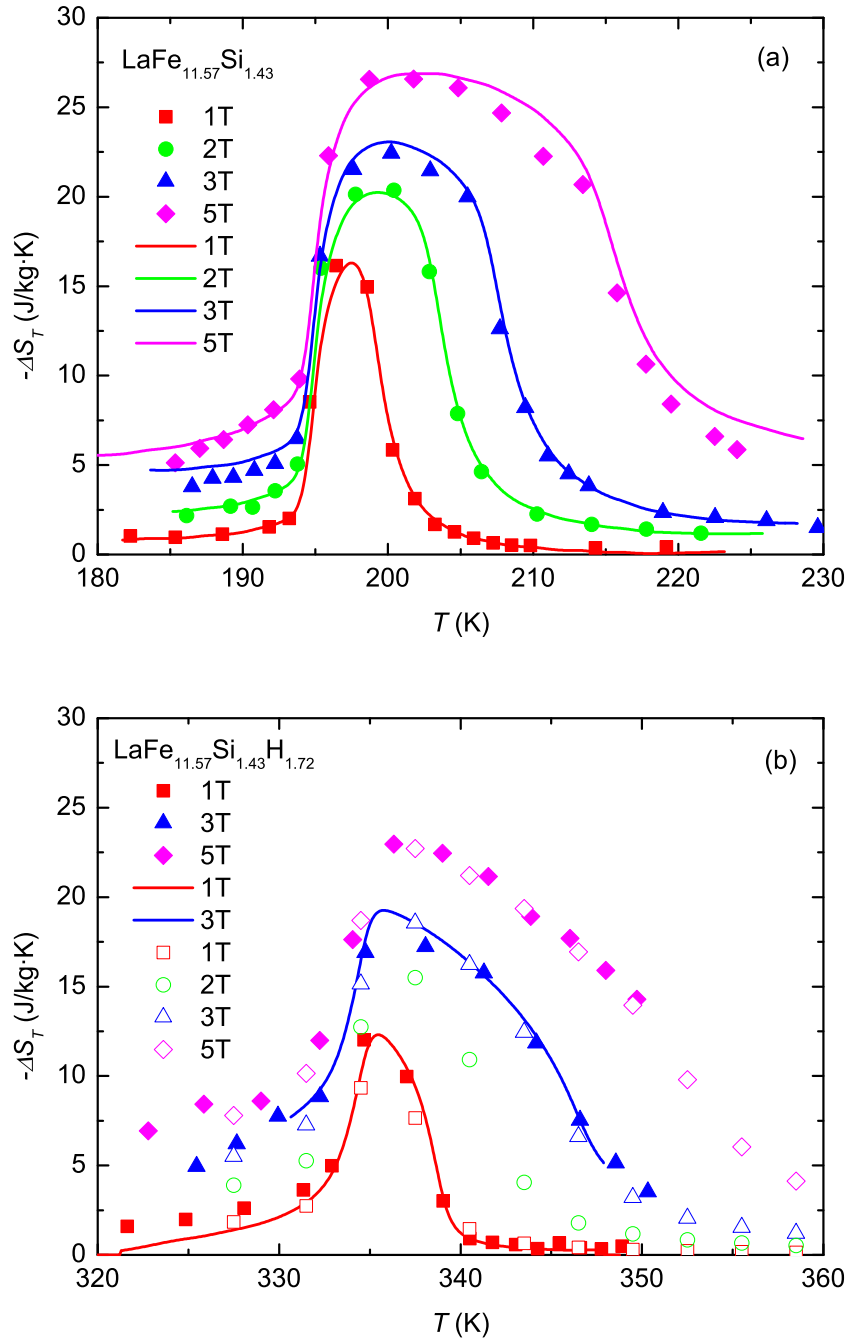Figure 6.17: Temperature dependence of the isothermal entropy change, (a) for the LaFe$_{11.57}$Si$_{1.43}$ ribbons and (b) for the hydrided ribbons. Solid lines represent ΔS_T calculated from heat capacity on heating. Solid symbols represent ΔS_T determined from direct measurement. Open symbols stand for ΔS_T obtained from isothermal magnetization measured on decreasing field.
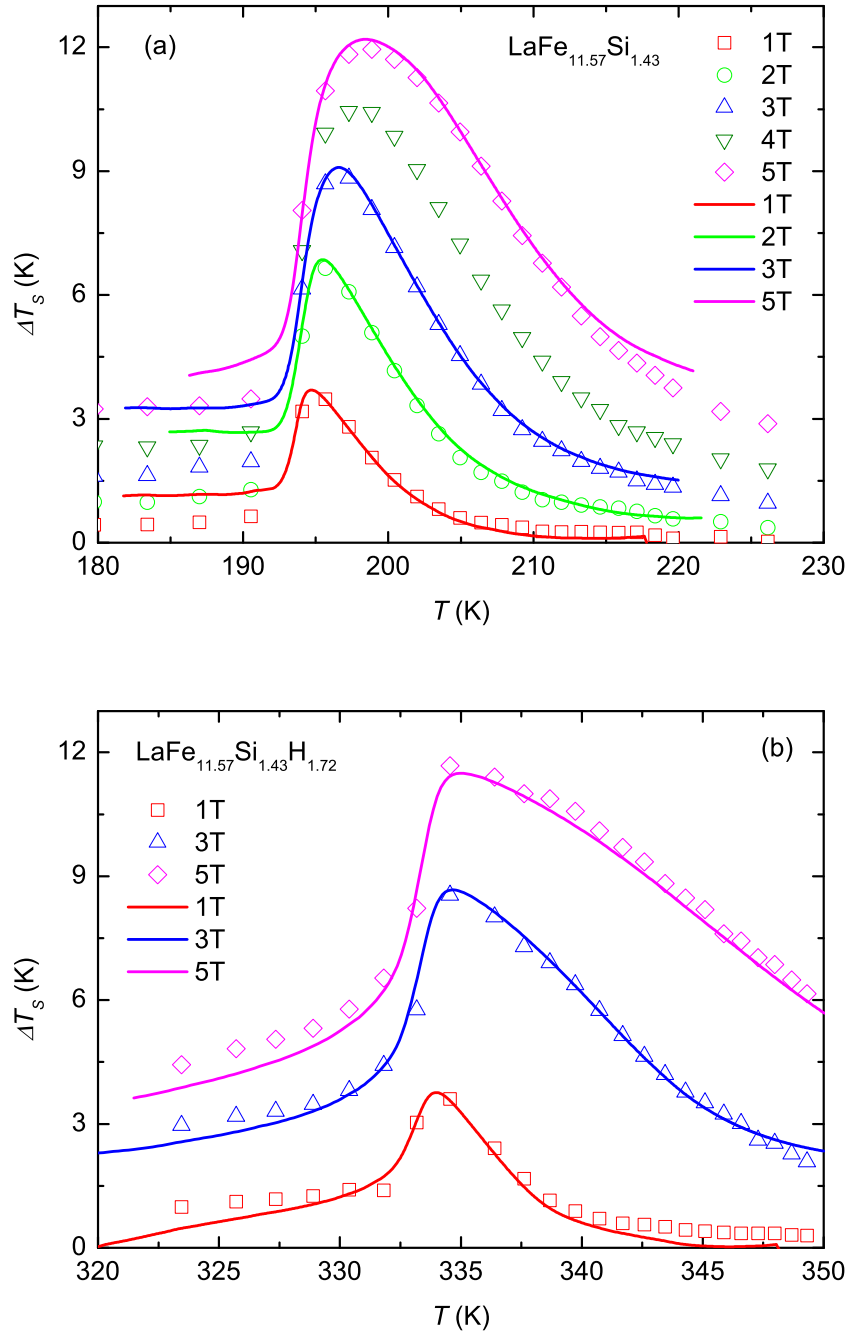
Figure 6.18: Temperature dependence of the adiabatic temperature change, (a) for the LaFe$_{11.57}$Si$_{1.43}$ ribbons, and (b) for the hydrided ribbons. Lines represent ΔT_S calculated from heat capacity on cooling. Symbols represent ΔT_S derived from direct measurement.

imum magnetocaloric parameters for magnetic field changes of 2 T and 5 T in the compounds with a common formula LaFe$_{13-x}$Si$_x$H$_y$. Some characteristics are found: (i) The lowest transition temperature is found to be 175 K in the bulk compound with a nominal composition of LaFe$_{11.83}$Si$_{1.17}$ [141] (the authors did not mention about the amount of impurity phases, especially the fraction of α-Fe, and how the transition temperature was obtained), and it is 184 K in the ribbons with nominal compositions of LaFe$_{12}$Si$_1$ and LaFe$_{11.8}$Si$_{1.2}$ [this Thesis]. Actually, the real Si concentration (about 1.3) is higher than the nominal one due to the presence of α-Fe. (ii) Significant discrepancies of the transition temperature, $\Delta S_{T,\mathrm{max}}$ and $\Delta T_{S,\mathrm{max}}$ in the compounds with the same nominal composition but made with different methods (e.g. those for the LaFe$_{11.57}$Si$_{1.43}$ compounds prepared by arc-melting [39] and melt-spinning [129] techniques), and also in the compounds with the same nominal composition and prepared with the same method but by different researchers (e.g. those for the LaFe$_{11.6}$Si$_{1.4}$ bulk compounds made by Chen *et al.* [40] and Liu *et al.* [142] and those for the LaFe$_{11.57}$Si$_{1.43}$ ribbons made by Yan *et al.* [130] and Gutfleisch *et al.* [129]). (iii) The nature of GMCE remains in both, the LaFe$_{13-x}$Si$_x$ compounds and their hydrides, when x is lower than 1.6. With a further increase of x, the MCE is significantly reduced due to the vanishing of the IEM FOPT and the nature of the transition becomes second order [122]. (iv) For the compounds with the same nominal composition, the observed MCEs in bulks are slightly higher than those in ribbons. (v) The hydrogenation improves significantly the transition temperature to high temperatures, meanwhile, it reduces slightly the MCE. The highest saturation of hydrogen content $y = 2.3$ is achieved in the LaFe$_{11.57}$Si$_{1.43}$ compound through mechanically milling the sample in the presence of hydrogen atmosphere [133].

Table 6.2: Transition temperature, maximum isothermal entropy change and maximum adiabatic temperature change for magnetic field changes of 2 T and 5 T in the compounds prepared with a nominal formula LaFe$_{13-x}$Si$_x$H$_y$.

Materials LaFe$_{13-x}$Si$_x$H$_y$	T_t (K)	$-\Delta S_{T,\max}$ (J/kg·K)		$\Delta T_{S,\max}$ (K)		References
		2 T	5 T	2 T	5 T	
$x = 1.0$, $y = 0$, ribbons	184	20^{abc}	23^{abc}	6.4^{ac}	9.9^{ac}	this Thesis
$x = 1.0$, $y = 0$, ribbons	195	—	25^b	—	—	[129]
$x = 1.1$, $y = 0$, bulk	179	19^b	27^b	—	—	[143]
$x = 1.17$, $y = 0$, bulk	175	21^b	28^b	—	—	[141]
$x = 1.2$, $y = 0$, ribbons	185	20^{abc}	27^{abc}	7.0^{ac}	11.6^{ac}	this Thesis
$x = 1.2$, $y = 0$, ribbons	195	25^b	31^b	—	—	[129]
$x = 1.2$, $y = 0$, bulk	185	24^b	25^b	7.3^c	—	[144]
$x = 1.3$, $y = 0$, bulk	188	25^b	29^b	4.0^{c*}	—	[137]
$x = 1.3$, $y = 0$, bulk	190	26^b	28^b	—	—	[123]
$x = 1.3$, $y = 0$, bulk	185	—	28^b	—	—	[145]
$x = 1.3$, $y = 0$, bulk	183	23^b	26^b	—	—	[141]
$x = 1.3$, $y = 0$, bulk	184	28^b	30^b	8.1^a	12.1^a	[39]
$x = 1.3$, $y = 1.1$, bulk	287	28^b	31^b	7.1^a	15.4^a	[39]
$x = 1.4$, $y = 0$, bulk	188	21^b	25^b	—	—	[141]
$x = 1.4$, $y = 0$, bulk	195	—	24^b	—	—	[40]
$x = 1.4$, $y = 0$, bulk	190	13^b	18^b	—	—	[142]
$x = 1.4$, $y = 0$, bulk	193	19^b	22^b	7.0^c	—	[144]
$x = 1.4$, $y = 0$, bulk	191	—	27^b	—	—	[145]
$x = 1.4$, $y = 0$, ball-milled	200	24^b	33^b	—	—	[146]
$x = 1.43$, $y = 0$, bulk	188	24^b	26^b	7.5^a	10.7^a	[39]

Table 6.2 continued

Materials LaFe$_{13-x}$Si$_x$H$_y$	T_t (K)	$-\Delta S_{T,\max}$ (J/kg·K)		$\Delta T_{S,\max}$ (K)		References
		2 T	5 T	2 T	5 T	
$x = 1.43$, $y = 1.3$, bulk	291	24^b	28^b	6.9^a	12.8^a	[39]
$x = 1.43$, $y = 0$, bulk	199	—	14^b	—	—	[147]
$x = 1.43$, $y = 0$, ribbons	198	—	21^b	—	—	[130]
$x = 1.43$, $y = 0$, ribbons	210	—	18^b	—	—	[129]
$x = 1.43$, $y = 0$, ribbons	194	20^{abc}	26^{abc}	6.6^{ac}	12.0^{ac}	this Thesis
$x = 1.43$, $y = 1.72$, ribbons	334	16^{abc}	23^{abc}	6.5^{ac}	11.7^{ac}	this Thesis
$x = 1.43$, $y = 0$, ball-milled	199	—	24^b	—	—	[133]
$x = 1.43$, $y = 0.8$, ball-milled	236	—	16^b	—	—	[133]
$x = 1.43$, $y = 1.2$, ball-milled	277	—	17^b	—	—	[133]
$x = 1.43$, $y = 2.3$, ball-milled	346	—	18^b	—	—	[133]
$x = 1.5$, $y = 0$, bulk	194	21^b	24^b	—	—	[148]
$x = 1.5$, $y = 0$, bulk	194	21^b	25^b	—	—	[141]
$x = 1.5$, $y = 0$, bulk	195	—	25^b	—	—	[149]
$x = 1.5$, $y = 0.3$, bulk	224	—	17^b	—	—	[149]
$x = 1.5$, $y = 0.6$, bulk	257	—	18^b	—	—	[149]
$x = 1.5$, $y = 0.9$, bulk	272	—	17^b	—	—	[149]
$x = 1.5$, $y = 1.3$, bulk	288	—	17^b	—	—	[149]
$x = 1.5$, $y = 1.5$, bulk	312	—	17^b	—	—	[149]
$x = 1.5$, $y = 1.8$, bulk	341	—	21^b	—	—	[149]
$x = 1.56$, $y = 0$, bulk	195	20^b	23^b	6.5^a	10.7^a	[39]
$x = 1.56$, $y = 0.5$, bulk	233	20^b	24^b	6.0^a	10.7^a	[39]
$x = 1.56$, $y = 1.0$, bulk	274	19^b	23^b	6.2^a	11.1^a	[39]

Table 6.2 continued

Materials LaFe$_{13-x}$Si$_x$H$_y$	T_t (K)	$-\Delta S_{T,\text{max}}$ (J/kg·K) 2 T	5 T	$\Delta T_{S,\text{max}}$ (K) 2 T	5 T	References
$x = 1.56$, $y = 1.5$, bulk	323	19^b	23^b	6.8^a	12.6^a	[39]
$x = 1.56$, $y = 0$, bulk	200	—	21^b	—	—	[125]
$x = 1.56$, $y = 0$, ribbons	203	—	14^b	—	—	[150]
$x = 1.6$, $y = 0$, bulk	208	14^b	19^b	—	—	[33]
$x = 1.6$, $y = 0$, bulk	195	—	18^b	—	—	[151]
$x = 1.6$, $y = 0$, bulk	199	14^b	19^b	—	—	[141]
$x = 1.6$, $y = 0$, bulk	203	—	24^b	—	—	[145]
$x = 1.6$, $y = 0$, ball-milled	203	17^b	25^b	—	—	[146]
$x = 1.6$, $y = 0$, bulk	211	—	15^b	—	—	[152]
$x = 1.6$, $y = 0$, ribbons	222	—	13^b	—	—	[129]
$x = 1.7$, $y = 0$, bulk	212	—	17^b	—	—	[145]
$x = 1.7$, $y = 0$, bulk	206	12^b	18^b	—	—	[141]
$x = 1.8$, $y = 0$, ribbons	231	5^b	10^b	—	—	[129]
$x = 1.8$, $y = 0$, bulk	222	7^b	13^b	—	—	[37]
$x = 1.8$, $y = 0$, bulk	210	8^b	13^b	—	—	[141]
$x = 1.8$, $y = 0$, bulk	216	8^b	14^b	—	—	[148]
$x = 1.8$, $y = 0$, bulk	216	—	14^b	—	—	[145]
$x = 1.8$, $y = 0$, ball-milled	217	7^b	12^b	—	—	[146]

* for a field change of 1.4 T.

^{a} obtained from heat capacity.

^{b} obtained from magnetization.

^{c} obtained from direct measurement.

6.5 Conclusions

In summary, we have studied the calorimetric and magnetocaloric properties in melt-spun LaFe$_{13-x}$Si$_x$H$_y$ ribbons by means of direct and indirect measurements. Some conclusions can be made:

- The actual concentration of Si in the ribbon samples with nominal compositions LaFe$_{12}$Si$_1$ and LaFe$_{11.8}$Si$_{1.2}$ was determined with the help of XRD analysis, obtaining values close to $x = 1.3$, that agrees with the minimum value reported in the literature for bulk compounds.

- Although the real compositions and the transition temperatures of the LaFe$_{12}$Si$_1$ and LaFe$_{11.8}$Si$_{1.2}$ ribbons are almost the same, the observed hysteresis in the former sample is smaller. The application of magnetic field produces different effects on the shape of the heat-capacity anomalies for these two samples.

- The $|\Delta S_T|$ values obtained from isothermal magnetization data are slightly underestimated on increasing field and overestimated on decreasing field due to the irreversibility.

- The magnetocaloric parameters obtained from heat-capacity and direct measurements are in good agreement with each other within the experimental errors of each technique for both of LaFe$_{12}$Si$_1$ and LaFe$_{11.8}$Si$_{1.2}$. The maximum values of the magnetocaloric parameters for magnetic field changes of 2 T and 5 T are $-\Delta S_{T,\max}$ = 19.6 J/kg·K and 23.4 J/kg·K, $\Delta T_{S,\max}$ = 6.4 K and 9.9 K for the LaFe$_{12}$Si$_1$ ribbons, and $-\Delta S_{T,\max}$ = 22.1 J/kg·K and 27.2 J/kg·K, $\Delta T_{S,\max}$ = 7.0 K and 11.6 K for the LaFe$_{11.8}$Si$_{1.2}$ ribbons.

- The hydrogenation in the LaFe$_{11.57}$Si$_{1.43}$ ribbons does not change the structure of the main 1:13 phase, the fraction of the phases and the magnitude of the hysteresis, but it changes the lattice constant and the transition temperature.

- The concentration of H in the studied LaFe$_{11.57}$Si$_{1.43}$ ribbons is found to be 1.72, leading to a transition temperature increase from 194 K to 334 K. The MCE in the LaFe$_{11.57}$Si$_{1.43}$ ribbons is slightly reduced by the hydrogenation. For magnetic field changes of 2 T and 5 T, the maximum values $-\Delta S_{T,\max}$ decrease from 20 J/kg·K to 16 J/kg·K and from 26 J/kg·K to 23 J/kg·K, respectively, and $\Delta T_{S,\max}$ changes very slightly from 6.6 K to 6.5 K and from 12.0 K to 11.7 K. The hydrided ribbons are promising candidates as working refrigerants for magnetic refrigeration near room temperature.

Chapter 7

Series of $Mn_xT_{1-x}As$ compounds with T = Fe and Co

7.1 Introduction

In 2001, Wada *et al.* [28] were the first to report the GMCE ($-\Delta S_{T,\text{max}} = 32$ J/kg·K and $\Delta T_{S,\text{max}} = 13$ K for a field change of 5 T) in MnAs which undergoes a FOPT from FM to PM phase combined with a structural variation from the hexagonal NiAs-type structure to the orthorhombic MnP-type structure at 318 K upon increasing temperature. Later, Gama *et al.* [97] proposed that when applying a hydrostatic pressure, MnAs exhibits what the authors called "colossal" MCE with a maximum of $-\Delta S_{T,\text{max}} = 267$ J/kg·K. The authors explained that the "colossal" MCE results from the lattice entropy variation through the magnetoelastic coupling induced by applying hydrostatic pressure [97]. The "colossal" MCE in MnAs is merely a spurious peak (the "spike" effect) due to an inadequate application of the Maxwell relation to the magnetization data measured in the two-phases-coexistence (TPC) region, as illustrated in section 4.4. The correct ΔS_T values were determined from heat-capacity measurements by Tocado *et al.* [30]. They found that the maximum is $-\Delta S_{T,\text{max}} = 28.2$ J/·K for a field change from 0 to 6 T.

In practice, the "spike" effect appears in most materials exhibiting FOPTs, such as the Fe-, Cu- or Al-doped MnAs derivatives [32, 98, 153], and $Mn_{1.1}Fe_{0.9}$ $P_{0.8}Ge_{0.2}$ [96]. However, all of these spurious peaks of ΔS_T have been reported as the "colossal" MCE.

In this chapter, correct values of ΔS_T for $Mn_{1-x}T_xAs$ compounds with T = Fe and Co were determined by means of heat-capacity and direct measurements. The results are compared with those derived from magnetization

data, including from isothermal magnetization data measured following different protocols and from isofield magnetization data. Moreover, ΔT_S for each compound has also been determined from heat-capacity and direct measurements. Finally, the framework of the Bean-Rodbell model was employed to understand the phase transition and MCE in the $Mn_{1-x}T_x As$ compounds.

7.2 Sample preparation

Polycrystal samples with nominal compositions $Mn_{1-x}Fe_x As$ ($x = 0.006$, 0.01 and 0.015) and $Mn_{1-x}Co_x As$ ($x = 0.003$, 0.01 and 0.02) (provided by S. Gama's group) had been synthesized by the arc-melting method. As described in Ref. [32], a mother Fe / Mn alloy was first arc-melted under an Ar atmosphere, each alloy was then prepared with all the Fe coming from the mother alloy plus the appropriate amounts of pure Mn and As to complete the 1:1 (MnAs) stoichiometry, the as-prepared alloys sealed in a quartz tube under vacuum were heat treated in a resistive furnace at 1070 °C for 2 h to assure the melting and thorough mixing of the components, and were then quenched to room temperature, the tube containing the sample was then reheated to 800 °C for 48 h and subsequently water quenched to ambient temperature.

7.3 $Mn_{1-x}Fe_x As$

7.3.1 Differential scanning calorimetry

Figure 7.1 shows the temperature dependence of the heat flow measured in heating and cooling processes for the $Mn_{1-x}Fe_x As$ compounds with $x = 0.006$, 0.01 and 0.015. A heating / cooling rate of 10 K/min was used in the measurements. For each compound, an endothermic peak on heating and an exothermic peak on cooling are observed, indicating the transitions from FM to PM phase and from PM to FM phase, respectively. The endothermic peak locates at a higher temperature than the exothermic peak. The temperature difference between the two peaks is much higher than the systematic errors caused by fast heating and cooling rates used in the measurement. Namely, the compounds exhibit thermal hysteresis, implying that the nature of transitions is of first order. The multipeaks in the cooling curves should be attributed to the avalanche effects which normally happen in FOPTs. The transition temperatures (taken as the peak temperatures) and the calculated latent heat for the $Mn_{1-x}Fe_x As$ compounds are listed in table 7.1. With increasing Fe content, both of the transition temperature and the latent heat decrease, resulting in an insignificant influence on the transition entropy.
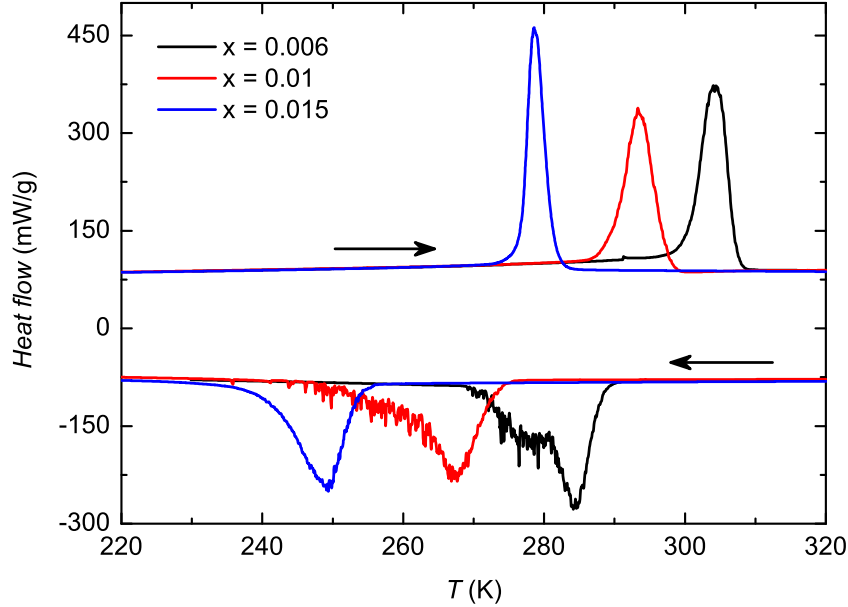
Figure 7.1: Heat flow as a function of temperature measured in cooling and subsequent heating processes for the $Mn_{1-x}Fe_xAs$ compounds.

7.3.2 X-ray diffraction

The XRD patterns of the $Mn_{1-x}Fe_xAs$ compounds with $x = 0.006$, 0.01 and 0.015 have been measured at different temperatures. According to the positions of the endothermic and exothermic peaks observed in figure 7.1, the selected measuring temperatures are well below and above the peak temperatures for each sample. In addition, a pattern was made at 473 K on each sample to examine an additional structural transition in the PM phase. In the parent compound MnAs, this second transition takes place at 398 K [154]. In figure 7.2 we present the XRD patterns measured at 183 K, 373 K and 473 K for $Mn_{0.985}Fe_{0.015}As$ which contains the highest Fe content in the studied compounds. Rietveld refinements confirm that the compound crystallizes in a hexagonal structure at 183 K, in an orthorhombic structure at 373 K and in an hexagonal structure again at 473 K. It indicates the occurrence of the transitions from the hexagonal to the orthorhombic and then back to the hexagonal structure with increasing temperature. The same structure variations are also observed in the XRD patterns of the compounds with $x = 0.006$ and 0.01. Accordingly, the first-order magnetostructural transition happening in MnAs remains in the Fe-doped compounds with an Fe content lower than 0.015.
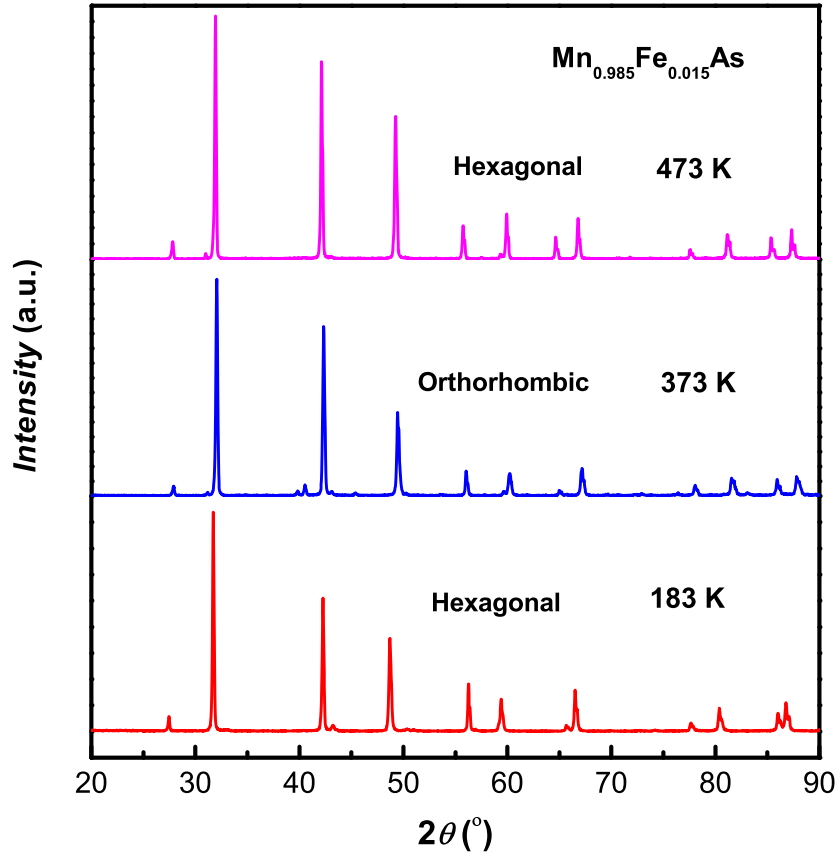
Figure 7.2: X-ray diffraction patterns collected at different temperatures for $Mn_{0.985}Fe_{0.015}As$.

7.3.3   Magnetization

● **$Mn_{0.994}Fe_{0.006}As$**

The three dimensional figure 7.3 shows the temperature dependence of the magnetization measured at various constant magnetic fields between 0.02 T and 9 T in heating and cooling processes for $Mn_{0.994}Fe_{0.06}As$. We found that the transition temperature shifts to higher temperatures with increasing field. The transition temperatures upon heating and cooling are 283 K and 311 K at 0.02 T, increasing to 323 K and 345 K at 9 T, respectively. The thermal hysteresis slightly decreases with increasing magnetic field. The fast heating / cooling rates (5 K/min) used in the experiments may lead to an overestimation / underestimation of the transition temperature on heating /cooling, conse-
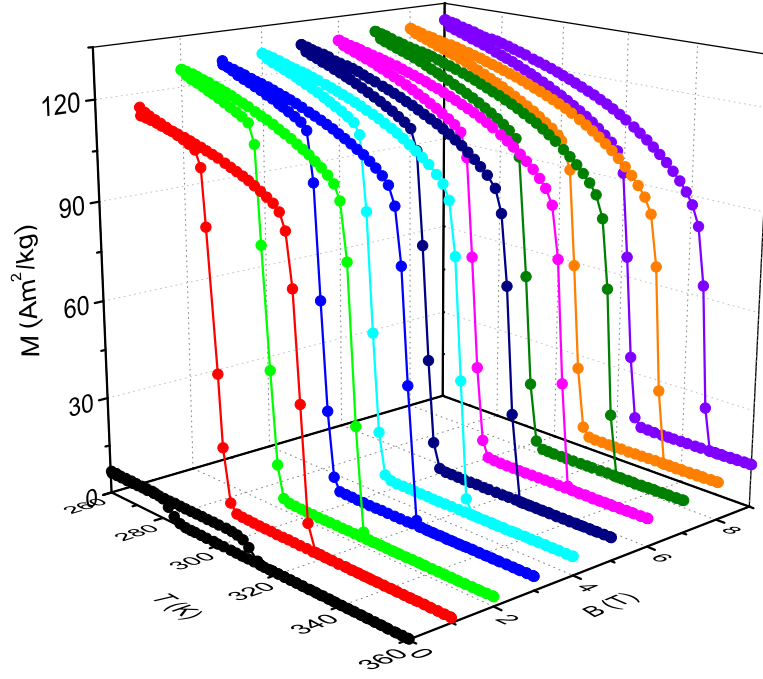
Figure 7.3: Temperature dependence of the magnetization measured at constant magnetic fields on heating and cooling for $Mn_{0.994}Fe_{0.06}As$.

quently, showing a larger thermal hysteresis than it should be. Correct and small hysteresis is determined in the following heat-capacity measurements. The sharp changes of magnetization occurring at low fields remain even at a field of 9 T in both heating and cooling curves.

The isothermal magnetization curves of $Mn_{0.994}Fe_{0.06}As$ have been measured in the vicinity of its transition temperature on increasing field up to 9 T and then on decreasing field. The measurements were carried out in two different ways, namely, following protocols 1 and 2. The resulting magnetization curves are displayed in figures 7.4(a) and 7.4(b). In figure 7.4(a), step-like behaviors are observed on both increasing and decreasing magnetization curves, characterizing the occurrence of field-induced metamagnetic phase transitions. The curve at 304 K on increasing field exhibits two steps, indicating that the sample is at a state with a mixed phase when initiating the measurement. The magnetizing process of the FM phase fraction is responsible for the lower magnetization step. The higher magnetization jump is attributed to the field-induced PM-FM transition of the PM phase fraction. The two-steps-like magnetization curve is neither observed on increasing field nor on decreasing field in figure 7.4(b). By using protocol 2, the initial state of the sample in the
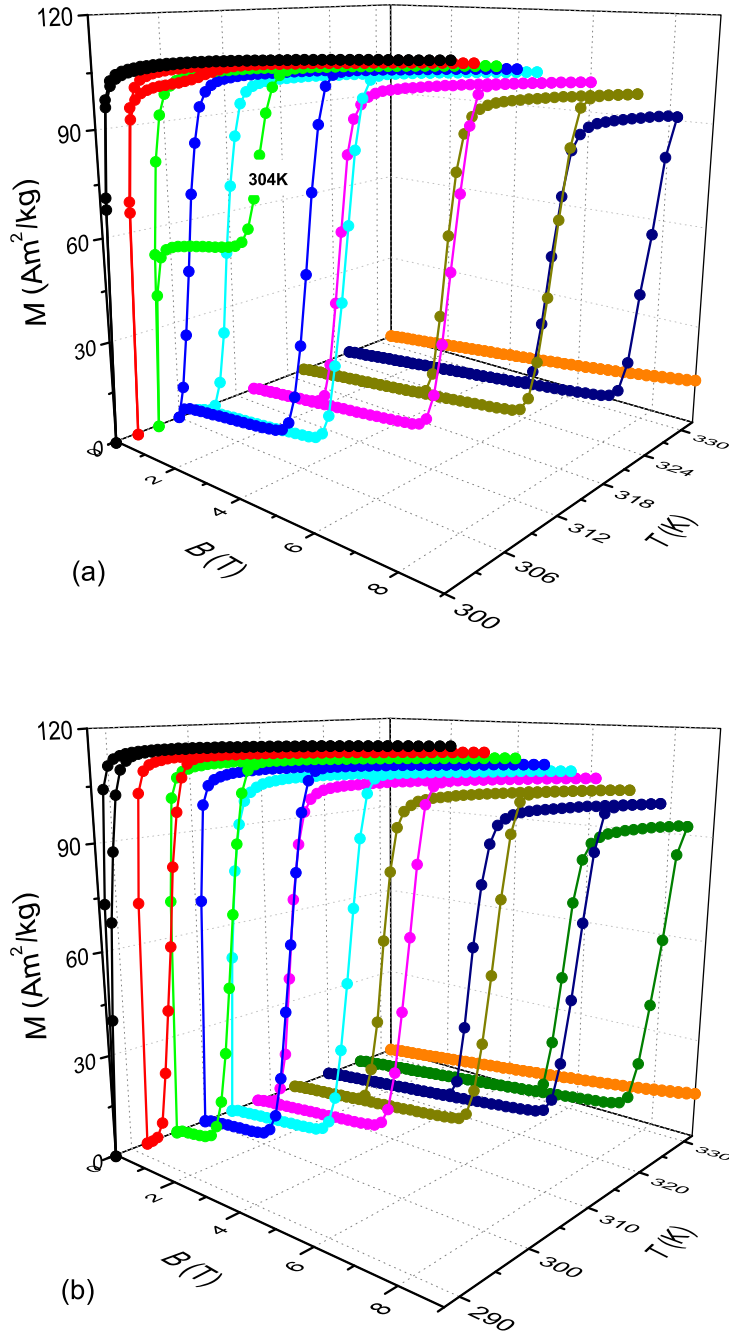
Figure 7.4: Magnetic field dependence of the magnetization measured on increasing and decreasing fields for $Mn_{0.994}Fe_{0.06}As$, (a) following protocol 1, and (b) following protocol 2.

hysteretic region is tailored to be a single PM phase, and the occurrence of the field-induced transition extends to a lower temperature region (below 304 K), where only the FM behavior is present in figure 7.4(a). Beyond the hysteretic region, the protocols 1 and 2 produce the same magnetization curves on both increasing field and decreasing field.

• **$Mn_{0.99}Fe_{0.01}As$**

Isofield magnetization data have been measured at fields between 0.02 to 4 T at a step of 0.2 T in heating and cooling processes, and isothermal magnetization data have been measured following protocol 1 on increasing and decreasing fields with maximum fields of 4 T and 9 T for $Mn_{0.99}Fe_{0.01}As$. The isofield magnetization curves are plotted in figure 7.5. The isothermal magnetization curves are plotted in figures 7.6(a) and 7.6(b) for maximum fields of 4 and 9 T, respectively. In both of the isothermal and isofield magnetization measurements, the magnetization is a function of two variables, temperature and magnetic field. In principle, the isothermal and isofield magnetization data can be equivalently converted to each other, obeying the rules that cooling / heating processes at constant magnetic fields correspond to increasing / decreasing magnetic field processes at constant temperatures, and viceversa. The isothermal magnetization curves converted from the isofield magnetization data of figure 7.5 are plotted in figure 7.7(b) for heating processes and in figure 7.7(a) for cooling processes. On the other hand, the isofield magnetization curves converted from the isothermal magnetization data of figures 7.6(a) and 7.6(b) are displayed in figures 7.8(a) and 7.8(b), respectively.

In figure 7.5, the sharp changes of magnetization related to the temperature-induced FOPTs are observed on heating and cooling. The position of the magnetization change equally moves to high temperatures with increasing magnetic field, which typically characterizes the FOPT in a ferromagnet.

In figure 7.6(a), the magnetization curves at temperatures below 296 K show a FM behavior with small hysteresis, and the magnitude of the curves reduces with an increase of temperature. Above 296 K, a PM behavior is observed. No field-induced metamagnetic transition is found neither on increasing field nor on decreasing field. It is understood that, in $Mn_{0.99}Fe_{0.01}As$, applying a field of 4 T is not enough to convert the phase from PM to FM at the temperatures above the transition temperature on heating ($T_{t,h} \approx 296$ K), below which the sample keeps in the FM phase, when performing the isothermal magnetization measurement following protocol 1. The decreasing magnitude of the magnetization is due to the reduction of the FM phase fraction in the sample with increasing temperature.

If a stronger magnetic field is applied in the isothermal magnetization measurement performed following protocol 1, the field-induced phase transition
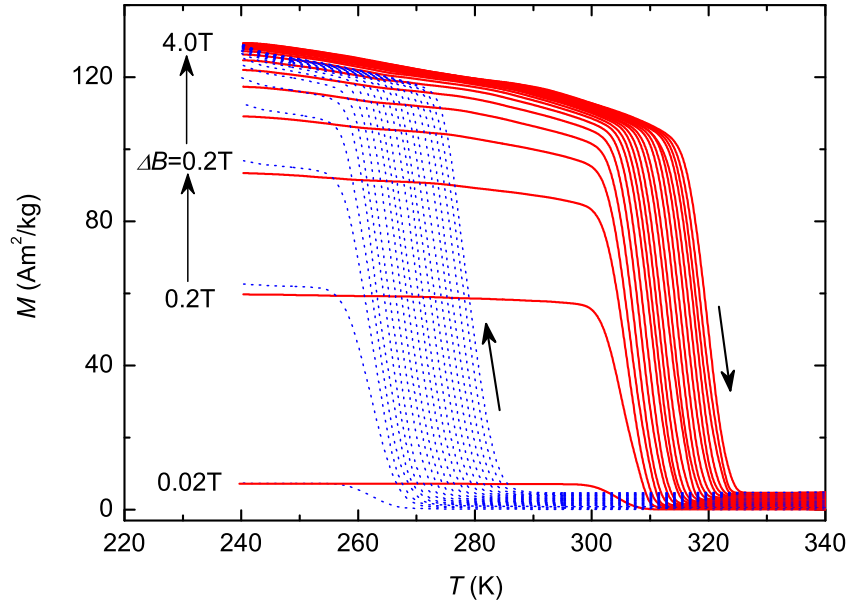
Figure 7.5: Temperature dependence of the magnetization measured at constant magnetic fields on heating (red solid lines) and cooling (blue dotted lines) for $Mn_{0.99}Fe_{0.01}As$.

could happen at fields greater than 4 T on increasing field at some temperatures above $T_{t,h}$. Once the phase of the sample is converted from PM to FM by applying the magnetic field, the metamagnetic transition would also occur in a demagnetization process. For example, the extracted magnetization curves from those measured with a maximum field of 9 T are shown in figure 7.6(b). As expected, it is seen that below 4 T the field-induced phase transition does not happen on increasing field but happens on decreasing field. Consequently, different demagnetization curves are observed in the measurements performed following the same protocol but with different maximum fields.

The isothermal magnetization curves converted from the isofield magnetization data of figure 7.5 on cooling are shown in figure 7.7(a), relating to magnetizing processes. And those converted from the isofield magnetization data of figure 7.5 on heating are shown in figure 7.7(b), relating to demagnetizing processes. It is found that field-induced metamagnetic phase transitions are observed on both increasing field and decreasing field, although the maximum field is 4 T, too. In addition to that, the transition occurs in a broader temperature region than those in figure 7.6(b). The transitions in figure 7.7(b) happen at higher temperatures (from 306 to 320 K) than those (from 297 to 305 K) in 7.6(b) for decreasing field, which should be attributed to the experi-

mental errors caused by the fast heating rate used in the isofield magnetization measurement.

On the other hand, the isothermal magnetization data can be converted to the isofield magnetization curves. Figures 7.8(a) and 7.8(b) display the isofield magnetization curves converted from the isothermal magnetization data of figures 7.6(a) and 7.6(b), respectively. It is interestingly found that sharp magnetization change takes place at each field in figures 7.8(a) and 7.8(b), but they occur unreasonably at almost the same temperature except for the curves on decreasing field in the second figure. The observed sharp changes in the magnetization curves occurring at the same temperature are not really related to the occurrence of FOPTs, since no field-induced transition takes place in the corresponding isothermal magnetization curves. Those "transitions" are spurious but they are considered as real ones when the original isothermal magnetization data are used to evaluate ΔS_T with the help of the Maxwell relation, resulting in the "spike" effect. These conversions also confirm that the use of isofield magnetization data is more suitable for the determination of ΔS_T in the present compounds than the use of isothermal magnetization data.

For each heating or cooling magnetization curve in figures 7.5, 7.8(a) and 7.8(b), the transition temperature was taken as the temperature of its middle height. Then different magnetic phase diagrams were constructed for $Mn_{0.99}Fe_{0.01}As$, as shown in figure 7.9. The transition temperatures obtained from figures 7.8(a) and 7.8(b) indeed are determined from the isothermal magnetization measurements, so some of them correspond to the spurious transitions. Open and solid symbols represent PM-FM and FM-PM transition lines, respectively. The thick line denotes the spurious transitions deduced from figure 7.8(a), where the spurious transitions on heating and cooling lead to the overlapped transition lines. It can be seen that the PM-FM / FM-PM transition line obtained from the isofield magnetization measurement shifts to lower / higher temperature than that determined from the heat-capacity measurement, but they are parallel to each other. It is because the heating / cooling rate (5 K/min) used in the isofield magnetization measurement is much faster than (0.1 K/min) used in the heat-capacity measurement, and the faster heating / cooling rate leads to a larger difference (about 10 K in the present case) between the temperature indication of the thermal sensor and the real temperature of the sample. Moreover, the spurious transition lines (or parts of the lines) are nearly perpendicular to the temperature axis since the spurious transition does not change with increasing field. Parts of the transition lines obtained from the isothermal magnetization data coincide with those obtained from the heat-capacity measurement, revealing the occurrence of the field-induced FOPTs.
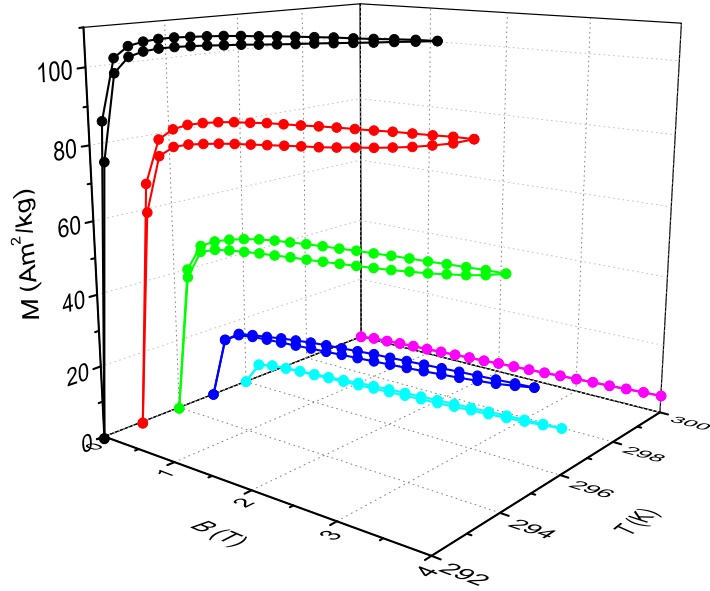
(a)
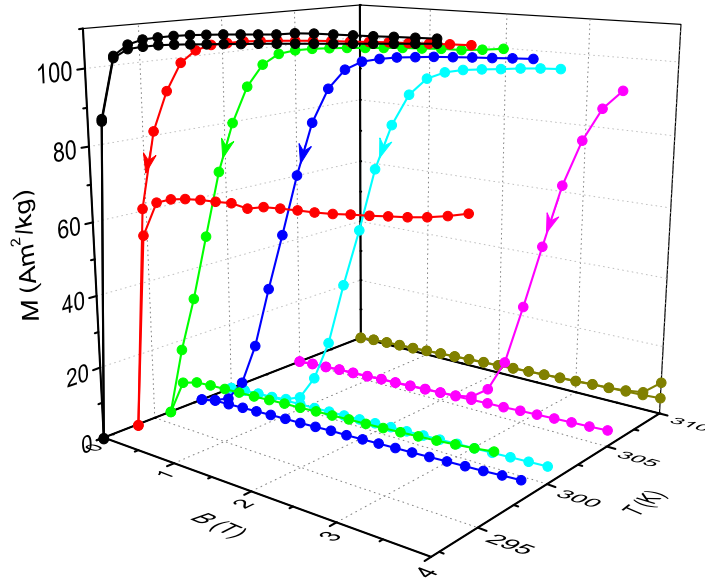
(b)

Figure 7.6: Isothermal magnetization as a function of magnetic field measured following protocol 1 on increasing and decreasing fields for $Mn_{0.99}Fe_{0.01}As$. (a) with a maximum field of 4 T. (b) extracted from the data measured with a maximum field of 9 T.
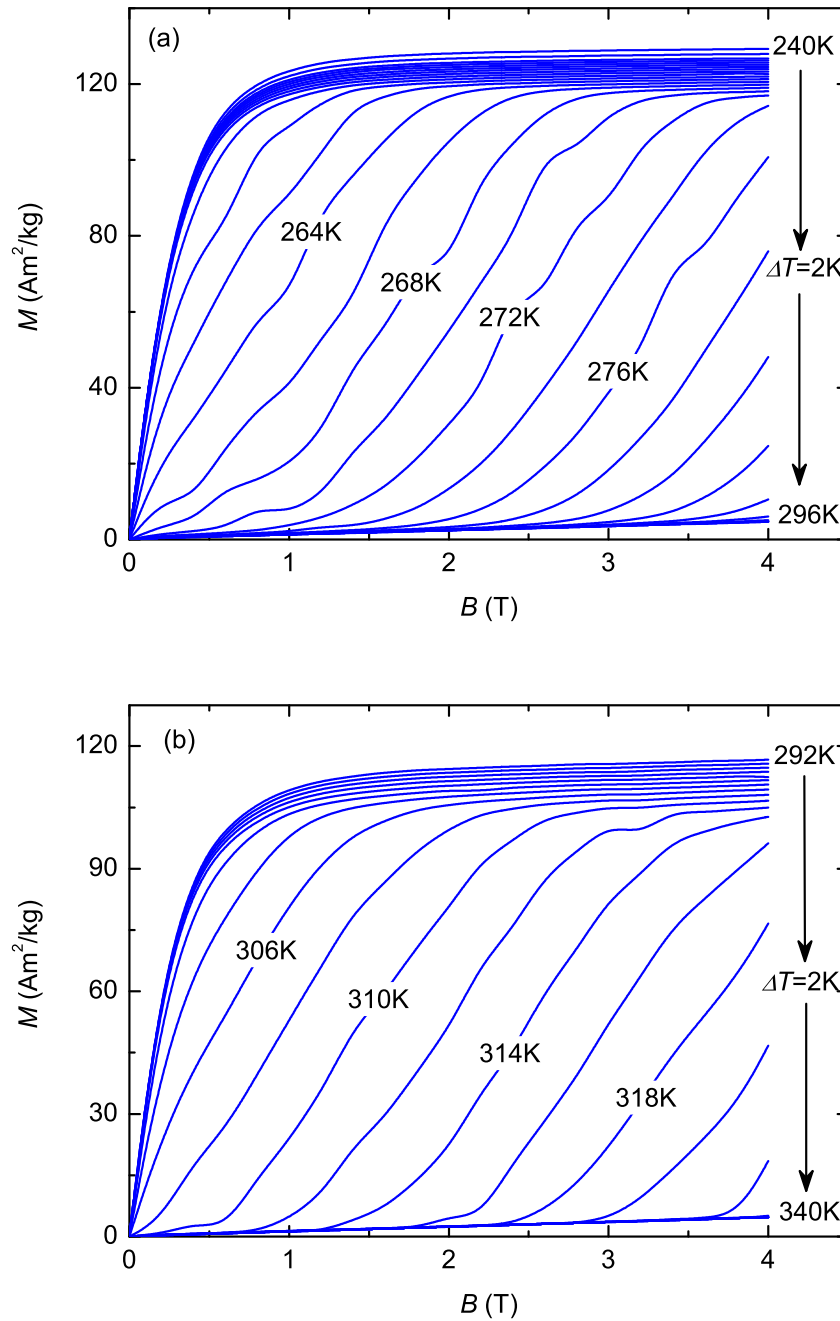
Figure 7.7: Converted isothermal magnetization curves from isofield magnetization data for Mn$_{0.99}$Fe$_{0.01}$As. (a) obtained from the cooling curves of figure 7.5. (b) obtained from the heating curves of figure 7.5.
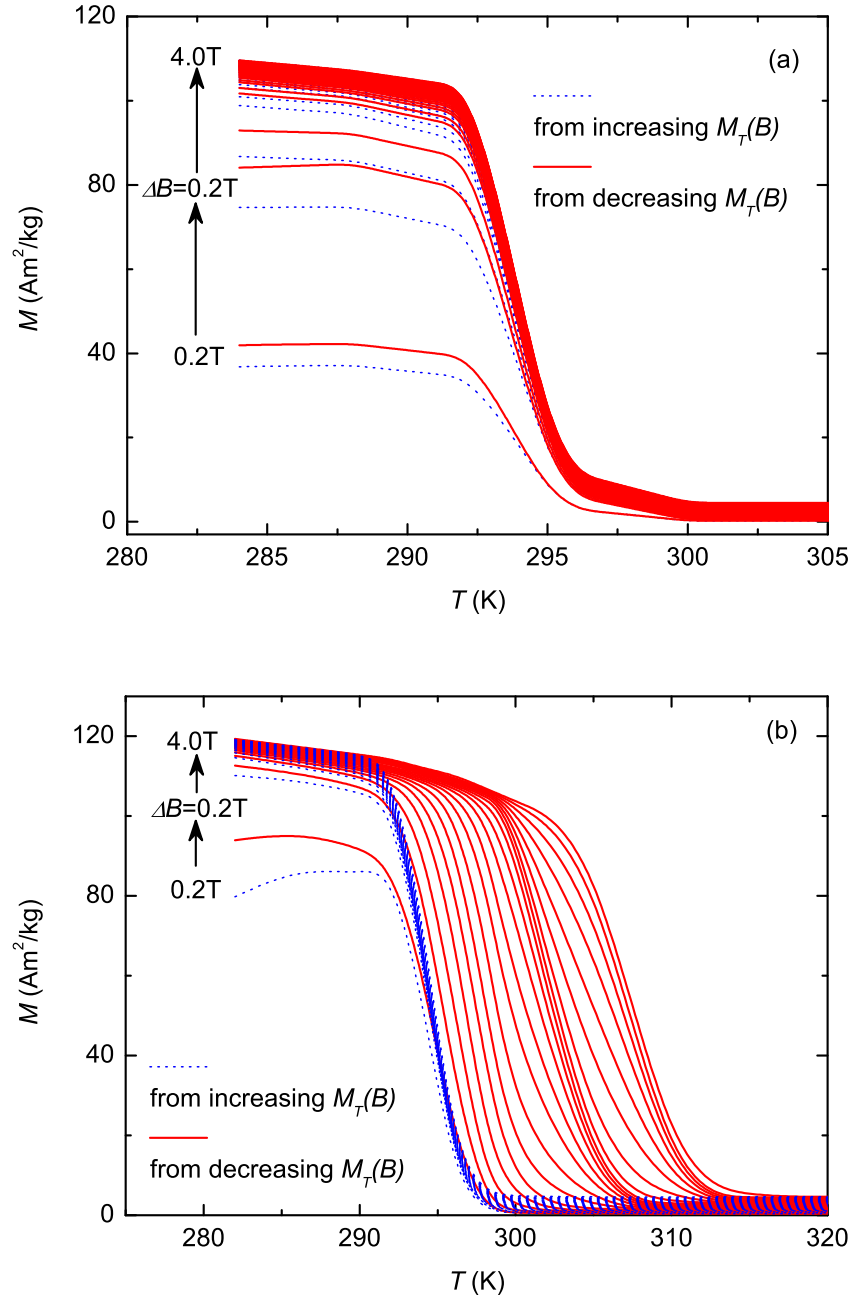
Figure 7.8: Converted isofield magnetization curves from isothermal magnetization data for $Mn_{0.99}Fe_{0.01}As$. (a) obtained from the data of figure 7.6(a). (b) obtained from the data of figure 7.6(b).
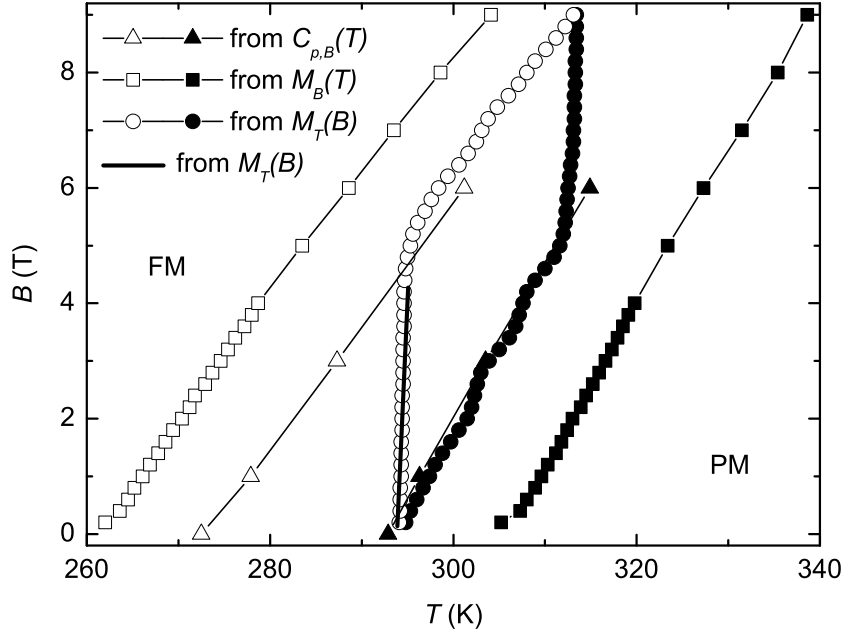
Figure 7.9: Magnetic phase diagram of $Mn_{0.99}Fe_{0.01}As$. Square and triangular symbols represent the transition temperatures obtained from isofield magnetization and heat-capacity data, respectively. The thick line and circle symbols denote the transition temperatures obtained from isothermal magnetization data measured following protocol 1 with maximum fields of 4 T and 9 T, respectively. Thin lines are guides to the eye.

● $\mathbf{Mn_{0.985}Fe_{0.015}As}$

Figure 7.10 shows the isofield magnetization as a function of temperature measured on heating and cooling for $Mn_{0.985}Fe_{0.015}As$. They are very similar to those of $Mn_{0.994}Fe_{0.006}As$ and $Mn_{0.99}Fe_{0.01}As$ but with larger hysteresis and lower transition temperatures. The transition temperatures on cooling and heating increase from 245 K and 285 K to 291 K and 322 K when the applied field changes from 0.02 T to 9 T, respectively.

7.3.4 Heat capacity

A remarkable behavior known as the virgin effect is observed in $Mn_{0.985}Fe_{0.015}As$ when performing heat-capacity measurements on a fresh sample. This effect is represented by the heat-capacity curves displayed in figure 7.11. The heat-capacity measurements were carried out following a sequence of (1), (2), (3),
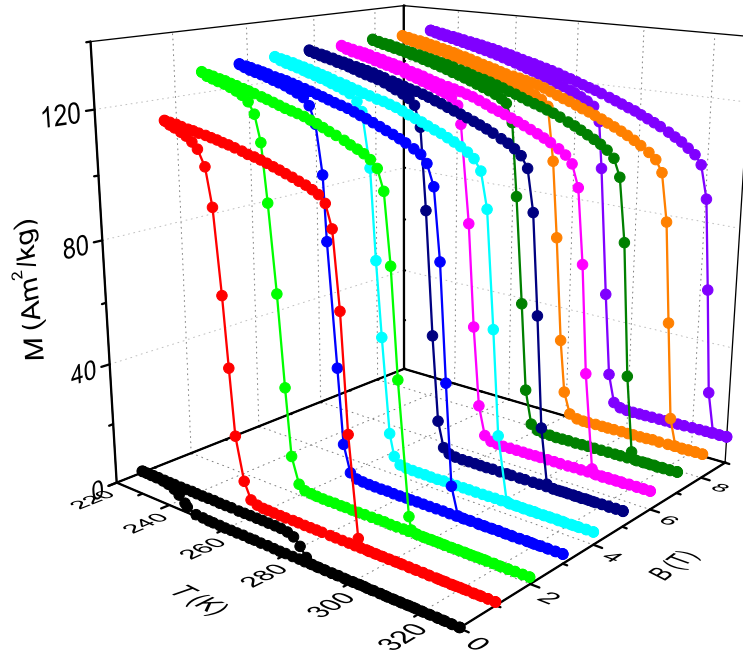
Figure 7.10: Temperature dependence of the magnetization measured at constant magnetic fields of 0.02 T, 1 T, 2 T, 3 T, 4 T, 5 T, 6 T, 7 T, 8 T and 9 T on heating and cooling for $Mn_{0.985}Fe_{0.015}As$.

(4) and (5). The first heating run of the heat capacity at zero field shows a sharp anomaly at 209 K, and no more anomalies are observed below 350 K. The anomaly is completely reproducible in a subsequent heating run at zero field. The sharp anomaly implies the occurrence of a temperature-induced FOPT. No obvious hysteretic behavior was detected at the transition. By applying a magnetic field of 6 T, a reproducible anomaly occurs at 303 K in the heat capacity on heating. After that, there is no anomalous heat capacity around 209 K at zero field while a new sharp anomaly happens at 281 K on heating. The new anomaly can be reproduced in the later heating runs at zero field, simultaneously, accompanied by a large thermal hysteresis.

The virgin effect observed in $Mn_{0.985}Fe_{0.015}As$ is different from that of MnFe(P,Si,Ge) compounds [50, 109], in which the virgin effect can be eliminated by the first cooling run at zero field. The virgin effect in the present compound is not influenced by the first cooling process at zero field, but it is removed by performing a heating or cooling process at a field of 6 T. This behavior can be understood with the help of the earlier work of Fjellvåg *et al.* [155]. According to the compositional and magnetic phase diagram built by Fjellvåg *et al.* (the inset of figure 7.11), the content of Fe $x = 0.015$ lies just
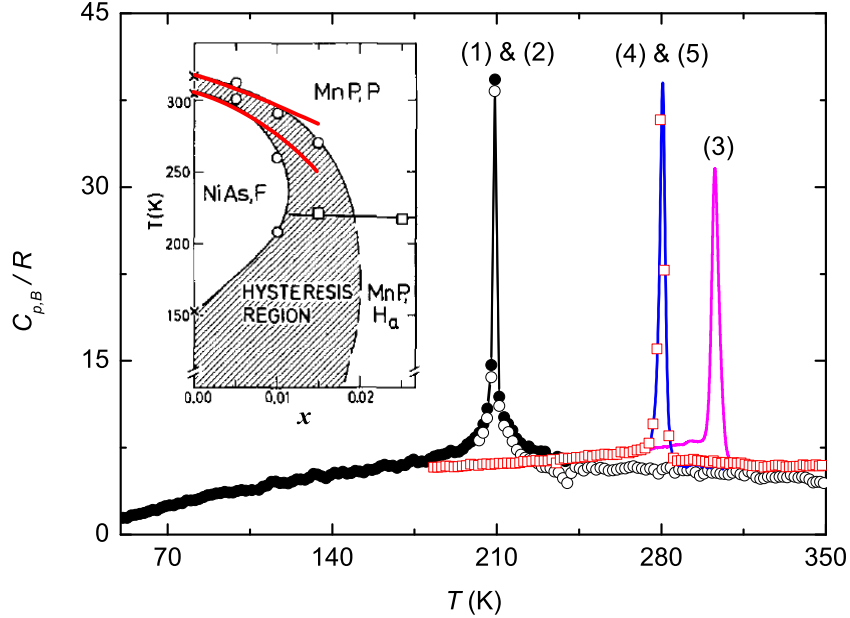
Figure 7.11: Temperature dependence of the heat capacity for $Mn_{0.985}Fe_{0.015}As$. (1) and (2) the first and second heating runs at zero field for as-prepared sample. (3) subsequent heating run at a constant magnetic field of 6 T. (4) and (5) subsequent heating runs at zero field. Inset shows structural and magnetic phase diagram for $Mn_{1-x}Fe_xAs$ ($0 \leq x \leq 0.02$) taken from Ref. [155]. Red lines represent the modified phase diagram after removing the virgin effect.

at the hysteretic region between the FM hexagonal NiAs-type structure and the helimagnetic (HM) orthorhombic MnP-type structure. The as-prepared sample (quenched) crystalizes in a metastable orthorhombic MnP-type structure, and has a magnetoelastic transition at 209 K between the HM and PM phases. On thermal cycling, it is impossible to cross the transition line (the inner curve in the inset of figure 7.11), and to change the structure to the FM hexagonal NiAs-type, since the composition $x = 0.015$ lies outside of the stability region of the hexagonal structure. The maximum temperature (350 K) of the calorimeter is not enough to anneal and convert it to the stable phase. But an applied magnetic field can make the FM phase more stable (because the free energy term, $-MB$, is negligible in HM phase and small in PM phase), expanding the NiAs-type region. After removing the magnetic field, the phase diagram is modified, represented with the red lines in the inset of figure 7.11.

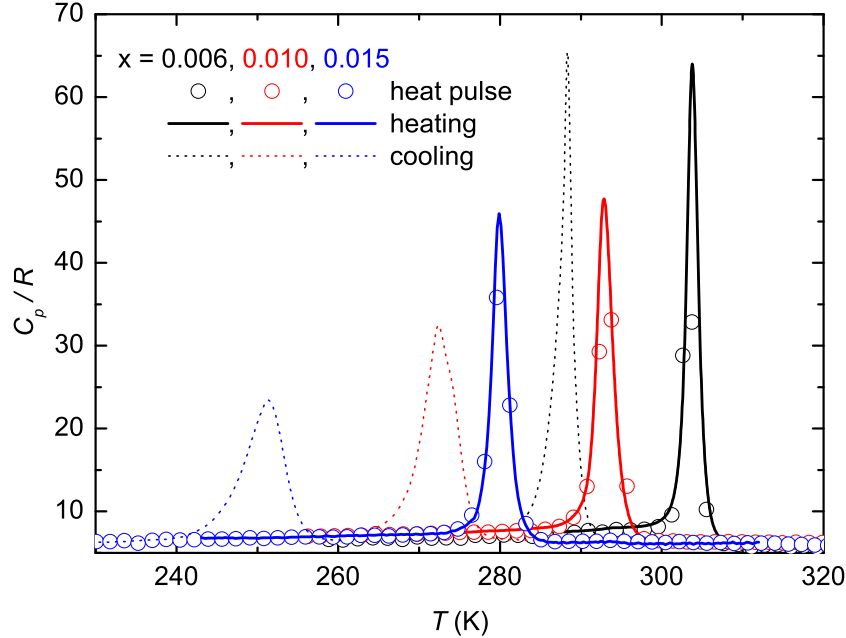Figure 7.12 shows the temperature dependence of the heat capacity mea-

Figure 7.12: Temperature dependence of the heat capacity measured at zero field on heating (solid lines) and cooling (dotted lines) for the $Mn_{1-x}Fe_x$As compounds. Symbols: measured with the heat-pulse method. Solid and dotted lines: measured with thermogram technique.

sured at zero field on heating and cooling for the $Mn_{1-x}Fe_x$As compounds. The heat-capacity data obtained with the heat-pulse method are in good agreement with those obtained from a heating thermogram for each compound. The presence of sharp peaks and thermal hysteresis in the heat-capacity curves reveals the occurrence of FOPTs in the studied compounds. With an increase of Fe content, the transition temperature decreases while the hysteresis increases, which agrees with that observed in the magnetization measurements. Taking the temperature of the heat-capacity maximum as the transition temperature, the obtained transition temperatures at zero field on cooling and heating are 288 K and 304 K, 273 K and 293 K, 251 K and 280 K, for $x = 0.006$, 0.01 and 0.015, respectively. They are higher / lower than those obtained from the isofield magnetization measurements on cooling / heating, as shown in figure 7.9 in the case of $x = 0.01$. In addition, the heat-capacity peaks are broadened and lowered with increasing x, which is probable an indication of more compositional inhomogeneity in the compounds with higher x.

The plots of the heat capacity as a function of temperature measured at dif-

ferent constant magnetic fields for the $Mn_{1-x}Fe_xAs$ compounds are displayed in figures 7.13(a), 7.13(b) and 7.13(c). In each compound, the anomaly moves to higher temperatures, meanwhile, the magnitude of hysteresis is slightly reduced with increasing magnetic field, that is consistent with those found in the isofield magnetization measurements.

According to the method described in section 2.4, the transition enthalpy ΔH and the transition entropy ΔS have been calculated from the heat-capacity data. The resulting values are listed in table 7.1. In absence of magnetic field, the values of ΔH and ΔS determined from the heat-capacity data agree well with those obtained from the DSC measurements. The magnitudes of ΔH and ΔS are reduced by an increase of x or magnetic field. For the same magnetic field, the values of ΔH and ΔS on cooling are higher than those on heating. The high values of ΔH and ΔS are associated with the GMCEs in the $Mn_{1-x}Fe_xAs$ compounds.

Figures 7.14(a) and 7.14(b) show the total enthalpy and total entropy calculated from the heat capacity at constant magnetic fields of 0 and 6 T on heating and cooling, respectively, for $Mn_{0.994}Fe_{0.006}As$. At each constant field, the heating and cooling curves of enthalpy or entropy have been adjusted to be equal at a temperature well above the transition temperature (in PM phase). As a result, some differences are observed at temperatures below the transition temperature (in FM phase). The size of the differences is almost independent of temperature in the FM phase.

It is well-known that, enthalpy and entropy, both are thermodynamic state functions, therefore, the enthalpy or entropy of an initial state is completely recovered when a temperature loop is performed at constant external pressure and magnetic field. However, a difference of the enthalpy between the heating and cooling curves is observed in the FM phase (denoted with a pair of arrows) at both zero field and nonzero field in figure 7.14(a). A difference is also found in the entropy curves in figure 7.14(b). The difference of the enthalpy should be ascribed to the experimental errors due to the imperfect control of the heat exchange. It amounts to the total heat gained or lost but not computed during the measurement. The errors are found to be $\sigma_{0T} = 0.45$ J/g at 275 K and $\sigma_{6T} = 0.32$ J/g at 294 K at 0 and 6 T, respectively. These errors mainly originate from the experimental determination of ΔH at the FOPT, therefore, the relative errors are expressed as $\sigma_B/(\Delta H_{h,B} + \Delta H_{c,B})$, being 2.7 % and 2.2 % at 0 and 6 T, respectively. The differences between the heating and cooling entropy curves are found to be $(\sigma + \delta)_{0T} = 3.3$ J/kg·K (5.8 %) at 275 K and $(\sigma + \delta)_{6T} = 1.8$ J/kg·K (4.0 %) at 294 K at 0 and 6 T, respectively. The larger difference of the entropy curves is an combination of the experimental error σ and the error δ due to irreversibility. According to equations (2.71)
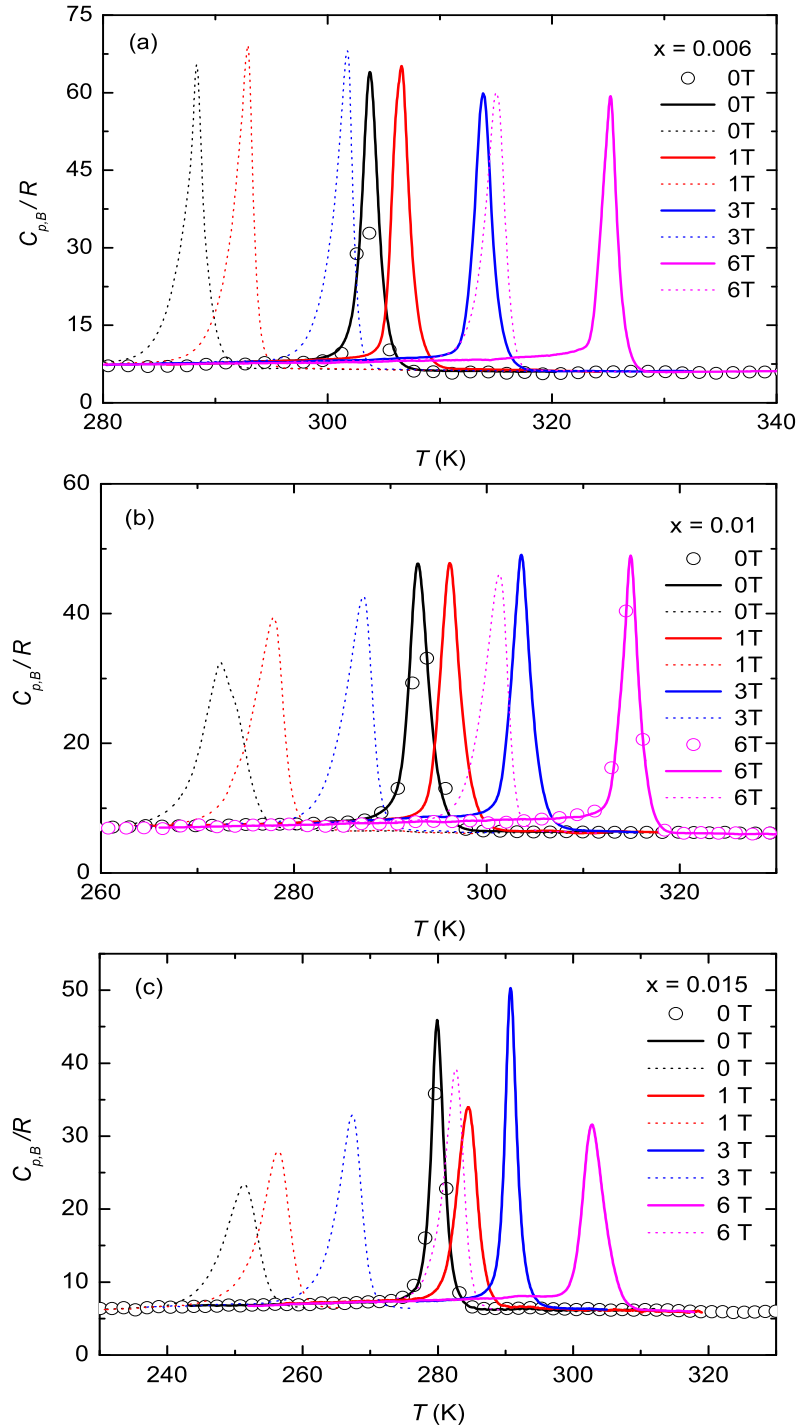
Figure 7.13: Temperature dependence of the heat capacity measured at constant magnetic fields of 0, 1 T, 3 T and 6 T on heating (solid lines) and cooling (dotted lines) for the $Mn_{1-x}Fe_xAs$ compounds. Open symbols denote the heat capacity obtained with the heat-pulse method.
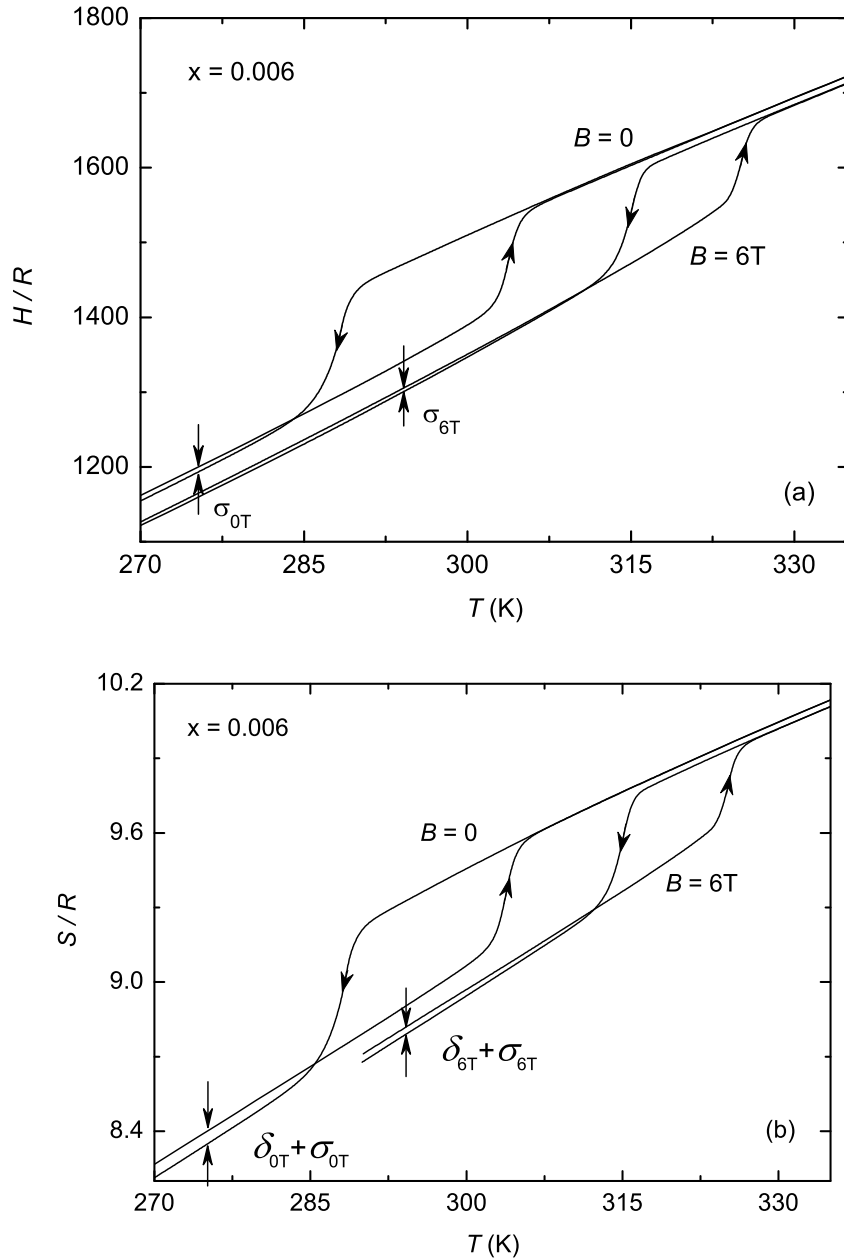
Figure 7.14: (a) Enthalpy and (b) entropy as functions of temperature on heating and cooling for Mn$_{0.994}$Fe$_{0.006}$As, obtained from the heat capacity at constant magnetic fields of 0 and 6 T, respectively. Vertical arrows indicate the differences between the heating and cooling curves.

Table 7.1: Transition temperature, transition enthalpy and transition entropy of the $Mn_{1-x}Fe_xAs$ compounds obtained at different constant magnetic fields.

Compounds	B	$T_{t,h}$	ΔH_h	ΔS_h	$T_{t,c}$	ΔH_c	ΔS_c
	(T)	(K)	(J/g)	(J/kg·K)	(K)	(J/g)	(J/kg·K)
$x = 0.006$	0	304*	7.7*	25.3*	284*	9.9*	34.8*
	0	303.8	7.6	25.0	288.3	9.3	32.2
	1	306.6	7.4	24.1	292.9	9.2	31.4
	3	313.9	7.2	22.9	301.7	9.1	30.2
	6	325.2	6.0	18.5	315.0	8.4	26.7
$x = 0.01$	0	293*	7.4*	25.2*	267*	9.3*	34.8*
	0	292.9	7.4	25.3	272.5	8.8	32.3
	1	296.2	7.2	24.3	277.8	8.8	31.7
	3	303.6	6.9	22.7	287.2	8.6	29.9
	6	314.9	6.3	20.0	301.3	8.1	26.9
$x = 0.015$	0	279*	6.8*	24.4*	249*	7.9*	31.7*
	0	279.9	6.8	24.3	251.3	7.6	30.2
	1	284.5	7.1	25.0	256.2	7.9	30.8
	3	290.7	6.8	23.4	267.3	8.1	30.3
	6	302.8	6.7	22.1	282.7	7.8	27.6

* obtained from DSC measurement.

Indexes h and c denote heating and cooling processes, respectively.

and (2.72), the values of δ are evaluated to be 2.6 % and 1.6 % at 0 and 6 T, which are in good agreement with 3.1 % (1.8 J/kg·K) and 1.8 % (1.0 J/kg·K) found in the experimental data, respectively. Moreover, the value $\delta_{6T} = 1.0$ J/kg·K indicates that $|\Delta S_T|$ determined from the heat-capacity data will be overestimated by the amount 0.5 J/kg·K on cooling and underestimated by the amount 0.5 J/kg·K on heating, assuming that the dissipated energies in the heating and cooling processes are equal.

7.3.5   Magnetocaloric effect

We have employed different methods to determine the magnetocaloric parameters ΔS_T and ΔT_S for the $Mn_{1-x}Fe_xAs$ compounds. The values of ΔS_T were determined by means of isofield magnetization, isothermal magnetization, isofield heat-capacity and direct measurements. The values of ΔT_S were determined from the isofield heat-capacity and direct measurements.

- **$Mn_{0.994}Fe_{0.006}As$**

In figures 7.15(a) and 7.15(b), we present the temperature dependence of the isothermal entropy change obtained from the isothermal magnetization data of figure 7.4(a) using the Maxwell relation, for $Mn_{0.994}Fe_{0.006}As$. As the isothermal magnetization measurements were carried out following protocol 1 on increasing and decreasing fields with a maximum field of 9 T, the presence of the two-steps-like magnetization curves in the TPC region leads to the "spike" effect in the results of ΔS_T. The spurious peak with a maximum $-\Delta S_{T,\max}$ = 124 J/kg·K for a field change of 9 T is observed at 305 K in figure 7.15(a). One can see that the maximum of the "spike" is proportional to the magnetic field for fields below a threshold field of 5 T, above which the "spike" does not increase anymore. That agrees with the description in section 4.4. The present maximum of the "spike" is much smaller than 230 J/kg·K reported by Campos *et al.* [32]. It should be due to the fact that a smaller temperature interval of 0.3 K between two adjacent isothermal magnetization curves was employed in Ref. [32] in the TPC region, while it was set to be 1 K in our experiments. It is known from section 4.4 that the magnitude of the "spike" for sharp transitions is inversely proportional to the temperature interval.

According to equation (4.10), the maximum of the "spike" is limited to a finite value. Taking the experimental heat capacity $C_{an,0T}(T_t) - C_{nor,0T}(T_t) =$ $57R$ at $T_t = 303.8$ K, the magnetization change $M_{FM} - M_{PM} = 108$ Am^2/kg, the transition enthalpy $\Delta H_{0T} = 7.6$ J/g, and the threshold field $B_{th,in} = 5$ T, the predicted maximum value of the extra contribution to the spurious peak is $|\Delta S_{extra}| = 259$ J/kg·K. The maximum is slightly higher than 230 J/kg·K reported in Ref. [32], the latter value includes the extra contribution of the "spike" effect and the normal ΔS_T. On decreasing field, the "spike" effect is weak, because a large temperature interval of 6 K was used in the measurements. A spurious spike with a maximum of $-\Delta S_{T,\max} = 38$ J/kg· is observed at 329 K for a field change of 9 T in figure 7.15(b). The "spike" effect is not obvious for the other field changes.

Figures 7.16(a) and 7.16(b) show the temperature dependence of the isothermal entropy change derived from the magnetization data of figure 7.4(b) for $Mn_{0.994}Fe_{0.006}As$. The measurement, which has been measured following protocol 2, avoids the presence of the two-steps-like magnetization curves, leading to a considerable reduction of the "spike" effect on increasing field, but not on decreasing field. Nearly the same plots of ΔS_T as those shown in figure 7.15(b) are found for decreasing field. The maximum $-\Delta S_{T,\max} = 28.5$ J/kg·K was obtained for a field change from 0 to 9 T at 293.8 K, however, the MCE is very small ($\sim$4.0 J/kg·K) at this temperature in figure 7.15(a). For decreasing field, taking no account of the "spike" effect, the maximum is found to be $-\Delta S_{T,\max} = 32.8$ J/kg·K for a field change of 9 T. As we discussed in chapter 4, the Maxwell relation overestimates / underestimates $|\Delta S_T|$ on decreasing /
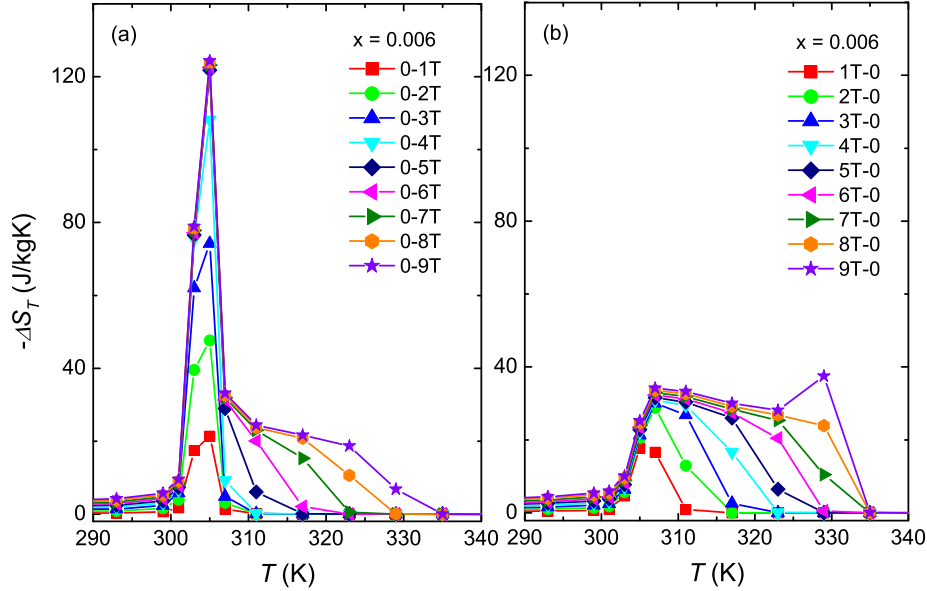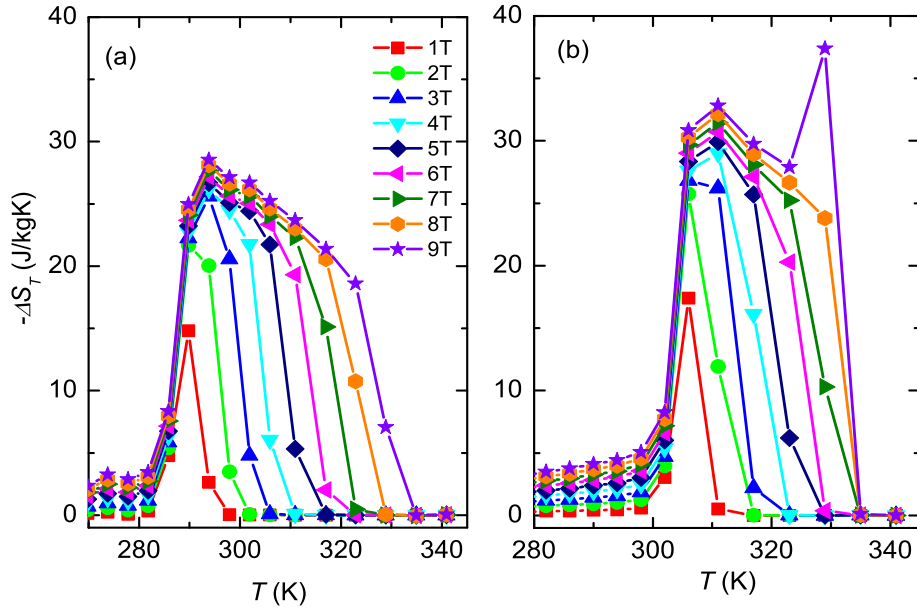
Figure 7.15: Temperature dependence of the isothermal entropy change deduced from isothermal magnetization data measured following protocol 1 for $Mn_{0.994}Fe_{0.006}As$. (a) on increasing field. (b) on decreasing field.

increasing field due to irreversibility. According to the isothermal magnetization loops shown in figure 7.4(b), the correction term $dA/dT = -4.5$ J/kg·K was obtained. It is about 15 % of the $-\Delta S_{T,\max} = 32.8$ J/kg·K. Eventually, for a field change of 9 T, the maximum $-\Delta S_{T,\max}$ is found to be 33.0 J/kg·K on increasing field, and 28.3 J/kg·K on decreasing field. It can be seen that the original Maxwell relation gives a larger $-\Delta S_{T,\max}$ on increasing field than on decreasing field, but just the opposite after the correction. The corrected values agree with those obtained from the heat capacity (seen below).

Moreover, in figures 7.16(a) and 7.16(b), the absolute values of ΔS_T at 311 K are found to be 23.7 J/kg·K for a field change from 0 to 9 T and 32.8 J/kg·K for a field change from 9 T to 0. With a maximum field of 9 T, the transition at 311 K may be completed on both increasing field and decreasing field. The true entropy changes should be exactly the same on increasing and decreasing fields since the entropy is a state function. Taking into account the correction dA/dT, the resulting $|\Delta S_T| = 28.2$ J/kg·K on increasing field coincides very well with the value 28.3 J/kg·K on decreasing field. The coincidence between the corrected ΔS_T values on increasing and decreasing fields supports the accuracy of the correction due to the irreversibility.

The ΔS_T values of $Mn_{0.994}Fe_{0.006}As$ were also calculated from the isofield

Figure 7.16: Temperature dependence of the isothermal entropy change deduced from isothermal magnetization data measured following protocol 2 for $Mn_{0.994}Fe_{0.006}As$. (a) on increasing field. (b) on decreasing field.
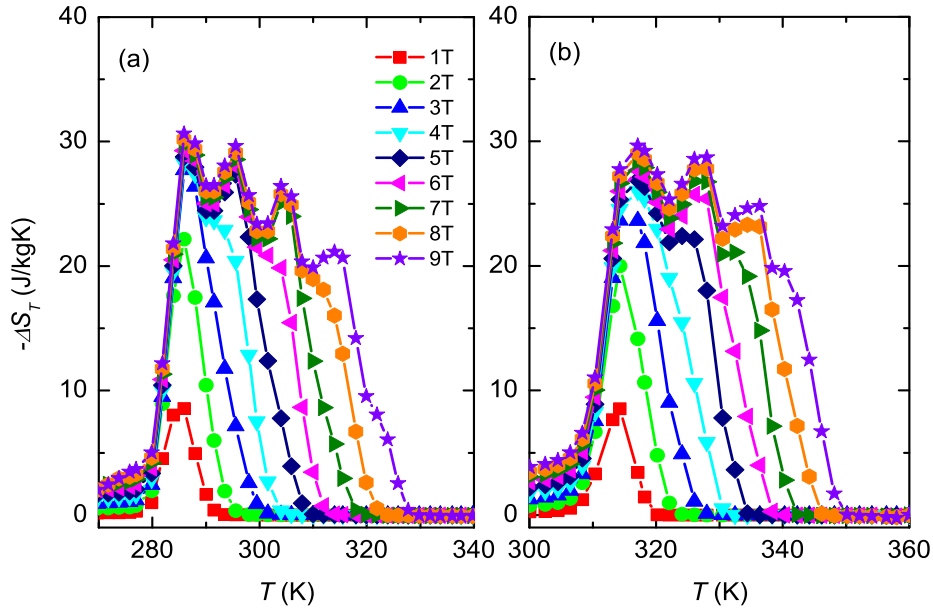
Figure 7.17: Temperature dependence of the isothermal entropy change deduced from isofield magnetization data for $Mn_{0.994}Fe_{0.006}As$. (a) on cooling. (b) on heating.
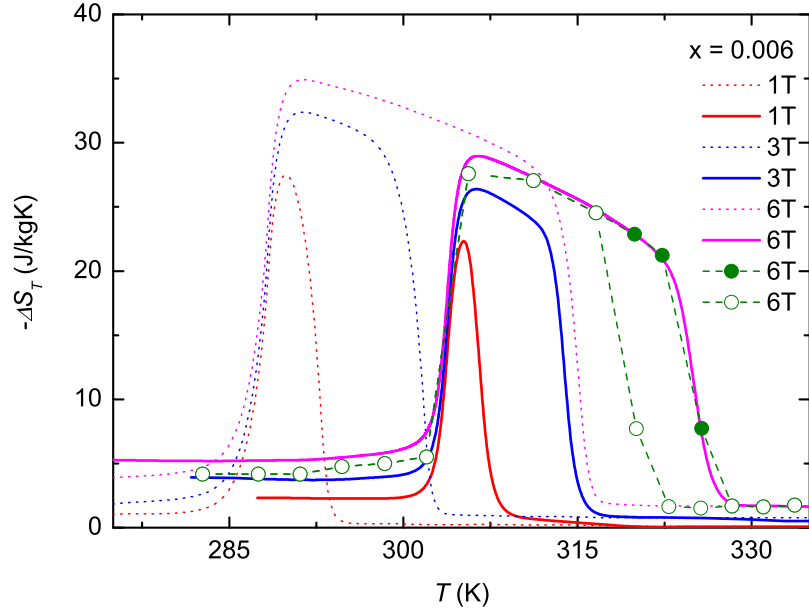
Figure 7.18: Temperature dependence of the isothermal entropy change for $Mn_{0.994}Fe_{0.006}As$. Solid lines: obtained from heat capacity on heating. Dotted lines: obtained from heat capacity on cooling. Dashed lines are guides to the eye. Solid and open symbols represent ΔS_T obtained from direct measurements performed following protocols 3 and 4, respectively.

magnetization data displayed in figure 7.3. The results are plotted in figures 7.17(a) and 7.17(b) for cooling and heating processes, respectively. The fluctuation of ΔS_T at high fields in the transition region is due to the fact that the isofield magnetization curves have been measured with a field interval of 1 T which is so large that the calculation of equation (4.3) is not precise. Smooth ΔS_T curves may be obtained when the measurement is carried out with a small field interval. The same correction of the irreversibility as in the isothermal magnetization data also has to be made in these data.

Figure 7.18 shows the temperature dependence of the isothermal entropy change determined from direct measurements (symbols), and from heat capacity on heating (solid lines) and cooling (dotted lines) for $Mn_{0.994}Fe_{0.006}As$. It has to be pointed that the direct measurements have been carried out following protocol 3 at some measuring temperatures in the hysteretic region (solid symbols), where the fraction of FM phase is temperature and field dependent. The use of protocol 4 results in only a small amount of FM phase in the sample at these temperatures under a field of 6 T, leading to the small values of

ΔS_T (open symbols). In this case, the corrections of irreversibility are small in ΔS_T derived from both heat-capacity and direct measurements. According to equations (2.75), (2.77) and (4.8), for a field change of 6 T, the corrections are evaluated to be 0.3 J/kg·K on heating and 0.4 J/kg·K on cooling in the heat-capacity measurements, and 0.6 J/kg·K on decreasing field in the direct measurement. In the temperature range from 306 K to 310 K where an applied field of 6 T can complete the transition on both increasing field and decreasing field, the ΔS_T curves on heating and cooling, in principle, should overlap. The difference between ΔS_T on heating and cooling is found to be 0.8 J/kg·K which agrees well with the sum of the calculated corrections 0.7 J/kg·K. Consequently, the directly measured ΔS_T exhibits a perfect agreement with that obtained from heat capacity on heating. We obtained the maxima $-\Delta S_{T,\max}$ being 34.5 J/kg·K and 28.6 J/kg·K for a field change of 6 T on cooling and heating, respectively. These values agree with those obtained from the isothermal magnetization data measured following protocol 2.

In addition, the ΔS_T values show a good coincidence between those obtained from heat-capacity and direct measurements in the PM phase in figure 7.18. However, the $|\Delta S_T|$ values derived from the heat capacity on heating are about 0.9 J/kg·K higher than those determined from the direct measurements in the FM phase. In other words, the ΔS_T values derived from heat capacity on heating have been overestimated by the amount 0.9 J/kg·K when we consider ΔS_T in the direct measurement as the reference results because of their small experimental errors. That agrees well with the total error $[(\sigma + \delta)_{0T} - (\sigma + \delta)_{6T}]/2 = 0.8$ J/kg·K observed in figure 7.14(b).

In figure 7.19 we present the adiabatic temperature change as a function of temperature for $Mn_{0.994}Fe_{0.006}As$ derived from direct and heat-capacity measurements. In the hysteretic region, the direct measurements were carried out following protocol 2 at the temperatures marked with arrows. A good agreement between ΔT_S derived from the direct measurement and that calculated from the heat capacity on cooling is observed except for few points near the maximum for a field change of 6 T which can be ascribed to the experimental errors. Unlike the plots of ΔS_T, the height and the width of the ΔT_S plots are proportional to the magnetic field. The maxima $\Delta T_{S,\max}$ for a field change of 6 T are found to be 16.4 K and 20.1 K on heating and cooling, respectively.

• **$Mn_{0.99}Fe_{0.01}As$**

Figure 7.20 shows the plots of the isothermal entropy change for $Mn_{0.99}Fe_{0.01}As$ derived from the magnetization data of figure 7.6(a). Similar magnetizing and demagnetizing curves lead to the overlapped ΔS_T curves. For the present compound, a maximum applied field of 4 T corresponds to more or less B_2 in figure 4.1, therefore, overlapped ΔS_T curves on increasing and decreasing
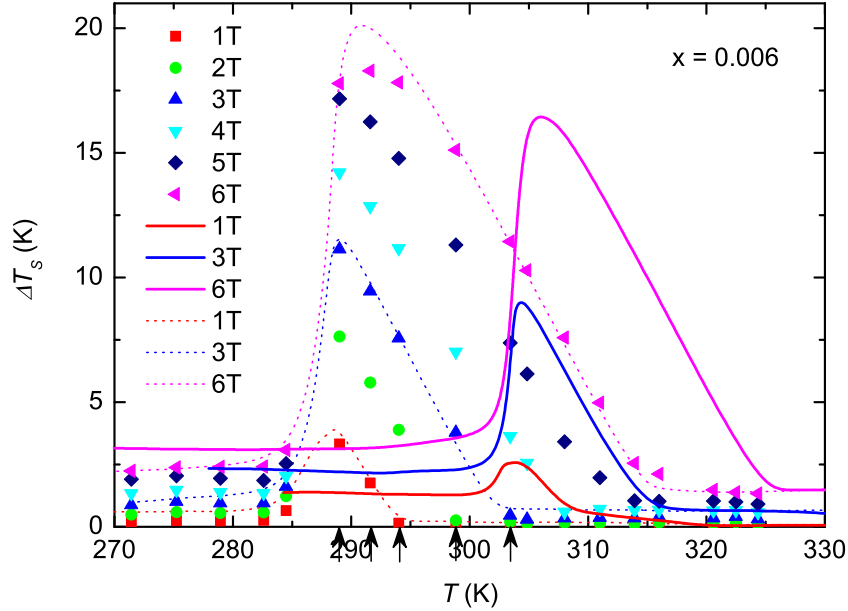
Figure 7.19: Temperature dependence of the adiabatic temperature change for $Mn_{0.994}Fe_{0.006}As$. Symbols: obtained from direct measurements. Solid lines: obtained from heat capacity on heating. Dotted lines: obtained from heat capacity on cooling. At arrowed temperatures, the direct measurements have been carried out following protocol 2.

fields are obtained at $T_2 = 293$ K. The observed peaks of ΔS_T are mainly attributed to the "spike" effect. The maximum, $-\Delta S_{T,\max} = 115$ J/kg·K, agrees with the estimated value $|\Delta S_{extra}| = 119$ J/kg·K using equation (4.9). The contributions to the true ΔS_T in figure 7.20 are approximately the MCEs in the FM and PM phases.

When we use the magnetization data extracted for a partial range (0 - 4 T and 4 T - 0) from those measured with a maximum field of 9 T, the resulting plots of ΔS_T are different from those of figure 7.20 on decreasing field. As seen in figure 7.21, lower and broader ΔS_T curves, rather than sharp peaks, are observed on decreasing field, while the curves with the same magnitude and position as those of figure 7.20 are found on increasing field. These characteristics of the ΔS_T curves are related to the absence and presence of the field-induced transitions in figures 7.6(a) and 7.6(b). According to the discussions made in section 4.4, the maximum field 9 T is a field between B_2 and B_{crit}, and the field 4 T is lower than $B_{th,de} = 5$ T (see figure 7.9). Therefore, on decreasing field, there is no "spike" effect for all the field changes smaller than 4 T, as given by equation (4.12). For a field change from 4 T to 0, a maximum
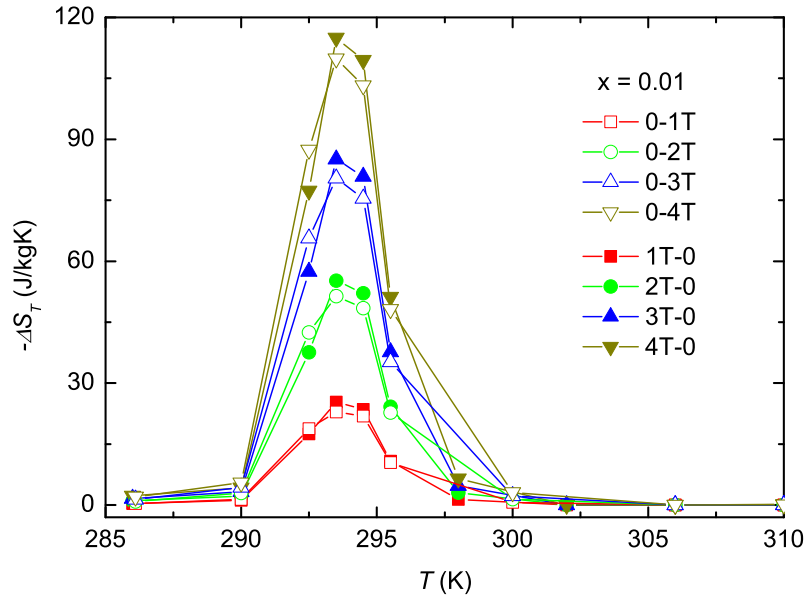
Figure 7.20: Temperature dependence of the isothermal entropy change obtained from isothermal magnetization data measured following protocol 1 with a maximum magnetic field of 4 T for $Mn_{0.99}Fe_{0.01}As$.
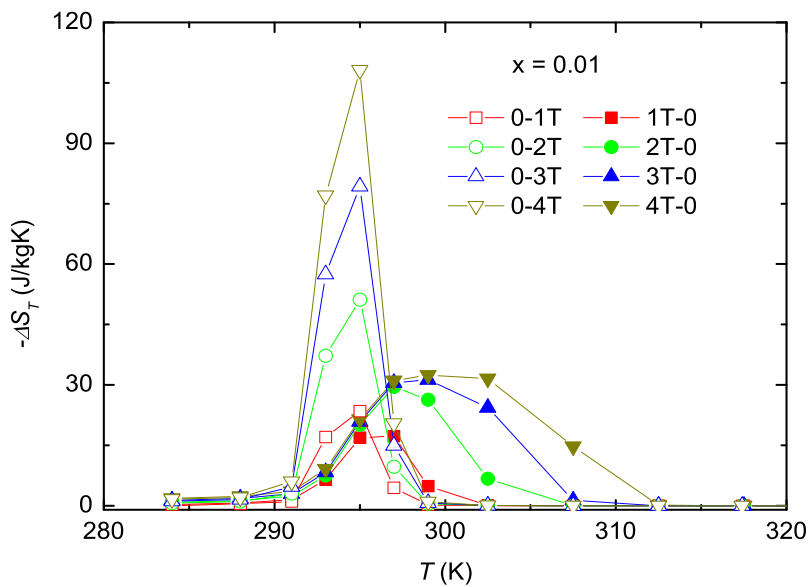
Figure 7.21: Temperature dependence of the isothermal entropy change obtained from isothermal magnetization data measured following protocol 1 with a maximum magnetic field of 9 T for $Mn_{0.99}Fe_{0.01}As$.
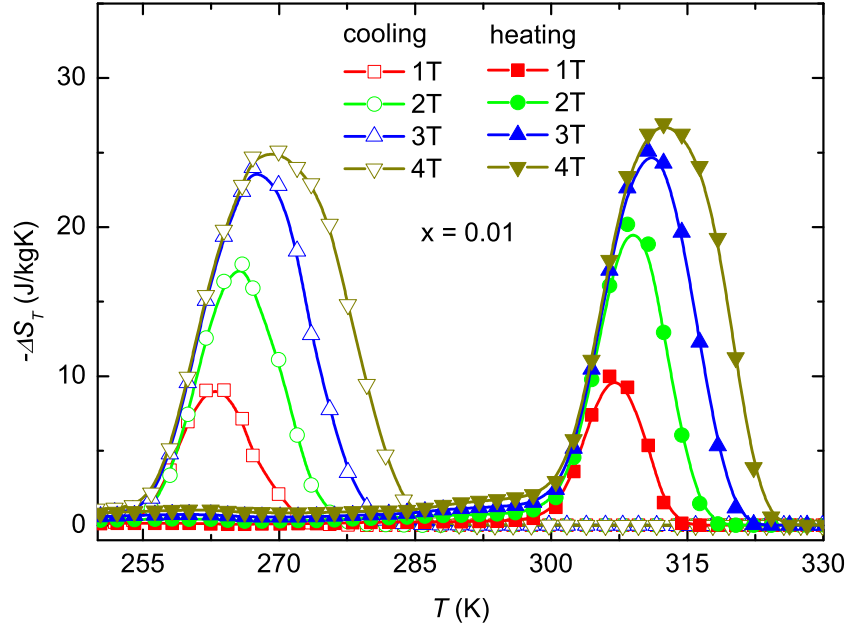
Figure 7.22: Temperature dependence of the isothermal entropy change obtained from isofield magnetization data for $Mn_{0.99}Fe_{0.01}As$.

of $-\Delta S_{T,\text{max}} = 32.4$ J/kg·K at 299 K is found in the present compound. The correction term of the irreversibility is evaluated to be $dA/dT = -6.0$ J/kg·K (about 20 % of $\Delta S_{T,\text{max}}$) on the basis of the isothermal magnetization loops (the complete data of figure 7.6(b)). Although the area of the magnetization loop for 4 T would be much smaller than that for 9 T, we can assume that the values of the derivative dA/dT for the two fields are approximately the same. Thus, the corrected value $-\Delta S_{T,\text{max}} = 26.4$ J/kg·K was obtained for a field change from 4 T to 0.

Figure 7.22 shows the isothermal entropy change as a function of temperature calculated from the isofield magnetization data of figure 7.5 on heating and cooling for $Mn_{0.99}Fe_{0.01}As$. Taking into account the same correction of irreversibility as in the isothermal magnetization data, i.e. adding the amount 6 J/kg·K to the maximum of $|\Delta S_T|$ on cooling and subtracting the same amount from the maximum of $|\Delta S_T|$ on heating, the resulting maxima, $-\Delta S_{T,\text{max}} = 31.1$ J/kg·K at 270 K on cooling and $\Delta S_{T,\text{max}} = 20.9$ J/kg·K at 312 K on heating, were obtained for a field change of 4 T.

Figure 7.23 shows the temperature dependence of the isothermal entropy change determined from direct measurements (symbols), and from heat ca-
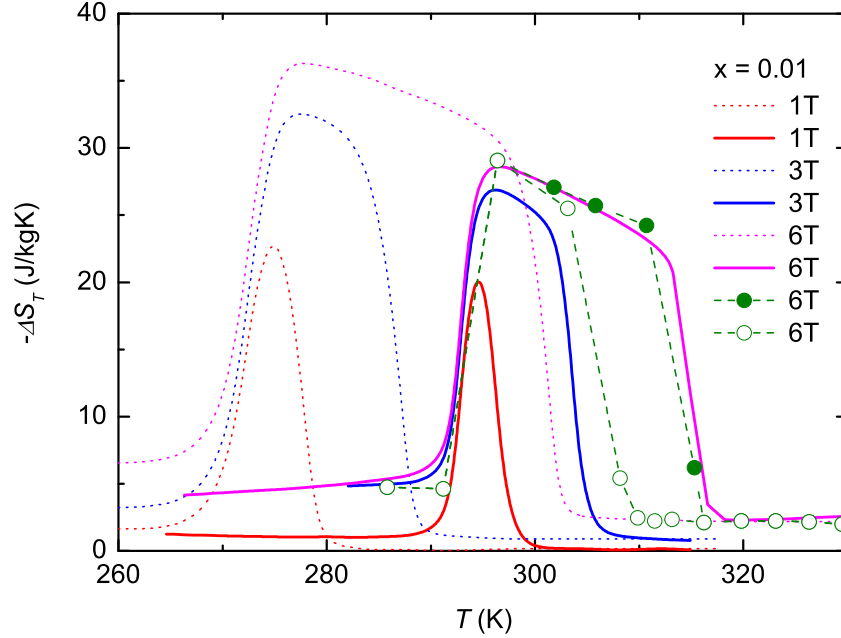
Figure 7.23: Temperature dependence of the isothermal entropy change obtained from heat-capacity and direct measurements for $Mn_{0.99}Fe_{0.01}As$. Solid lines: from heat capacity on heating. Dotted lines: from heating capacity on cooling. Dashed lines are guides to the eye. Solid and open symbols represent ΔS_T determined from direct measurements performed following protocols 3 and 4, respectively.

pacity on heating (solid lines) and cooling (dotted lines) for $Mn_{0.99}Fe_{0.01}As$. The points marked as solid symbols were measured following protocol 3, leading to a good agreement between the values of ΔS_T obtained from the heat capacity on heating and from direct measurements. For a field change of 6 T, the corrections of irreversibility are estimated to be 0.5 J/kg·K on heating and 0.6 J/kg·K on cooling in the heat-capacity measurement (about 2 % of $\Delta S_{T,\max}$), and 0.8 J/kg·K in the direct measurement on decreasing field (about 3 % of $\Delta S_{T,\max}$). The resulting maxima $-\Delta S_{T,\max}$ are 35.8 J/kg·K at 277 K and 29.2 J/kg·K at 297 K on cooling and heating, respectively. In the direct measurement on decreasing field, the correction of irreversibility is found to be 0.8 J/kg·K (about 3 % of $\Delta S_{T,\max}$). The resulting maximum $-\Delta S_{T,\max}$ = 29.8 J/kg·K at 296 K agrees with that derived from the heat capacity on heating, as well as with $-\Delta S_{T,\max}$ = 29.4 J/kg·K obtained from the isothermal magnetization data on decreasing field.

Shown in figure 7.24 is the adiabatic temperature change as a function of
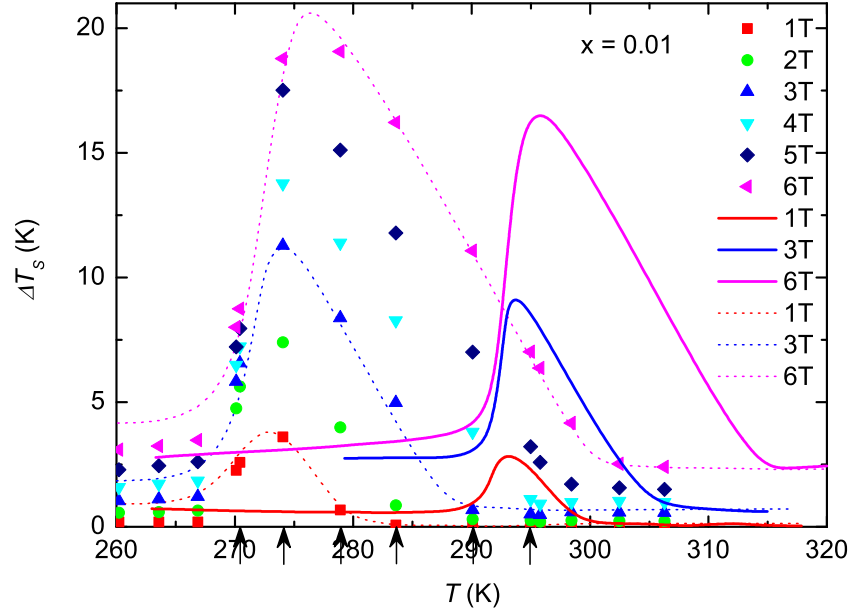
Figure 7.24: Adiabatic temperature change as a function of temperature for $Mn_{0.99}Fe_{0.01}As$. Symbols: obtained from direct measurements. Solid lines: obtained from heat capacity on heating. Dotted lines: obtained from heating capacity on cooling. At arrowed temperatures, the direct measurements have been carried out following protocol 2.

temperature for $Mn_{0.99}Fe_{0.01}As$. In the direct measurements, the temperatures marked by arrows were measured following protocol 2. The characteristics of the ΔT_S plots of $Mn_{0.99}Fe_{0.01}As$ are quite similar to those of $Mn_{0.994}Fe_{0.006}As$ but shifted to lower temperatures. The ΔT_S data obtained from the heat-capacity and direct measurements show a good coincidence. The maxima of ΔT_S, for a field change of 6 T, are found to be 16.5 K and 20.6 K on heating and cooling, respectively.

• **$Mn_{0.985}Fe_{0.015}As$**

The isothermal entropy changes of $Mn_{0.985}Fe_{0.015}As$ derived from isofield magnetization data are shown in figures 7.25(a) and 7.25(b) for cooling and heating processes, respectively. The results obtained from heat-capacity and direct measurements are shown in figure 7.26. The corrections of irreversibility in the present compound are evaluated to be 0.6 J/kg·K on heating and 0.7 J/kg·K on cooling in the heat-capacity measurements. The isothermal magnetization loops were not measured for this compound, but the corrections are expected to be no less than 6 J/kg·K and 0.8 J/kg·K (the values for $Mn_{0.99}Fe_{0.01}As$) in the magnetization and direct measurements, respectively. Because the hystere-
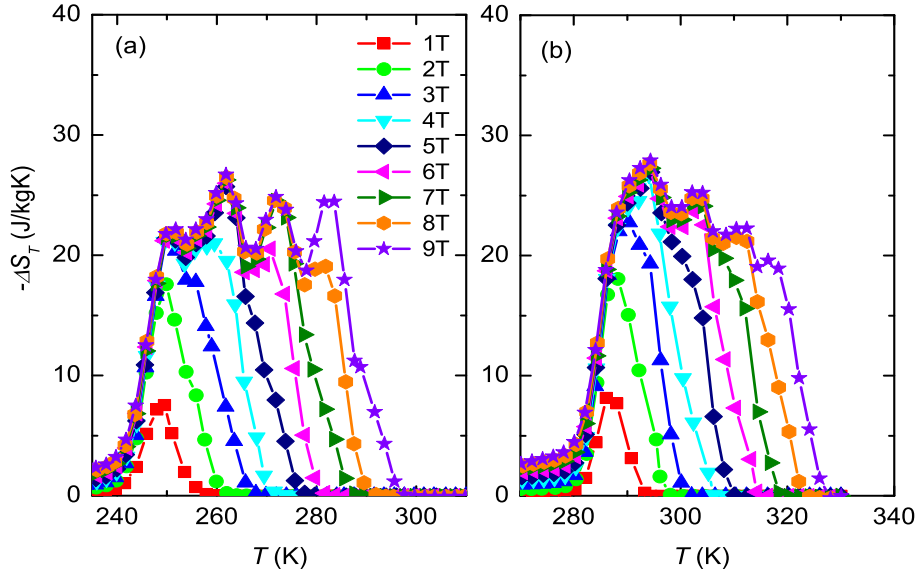
Figure 7.25: Temperature dependence of the isothermal entropy change calculated from isofield magnetization data for $Mn_{0.985}Fe_{0.015}As$. (a) on cooling. (b) on heating.
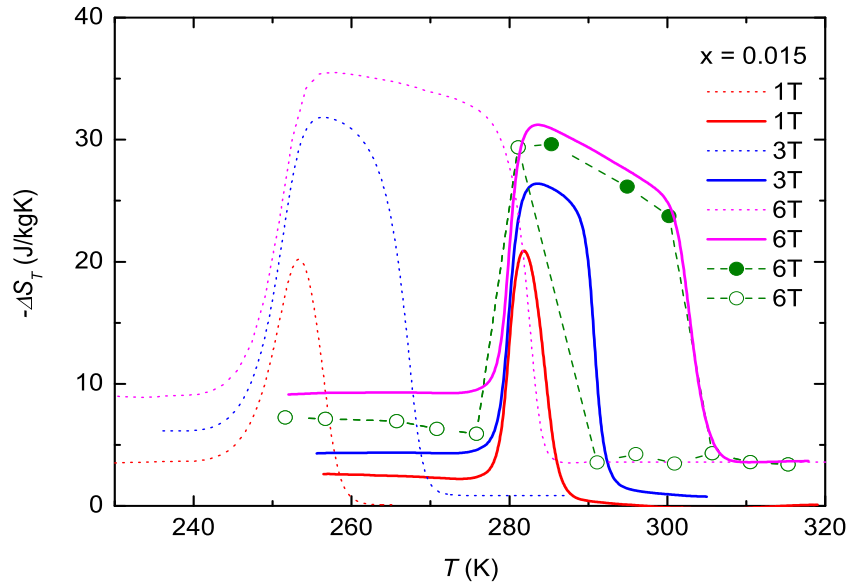

Figure 7.26: Temperature dependence of the isothermal entropy change obtained from heat-capacity and direct measurements for $Mn_{0.985}Fe_{0.015}As$. Solid lines: from heat capacity on heating. Dotted lines: from heating capacity on cooling. Dashed lines are guides to the eye. Solid and open symbols represent ΔS_T determined from direct measurements performed following protocols 3 and 4, respectively.

sis is larger and the transition temperature is lower in the present compound. Taking into account the points measured following protocol 3 in the direct measurement as well as the correction of the irreversibility in each method, the directly determined ΔS_T agrees with that obtained from the heat capacity on heating. For a field change of 6 T, the observed maxima of $|\Delta S_T|$ in figure 7.26 are 34.8 J/kg·K and 31.8 J/kg·K on cooling and heating, respectively.

Figure 7.27 shows the adiabatic temperature change as a function of temperature for $Mn_{0.985}Fe_{0.015}As$. In direct measurements, the points denoted by arrows were measured following protocol 2. For a field change of 6 T, the maxima of ΔT_S are found to be 17.5 K and 20.4 K on heating and cooling, respectively.
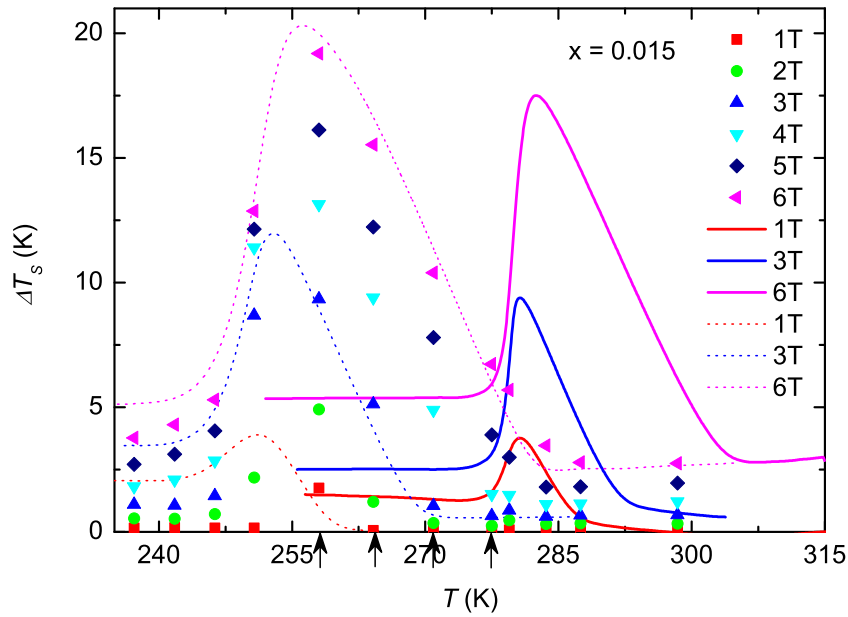
Figure 7.27: Temperature dependence of the adiabatic temperature change for $Mn_{0.985}Fe_{0.015}As$. Symbols: determined from direct measurements. Solid lines: obtained from heat capacity on heating. Dotted lines: obtained from heat capacity on cooling. At arrowed temperatures, the direct measurements have been carried out following protocol 2.

7.3.6   Magnetic phase diagram

It is found that the values of dT_t/dB in the Fe-doped compounds are 3.6 K/T, 3.7 K/T and 3.8 K/T on heating and 4.5 K/T, 4.8 K/T and 5.2 K/T on cooling for $x = 0.006$, 0.01 and 0.015, respectively. These values are comparable

to 3.3 K/T on heating and 4.2 K/T on cooling exhibited by the undoped compound MnAs [30, 156]. If the transition line in the $B - T$ phase diagram maintains a linear dependence in the Fe-doped compounds, the critical fields would be about 17 T, 19 T and 20 T for $x = 0.006$, 0.01 and 0.015, respectively. Nevertheless, the transition temperature probably does not change linearly at high fields, as what happens in MnAs which has a critical point at 360 K and 9 T. Apparently, the phase diagrams of the $Mn_{1-x}Fe_xAs$ compounds look as a prolongation of that of MnAs [30, 156] because they have similar values of dT_t/dB as those of MnAs, but lower transition temperatures and larger hysteresis than MnAs has.
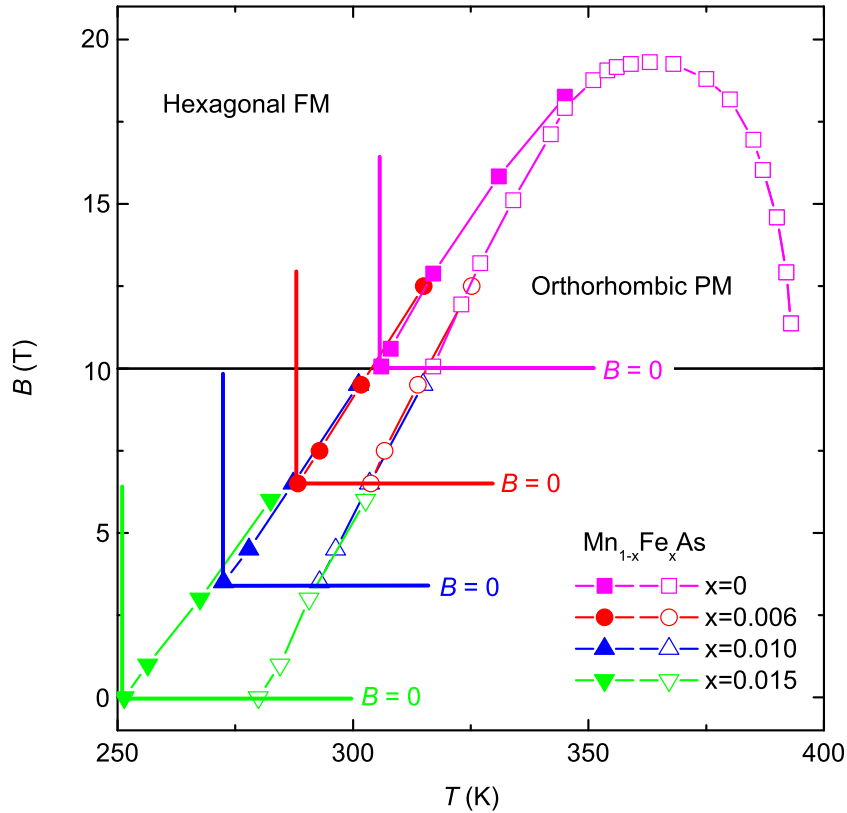
Figure 7.28: Scaled magnetic phase diagram of $Mn_{1-x}Fe_xAs$. The data for MnAs were taken from Ref. [156]. Thick lines are the real axes of the samples.

Assuming that some kind of corresponding states law holds, when an appropriate value is subtracted in the B-axis scale for each Fe-doped compound, an excellent coincidence of the linear extrapolations of the transition lines going towards low temperature and negative field of those of MnAs can be achieved.

Then a common phase diagram of the $Mn_{1-x}Fe_xAs$ compounds is obtained in this way, as shown in figure 7.28. The subtracted value is called the scaled field. The transition temperatures on heating and cooling at the scaled field of each Fe-doped compound are identical to those of MnAs at zero field. As a result, the scaled fields are found to be 3.5 T, 6.5 T and 10.0 T for $x = 0.006$, 0.01 and 0.015, respectively.

We have only characterized the transition temperatures of the $Mn_{1-x}Fe_xAs$ compounds with a maximum field of 6 T which is far below the critical field, but a complete magnetic phase diagram of each Fe-doped compound can be achieved by joining the phase diagram of MnAs to the scaled transition lines of the Fe-doped compound. Consequently, we estimated the critical fields to be 12.5 T, 15.5 T and 19.0 T for $x = 0.006$, 0.01 and 0.015, respectively. Nevertheless, in the future, high-field measurements are necessary to demonstrate the assumption we made. Moreover, it is worth to note that although the critical field increases with increasing x in the $Mn_{1-x}Fe_xAs$ compounds, the critical temperature remains the same value at 360 K.

7.4 $Mn_{1-x}Co_xAs$

Figure 7.29 shows the heat flow as a function of temperature obtained from DSC measurements performed in cooling and subsequent heating processes for $Mn_{1-x}Co_xAs$ compounds. The observation of endothermic and exothermic peaks associated with transitions at different temperatures in the heating and cooling processes reveals that the nature of the transitions occurring in the $Mn_{1-x}Co_xAs$ compounds is of first order. With an increase of Co content, the transition temperature moves to lower temperature, and the sharp peaks are significantly lowered and broadened. The Co-doping and the Fe-doping have quite similar influences on the calorimetric properties of MnAs. The resulting values of the latent heat of the Co-doped compounds are comparable to those of the Fe-doped compounds on both heating and cooling, as seen in table 7.2.

As shown in figure 7.30, the heat-capacity curves of the $Mn_{1-x}Co_xAs$ compounds at zero field have similar features to the DSC plots. We have also measured the heat capacities in the presence of constant magnetic fields between 1 T and 6 T on heating and cooling, as displayed in figures 7.31(a), 7.31(b) and 7.31(c). Analogously, the temperature of the heat-capacity peak was taken as the transition temperature for each curve. Transition enthalpy and transition entropy were calculated using the method described in section 2.4. The resulting values of the transition temperature, transition enthalpy, and transition entropy for the $Mn_{1-x}Co_xAs$ compounds are summarized in table 7.2. We found that with an increase of field, the transition temperature increases, and
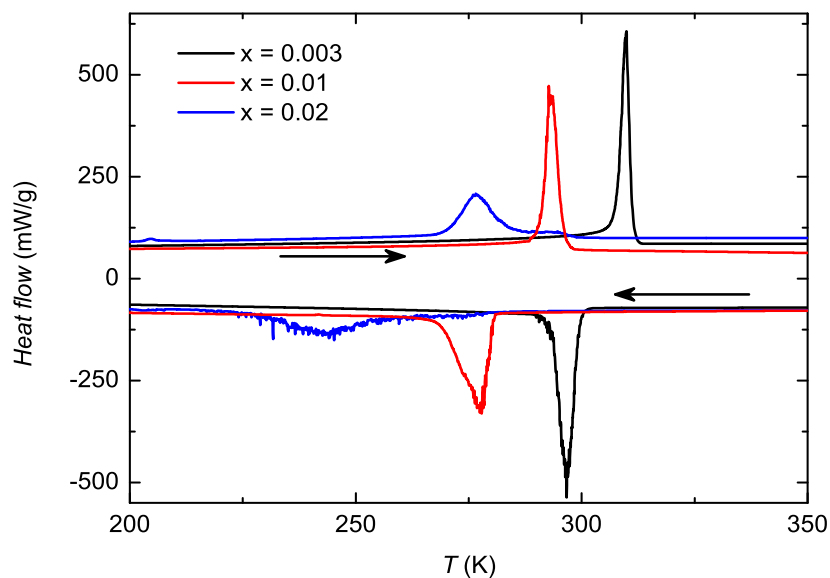
Figure 7.29: Heat flow as a function of temperature measured in cooling and subsequent heating processes for the $Mn_{1-x}Co_xAs$ compounds.
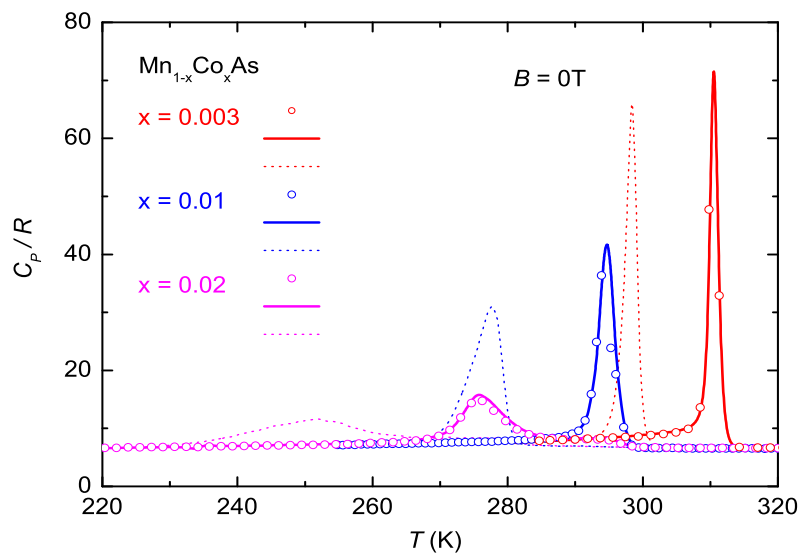

Figure 7.30: Temperature dependence of the heat capacity measured at zero field on heating and cooling for the $Mn_{1-x}Co_xAs$ compounds. Symbols: measured with the heat-pulse method. Solid lines: measured with the thermogram technique on heating. Dotted lines: measured with the thermogram technique on cooling.
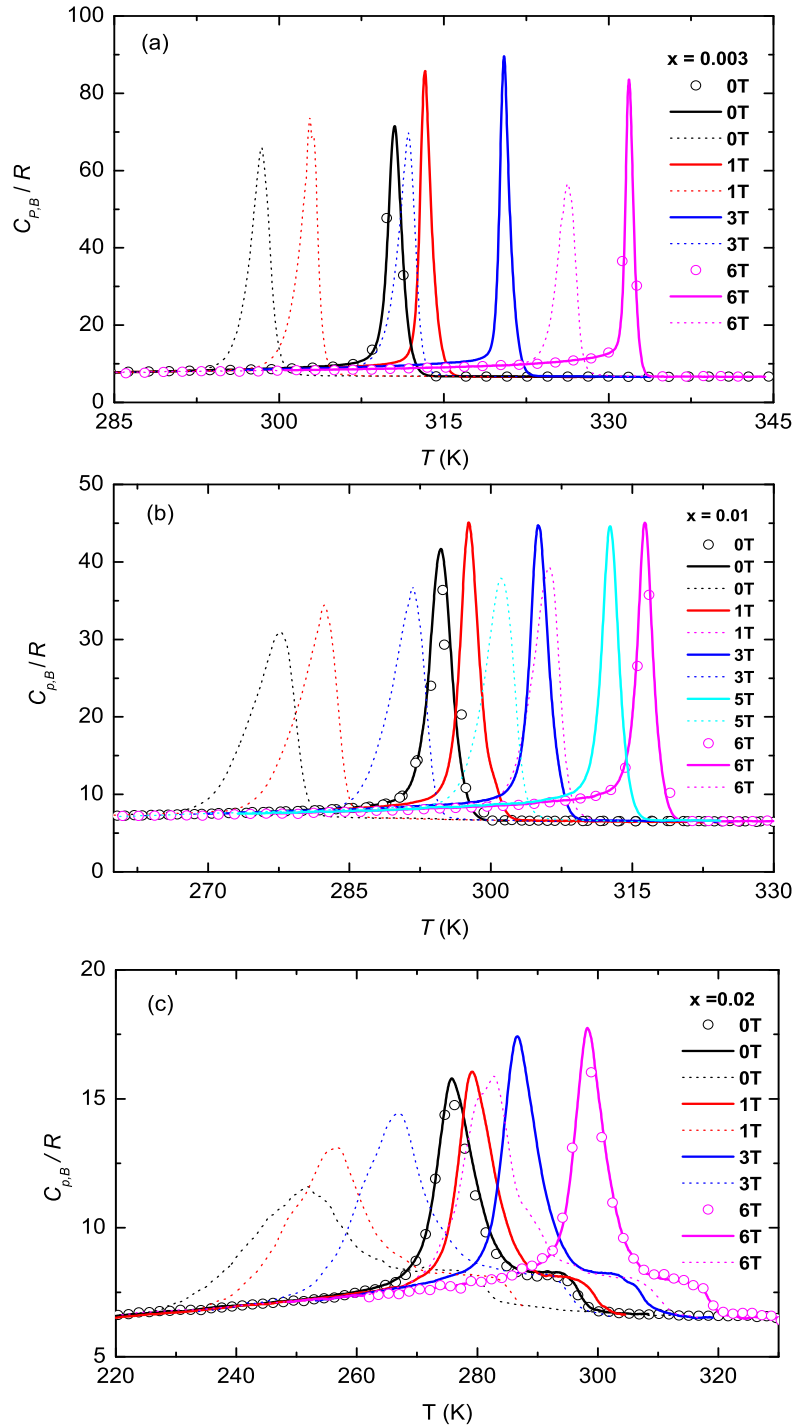
Figure 7.31: Temperature dependence of the heat capacity measured at different constant magnetic fields on heating (solid lines) and cooling (dotted lines) for the $Mn_{1-x}Co_xAs$ compounds. Open symbols denote the heat capacity obtained with the heat-pulse method.

Table 7.2: Transition temperature, transition enthalpy and transition entropy at several constant magnetic fields for the $Mn_{1-x}Co_xAs$ compounds.

Compounds	B (T)	$T_{t,h}$ (K)	ΔH_h (J/g)	ΔS_h (J/kg·K)	$T_{t,c}$ (K)	ΔH_c (J/g)	ΔS_c (J/kg·K)
$x = 0.003$	0	309.7*	7.6*	24.5*	296.7*	9.5*	32.0*
	0	310.5	7.2	23.2	298.4	9.0	30.2
	1	313.3	6.9	22.0	302.9	8.9	29.4
	3	320.5	6.6	20.6	311.8	8.2	26.3
	6	331.9	5.5	16.6	326.3	6.8	20.8
$x = 0.01$	0	293.3*	8.2*	28.0*	277.4*	9.6*	34.6*
	0	294.7	7.0	23.8	277.6	9.0	32.4
	1	297.7	6.9	23.2	282.4	9.0	31.9
	3	305.0	6.7	22.0	291.7	8.7	29.8
	5	312.6	6.1	19.5	301.1	8.1	26.9
	6	316.3	5.7	18.0	306.2	7.5	24.5
$x = 0.02$	0	276.6*	7.1*	25.7*	243.7*	9.4*	38.6*
	0	275.9	6.4	23.2	251.6	9.2	36.6
	1	279.2	6.3	22.6	256.4	9.1	35.5
	3	286.7	7.1	24.8	266.6	9.6	36.0
	6	298.4	6.9	23.1	281.9	9.5	33.7

* obtained from DSC measurement.

Indexes h and c denote heating and cooling processes, respectively.

both the transition enthalpy and transition entropy decrease. The transition enthalpy and transition entropy on cooling are larger than those on heating for each constant field. All of these characteristics are the same as those observed in the Fe-doped compounds.

The virgin effect observed in $Mn_{0.985}Fe_{0.015}As$ is also present in the Co-doped compound with $x = 0.02$, but it is not found in the other compounds with lower x. Figure 7.32 displays the heat capacity as a function of temperature measured following a sequence from (1) to (7) in $Mn_{0.98}Co_{0.02}As$. Two separated anomalies concentrating at 204.8 K and 276.6 K are observed in the heat capacity of the as-prepared sample (process (1)). The low-temperature anomaly is attributed to the virgin effect, and the high-temperature one results from the normal stable phase of the sample. The bump at a temperature just above the high-temperature anomaly should be ascribed to a compositional inhomogeneity, since it is affected in the same way as the main anomaly by applying a magnetic field and no more than the main phase is indicated in
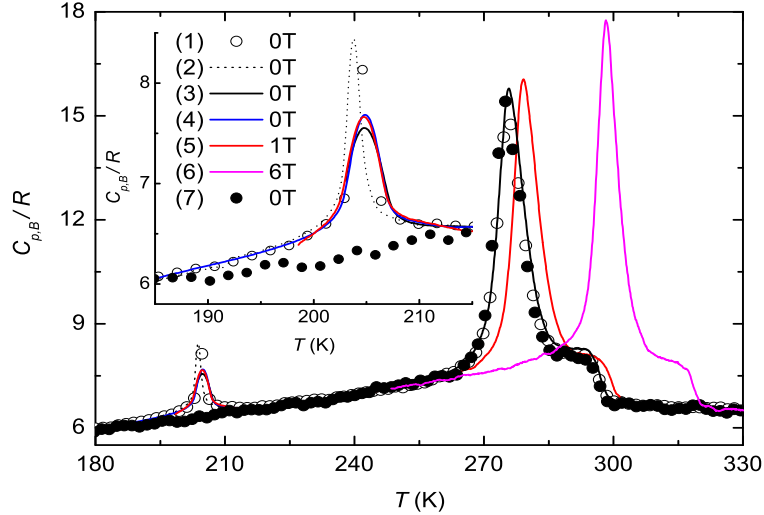
Figure 7.32: Temperature dependence of the heat capacity for $Mn_{0.98}Co_{0.02}As$. (1) Open circles denote the heat-capacity data measured in the 1st heating run at zero field for an as-prepared sample. (2) Dotted line is the subsequent cooling run at zero field. (3) Black solid line is the 2nd heating run at zero field. (4) Blue solid line is the 3nd heating run at zero field. (5) Red solid line is the 1st heating run at a constant field of 1 T. (6) Magenta solid line is the 1st heating run at a constant field of 6 T. (7) Solid circles denote the heat-capacity data measured at zero field after the heating run at 6 T. The inset shows the zoomed-in plots around 205 K.

the XRD pattern (see figure 7.33 below). Comparing to the sharp peak at 276.6 K, the lower and narrower anomaly at 204.8 K reveals that only a small amount of metastable HM phase was formed in the sample preparation. In the subsequent cooling process (process (2)), the anomaly shifts to 203.8 K, which is 1 K lower than the one on heating. Namely, the transition is accompanied by a hysteretic behavior, which differs from what happens in $Mn_{0.985}Fe_{0.015}As$. The existence of the hysteresis indicates that the nature of the transition is of first order. The virgin anomaly can neither be removed by temperature cycling (below 350 K) nor by applying a low magnetic field (the red line in figure 7.32 is at 1 T), but it no longer appears after a heating run at 6 T.

To clarify the structural transformations occurring in the Co-doped compounds, XRD measurements have been performed in $Mn_{0.98}Co_{0.02}As$ following a temperature sequence indicated in the inset of figure 7.33, where each blue solid circle stands for a measuring temperature and the red arrowed line de-
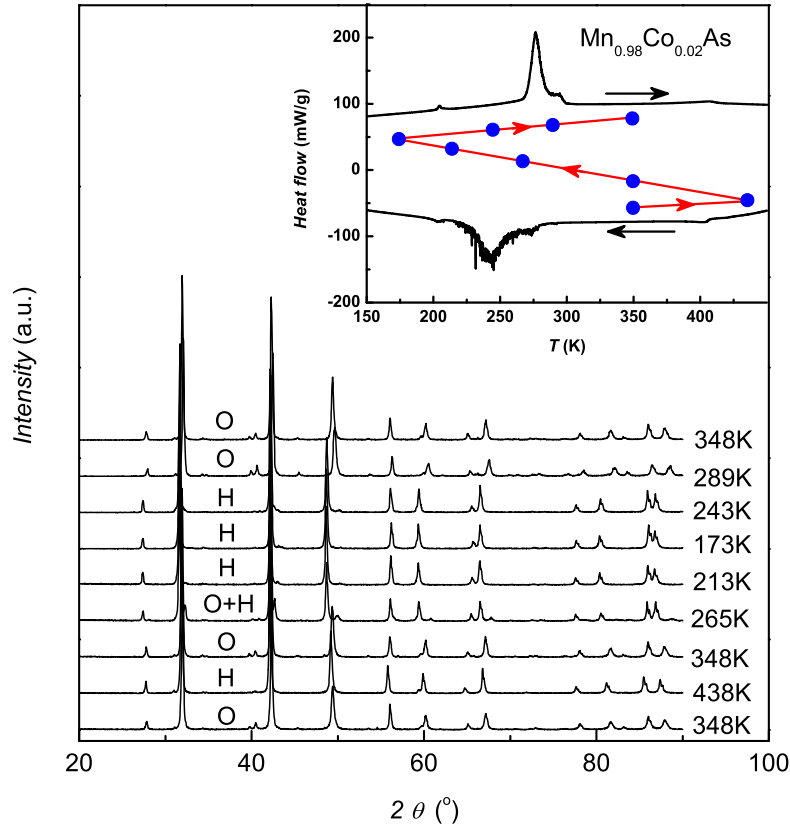
Figure 7.33: X-ray diffraction patterns collected at different temperatures for $Mn_{0.98}Co_{0.02}As$. Inset shows the temperature sequence used in the XRD measurements based on the DSC curves.

notes the evolution of the temperature. The resultant XRD patterns are shown in figure 7.33. The combination of the DSC curves and the XRD patterns reveals that structural transformations from the NiAs-type to MnP-type and to NiAs-type occur at ~276 K and ~406 K on heating, and the opposite ones occur at ~406 K and ~243 K on cooling. In the cooling process, the coexistence of the two structures is clearly seen at 265 K. Moreover, no structural change was detected below and above 204 K where the virgin effect shows. The same structural transitions are observed in the temperature-dependent XRD patterns of $Mn_{0.997}Co_{0.003}As$ and $Mn_{0.99}Co_{0.01}As$.

In figure 7.34, the unit cell parameters as functions of temperature have been obtained based on the analyses of the XRD patterns displayed in figure

7.33 for $Mn_{0.98}Co_{0.02}As$. It is seen that the lattice constant a decreases but c increases with a rise of temperature in the NiAs-type structure, resulting in an unchanged unit cell volume. All the lattice parameters a, b and c increase with increasing temperature in the MnP-type structure, leading to an expansion of the unit cell volume. That is coincident with the results observed in MnAs [157]. The observed ~ 3 % of the unit cell volume change occurring at the structural transition in $Mn_{0.98}Co_{0.02}As$ is greater than ~ 2 % in MnAs [154]. The gradual expansion of the unit cell volume in the MnP-type structure could be due to a normal thermal expansion. The nature of the structural transition at 406 K is of second order, since no sharp change of the unit cell volume is predicted when using a linear extrapolation (the dotted line in figure 7.34).

We have measured isothermal magnetization curves following protocol 1 for the $Mn_{1-x}Co_xAs$ compounds, as displayed in figures 7.35(a), 7.35(b) and 7.35(c) for $x = 0.003$, 0.01 and 0.02, respectively. The resulting entropy changes, with the help of the Maxwell relation, on increasing and decreasing fields are presented in figure 7.36. It has to be mentioned that the measurements were carried out with a maximum field of 9 T. In order to compare with ΔS_T obtained from direct and heat-capacity measurements, the extracted data below 6 T are considered. Consequently, the "spike" effect is observed in the ΔS_T curves on increasing field for each compound, but not in the ΔS_T curves on decreasing field. The maxima of the spurious spikes are found to be 100 J/kg·K, 138 J/kg·K and 60 J/kg·K for $x = 0.003$, 0.01 and 0.02, respectively. These values are comparable to those seen above in the Fe-doped compounds. Taking into account the correct $-\Delta S_T \cong 25$ J/kg·K at the transition, the extra contributions to the spurious MCE peaks are 75 J/kg·K, 113 J/kg·K and 35 J/kg·K for $x = 0.003$, 0.01 and 0.02, respectively. Taking $C_{an,0T}(T_t) - C_{nor,0T}(T_t) = 64.9R$, $35.1R$ and $9.2R$, $B_{th,in} = 2.8$ T, 3.6 T and 5.0 T, $M_{FM} - M_{PM} = 100$ Am^2/kg for all the three compounds, the resulting values of $-\Delta S_{extra}$ are 161 J/kg·K, 115 J/kg·K and 46 J/kg·K for $x = 0.003$, 0.01 and 0.02, respectively. The experimental values of $-\Delta S_{extra}$ are smaller than the calculated ones, and limited to the latter. For the compound with $x = 0.01$, the observed ΔS_{extra} is closer to the evaluated limit than those for $x = 0.003$ and 0.02 because of the smaller temperature interval used in the isothermal magnetization measurement.

To make the corrections of irreversibility in ΔS_T obtained by means of the Maxwell relation, we have computed the area enclosed by each isothermal magnetization loop of figures 7.35(a), 7.35(b) and 7.35(c) for the studied Co-doped compounds, as shown in figure 7.37. The magnetization measurements were performed following protocol 1 with a maximum field of 9 T. The values of $-dA/dT$ are found to be 4.1 J/kg·K, 3.9 J/kg·K and 4.1 J/kg·K. These values are slightly higher than 3.7 J/kg·K in MnAs obtained by Tocado [29]
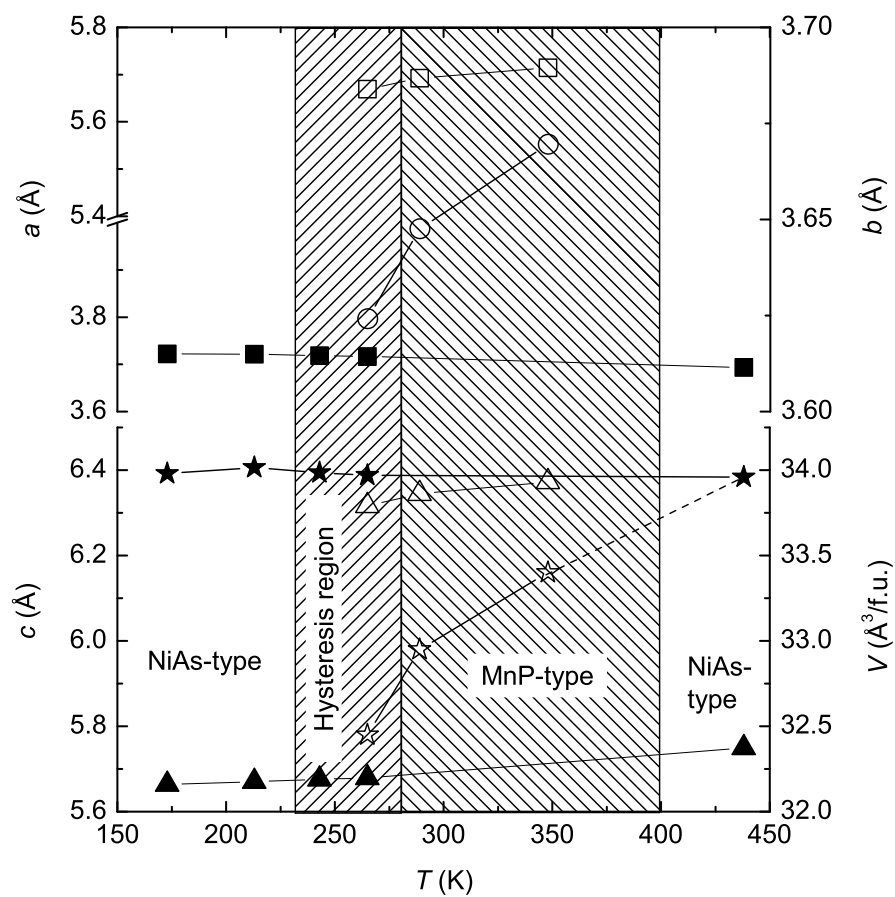
Figure 7.34: Unit cell dimensions as a function of temperature for $Mn_{0.98}Co_{0.02}As$. Filled and open symbols represent the lattice parameters of the hexagonal NiAs-type and the orthorhombic MnP-type structures, respectively. Squares, circles, triangles and stars represent the unit cell constants a, b, c, and the volume V, respectively. Solid and dashed lines are guides for the eye.
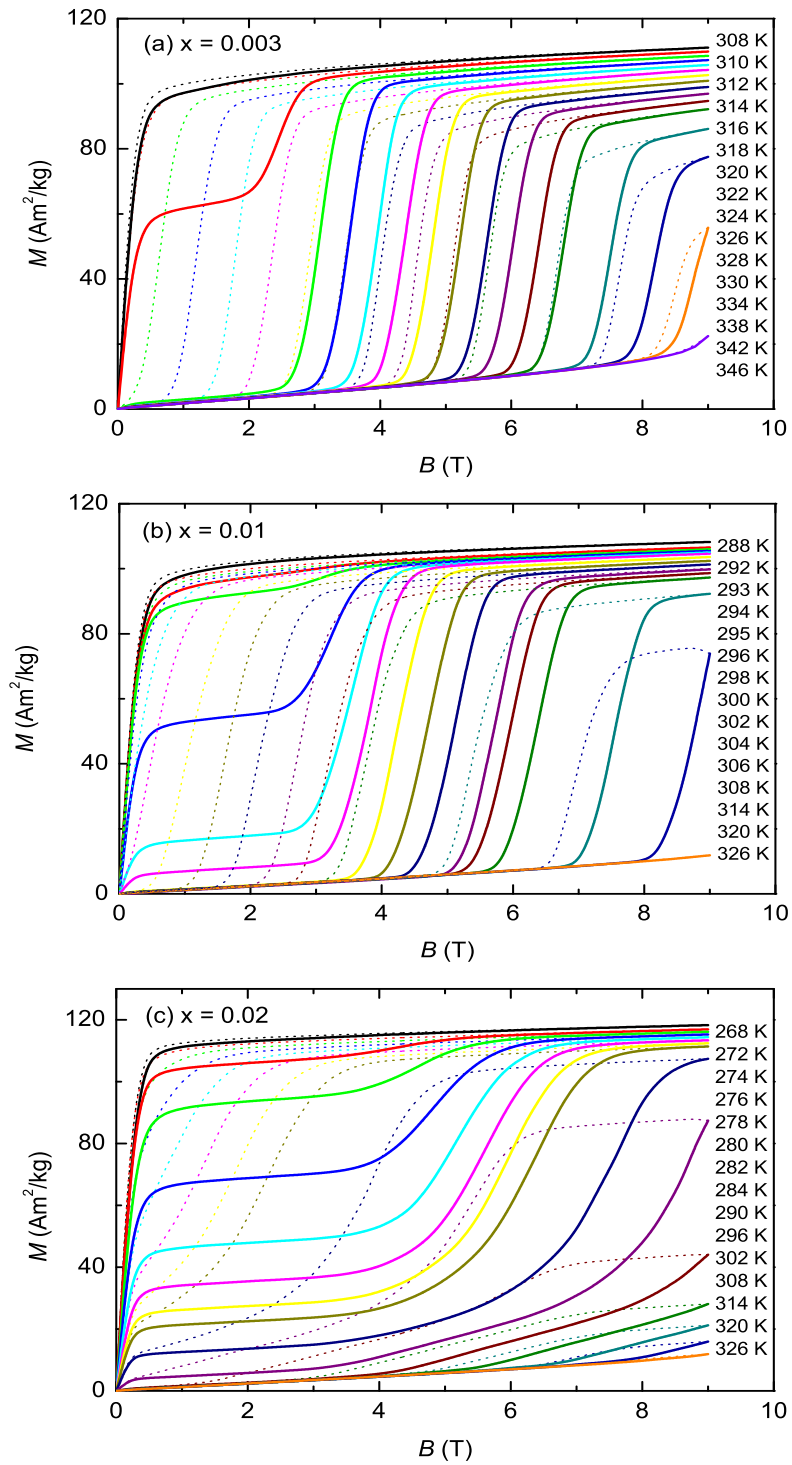
Figure 7.35: Magnetic field dependence of the isothermal magnetization measured on increasing (solid lines) and decreasing (dotted lines) fields for the $Mn_{1-x}Co_xAs$ compounds.
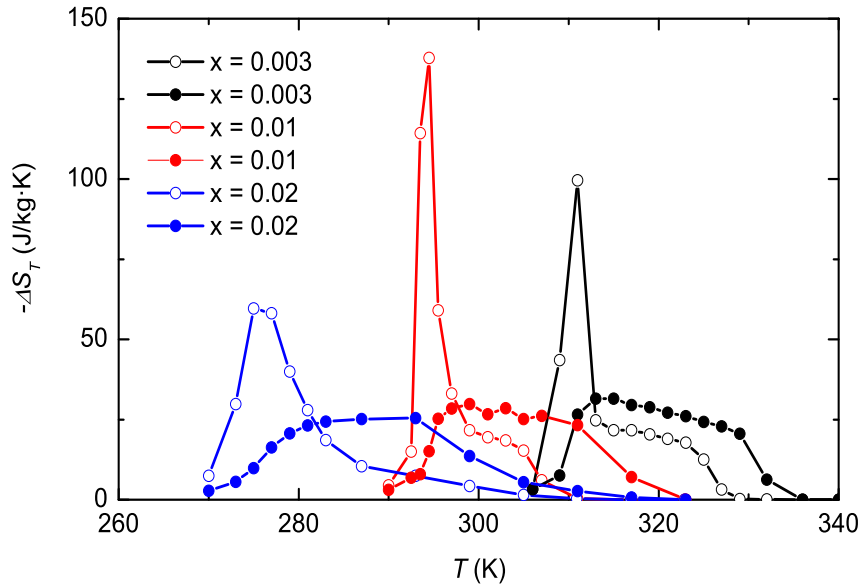
Figure 7.36: Isothermal entropy change as a function of temperature for a magnetic field change of 6 T calculated from isothermal magnetization data measured following protocol 1 for the $Mn_{1-x}Co_xAs$ compounds. Open symbols: on increasing field. Solid symbols: on decreasing field.
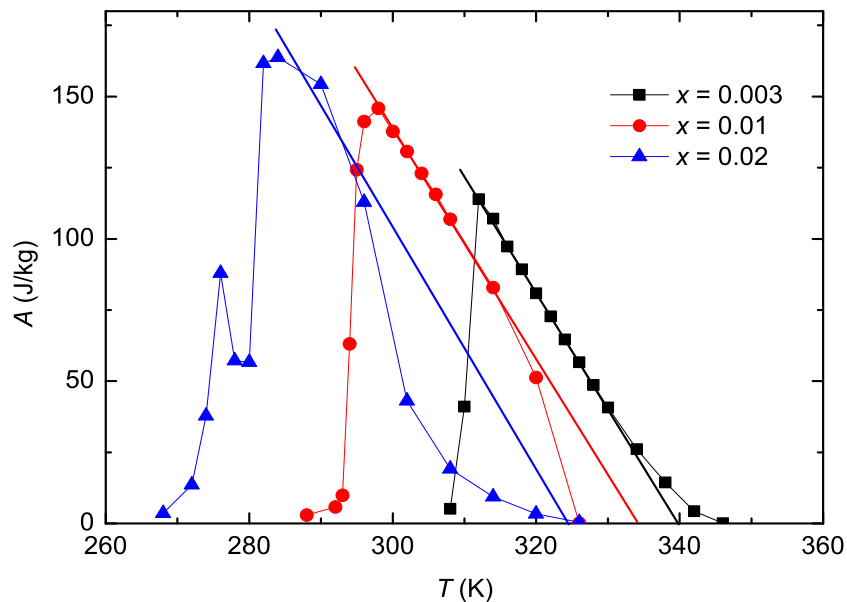
Figure 7.37: One half of the area enclosed by the isothermal magnetization loop as a function of temperature for the $Mn_{1-x}Co_xAs$ compounds. Lines are the linear fits of the data in the transition region for each sample.
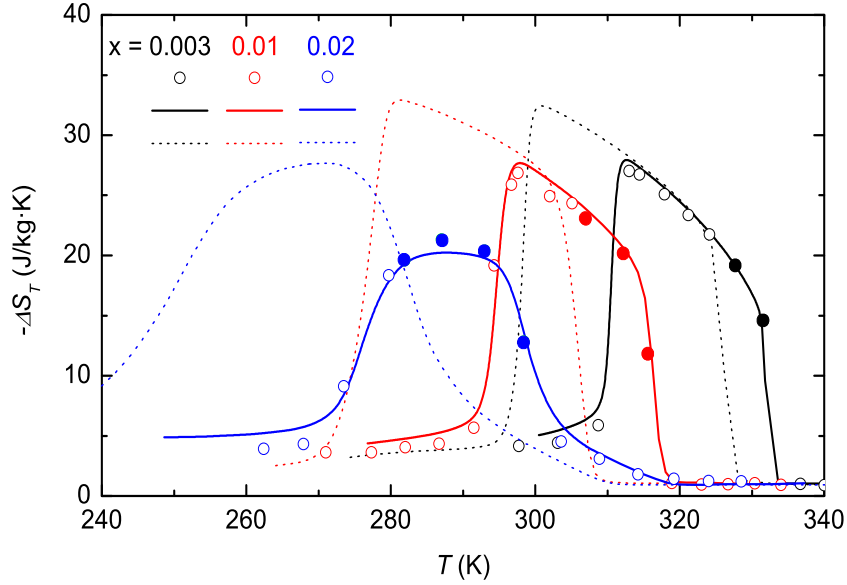
Figure 7.38: Isothermal entropy change as a function of temperature for a magnetic field change of 6 T for the $Mn_{1-x}Co_xAs$ compounds. Solid and open symbols denote the results obtained from direct measurement performed following protocols 3 and 4, respectively. Solid and dotted lines represent the results derived from heat capacity on heating and cooling, respectively.

but slightly smaller than those in the Fe-doped compounds. When applying the corrections to ΔS_T displayed in figure 7.36, the maxima, $-\Delta S_{T,\text{max}}$, are found to be 27.5 J/kg·K, 25.9 J/kg·K and 21.3 J/kg·K for a magnetic field change from 6 T to 0 for $x = 0.003$, 0.01 and 0.02, respectively.

Shown in figure 7.38 are the plots of ΔS_T determined from heat-capacity and direct measurements for the $Mn_{1-x}Co_xAs$ compounds. It is seen that ΔS_T derived from the heat capacity on heating agrees well with that determined from the direct measurements on decreasing field. The errors caused by irreversibility are small in the heat-capacity and direct measurements. According to the discussion in section 2.7, the $|\Delta S_T|$ values obtained from the heat-capacity data at 0 and 6 T have been underestimated by 0.1 J/kg·K, 0.3 J/kg·K, 0.7 J/kg·K on heating, and overestimated by 0.2 J/kg·K, 0.4 J/kg·K, 1.0 J/kg·K on cooling for $x = 0.003$, 0.01 and 0.02, respectively. These errors are much smaller than those in the isothermal magnetization measurements. In the direct measurements, the maximum entropy production terms were evaluated with the help of equation (4.8), to be 0.4 J/kg·K, 0.5 J/kg·K and 0.6 J/kg·K for $x = 0.003$, 0.01 and 0.02, respectively. These values are compa-
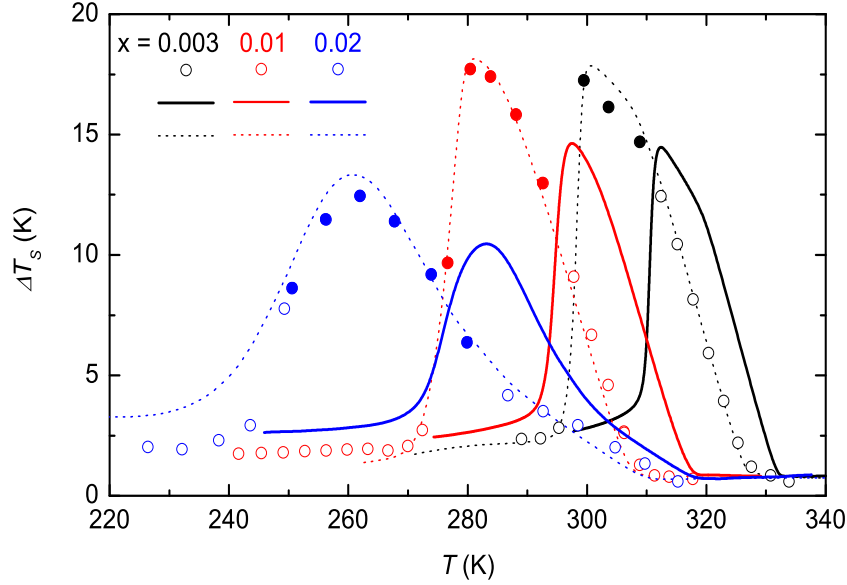
Figure 7.39: Adiabatic temperature change as a function of temperature upon a field change of 6 T for the $Mn_{1-x}Co_xAs$ compounds. Open and solid symbols represent ΔT_S obtained from direct measurements performed following protocols 1 and 2, respectively. Solid and dotted lines represent ΔT_S derived from heat capacity on heating and cooling, respectively.

rable to the irreversible errors in the heat-capacity measurements, of course, also much smaller than those in the isothermal magnetization measurements. Eventually, by taking into account the effect of the irreversibility, for a field change of 6 T, the maximum values of $|\Delta S_T|$ determined from the heat capacity on heating are found to be 28.0 J/kg·K, 28.0 J/kg·K and 20.9 J/kg·K for $x = 0.003$, 0.01 and 0.02, respectively. These maxima are also consistent with those obtained from the isothermal magnetization measurements on decreasing field. For other field changes lower than 6 T, the values of $\Delta S_{T,\mathrm{max}}$ are summarized in table 7.3 for heating and cooling processes.

Let's turn our attention to the other magnetocaloric parameter ΔT_S of the $Mn_{1-x}Co_xAs$ compounds. The ΔT_S data determined from heat-capacity and direct measurements with a magnetic field change of 6 T for the $Mn_{1-x}Co_xAs$ compounds are plotted in figure 7.39. As the direct measurements were carried out on increasing field, the values of ΔT_S from direct measurements are in agreement with those derived from the heat capacity on cooling. In the hysteretic region, the direct measurements have been carried out following protocol 2, indicated by the solid symbols in figure 7.39. The maximum values, $\Delta T_{S,\mathrm{max}}$

Table 7.3: Maxima of isothermal entropy change and adiabatic temperature change obtained from heat-capacity and direct measurements with various magnetic field changes for the $Mn_{1-x}Co_xAs$ compounds.

Compounds	ΔB (T)	$-\Delta S_{T,\mathrm{max}}$ (J/kg·K)			$\Delta T_{S,\mathrm{max}}$ (K)		
$x = 0.003$	1	20.8^a	27.6^b	—	2.6^a	3.9^b	3.5^c
	2	—	—	—	—	—	7.5^c
	3	25.3^a	30.4^b	—	9.0^a	11.6^b	10.6^c
	4	—	—	—	—	—	14.4^c
	5	—	—	—	—	—	16.6^c
	6	27.9^a	32.4^b	27.0^c	14.5^a	17.9^b	17.3^c
$x = 0.01$	1	18.5^a	21.4^b	—	2.7^a	3.6^b	3.1^c
	2	—	—	—	—	—	6.7^c
	3	24.6^a	30.2^b	—	8.6^a	10.8^b	10.5^c
	4	—	—	—	—	—	13.7^c
	5	26.7^a	32.5^b	—	13.4^a	17.0^b	16.8^c
	6	27.7^a	32.9^b	26.9^c	14.6^a	18.1^b	17.7^c
$x = 0.02$	1	5.8^a	6.9^b	—	1.7^a	2.4^b	2.3^c
	2	—	—	—	—	—	4.5^c
	3	16.7^a	19.2^b	—	6.3^a	7.3^b	7.0^c
	4	—	—	—	—	—	9.2^c
	5	—	—	—	—	—	10.6^c
	6	20.2^a	26.7^b	21.3^c	10.5^a	13.0^b	12.5^c

^{a} obtained from heat capacity on heating.
^{b} obtained from heat capacity on cooling.
^{c} obtained from direct measurement.
the effects of irreversibility were not taken into account.

$= 17.3$ K, 17.7 K and 12.5 K, were obtained from the direct measurement for a field change from 0 to 6 T for $x = 0.003$, 0.01 and 0.02, respectively. For other field changes, the values of $\Delta T_{S,\mathrm{max}}$ are listed in table 7.3. The magnitudes of $\Delta T_{S,\mathrm{max}}$ in the $Mn_{1-x}Co_xAs$ compounds are similar to those found in the Fe-doped compounds.

So far, we have determined ΔS_T of the $Mn_{1-x}T_xAs$ (T = Fe and Co) compounds by means of three different methods, i.e. from heat-capacity, isothermal magnetization and direct measurements. As an example, figure 7.40 shows the entropy change as a function of temperature for a field change of 6 T determined by the three methods for the compound $Mn_{0.997}Co_{0.003}As$. We found that comparable values of ΔS_T are observed between 312 K and 325 K which
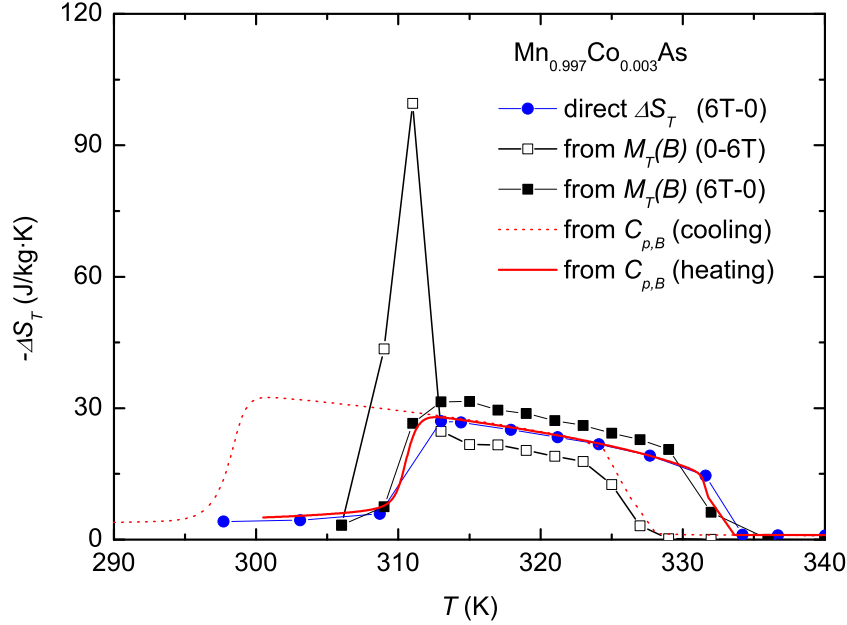
Figure 7.40: Isothermal entropy change as a function of temperature with a field change of 6 T for $Mn_{0.997}Co_{0.003}As$. Solid line: calculated from heat capacity on heating. Dotted line: calculated from heat capacity on cooling. Open and solid squares stand for the results calculated from isothermal magnetization data measured following protocol 1 on increasing and decreasing fields, respectively. Solid circles represent the directly determined ΔS_T with a field change from 6 T to 0. The effects of irreversibility in the data are not taken into account.

correspond to the transition temperature at 0 T on heating and the transition temperature at 6 T on cooling, respectively, i.e. the transition temperatures T_2 and T_3 indicated in the magnetic phase diagram of figure 4.1. In this temperature range, a magnetic field of 6 T can complete the magnetostructural transition on both magnetizing and demagnetizing processes. Taking into account the effect of irreversibility in each method, an excellent agreement among them is achieved. The correction of the irreversibility in magnetization measurement is more important than in heat-capacity and direct measurements. The magnitude of the correction is related to the derivative of the dissipated energy with respect to temperature in the former case, but it is linked to the dissipated energy divided by temperature in the latter two methods. Just below and above this temperature range, protocols 2 and 3 need to be followed in the magnetization and direct measurements in order to have comparable
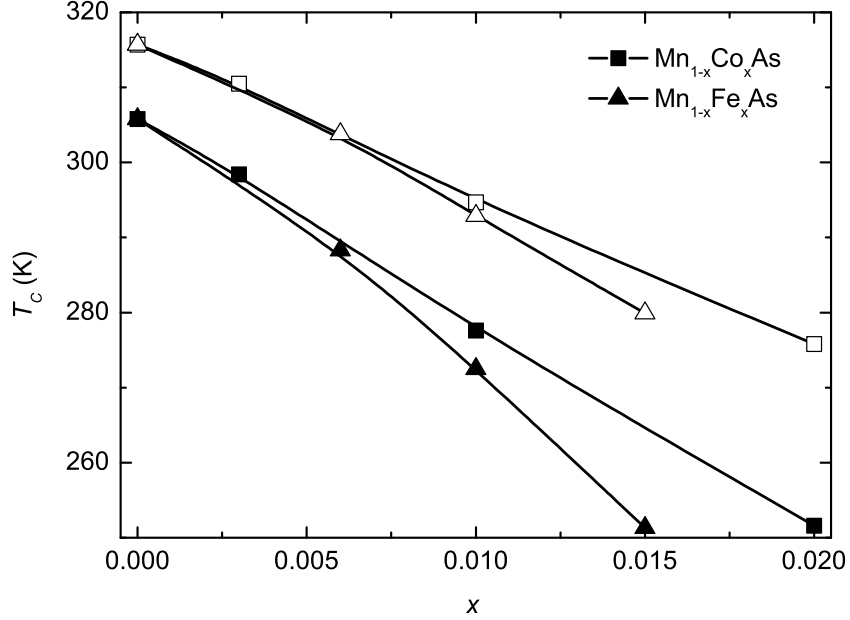
Figure 7.41: Transition temperature as a function of x for the $Mn_{1-x}Fe_xAs$ and $Mn_{1-x}Co_xAs$ compounds. Open and solid symbols denote heating and cooling processes, respectively.

results with those obtained from the heat-capacity measurement.

The area under ΔS_T versus T curve, called the refrigeration capacity (RC), is calculated as $RC^S = -\int_{T_1}^{T_2} \Delta S_T(T)dT$ (see section 2.5). The quantity RC^S is a measure of how much heat can be transferred between the cold (T_1) and hot (T_2) sinks in an ideal refrigeration cycle. In the $Mn_{1-x}T_xAs$ compounds, we found that $RC_c^S > RC_{in}^S \approx RC_{de}^S > RC_h^S \approx RC_{dir}^S$, where the subscripts c and h refer to ΔS_T obtained from heat capacity on cooling and heating, in and de stand for ΔS_T obtained from magnetization on increasing and decreasing fields, and dir represents ΔS_T obtained from direct measurement on decreasing field. The energy loss in a heating-cooling temperature loop is responsible for the difference between RC_c^S and RC_h^S. The approximate equivalence of RC_{in}^S and RC_{de}^S is phenomenologically reasonable because they represent the area enclosed by the isothermal magnetization curve at T_1 and T_2, at which the magnetization curves on increasing and decreasing fields overlap. When taking into account the effect of irreversibility in each method, the corrected order would be $RC_c^S \approx RC_{in}^S > RC_h^S \approx RC_{de}^S \approx RC_{dir}^S$.

Slight Fe-doping and Co-doping in MnAs have quite similar effects on the calorimetric and magnetocaloric properties due to the similar physical charac-

teristics of Fe and Co. However, to some extent some differences can be found. As one can see in the plots of transition temperature as a function of x in figure 7.41, the Fe-doping has a stronger influence on reducing the transition temperature and enlarging the hysteresis than the Co-doping does. Any different properties in the Fe- and Co-doped compounds should be related to the difference between the exchange interactions of Mn-Fe and Mn-Co atoms.

7.5 The Bean-Rodbell model

In this section, we shall present a semi-quantitative description of the phase transition and magnetocaloric properties of the $Mn_{1-x}T_xAs$ compounds with the help of the Bean-Rodbell model which we have introduced in section 2.6.

According to that, MnAs exhibits a saturation magnetization of 3.4 μ_B [158], a total angular momentum of $J = 3/2$ results in the Landé factor $g = 2.27$. We assume $T_0 = 285$ K. Using equation (2.57), the zero-field Gibbs free energy has been calculated at temperature T_0 for different values of η ($\eta = 0, 0.75, 1, 1.25, 1.5, 1.75$ and 2). The results are displayed in figure 7.42. In the absence of external field, the Gibbs free energy curves at $T/T_0 = 1$ are divided into two types by the curve with $\eta = 1$, i.e. the curves with their minima at $\sigma = 0$ for $\eta < 1$ and the curves with their absolute minima at $\sigma \neq 0$ for $\eta > 1$. For $\eta < 1$, the states at $\sigma = 0$ are stable and SOPTs occur. In the case of $\eta = 0$, T_0 is identical to the Curie temperature and is no longer a function of the lattice spacing. It is worth noting that when $\eta = 0$, the model reduces to the mean field approximation which is a well-known framework for illustrating SOPTs [159]. For $\eta > 1$, the stable state with $\sigma \neq 0$ is due to the lattice distortion, which in turn is caused by the magnetization. Upon a rise of temperature, both distortion and magnetization decrease sharply to zero at a temperature greater than T_0, indicating a FOPT.

We may further illustrate some characteristics of a FOPT from the evolution of magnetization curves. By solving the state equation (2.62), the curves of magnetization versus temperature were obtained, as plotted in figure 7.43. For $\eta < 1$, the curves show smooth changes in magnetization, and the transitions for different values of η happen at the same temperature $T_C = T_0$. For $\eta > 1$, the transition does not occur at T_0 on heating since $\sigma(T_0) \neq 0$ is at a stable state. With a further rise of temperature, the transition occurs when the thermal excitations overcome the energy barrier between $\sigma \neq 0$ and $\sigma = 0$. On cooling, the magnetization is not reestablished until a temperature close to the "true" Curie temperature (T_0) is reached, resulting in the presence of thermal hysteresis [73]. In figure 7.43, the discontinuous changes of the magnetization take place at temperatures indicated by a series of dotted vertical lines
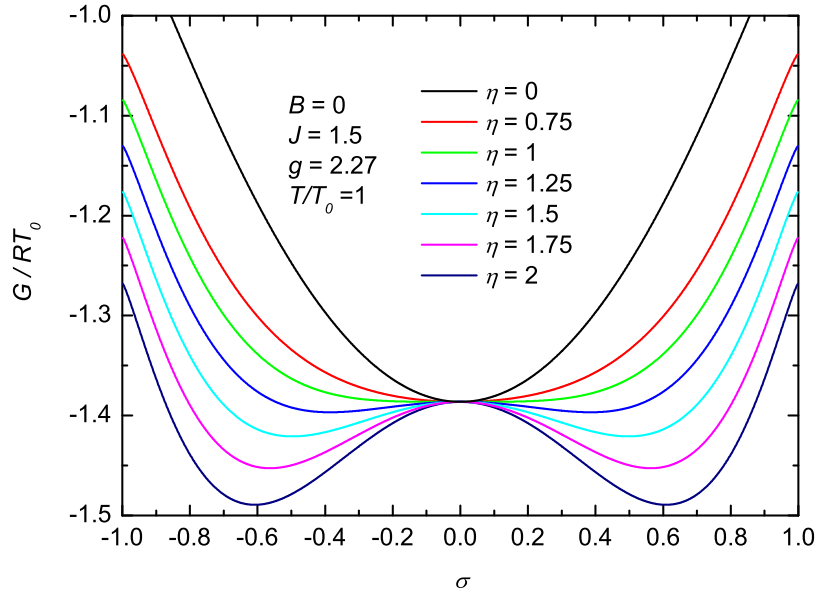
Figure 7.42: Gibbs free energy as a function of relative magnetization calculated with the help of equation (2.57) for different values of η.
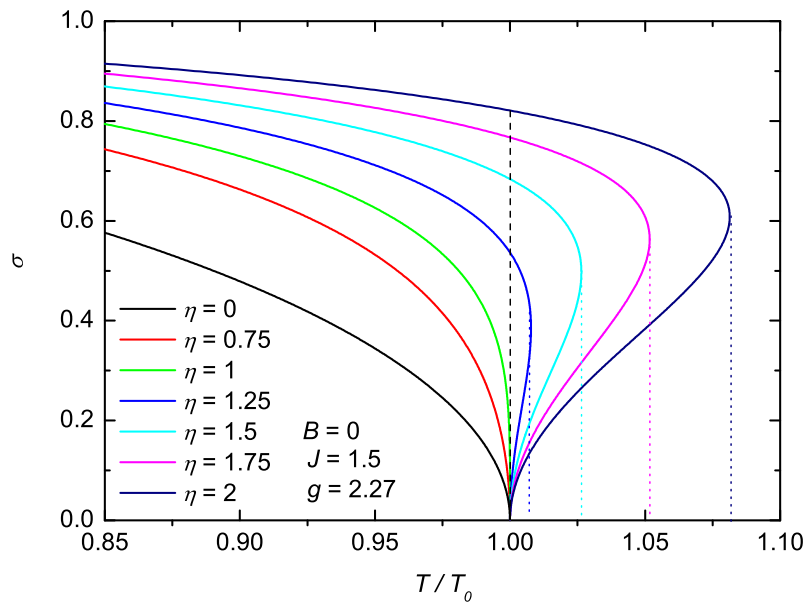

Figure 7.43: Relative magnetization as a function of normalized temperature determined at zero field for different values of η.
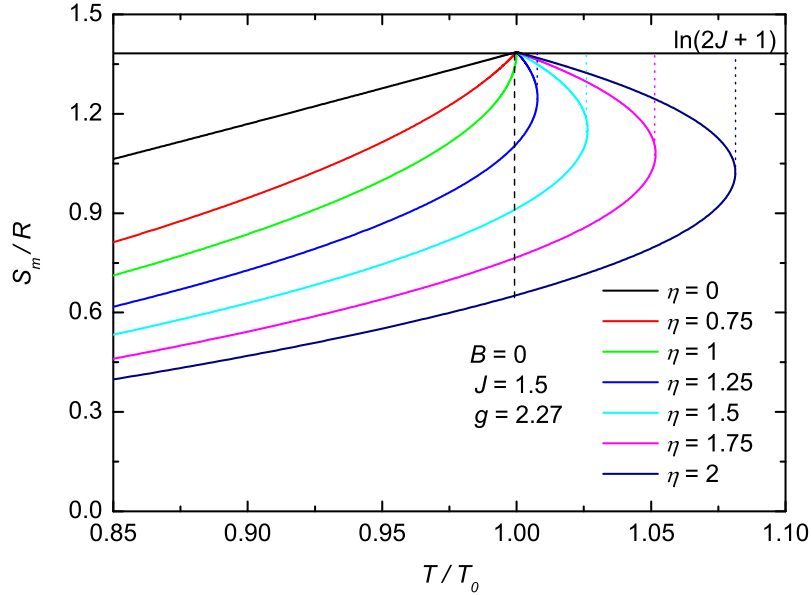
Figure 7.44: Magnetic entropy as a function of normalized temperature determined at zero field for different values of η.

on heating and at T_0 denoted by a dashed line on cooling. With increasing η, the transition occurs at a higher temperature on heating, however, maintains at the same temperature T_0 on cooling, leading to an increase of the thermal hysteresis.

Figure 7.44 shows the magnetic entropy as a function of temperature at zero field calculated on the basis of equation (2.66) for different values of η. Just like what happens in the magnetization curves, continuous entropy curves are seen for $\eta < 1$, while discontinuous entropy jumps take place at the same temperatures as those happen in the magnetization curves for $\eta > 1$. The total magnetic entropy is lowered and the entropy jump is enhanced with increasing values of η. However, the maxima of the magnetic entropy are limited to $R\ln(2J+1)$ for all the values of η.

On one hand, isofield magnetization curves can be obtained by solving the state equation (2.62) at constant external fields. On the other hand, isothermal magnetization curves can be obtained at constant temperatures. In the case of $\eta = 2$, the resulting isofield and isothermal magnetization curves are plotted in figures 7.45 and 7.46, respectively. In figure 7.45, the transition temperatures shift to high temperatures with increasing field in both heating and cooling curves. The rate dT_t/dB on heating is smaller than that on cooling, resulting
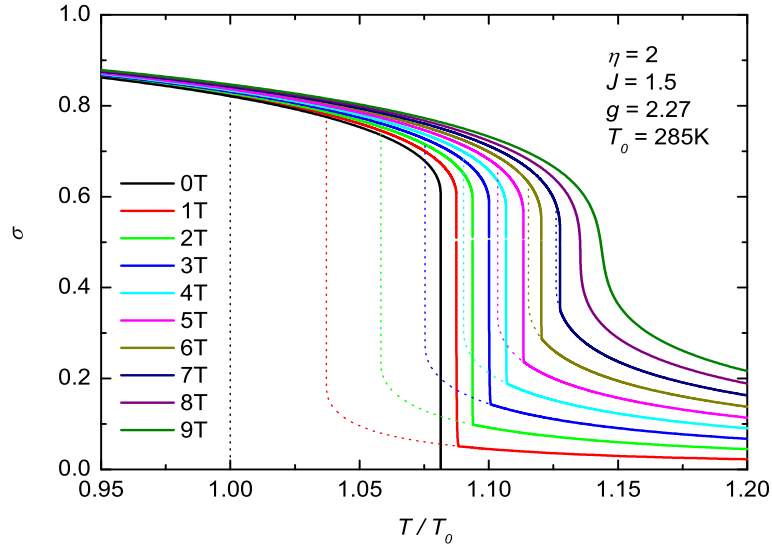
Figure 7.45: Relative magnetization as a function of normalized temperature at constant magnetic fields in the case of $\eta = 2$. Solid lines: on heating. Dotted lines: on cooling.
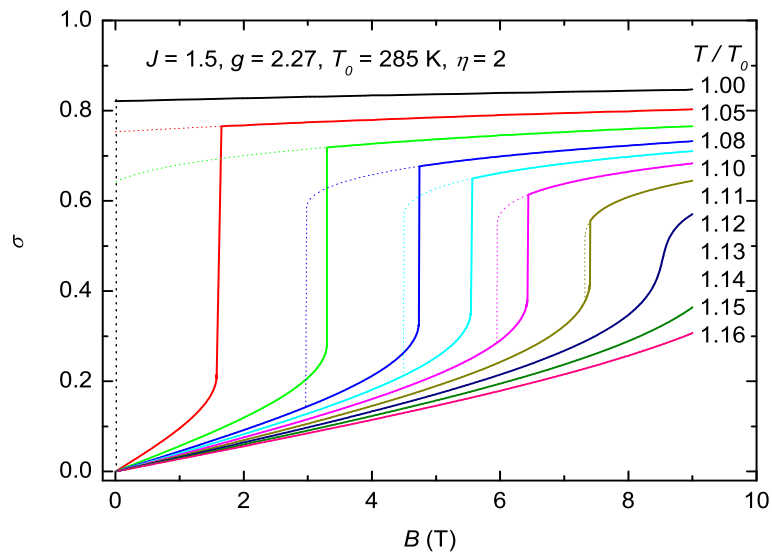

Figure 7.46: Relative magnetization as a function of magnetic field at constant temperatures in the case of $\eta = 2$. Solid lines: on increasing field. Dotted lines: on decreasing field.

in a decrease of thermal hysteresis. In the present case, the hysteresis reaches zero at the critical field $B_{crit} = 8$ T.

In figure 7.46, field-induced metamagnetic phase transitions occur at temperatures just above T_0 on increasing field and above $T_0 + \Delta T_{hys}$ on decreasing field (ΔT_{hys} refers to the thermal hysteresis at zero field). The irreversible magnetization evolution on a magnetic field loop manifests as magnetic hysteresis. The hysteresis decreases with increasing temperature, disappearing at the critical temperature $T_{crit}/T_0 = 1.14$. At the critical point, the transition is of second order. All these features semi-quantitatively agree with those experimentally observed in the $Mn_{1-x}T_xAs$ compounds.

Using the transition temperatures at different fields, three sets of magnetic phase diagrams have been built with different values of η. Other parameters, such as J, g and T_0, are fixed, because they are constant parameters for a given compound. The resulting plots are shown in figure 7.47. It is found that a large η yields a large thermal hysteresis as well as high values of the critical field and critical temperature. In each diagram, a curved line and an almost straight line are observed for the PM-FM and FM-PM transitions, respectively. The slope of the FM-PM transition line is nearly independent of η, but that is not the case for the PM-FM transition lines. The slope of the PM-FM transition line (dotted line) is smaller than that of the FM-PM transition line (solid line). With an increase of field, the slope of the dotted line becomes higher and higher, while that is almost field independent for the solid line, leading to a reduction of the hysteresis. At the critical point, the slopes of both lines are equal. For the FM-PM transition lines with $\eta = 1.5$, 1.75 and 2, the values of dB_t/dT are found to be around 0.40 T/K, 0.45 T/K and 0.5 T/K, respectively. Namely, the values of dT_t/dB are 2.5 K/T, 2.2 K/T and 2.0 K/T. These values are only about one half of those of the $Mn_{1-x}T_xAs$ compounds. In addition to that, nearly straight transition lines are experimentally observed in the $Mn_{1-x}T_xAs$ compounds below 9 T. For instance, one can see the phase diagram of $Mn_{0.99}Fe_{0.01}As$ in figure 7.9. Therefore, we expect that the model will give a better fit of magnetic and magnetocaloric properties on heating (or decreasing field) than on cooling (or increasing field).

The total entropy curves at constant fields have been obtained from the summation of three contributions, electronic, lattice and magnetic entropies. The magnetic entropy was determined with the help of equation (2.66) with the same parameters used in figure 7.45. The lattice entropy was estimated by using the Debye approximation with an atomic number of 2 and a Debye temperature $T_D = 350$ K. The electronic entropy was calculated with $\gamma_e = 0.0088$ J/mol·K, taken from Ref. [29] for MnAs. In the case of $\eta = 2$, the resulting entropy curves are displayed in figure 7.48 at constant fields between
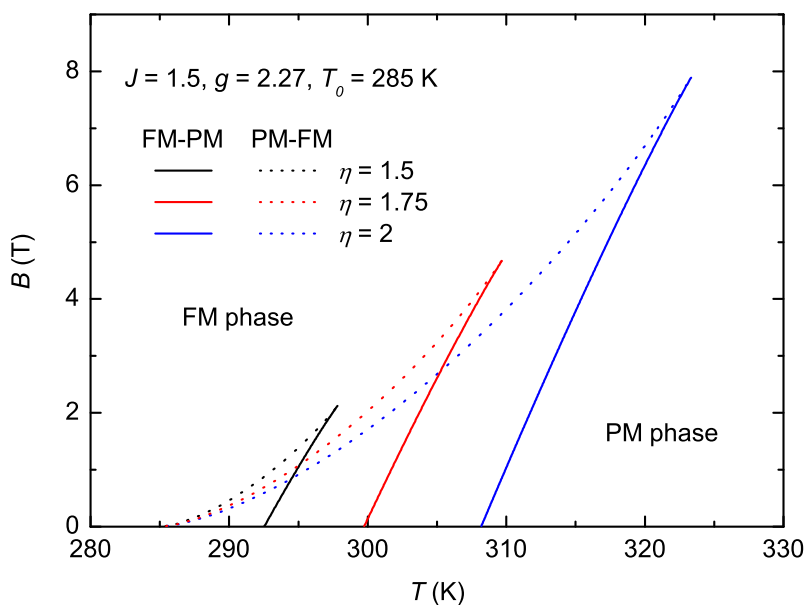
Figure 7.47: Theoretically predicted magnetic phase diagrams on the basis of the Bean-Rodbell model with different values of η. Dotted and solid lines denote the phase transitions from PM to FM and from FM to PM, respectively.

0 and 9 T. Unlike the pure magnetic entropy curves displayed in figure 7.44, where the magnitude of each curve is limited to $R\ln(2J+1)$ above the transition temperature, the total entropy increases monotonically with increasing temperature due to the presence of the lattice and electronic contributions. These curves semi-quantitatively agree with the entropy curves obtained from the experimental heat-capacity data for the $Mn_{1-x}T_xAs$ compounds.

From the total entropy curves, ΔS_T and ΔT_S can be determined by using equations (2.23) and (2.24), respectively. In figures 7.49 and 7.50, the temperature dependence of ΔS_T and the temperature dependence of ΔT_S are shown, respectively. Dotted and solid curves denote the results calculated from the entropy curves of figure 7.48 on cooling and heating, respectively. Dashed lines represent the experimental data of $Mn_{0.994}Fe_{0.006}As$. One can see that the profiles of the ΔS_T and ΔT_S curves predicted by the Bean-Rodbell model are similar to the experimental ones. However, the magnitude and width of the theoretical peaks are not well coincident with the experimental ones. The model gives higher discrepancies on cooling than on heating. Moreover, for a field change of 5 T, the maxima, $-\Delta S_{T,\max} = 0.55R$ on heating and $-\Delta S_{T,\max} = 0.77R$ on cooling, derived from the Bean-Rodbell model are in agreement
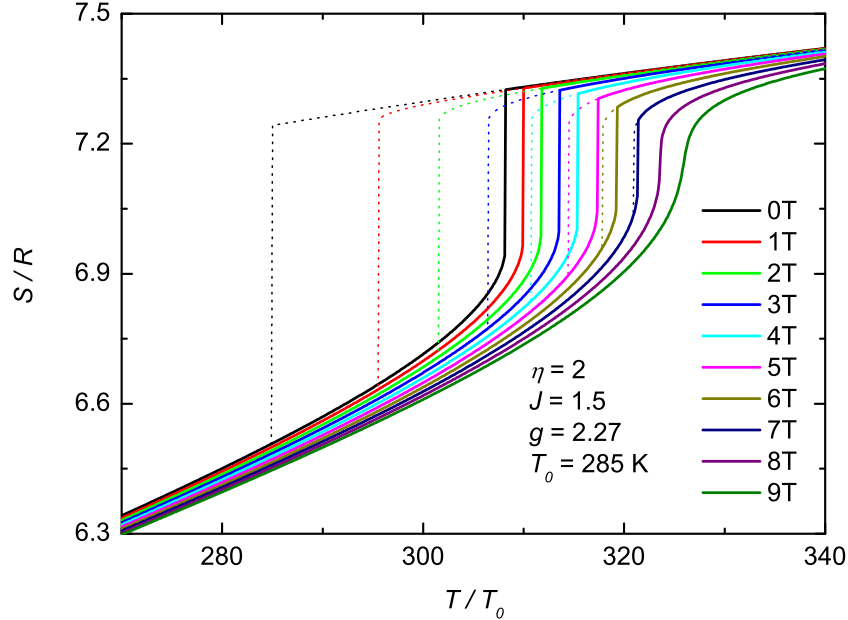
Figure 7.48: Total entropy as a function of temperature at constant magnetic fields in the case of $\eta = 2$. Solid lines: on heating. Dotted lines: on cooling.

with $-\Delta S_{T,\text{max}} = 0.58R$ and $-\Delta S_{T,\text{max}} = 0.73R$, respectively, obtained on the basis of Landau theory [160].

Accordingly, the Bean-Rodbell model can only provide a semi-quantitative description of the isofield magnetization, isothermal magnetization, total entropy, isothermal entropy change, adiabatic temperature change, in the Mn_{1-x} $T_x As$ compounds. The discrepancies between the theoretical and experimental results are probably explained as follows: First of all, the Bean-Rodbell model assumes that only the spin system is magnetic field dependent, however, the lattice and electronic contributions, especially the latter could be strongly influenced by applying an external magnetic field in real materials. Second, the Bean-Rodbell model takes into account only the coupling between the exchange interaction and volume, but without considering the orthorhombic lattice distortion which actually occurs in the $Mn_{1-x}T_x As$ compounds. Therefore, coupled order parameters should be employed to describe the strong interplay of the structural and magnetic properties in the $Mn_{1-x}T_x As$ compounds. It has been pointed out that the phase diagram of MnAs can be properly described by the Pytlik-Zięba model with two coupled order parameters [27]. The Pytlik-Zięba model gives a more effective simulation of the magnetic properties of MnAs than the Bean-model does [29]. Third, the Bean-Rodbell model de-
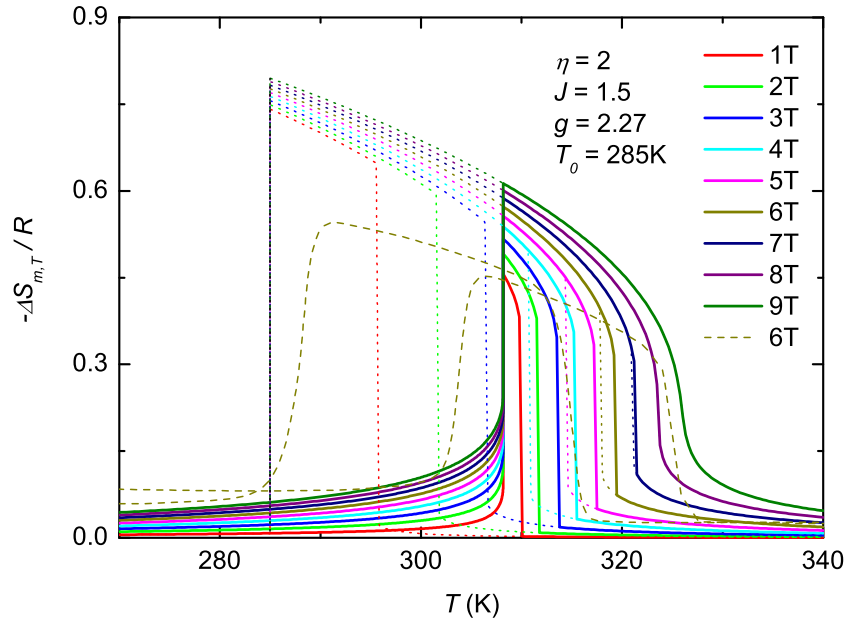
Figure 7.49: Magnetic entropy change as a function of temperature obtained from the total entropy curves in the case of $\eta = 2$. Solid lines: on heating. Dotted lines: on cooling. Dashed lines: the experimental data of $Mn_{0.994}Fe_{0.006}As$.
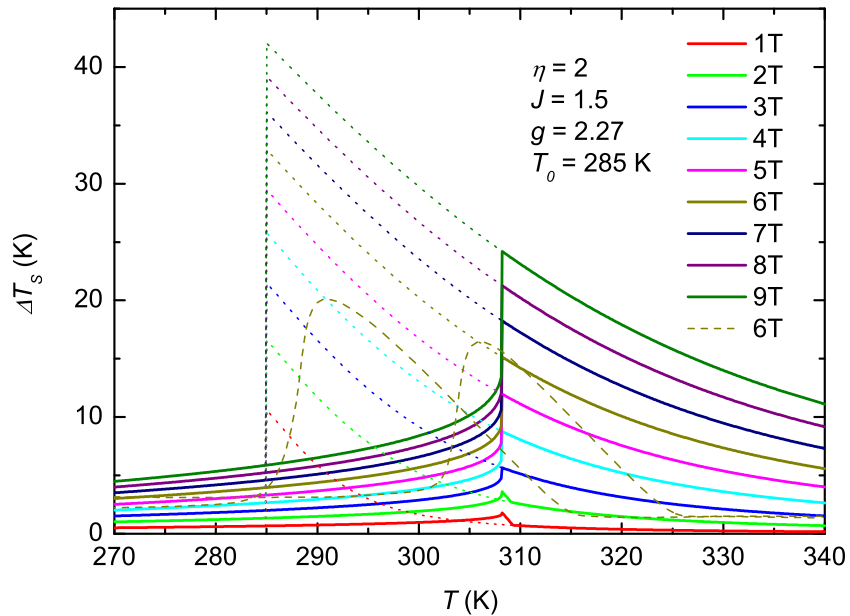

Figure 7.50: Adiabatic temperature change as a function of temperature obtained from the total entropy curves in the case of $\eta = 2$. Solid lines: on heating. Dotted lines: on cooling. Dashed lines: the experimental data of $Mn_{0.994}Fe_{0.006}As$.

scribes magnetoelastic transitions occurring in perfect systems which are not the case for the present $Mn_{1-x}T_xAs$ compounds. For instance, the existence of defects may lower the energy barrier of the FOPT, leading to smaller hystereses than the calculated ones. Last but not least, only the long-range interaction but no short-range order is considered in the Bean-Rodbell model, whereas the latter term is usually observed experimentally just above the transition temperature. That, definitely results in a larger entropy change of the system in the model than in a real material.

7.6 Conclusions

We have studied the structural, magnetic and magnetocaloric properties of $Mn_{1-x}T_xAs$ compounds with T = Fe and Co by means of XRD, magnetization and calorimetry techniques. The corrections of irreversibility have been carried out to obtain precise ΔS_T. The Bean-Rodbell model was employed to illustrate the phase transition and the magnetic properties of the studied compounds semi-quantitatively. Then, some conclusions can be made:

- Up to 1.5 % and 2 % substitutions of Mn by Fe and Co do not destroy the first-order magnetostructural transition occurring in MnAs. The doping with Fe and Co has similar effects on the magnetic and magnetocaloric properties of MnAs. That is, with increasing content of Fe or Co, the transition shifts to lower temperatures, the hysteresis increases, the heat-capacity anomaly decreases and broadens. An unusual virgin behavior is found in the heat capacity at zero field in as-prepared samples $Mn_{0.985}Fe_{0.015}As$ and $Mn_{0.98}Co_{0.02}As$.

- The plots of ΔS_T of all the studied $Mn_{1-x}T_xAs$ compounds exhibit spurious "spikes" when determined from isothermal magnetization data measured following protocol 1 on increasing and decreasing fields. On increasing field, the height of the "spike" is significantly reduced by performing the isothermal magnetization measurements following protocol 2. On decreasing field, the "spike" effect does not show when taking into account only the data at low fields (e.g. below 6 T) after applying a higher maximum field (e.g. 9 T).

- The "spike" effect does not happen in ΔS_T derived from isofield magnetization data. However, there could be an underestimation of $\left(\frac{\partial M}{\partial T}\right)_B$ in the case of sharp transitions as occur in the $Mn_{1-x}T_xAs$ compounds, leading to an underestimation of $|\Delta S_T|$. The heat capacities at constant magnetic fields produce more precise results of ΔS_T and ΔT_S. Direct measurements give coinciding results with those from heat capacity only

when the direct measurements in the transition region are carried out following protocols 2 and 3.

- Taking into account the corrections of irreversibility in each technique, precise and coinciding ΔS_T values can be obtained from all the three techniques, i.e. magnetic, calorimetric and direct methods. Consequently, giant but not colossal MCE is found in the $Mn_{1-x}T_xAs$ compounds over a large temperature range near room temperature. The MCEs of the studied $Mn_{1-x}T_xAs$ compounds are comparable to that of MnAs, but locate at lower temperatures.

- The phase transition and magnetocaloric properties of the $Mn_{1-x}T_xAs$ compounds can be semi-quantitatively illustrated with the Bean-Rodbell model.

Chapter 8

Series of Mn$_{2-x}$Fe$_x$P$_{0.75}$Ge$_{0.25}$

8.1 Introduction

MnFeP$_{1-x}$As$_x$ compounds with $0.32 < x < 0.6$ crystallize in the hexagonal Fe$_2$P-type structure (space group $P\bar{6}2m$) and exhibit a magnetoelastic transition from FM to PM phase upon increasing temperature [161]. The Fe$_2$P-type compounds show their great potentials to be magnetic refrigerants, such as large MCE, tunable transition temperature and low price of raw materials [42, 162]. Although the parent compounds MnFeP$_{1-x}$As$_x$ contain the toxic element As, it can be completely replaced by Si or / and Ge without losing the characteristics of GMCE, while producing larger hysteresis [46, 47, 49–52]. In a recent paper, Trung *et al.* [48] have pointed out that the thermal hysteresis can be reduced or even eliminated via adjusting the ratio of Mn / Fe and improving the preparation technology. They reported the values of ΔS_T calculated from isothermal magnetization data in (Mn,Fe)$_2$(P,Ge) compounds which were prepared by means of ball-milling and melt-spinning methods. The peak values of $|\Delta S_T|$ are between 10 J/kg·K and 20 J/kg·K in those compounds for a low magnetic field change of 2 T, being much larger than ~ 4 J/kg·K in Gd metal for the same field change [48]. That is favorable to magnetic refrigeration working with permanent magnets. Therefore, it is meaningful to study the calorimetric properties as well as to characterize ΔS_T and ΔT_S precisely in these compounds for the purpose of application.

In this chapter, we report on the calorimetric measurements providing the field dependent heat capacity $C_{p,B}$, ΔS_T and ΔT_S in two bulk compounds, Mn$_{1.26}$Fe$_{0.74}$P$_{0.75}$Ge$_{0.25}$ and Mn$_{1.18}$Fe$_{0.82}$P$_{0.75}$Ge$_{0.25}$ (provided by E. Brück's group). The first compound exhibits the smallest thermal hysteresis (~ 0 K) among the bulk samples reported in Ref. [48] and the second one shows a visible hysteresis of ~ 3 K.

8.2   Sample preparation

Two polycrystalline samples with nominal compositions Mn$_{2-x}$Fe$_x$P$_{0.75}$Ge$_{0.25}$ with $x = 0.74$ and 0.82 were prepared by means of the high-energy ball milling, the details of the preparation can be found elsewhere [48]. The ground powder was sintered at 1100 °C for 10 h and then homogenized at 650 °C for 60 h, and then quenched into water at room temperature.

8.3   Mn$_{1.26}$Fe$_{0.74}$P$_{0.75}$Ge$_{0.25}$

8.3.1   Heat capacity

The plots of the heat capacity versus temperature at zero field and a field of 5 T for Mn$_{1.26}$Fe$_{0.74}$P$_{0.75}$Ge$_{0.25}$ are displayed in figure 8.1. A sharp peak centering at 268 K in the heat capacity at zero field ($C_{p,0}$) indicates a phase transition occurring at the Curie temperature T_C. The value of T_C agrees with the value 267 K derived from magnetization curves by Trung *et al.* [48], where T_C was determined as the temperature corresponding to the minimum of $(\partial M/\partial T)_B$, as shown in the inset of figure 8.1. The weak anomaly at $\sim$117 K can be ascribed to a small amount of impurity phase MnO [163] which could come from the oxidization during preparation or the oxidized starting manganese. By comparing the transition enthalpy of the impurity phase with the standard transition enthalpy of pure MnO, the presence of $\sim$1.7 % MnO in mass has been concluded. In the presence of a field of 5 T, the heat-capacity anomaly moves to a higher temperature, and becomes weaker and broader when comparing with the zero-field one.

Trung *et al.* claimed that the nature of the transition occurring in the compound with $x = 0.74$ is second order, since no thermal hysteresis was realized in the magnetization measurement [48]. However, as seen in figure 8.1, the shape of the heat-capacity anomaly is more like a FOPT rather than a SOPT. In order to ascertain the nature of the transition, we have also measured the heat capacity on cooling. Consequently, a thermal hysteresis of 0.8 K is observed, as shown in figure 8.2. The hysteresis is small, but it still implies that the nature of the transition is first order in the present compound.

The lattice and electronic heat capacities of Mn$_{1.26}$Fe$_{0.74}$P$_{0.75}$Ge$_{0.25}$ were estimated by using equations (2.33) and (2.36), respectively, providing that they are magnetic field independent. Using the Debye temperature $\theta_D = 420$ K and the electronic coefficient $\gamma_e = 24$ mJ/K^2·mol of Fe$_2$P [110] in the estimation, the resulting summation of the lattice and electronic heat capacities, $C_l + C_e$, is denoted as a green line in figure 8.1. Then the magnetic contri-
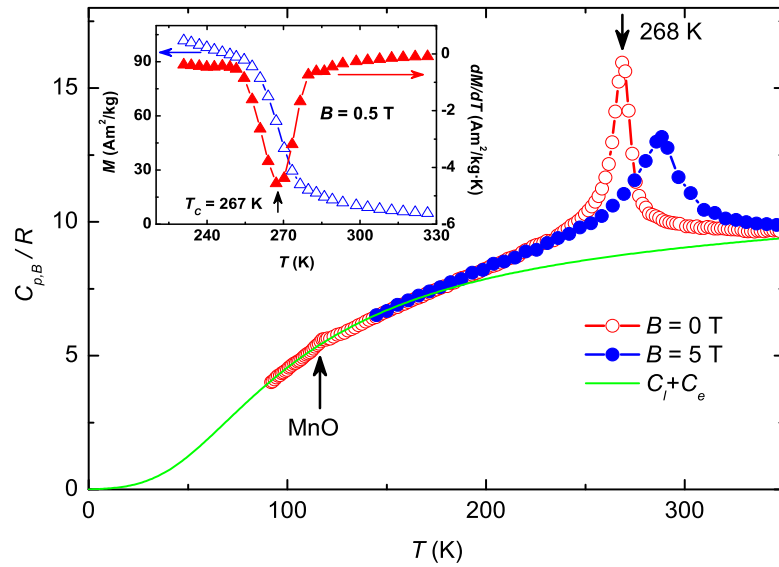
Figure 8.1: Heat capacity as a function of temperature measured at 0 and 5 T for $Mn_{1.26}Fe_{0.74}P_{0.75}Ge_{0.25}$. Green line represents the nonmagnetic heat capacity. Inset shows temperature dependence of the magnetization and its first derivative.
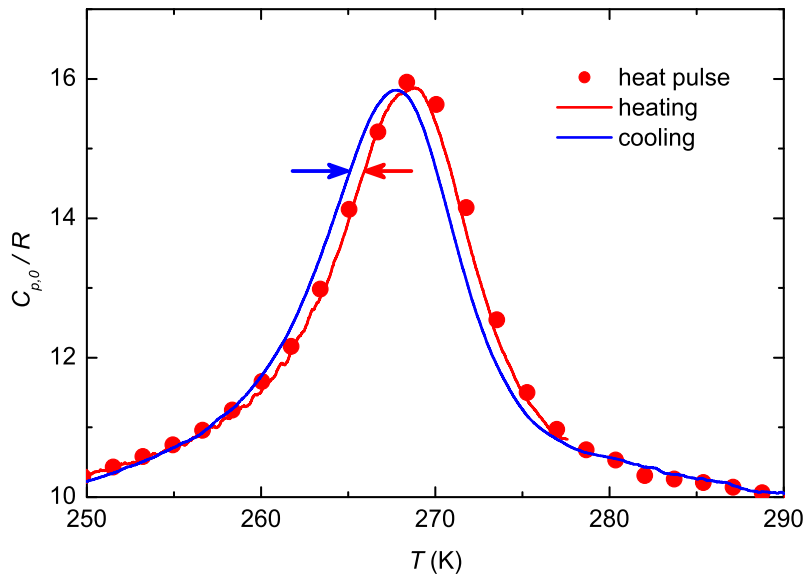

Figure 8.2: Heat capacity as a function of temperature measured at zero field near the transition temperature on heating and cooling for $Mn_{1.26}Fe_{0.74}P_{0.75}Ge_{0.25}$. Symbols and lines were obtained with the heat-pulse and thermogram techniques, respectively.
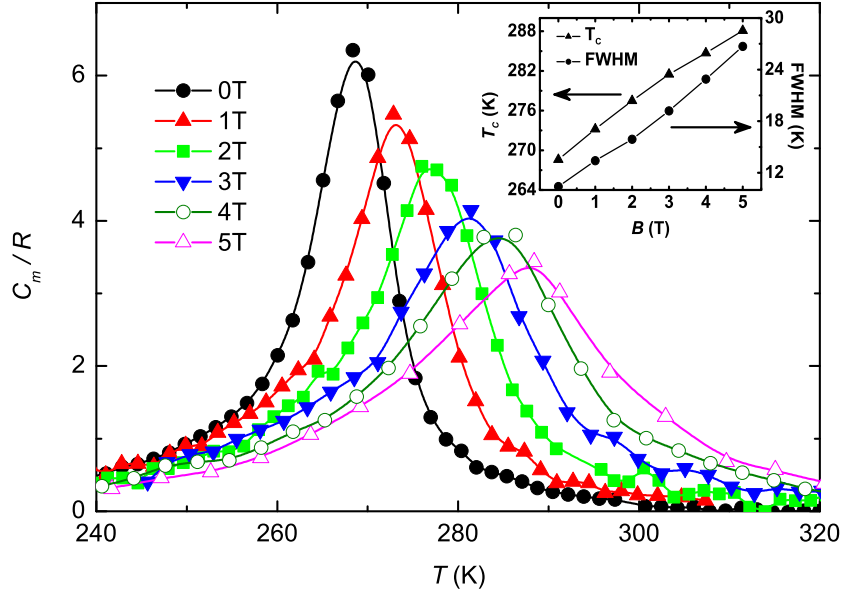
Figure 8.3: Magnetic heat capacity as a function of temperature at different constant magnetic fields for Mn$_{1.26}$Fe$_{0.74}$P$_{0.75}$Ge$_{0.25}$. Inset displays the plots of the transition temperature (left axis) and the full width at half maximum of the C_m peak (right axis) as functions of magnetic field.

bution was obtained by subtracting the nonmagnetic contributions from the total heat capacity. The plots of the temperature dependence of the magnetic heat capacity (C_m) at constant magnetic fields of 0, 1 T, 2 T, 3 T, 4 T and 5 T are displayed in figure 8.3. By applying magnetic fields, the C_m peak shifts to higher temperatures, simultaneously broadens and lowers. As seen in the inset of figure 8.1, the transition temperature and the full width at half maximum (FWHM) of the C_m peak increase approximately in a linear way with increasing field.

The transition temperature T_t at each constant field, which has been taken as the temperature corresponding to the maximum value of $C_{p,B}$, is listed in table 8.1. It is seen that T_t increases from 268 K at 0 T to 288 K at 5 T. The magnetic enthalpy of the transition, ΔH_m, and the magnetic entropy of the transition, ΔS_m, can be determined by using equations (2.45) and (2.46), respectively. In the present sample, the integration was done between $T_1 = 220$ K and $T_2 = 340$ K for each constant field. The resulting values of ΔH_m and ΔS_m at various constant fields are listed in table 8.1. The large value of ΔS implies a large MCE of Mn$_{1.26}$Fe$_{0.74}$P$_{0.75}$Ge$_{0.25}$.

Table 8.1: Transition temperature, transition enthalpy and transition entropy at various constant fields for $Mn_{1.26}Fe_{0.74}P_{0.75}Ge_{0.25}$.

B (T)	T_t (K)	ΔH_m (J/g)	ΔS_m (J/kg·K)
0	268	5.65	21.1
1	273	5.77	21.1
2	278	6.20	22.3
3	281	6.50	23.1
4	285	6.73	23.6
5	288	6.69	23.2

8.3.2 Magnetocaloric effect

The total entropies at different magnetic fields have been determined by integrating $C_{p,B}/T$. Then, the magnetocaloric parameters, ΔS_T and ΔT_S, were obtained using equations (2.23) and (2.24). The resulting curves of ΔS_T and ΔT_S are displayed in figures 8.4 and 8.5, respectively. For comparison, ΔS_T and ΔT_S were also determined from direct measurements, indicated as symbols in figures 8.4 and 8.5. Both, ΔS_T and ΔT_S derived from the $C_{p,B}$ data are found to be in good agreement with those obtained from the direct measurements. The values of ΔS_T for field changes of 1 T and 2 T are consistent with those calculated from isothermal magnetization data, reported earlier by Trung *et al.* [48].

For a magnetic field change of 5 T, the maximum value of $-\Delta S_T$ for $Mn_{1.26}Fe_{0.74}P_{0.75}Ge_{0.25}$ is found to be 14.7 J/kg·K which is larger than 10.5 J/kg·K for Gd metal. But the maximum, $\Delta T_{S,max} = 6.2$ K, is only one half of that for Gd metal (12 K) for the same field variation [5]. It should be attributed to the smaller heat capacity of Gd per unit mass comparing to the studied compound. For a low field change of 2 T, the maximum of ΔT_S is found to be 3.1 K.

8.4 $Mn_{1.18}Fe_{0.82}P_{0.75}Ge_{0.25}$

In $(Mn,Fe)_2(P,Ge)$-type compounds, the ratios of Mn:Fe and P:Ge have relevant influences on transition temperature and hysteresis. In general, a large Mn:Fe ratio leads to a decrease of both the transition temperature and hysteresis, a large P:Ge ratio leads to a decrease of the transition temperature and an increase of the hysteresis, and viceversa [164]. In this section, we report
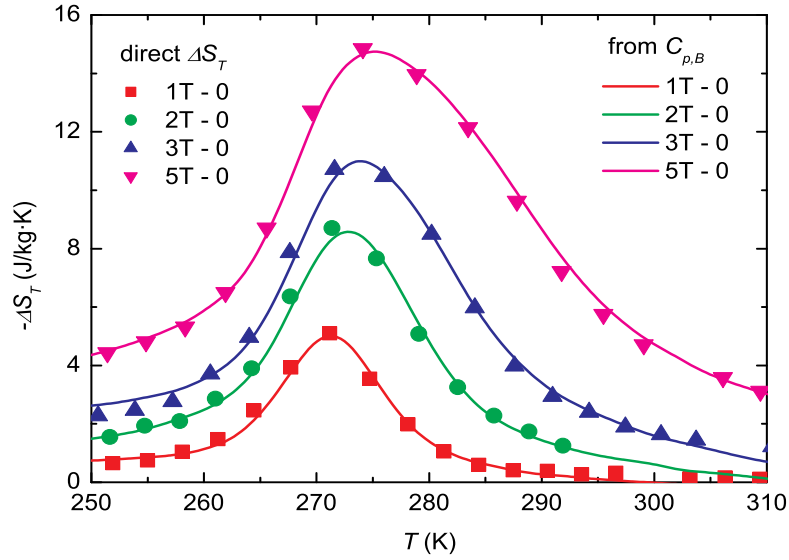
Figure 8.4: Temperature dependence of the isothermal entropy change for Mn$_{1.26}$Fe$_{0.74}$P$_{0.75}$Ge$_{0.25}$ upon magnetic field changes of 1 T, 2 T, 3 T and 5 T. Symbols: determined from direct measurement. Lines: calculated from heat capacity.
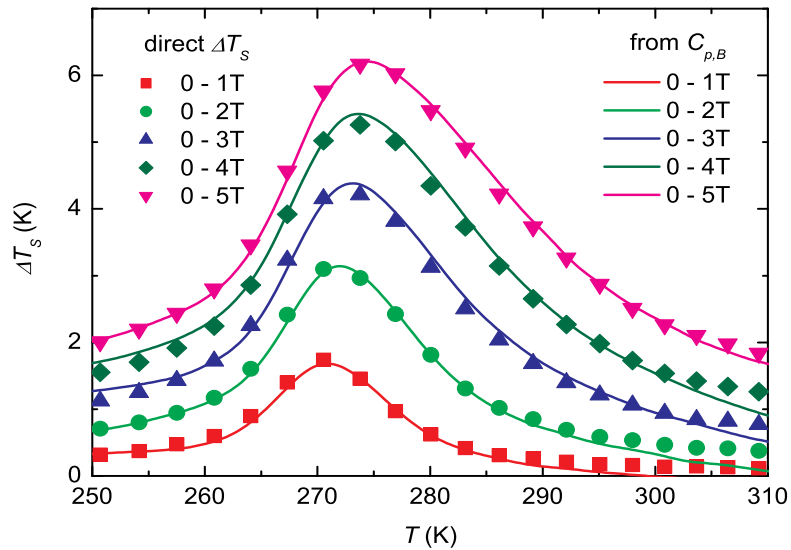

Figure 8.5: Temperature dependence of the adiabatic temperature change for Mn$_{1.26}$Fe$_{0.74}$P$_{0.75}$Ge$_{0.25}$ upon magnetic field changes of 1 T, 2 T, 3 T, 4 T and 5 T, respectively. Symbols: determined from direct measurement. Lines: calculated from heat capacity.

on the properties of $Mn_{1.18}Fe_{0.82}P_{0.75}Ge_{0.25}$ which contains less Mn than the previous sample.

8.4.1 Heat capacity

In figure 8.6, we present the temperature dependence of the heat capacity measured at zero field for the samples with $x = 0.74$ and 0.82. The heat-capacity anomaly, which is the indication of the transition of the main phase, shifts to higher temperature with a decrease of the Mn:Fe ratio. Specifically, the transition temperature varies from 268 K to 307 K when x changes from 0.74 to 0.82, that agrees with the magnetization curves of Ref. [48]. The heat-capacity anomaly for $Mn_{1.18}Fe_{0.82}P_{0.75}Ge_{0.25}$ becomes much sharper and higher than that for $Mn_{1.26}Fe_{0.74}P_{0.75}Ge_{0.25}$, indicating an enhancement of the temperature-induced FOPT. In addition, the observation of small peaks situated at the same temperature 117 K for both compounds further proves the existence of the unavoidable impurity of MnO.

Figure 8.7 shows the temperature dependence of the heat capacity measured at constant magnetic fields of 0, 1 T, 2 T, 3 T, 4 T and 5 T on heating and cooling processes for $Mn_{1.18}Fe_{0.82}P_{0.75}Ge_{0.25}$. The heat capacity obtained from the heating thermogram method agrees well with that measured with the heat-pulse technique. At zero field, a difference of 1.7 K between the anomalies on heating and cooling is observed in $Mn_{1.18}Fe_{0.82}P_{0.75}Ge_{0.25}$, defining a thermal hysteresis, that is larger than 0.8 K of $Mn_{1.26}Fe_{0.74}P_{0.75}Ge_{0.25}$. The existence of the hysteresis further indicates the nature of the transition being of first order. The size of the hysteresis is lower than 3 K derived from magnetization data in Ref. [48] for the same sample. The hysteresis decreases slowly with increasing field, but still maintains a non-zero value at 5 T. Coinciding result is also found in the isothermal magnetization measurement, where small magnetic hysteresis is visible at 5 T (see figure 8.8). The heat-capacity anomaly lowers and broadens, meanwhile, its position moves to higher temperatures with increasing field. These characteristics are very similar to those observed in $Mn_{1.26}Fe_{0.74}P_{0.75}Ge_{0.25}$.

8.4.2 Magnetocaloric effect

The total entropy at each magnetic field has been calculated from the heat-capacity data of figure 8.7. Figure 8.9 displays the resulting entropy curves at constant fields of 0, 1 T, 2 T, 3 T, 4 T and 5 T on heating. One can see that an entropy jump takes place at the transition temperature at zero field, originating from the sharp anomaly of the heat capacity, namely, a FOPT. The jump is gradually smoothed by applying magnetic fields. ΔS_T and ΔT_S have been
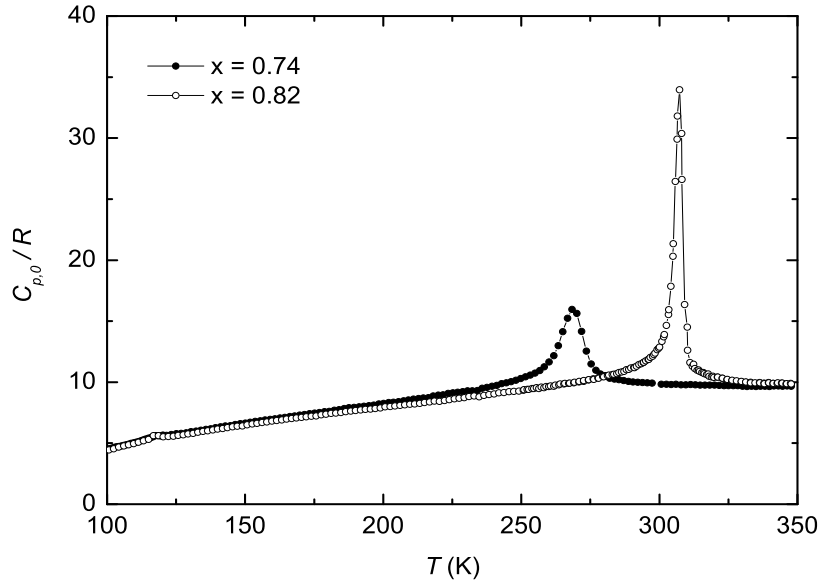
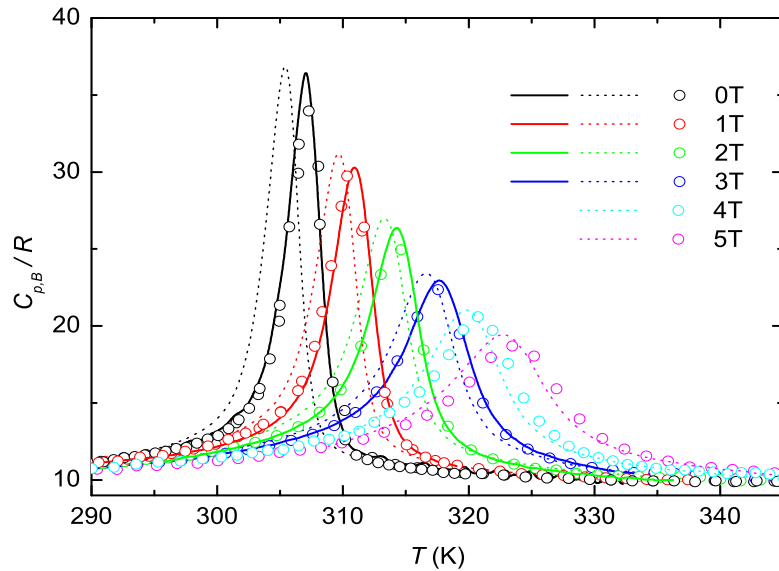Figure 8.6: Temperature dependence of the heat capacity measured at zero field for the compounds with $x = 0.74$ and 0.82.

Figure 8.7: Temperature dependence of the heat capacity measured at constant magnetic fields of 0, 1 T, 2 T, 3 T, 4 T and 5 T for $Mn_{1.18}Fe_{0.82}P_{0.75}Ge_{0.25}$. Solid lines: heating thermograms. Dotted lines: cooling thermograms. Symbols: measured with the heat-pulse technique.
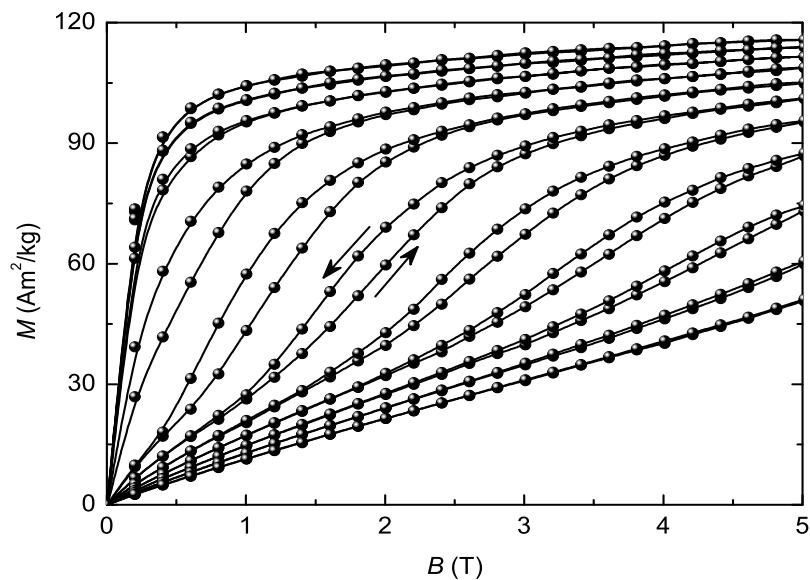
Figure 8.8: Isothermal magnetization as a function of magnetic field for $Mn_{1.18}Fe_{0.82}P_{0.75}Ge_{0.25}$ measured in the vicinity of its transition temperature on increasing and then decreasing fields. Measuring temperatures are from 298 K to 328 K with an interval of 3 K.
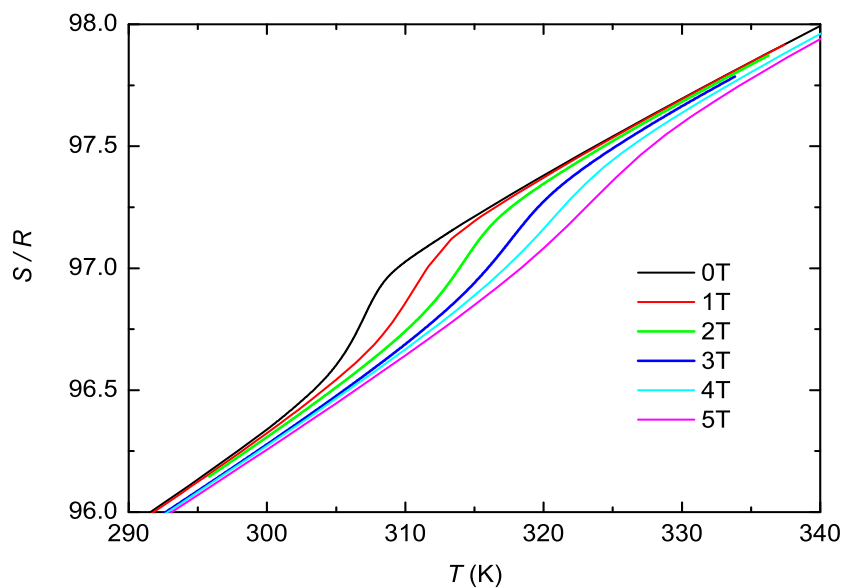

Figure 8.9: Total entropy curves obtained from heat capacity on heating at constant magnetic fields for $Mn_{1.18}Fe_{0.82}P_{0.75}Ge_{0.25}$.

determined from the total entropy curves for different field changes. The resulting ΔS_T and ΔT_S values are plotted in figures 8.10 and 8.11, respectively. For comparison, ΔT_S and ΔS_T determined from direct measurements performed following protocols 1 and 4, respectively, are plotted together. Because the effects of irreversibility in both methods are very small and negligible, a good agreement is observed between the data obtained from the heat-capacity and direct measurements for both ΔS_T and ΔT_S.

In figure 8.10, dashed and dotted lines represent ΔS_T for a field change of 5 T obtained from isothermal magnetization data on increasing and decreasing fields, respectively. Using the magnetization loops of figure 8.8, a value of $dA/dT = –0.5$ J/kg·K was computed. Therefore, the obtained maximum of $|\Delta S_T|$ on increasing field is expected to be 1.0 J/kg·K higher than that on decreasing field due to the irreversibility. In practice, we observed a difference of 0.9 J/kg·K between the dashed and dotted lines just above the transition temperature, agreeing well with the calculated value. Taking into account the correction of the irreversibility, the resulting values of ΔS_T are coincident with those determined from the heat-capacity and direct measurements.

In figures 8.10 and 8.11, it is found that the increment of the maximum of ΔS_T becomes smaller and smaller with increasing field, but $\Delta T_{S,\mathrm{max}}$ shows a nearly linear change with the field. We obtained the maxima, $-\Delta S_{T,\mathrm{max}}$ to be 11.5 J/kg·K, 15.8 J/kg·K, 18.5 J/kg·K, 19.6 J/kg·K and 21.0 J/kg·K, and $\Delta T_{S,\mathrm{max}}$ to be 2.9 K, 5.2 K, 6.8 K, 8.1 K and 9.3 K for field changes of 1 T, 2 T, 3 T, 4 T and 5 T, respectively. These values are larger than those of $Mn_{1.26}Fe_{0.74}P_{0.75}Ge_{0.25}$ for the same corresponding field change. For a field change of 2 T, the maximum, $-\Delta S_{T,\mathrm{max}} = 15.8$ J/kg·K, agrees with 16 J/kg·K determined from magnetization data in Ref. [48].

8.5   Refrigeration capacity

The observation of large MCE near room temperature and small hysteresis in the $Mn_{2-x}Fe_xP_{0.75}Ge_{0.25}$ compounds makes them to be promising candidates as magnetic refrigerants. The relative refrigeration capacities (RCPs) of the studied samples have been calculated with the help of equations (2.52) and (2.53). For field changes of 2 T and 5 T, the values of $RCP(S)$ and $RCP(T)$ are found to be 132 J/kg and 422 J/kg, 53 K^2 and 187 K^2 for $Mn_{1.26}Fe_{0.74}P_{0.75}Ge_{0.25}$, and 132 J/g and 399 J/kg, 44 K^2 and 160 K^2 for $Mn_{1.18}Fe_{0.82}P_{0.75}Ge_{0.25}$, respectively. For the latter compound, the energy loss caused by the irreversibility $Q_{loss} = 8$ J/kg was evaluated by $Q_{loss} = -\frac{1}{2} \oint M dB$ from the magnetization loop with a maximum magnetic field of 5 T at 310 K. That results in the value of $RCP(S)_{eff}$ to be 391 J/kg. The
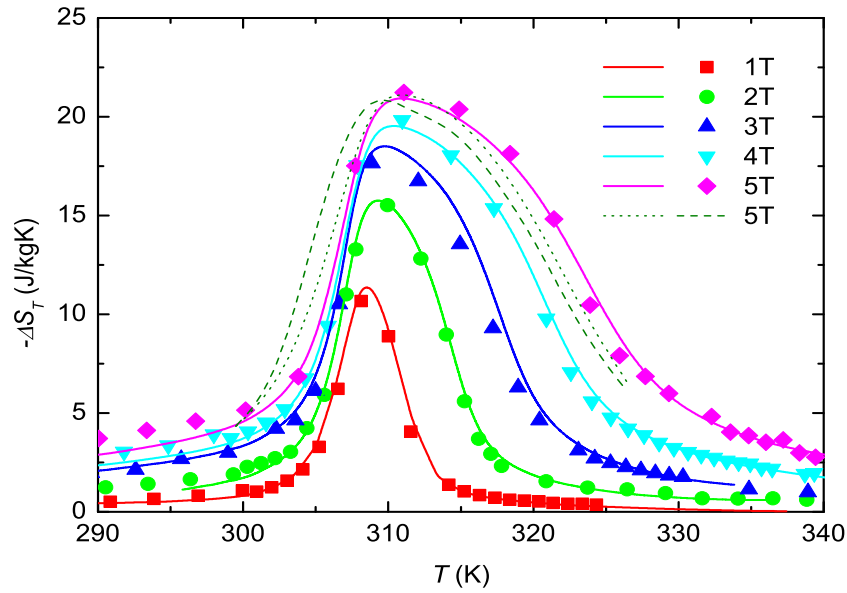
Figure 8.10: Isothermal entropy change as a function of temperature for $Mn_{1.18}Fe_{0.82}P_{0.75}Ge_{0.25}$. Solid lines: from heat capacity on heating. Symbols: from direct measurement. Dashed and dotted lines: from isothermal magnetization on increasing and decreasing fields, respectively.
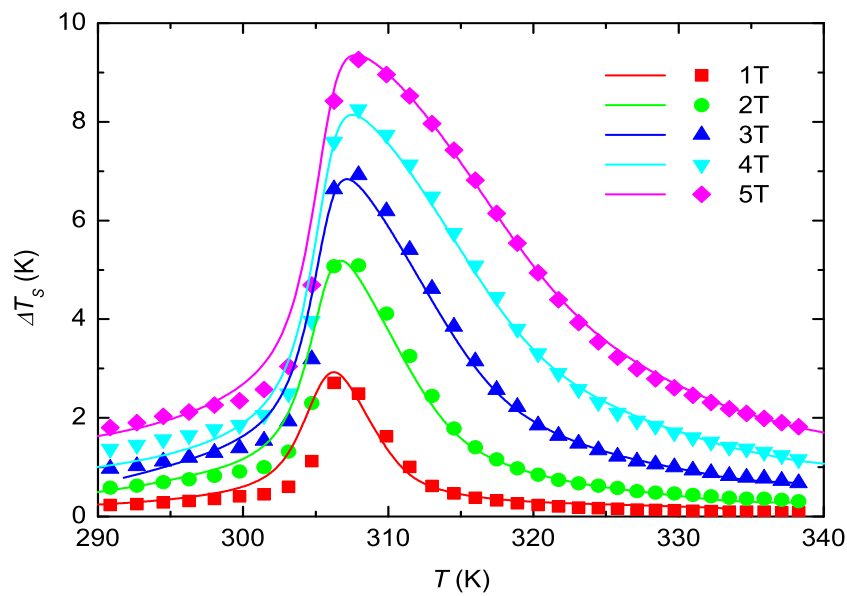

Figure 8.11: Adiabatic temperature change as a function of temperature for $Mn_{1.18}Fe_{0.82}P_{0.75}Ge_{0.25}$. Lines: determined from heat capacity on cooling. Symbols: obtained from direct measurement.

observed $RCP(S)_{eff}$ value of $Mn_{1.26}Fe_{0.74}P_{0.75}Ge_{0.25}$ is higher than that of $Mn_{1.18}Fe_{0.82}$ $P_{0.75}Ge_{0.25}$ for the same field change of 5 T, although the MCE of the latter compound is larger. The effective RCPs of the studied compounds are comparable to that of Gd metal. The studied compounds show large MCEs in a moderate temperature range, that is beneficial to multi-material active magnetic refrigeration working in a broad temperature range.

8.6   Conclusions

In summary, we have precisely determined the heat capacity and magnetocaloric parameters of $Mn_{2-x}Fe_xP_{0.75}Ge_{0.25}$ compounds. We concluded that:

- The nature of the transitions in the studied compounds is first order. The compounds present small, but clear, thermal hysteresis. The transition temperature and hysteresis are influenced by the Mn:Fe ratio, what also happens when changing the P:Ge ratio [164]. Therefore, improved magnetocaloric materials could be obtained by tailoring the ratios of Mn:Fe and P:Ge.

- Large MCE is observed in the studied compounds near room temperature. The maxima obtained upon field changes of 2 T and 5 T are $-\Delta S_{T,\max} = 8.6$ J/kg·K and 14.7 J/kg·K and $\Delta T_{S,\max} = 3.1$ K and 6.2 K for $Mn_{1.26}Fe_{0.74}P_{0.75}Ge_{0.25}$, and $-\Delta S_{T,\max} = 15.8$ J/kg·K and 21.0 J/kg·K, and $\Delta T_{S,\max} = 5.2$ K and 9.3 K for $Mn_{1.18}Fe_{0.82}P_{0.75}Ge_{0.25}$. The effective refrigeration capacities for the two compounds are comparable to that of Gd metal. Accordingly, they are promising as magnetic refrigerant materials working near room temperature.

Chapter 9

MnCo$_{0.98}$Cu$_{0.02}$GeB$_{0.02}$

9.1 Introduction

The intermetallic compound MnCoGe is a collinear ferromagnet ($T_C = 355$ K). It has the orthorhombic TiNiSi-type structure at room temperature, and the hexagonal Ni$_2$In-type structure at high temperatures (above $\sim$650 K) [165, 166]. In the two structures, their unit cell axes and volume are related as $a_{orth} = c_{hex}$, $b_{orth} = a_{hex}$, $c_{orth} = \sqrt{3}a_{hex}$ and $V_{orth} = 2V_{hex}$ [165]. The structural transition in MnCoGe is accompanied by a strong thermal hysteresis (about 40 K) and a large negative cell volume contraction (about 3.9 %) at a transition temperature T_{str} [166]. T_{str} is extremely sensitive to stoichiometry, therefore, quite different values of T_{str} (from 398 to 650 K) were reported by several groups [165–169]. Besides, it was found that T_{str} can also be changed by applying an external pressure [170–172].

Independently of the structural transition, the magnetic transition in MnCoGe behaves like a SOPT either in the orthorhombic structure or in the hexagonal structure [167, 173]. However, different values of saturation magnetization were observed in the two structures, being of 3.86 μ_B in the orthorhombic structure and 2.58 μ_B in the hexagonal structure [165]. The Curie temperature can be turned by varying the composition or by elemental substitution [165, 166, 172, 173].

The magnetocaloric properties of MnCoGe and related compounds have been studied by several research groups. In 2006, Song *et al.* reported the MCEs of MnCo$_{1-x}$Fe$_x$Ge compounds with $0 \leq x \leq 1$ [173]. They found that a structural change from the orthorhombic structure to the hexagonal structure is caused by substituting Co with Fe for $x > 0.2$. For a field change of 5 T, the value $-\Delta S_{T,\max} = 9$ J/kg·K was found in the compound with $x = 0.2$. The

value is larger than 6 J/kg·K observed in the parent MnCoGe for the same field change. Inverse MCEs were observed in the Si-rich MnCoGe$_{1-x}$Si$_x$ compounds ($x = 0.92$, 0.95 and 1), originating from a FOPT from low-temperature AFM to high-temperature FM phase [29, 174]. For the $x = 0.95$ compound, the maximum value $\Delta S_{T,\max} = 3.5$ J/kg·K for a field change of 6 T found by Tocado [29] is much lower than 9.0 J/kg·K for a field change of 5 T reported by Sandeman *et al.* [174]. The former value determined from direct measurement is more precise than the latter derived from isothermal magnetization measurement in such a compound undergoing FOPT. The Al-doped MnCoGe compounds exhibit quite similar properties as the Fe-doped compounds. The compositional boundary between the orthorhombic and hexagonal structures was found to be $x \sim 0.03$ in the Al-doped ones [175]. The highest MCE was found in the compound with $x = 0.08$, being $-\Delta S_{T,\max} = 1.5$ J/kg·K for a field change of 1.5 T. The nature of the transitions occurring in the Al-doped compounds is second order in both the orthorhombic and hexagonal structures.

The presence of a first-order magnetostructural transition from the low-temperature orthorhombic FM phase to the high-temperature hexagonal PM phase in MnCoGe$_{1-x}$Sn$_x$ compounds with $0.04 \leq x \leq 0.055$ was demonstrated by Hamer *et al.* [176]. They found a large MCE with $-\Delta S_{T,\max} = 4.5$ J/kg·K for a rather low field change of 1 T in the compound with $x = 0.05$. Moreover, the first-order magnetostructural transition was also observed in the off-stoichiometric compounds MnCo$_{0.95}$Ge$_{1.14}$ [177] and MnCo$_{0.98}$Ge [164]. GMCEs with maxima $-\Delta S_{T,\max} = 6.4$ J/kg·K for $\Delta B = 1$ T and $-\Delta S_{T,\max} = 30.2$ J/kg·K for $\Delta B = 5$ T were reported in the two compounds, respectively.

Recently, Trung *et al.* have pointed out that the structural transition temperature T_{str} of MnCoGe can be lowered by adding B atoms in interstitial positions or by partly substituting Mn with Cr, which results in a coincidence of T_{str} and T_C, that is, leads to the occurrence of a magnetostructural transition [164, 178, 179]. Figure 9.1 schematically shows the influence of the B-doping on T_{str} and MCE in the MnCoGeB$_x$ compounds. By increasing the content of B, T_{str} can be controlled from a temperature far above T_C to a temperature far below T_C. For instance, with $x = 0.03$, both T_{str} and T_C decrease to the same temperature 275 K [178]. It is surprising that the B-doping with $x = 0.04$ already makes T_{str} to be lower than T_C, leading to a decoupling of the magnetic and structural transitions [164]. In the temperature range $T_{C2} \leq T \leq T_{C1}$, coupled magnetostructural transitions result in GMCEs in the MnCoGeB$_x$ compounds. The values of $-\Delta S_{T,\max}$ determined from isothermal magnetization data are 14.6 J/kg·K, 47.3 J/kg·K and 37.7 J/kg·K for a magnetic field change of 5 T for $x = 0.01$, 0.02 and 0.03, respectively. For MnCoGeB$_{0.05}$, the maximum $-\Delta S_{T,\max} = 3.4$ J/kg·K was found to be comparable to that of the undoped MnCoGe [164].
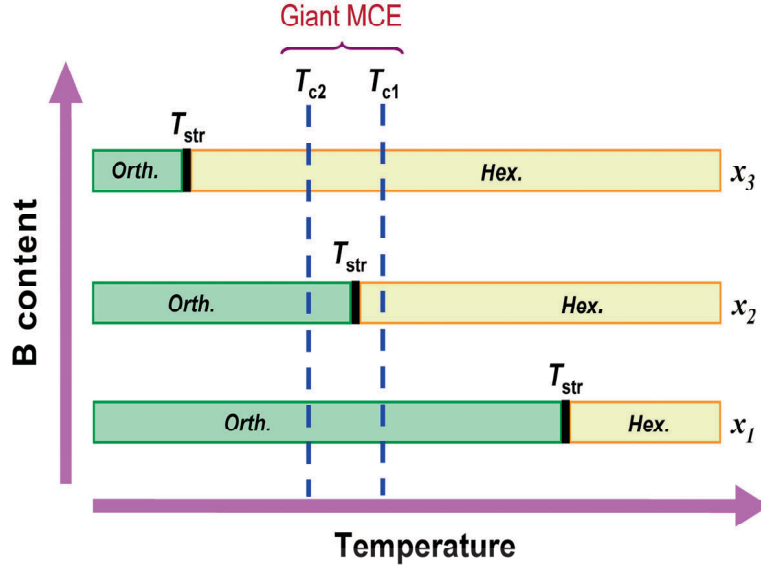
Figure 9.1: Schematic representation of the dependence of the structural transition temperature T_{str} on the B content for $MnCoGeB_x$. T_{C1} and T_{C2} denote the transition temperatures in orthorhombic and hexagonal structures, respectively, i.e. the temperature boundaries of the coupling between magnetic and structural transitions (taken from Ref.[164]).

Trung *et al.* [164] reported that the hexagonal Ni_2In-type phase in MnCoGe can be stabilized at ambient conditions by a slight substitution of Cu for Co. They found that T_C is lowered from 345 K for $x = 0$ to 329 K for $x = 0.02$ and to 315 K for $x = 0.04$. The presence of 4 K hysteresis in the compound with $x = 0.04$ indicates that the SOPT occurring in MnCoGe is changed to a FOPT by the substitution of Cu for Co. They reported that, for a field change of 5 T, the maximum value of $|\Delta S_T|$ increases from 5.6 J/kg·K for $x = 0$ to 10.6 J/kg·K for $x = 0.04$, although the saturation magnetization (at 5 K) decreases from 4.13 μ_B/f.u. to 3.93 μ_B/f.u.

The doping with Cr in MnCoGe does not only lead to a coupling of the magnetic and structural transitions at T_C, but also another transition appears from a low-temperature AFM phase to high-temperature FM phase at T_t, where T_t is lower than T_C [164, 179]. The compositional phase diagram of the $Mn_{1-x}Cr_xCoGe$ compounds is shown in figure 9.2. The magnetostructural transition in the compounds occurs up to a composition $x = 0.25$, above which the transition becomes a purely magnetic SOPT. The $Mn_{1-x}Cr_xCoGe$ compounds show GMCEs near their respective magnetostructural transition temperatures. Besides, similar results were also observed in some other element-doped compounds, such as the doping with Ni, V and C [164].
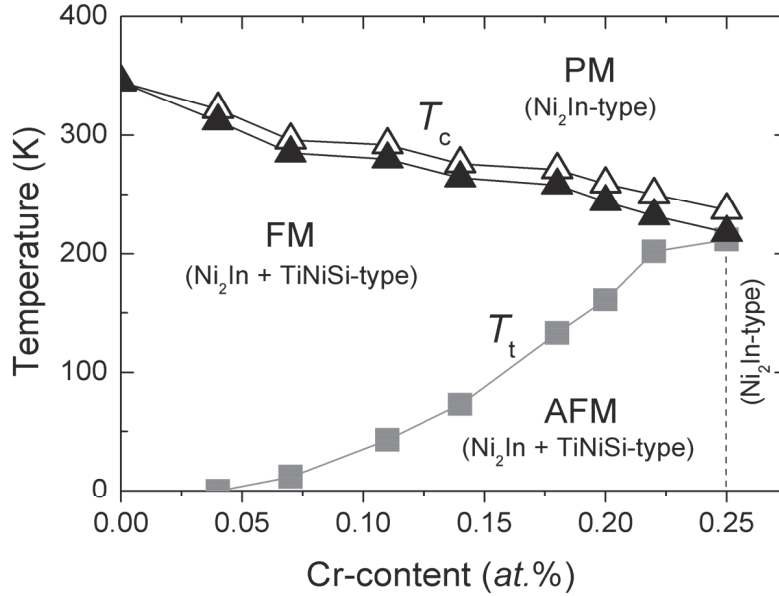
Figure 9.2: Phase diagram of Mn$_{1-x}$Cr$_x$CoGe with $0 \leq x \leq 0.25$. The AFM $\leftrightarrow$ FM transitions occur at T_t (filled squares) on heating and cooling. The FM $\leftrightarrow$PM transitions occur at T_C, open triangles for heating processes and filled triangles for cooling processes (taken from Ref.[164]).

Nevertheless, all the giant values of ΔS_T in the MnCoGe-type compounds mentioned above were derived from isothermal magnetization data with the help of the Maxwell relation [164, 176–179]. They could be overestimated due to the "spike" effect, since the first-order magnetostructural transitions happening in the MnCoGe-type compounds are accompanied by large hysteresis ($\sim$ 10 K). For the sake of seeking magnetocaloric materials for magnetic refrigeration, it is worth making the precise characterization of the MCE of the MnCoGe-type compounds. In this chapter, a compound with nominal composition MnCo$_{0.98}$Cu$_{0.02}$GeB$_{0.02}$ has been studied by means of magnetic and calorimetric measurements. The direct measurements of ΔS_T and ΔT_S were also carried out in the compound. The resulting values of ΔS_T and ΔT_S were compared among the different techniques.

9.2   Sample preparation

A polycrystalline sample with nominal composition MnCo$_{0.98}$Cu$_{0.02}$GeB$_{0.02}$ (provided by E. Brück's group) was prepared by arc-melting under an Ar atmosphere in a water cooled copper crucible. The ingot was melted several times to achieve a good homogeneity of the sample. The as-melted ingot was

sealed in a quartz ampoule under an inert atmosphere of 500 mbar Ar gas. Subsequently, it was annealed at 850 °C for 120 h and then quenched into water at room temperature [164, 178].

9.3 X-ray diffraction

The XRD patterns of $MnCo_{0.98}Cu_{0.02}GeB_{0.02}$ were collected in a heating process at 308 K, 324 K and 350 K which are below, in the middle of, and above the transition region, respectively. The patterns are displayed in figure 9.3 with a range of 2θ from 25° to 50°. The analyses of the patterns indicate the occurrence of a structural transition from the low-temperature orthorhombic TiNiSi-type structure to the high-temperature hexagonal Ni_2In-type structure. The orthorhombic phase is dominant with 88.2 wt.% at 308 K, but the hexagonal phase is dominant with 92.8 wt.% at 350 K. The two phases coexist nearly half-and-half at 324 K.

For the orthorhombic structure, the refined lattice parameters are $a_{orth} =$ 5.9595(13) Å, $b_{orth} = 3.8166(7)$ Å and $c_{orth} = 7.0411(15)$ Å, resulting in a unit cell volume of $V_{orth} = 160.15(6)$ Å^3. The unit cell dimensions for the hexagonal structure are $a_{hex} = b_{hex} = 4.0845(6)$ Å, $c_{hex} = 5.3257(8)$ Å, and $V_{hex} = 76.94(2)$ Å^3. The observation of 3.9 % contraction of the unit cell is in good agreement with 3.8 % occurring at ∼650 K in MnCoGe [166].

9.4 The virgin effect

The MnCoGe-type compounds exhibit a virgin effect when they are cooled for the first time after the synthesis [164]. We have carried out heat-capacity measurements at zero field on an as-prepared $MnCo_{0.98}Cu_{0.02}GeB_{0.02}$ to study the virgin effect. As shown in figure 9.4, a double anomaly is present in the heat capacity measured for the first time on cooling, centering in 285.0 K and 311.8 K. The anomaly at 285.0 K is a broad bump while the other one at 311.8 K is a sharp peak. The bump disappears, whereas the peak is obviously enhanced in the second cooling process. The heat-capacity peak shifts slightly from 311.8 K to 312.8 K in the third cooling process, and remains at the same temperature in further cooling runs. However, a fixed heat-capacity anomaly has been observed in all the heating processes at zero field. The observation of the double heat-capacity anomaly in the first cooling process may be explained as that a portion of the sample was formed at a metastable state after the quenching. The cooling processes overcame the energy barriers, and converted the sample to a stable state. That is just similar to what happens
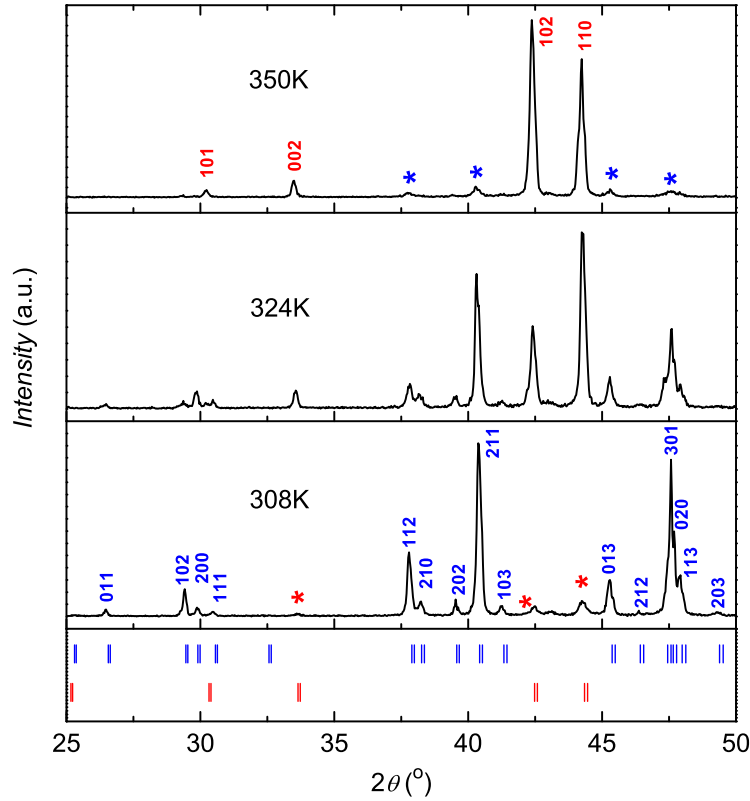
Figure 9.3: XRD patterns of $MnCo_{0.98}Cu_{0.02}GeB_{0.02}$ measured at different temperatures in a heating process. Blue and red ticks denote the positions of the Bragg reflections for the TiNiSi-type and Ni_2In-type structures, respectively. The peaks of the secondary phase component in the two structures are marked with ⋆ symbols.

in $Mn_{0.985}Fe_{0.015}As$, where the metastable state was brought to a stable one by applying a magnetic field of 6 T (see chapter 7).

We also performed magnetization measurements for a piece of sample taken from the as-prepared specimen. The obtained magnetization curves at constant fields of 0.05 T and 5 T are displayed in figures 9.5(a) and 9.5(b), respectively. The first time on cooling at 0.05 T, the magnetization shows a two-step curve. The changes of the magnetization occur at 284 K and 314 K, corresponding to the two anomalies in the heat-capacity curve. After a heating process (2) with a transition occurring at 331 K, the magnetization curve in a subsequent cooling process (3) shows only one transition at 315 K as a simple ferromagnet. After that, a magnetic field of 5 T was applied and the magnetization was measured
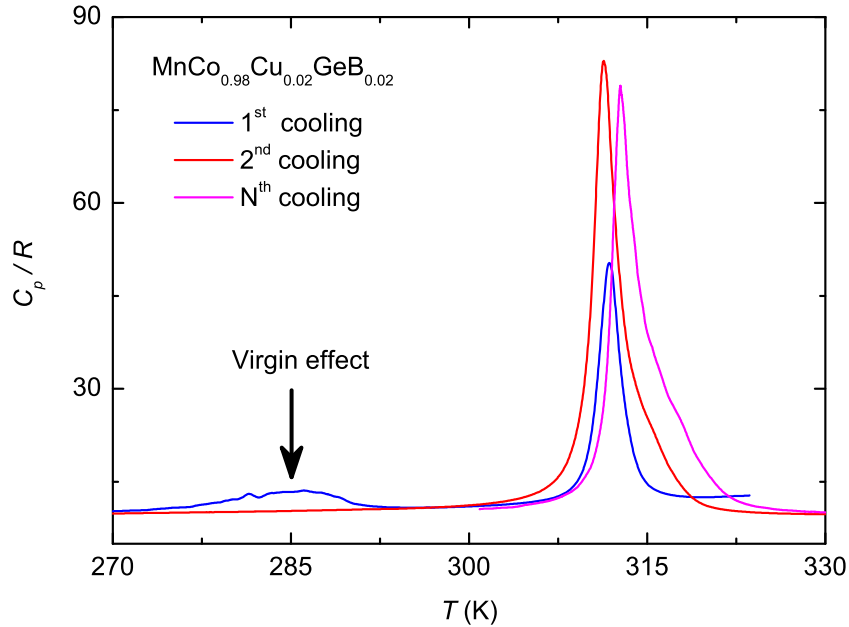
Figure 9.4: The virgin effect of $MnCo_{0.98}Cu_{0.02}GeB_{0.02}$.

following the processes (I), (II), (III) and (IV), as denoted in figure 9.5(b). It is found that the magnetization curves exhibit transitions at 334 K on heating and at 320 K on cooling. The characteristics of the magnetization curves agree well with those observed in the heat-capacity curves.

9.5 Heat capacity and isothermal magnetization

Figure 9.6 shows the temperature dependence of the heat capacity measured at constant magnetic fields of 0, 2 T and 5 T for $MnCo_{0.98}Cu_{0.02}GeB_{0.02}$. The data were obtained after removing the virgin effect. The heating curves (solid lines) determined with the thermogram technique agree well with the discrete heat-capacity values (symbols) obtained with the heat-pulse method except for few points in the transition region. A large thermal hysteresis ∼11 K indicated by the temperature difference between the heating and cooling curves is found. The hysteresis is hardly changed by applying external magnetic fields below 5 T. The temperature of the heat-capacity peak (the transition temperature) moves to higher temperatures with increasing field at rates of $dT_{t,c}/dB = 1.2$ K/T on cooling and $dT_{t,h}/dB = 0.9$ K/T on heating, which agrees with that derived from the magnetization curves of figure 9.5. The values of dT_t/dB observed in $MnCo_{0.98}Cu_{0.02}GeB_{0.02}$ are much smaller than those in other materials exhibiting FOPTs, such as $Gd_5Si_2Ge_2$ (see chapter
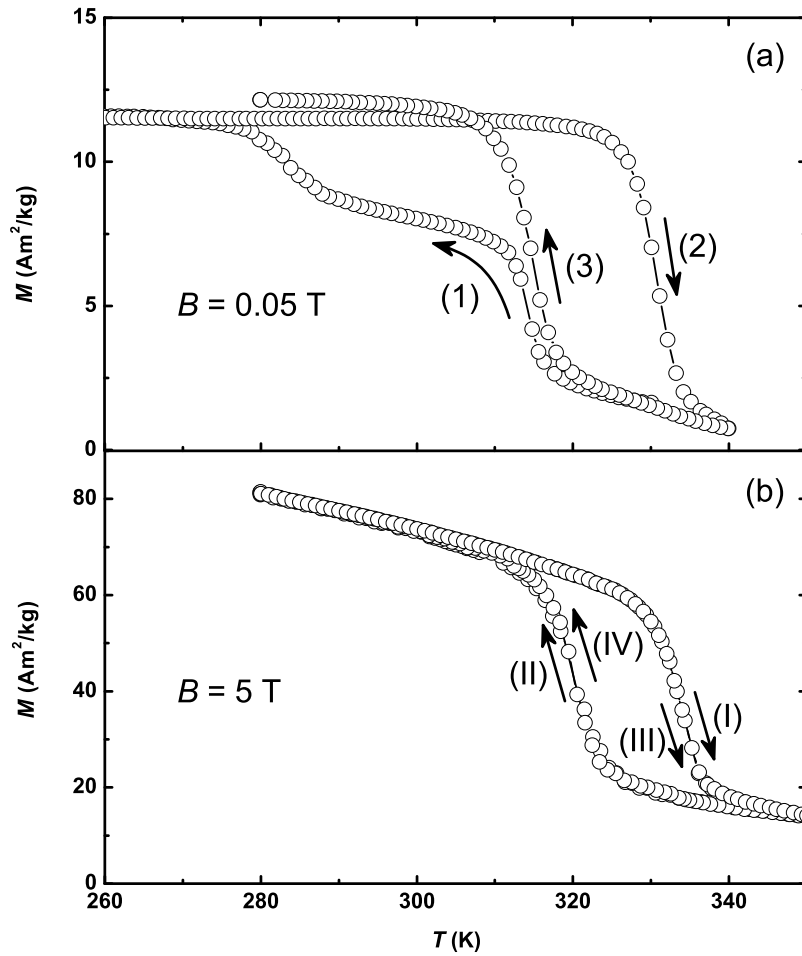
Figure 9.5: Temperature dependence of the magnetization at constant magnetic fields for $MnCo_{0.98}Cu_{0.02}GeB_{0.02}$. (a) measured at 0.05 T in the as-prepared sample following a sequence of (1) the first cooling process, (2) the subsequent heating process, and (3) the subsequent cooling process. (b) subsequently measured at 5 T following (I), (II), (III) and (IV) in the same sample.
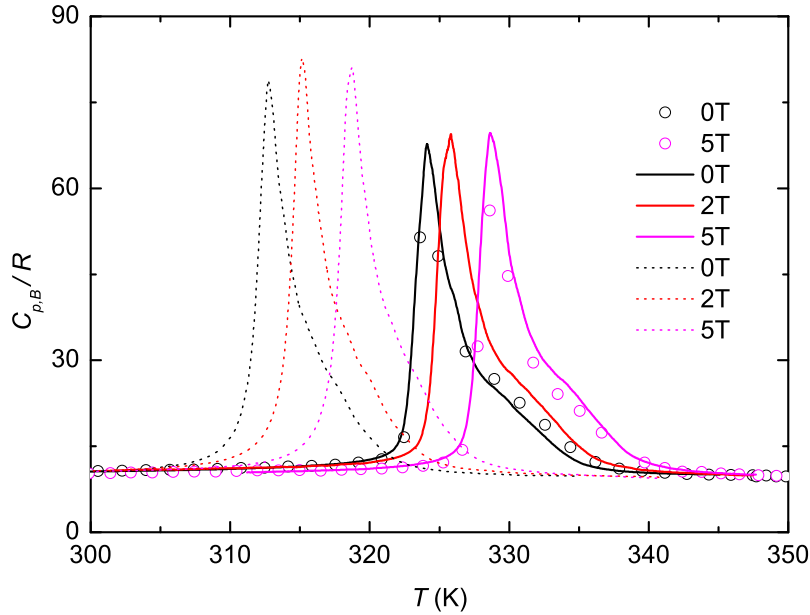
Figure 9.6: Heat capacity as a function of temperature measured at constant magnetic fields of 0, 2 T, and 5 T for $MnCo_{0.98}Cu_{0.02}GeB_{0.02}$. Symbols: determined with heat-pulse method. Solid lines: obtained from heating thermograms. Dotted lines: obtained from cooling thermograms.

5), $La(Fe,Si)_{13}$ (see chapter 6), $(Mn,T)As$ (see chapter 7) and $MnFe(P,Ge)$ (see chapter 8), but are comparable to those in Heusler alloys [180]. The small values of dT_t/dB would lead to small values of the adiabatic temperature change ΔT_S.

Moreover, we found in figure 9.6 that the heat capacity at zero field presents as a sharp peak followed with a tail above it. Geometrically, the anomaly can be regarded as a combination of a high and sharp peak with a low and broad bump, the bump might come from a slight inhomogeneity of Cu and B atoms in the sample, since the peak and the bump have the same field dependence. Unlike other materials exhibiting FOPTs, the heat-capacity anomalies of $MnCo_{0.98}Cu_{0.02}GeB_{0.02}$ are hardly broadened and lowered by applying fields below 5 T. When the temperature axis of the heat-capacity curve at each field is normalized by the corresponding transition temperature, nearly overlapped curves are obtained for all the studied magnetic fields on both heating and cooling processes, as shown in figure 9.7. Nevertheless, a difference between the heating and cooling curves exists. As one can see in figure 9.7, the cooling curves show higher peaks than the heating ones. The calculated values of
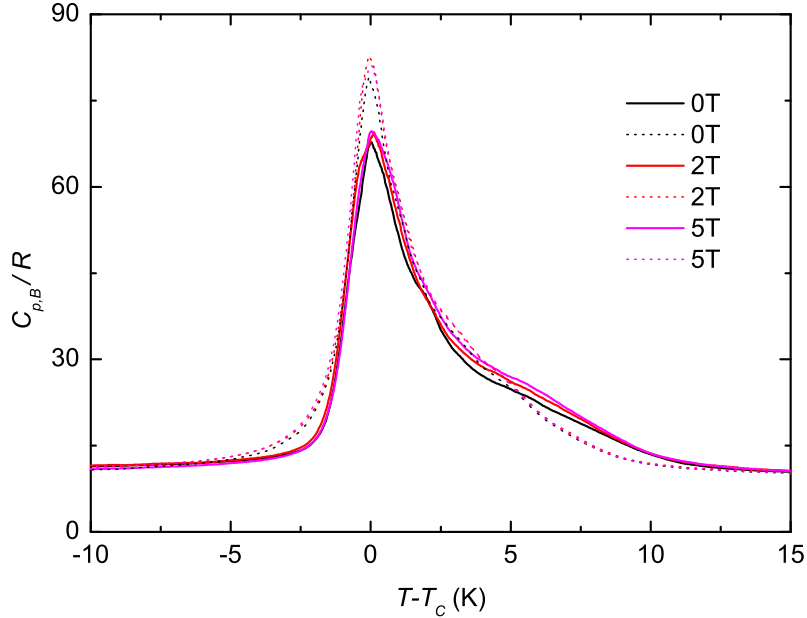
Figure 9.7: Heat capacity as a function of normalized temperature at constant magnetic fields for MnCo$_{0.98}$Cu$_{0.02}$GeB$_{0.02}$. Solid lines: on heating. Dotted lines: on cooling.

the transition enthalpy are 12.8 J/g and 13.6 J/g on heating and cooling, respectively. The resulting transition entropies are 39.5 J/kg·K and 43.5 J/kg·K on heating and cooling, respectively. The observation of the large transition entropy in MnCo$_{0.98}$Cu$_{0.02}$GeB$_{0.02}$ allows having a GMCE.

The magnetic phase diagram has been built using the transition temperatures determined from the heat capacity at constant fields, as displayed in figure 9.8. The threshold field is evaluated to be $B_{th,in} = 9.5$ T when using a linear extrapolation of the PM-FM transition line, i.e. $T_{t,c}(9.5\text{T}) = T_{t,h}(0\text{T}) = 324.1$ K. This will be helpful to understand the isothermal magnetization curves displayed below.

Figure 9.9 shows the magnetic field dependence of the magnetization measured with increasing and decreasing fields for MnCo$_{0.98}$Cu$_{0.02}$GeB$_{0.02}$. The measurement was performed following protocol 1, as a result, fully reversible magnetization curves were obtained at all measuring temperatures. It makes no sense since we observed a large thermal hysteresis (~ 11 K) in the plots of heat capacity and magnetization as functions of temperature (see figures 9.5 and 9.6). In fact, this phenomenon can be easily understood with the help
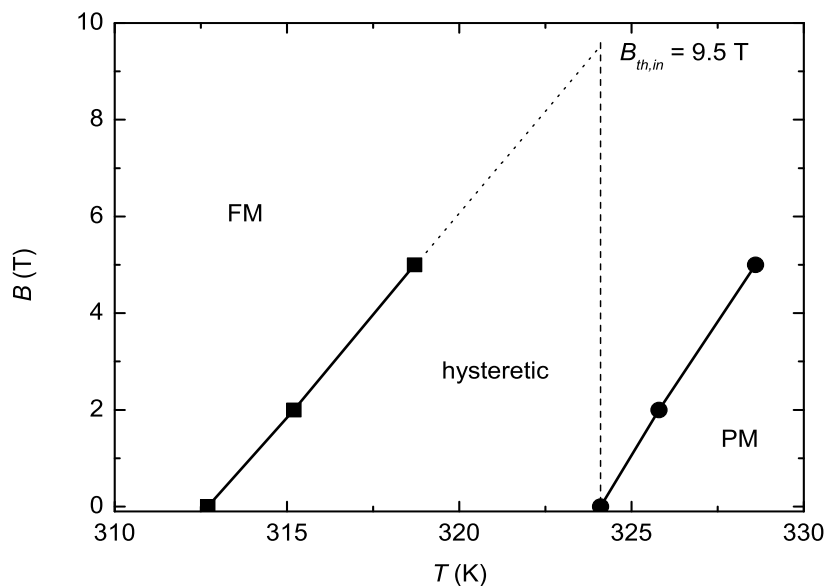
Figure 9.8: Magnetic phase diagram for $MnCo_{0.98}Cu_{0.02}GeB_{0.02}$. Dotted line is a linear extrapolation of the PM-FM transition line. Dashed line is a guide to the eye.
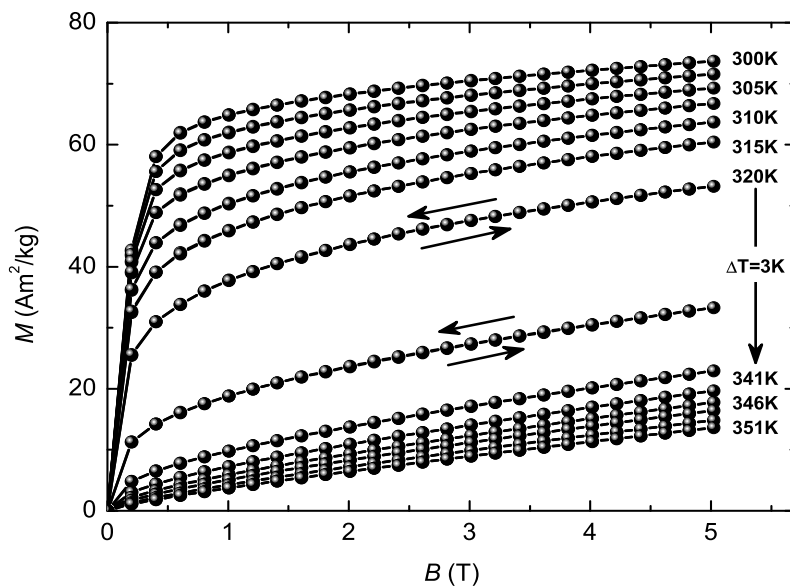

Figure 9.9: Isothermal magnetization as a function of magnetic field measured on increasing and subsequent decreasing magnetic fields for $MnCo_{0.98}Cu_{0.02}GeB_{0.02}$.

of the phase diagram. When the isothermal magnetization measurement is started from a temperature far below $T_{t,c}(0T)$, the sample maintains the orthorhombic FM phase for all temperatures below $T_{t,h}(0T)$. The magnetizing and demagnetizing curves at each temperature exhibit the same FM behavior. The sample converts from the orthorhombic FM phase to the hexagonal PM phase during the heating steps around $T_{t,h}(0T)$, leading to a decrease of the magnetization. In each heating period, the converted fraction cannot be brought back to the FM phase when the applied field is lower than the $B_{th,in}$. Eventually, the whole sample undergoes a transition from FM to PM phase during the heating periods, and then keeps in the PM phase at all temperatures above $T_{t,h}(0T)$. There is no field-induced phase transition on the magnetizing or demagnetizing processes. The maximum field 5 T used in the measurement is much smaller than the threshold field $B_{th,in} = 9.5$ T, therefore, reversible magnetization curves related to a dominant FM phase, a mixture of FM and PM phases or a dominant PM phase were obtained. A field-induced transition may be triggered by applying a stronger magnetic field or by performing the measurement following protocol 2 or 3.

9.6   Magnetocaloric effect

The parent compound MnCoGe shows a normal MCE originating from SOPT [173], but the B-doped compounds exhibit GMCEs due to the occurrence of coupled magnetic and structural FOPTs [164, 178]. For the present compound, the entropy change derived from heat-capacity and direct measurements for field changes of 2 T and 5 T are presented in figure 9.10, respectively. Taking into account ΔS_T measured following protocol 3 in the direct measurement, the values of ΔS_T obtained from both methods have an excellent agreement. In the transition region, the values of $|\Delta S_T|$ obtained from the direct measurement following protocol 3 are larger than those measured following protocol 4, because different amounts of FM phase in the sample at the same temperature were achieved by using the protocols. For field changes of 2 T and 5 T, the maximum values of $|\Delta S_T|$ are found to be 18.4 J/kg·K and 31.8 J/kg·K on cooling, and 13.2 J/kg·K and 26.1 J/kg·K on heating, respectively. The $\Delta S_{T,max}$ values of $MnCo_{0.98}Cu_{0.02}GeB_{0.02}$ are comparable to those of the $Mn_{1-x}T_xAs$ compounds.

The temperature dependence of the entropy change obtained from isothermal magnetization data with the Maxwell relation is displayed in figure 9.11. Definitely, the ΔS_T peaks are spurious, and most contributions to them are attributed to the "spike" effect, because the field-induced transition is absent in figure 9.9. The real entropy changes merely come from the pure FM and
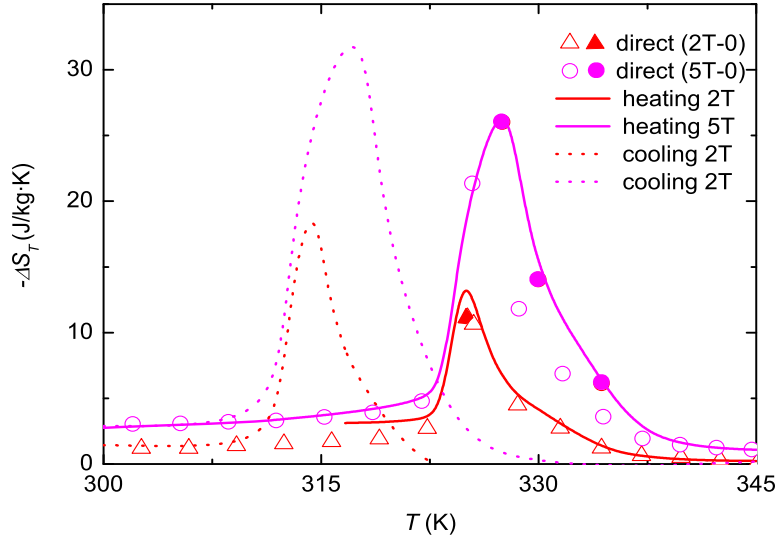
Figure 9.10: Temperature dependence of the isothermal entropy change for magnetic field changes of 2 T and 5 T for $MnCo_{0.98}Cu_{0.02}GeB_{0.02}$. Solid lines: obtained from heat capacity on heating. Dotted lines: obtained from heat capacity on cooling. Solid and open symbols represent the data determined from direct measurements performed following protocols 3 and 4, respectively.
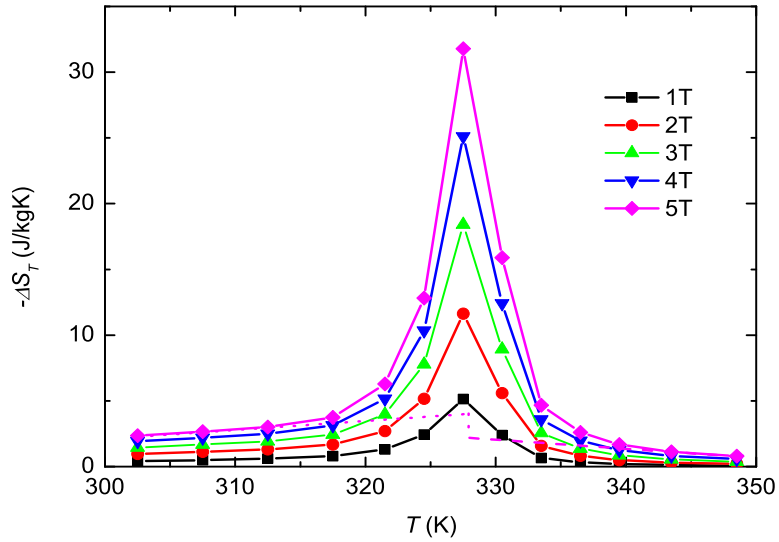

Figure 9.11: Isothermal entropy change calculated from magnetization data using the Maxwell relation for $MnCo_{0.98}Cu_{0.02}GeB_{0.02}$. For each field, the curves on increasing and decreasing fields completely overlap. Dotted and dashed lines represent the entropy change for a field change of 5 T in pure FM and PM phases, respectively.
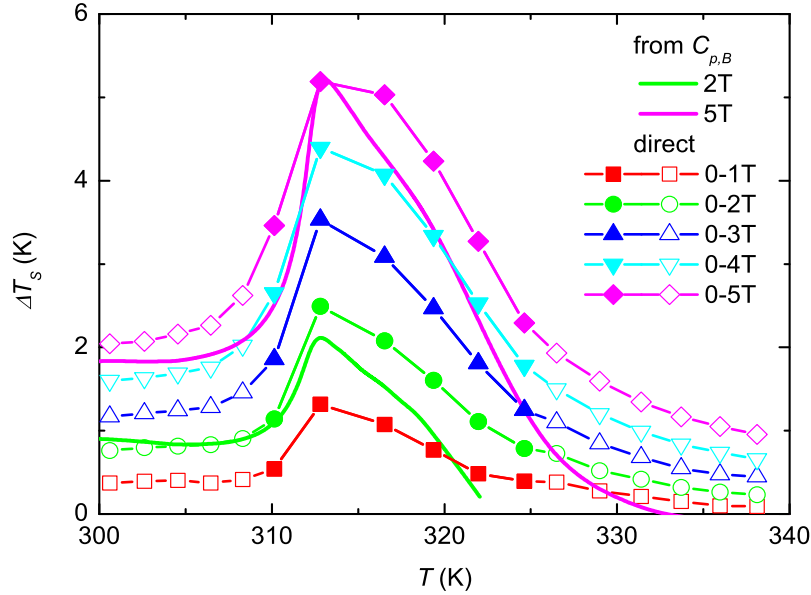
Figure 9.12: Temperature dependence of the adiabatic temperature change for magnetic field changes of 1 T, 2 T, 3 T, 4 T and 5 T for MnCo$_{0.98}$Cu$_{0.02}$GeB$_{0.02}$. Open and solid symbols represent ΔT_S determined from direct measurements performed following protocols 1 and 2, respectively. Thick lines stand for ΔT_S derived from heat capacity on cooling.

PM phases. For a field change of 5 T, the real values of $|\Delta S_T|$ in the FM and PM phases are evaluated to be $\sim$4 J/kg·K and $\sim$2 J/kg·K, respectively, as denoted by the dotted and dashed lines in figure 9.11. The observation of the maximum values of ΔS_T coinciding with the correct maxima obtained from the heat-capacity and direct measurements takes place merely by chance. The spurious spike could be higher than the observed one if a temperature step smaller than 3 K is employed in the magnetization measurements. According to equations (4.9) and (4.13), the limit of the spike for a field change of 5 T is evaluated to be 60 J/kg·K using $C_{an,0T}(T_t) - C_{nor,0T}(T_t) = 68R$ at $T_t = 312.8$ K, $\Delta H_{0T} = 12.8$ J/g and $M_{FM} - M_{PM} = 50$ Am^2/kg. Moreover, since the maximum field used in the magnetization measurements is much lower than the threshold field $B_{th,in}$, there is not any phase transition during the field cycles and, consequently, the isothermal magnetization curves become reversible, giving overlapped ΔS_T peaks on increasing and decreasing fields.

Figure 9.12 shows the adiabatic temperature change as a function of temperature for MnCo$_{0.98}$Cu$_{0.02}$GeB$_{0.02}$ for field changes from 0 to 1 T, 2 T, 3 T, 4 T, and 5 T. Comparable values are observed in the results obtained from heat-capacity and direct measurements. The obtained maximum values of ΔT_S are

2.5 K and 5.2 K for field changes of 2 T and 5 T, respectively. These values are much lower than those observed in other materials exhibiting FOPTs, such as $Gd_5Si_2Ge_2$ (see chapter 5), $La(Fe,Si)_{13}$ (see chapter 6), MnAs-type alloys (see chapter 7), but they are comparable to those found in Heusler alloys, such as $Ni_{50}Mn_{36}Co_1Sn_{13}$ [180]. The small ΔT_S of the present compound is related to the small slope of the transition temperature field dependence.

9.7 Conclusions

The compound $MnCo_{0.98}Cu_{0.02}GeB_{0.02}$ undergoes a first-order magnetostructural transition from the low-temperature FM phase with orthorhombic structure to the high-temperature PM phase with hexagonal structure. The heat capacity and magnetization of the fresh sample exhibit a virgin behavior that disappears after a thermal cycling. The shape of the heat-capacity anomalies does not change by applying magnetic fields below 5 T. With increasing field, the transition temperature increases slightly. It is evident that the isothermal magnetization data measured following protocol 1 cannot produce the correct entropy change in the transition region. The reliable values of ΔS_T were obtained from both heat-capacity measurement and direct measurement performed following protocol 3. Comparable values of ΔT_S are also determined from heat-capacity and direct measurements. The maximum values are found to be $-\Delta S_{T,\text{max}} = 31.8$ J/kg·K and $\Delta T_{S,\text{max}} = 5.2$ K for a field change from 0 to 5 T. The magnitude of $\Delta S_{T,\text{max}}$ for the MnCoGe-type compounds is comparable to those of other materials exhibiting first-order transitions.

Conclusions

This PhD Thesis has been devoted to the determination of magnetocaloric parameters, the isothermal entropy change ΔS_T and the adiabatic temperature change ΔT_S, upon a change of the magnetic field. The study has been done in materials exhibiting first-order phase transitions accompanied with hysteretic effect by means direct measurements and indirect methods based on magnetization and heat-capacity measurements. The "spike" effect (spurious peak) related to the determination of ΔS_T in hysteretic compounds using magnetization measurements has been discussed with the help of magnetic phase diagrams. Four different protocols have been employed in the isothermal magnetization and direct measurements. Specifically, the magnetocaloric effects (MCEs) of the following compounds have been studied: Gd, $Gd_5Si_2Ge_{1.9}X_{0.1}$, $LaFe_{13-x}Si_x(H_y)$, $Mn_{1-x}T_xAs$, $Mn_{2-x}Fe_xP_{0.75}Ge_{0.25}$ and $MnCo_{0.98}Cu_{0.02}Ge$ $B_{0.02}$, with X = Ga, Cu, Ge and T = Fe, Co.

The main conclusions are as follows:

- The values of ΔS_T for a sample can be determined by means of three different methods, i.e. magnetization, heat-capacity, and direct measurements. In principle, all the methods should give the same results for a given sample when correctly applied. However, this happens in practice only for samples exhibiting second-order transitions, and it does not hold in many published works for samples exhibiting first-order transitions with hysteresis.

  The application of the Maxwell relation to the isothermal magnetization data measured following protocol 1 results in the "spike" effect on increasing and decreasing fields. The "spike" effect on increasing field can be reduced by performing the measurement following protocol 2. On decreasing field it can be reduced by performing the measurement following protocol 3 or can be avoided by using a maximum field higher than the critical field. The application of the Maxwell relation to the isofield magnetization data does not produce the "spike" effect.

The Maxwell relation and the Clausius-Clapeyron equation, both underestimate $|\Delta S_T|$ in magnetizing or cooling processes, while they overestimate $|\Delta S_T|$ in demagnetizing or heating processes due to the irreversibility in first-order transitions. $|\Delta S_T|$ derived from heat capacity is underestimated in heating processes and overestimated in cooling processes due to the irreversibility. The effect of the irreversibility in heat-capacity measurement is smaller than in magnetization measurements, since the former is related to A/T, and the latter is denoted by the derivative dA/dT, being A one half of the area of the hysteresis loop.

The direct measurement following protocol 1 gives small ΔS_T values in the hysteretic region, where the phase fraction of the sample is temperature and field dependent. In order to get comparable values with those from heat capacity, the direct measurements have to be performed following protocol 2 on increasing field and following protocol 3 on decreasing field. Moreover, the entropy production $\Delta S_{prod} \approx -\frac{1}{2T} \oint M dB$ due to the irreversibility needs to be taken into account.

ΔT_S can be determined by means of heat-capacity and direct measurements. The resulting values of ΔT_S from these methods coincide for second-order transitions, but not for first-order ones. In the case of first-order transitions, the disagreement of ΔT_S caused by the irreversibility is small. The main difference is due to the thermal and magnetic history dependent phase fractions of the sample when the measurement is carried out following protocol 1. Nevertheless, values coinciding with those from heat capacity can also be obtained by performing the direct measurements following protocol 2 on increasing field and following protocol 3 on decreasing field.

- As an example for studying the materials exhibiting second-order transitions, we have characterized the heat capacity and MCE of a Gd sample. It is found that the heat capacity of Gd determined in our calorimeter shows a good agreement with the literature results. The magnetocaloric parameters obtained from the indirect (magnetization and heat capacity) measurements agree well with those from direct measurements. The demagnetization effect on the MCE is small for the studied Gd sample. It is more important below the Curie temperature than above it, and at low fields than at high fields.

The compound $Mn_{1.1}Fe_{0.9}P_{0.82}Ge_{0.18}$ has been taken as an example for studying the materials exhibiting first-order transitions with large hysteresis. Two independent isothermal magnetization measurements have been performed by applying maximum magnetic fields of 5 T and 9 T. The isothermal magnetization data were measured following three dif-

ferent protocols, namely, protocols 1, 2 and 3. At the transition region, the direct measurements of ΔS_T were performed following protocol 3. The results indicate that ΔS_T determined from isofield magnetization is consistent with that obtained from heat capacity, being considered this last the most accurate result. The ΔS_T results derived from the isothermal magnetization measured following protocol 1 show the "spike" effect on both increasing and decreasing fields. Reasonable values of ΔS_T on increasing and decreasing fields can be determined from the isothermal magnetization measurements by employing protocols 2 and 3, respectively. In the direct measurement of ΔS_T, protocol 3 is also required in order to obtain ΔS_T values coinciding with the results deduced from heat capacity, since the measurement has been carried out on decreasing field. This study gives a guide for determining the MCE in materials exhibiting first-order phase transition with large hysteresis.

- The analysis of the X-ray diffraction patterns obtained at different temperatures indicates that the structural transition occurring in $Gd_5Si_2Ge_2$ is suppressed by substituting Ge with about 5 at.% of Ga or Cu. The analysis of the hot neutron diffraction patterns reveals that the doped compounds exhibit a simple collinear ferromagnetism, which is the same as in the undoped compound. The observation of a λ-shape heat-capacity anomaly at zero field and its broadening by applying a magnetic field in $Gd_5Si_2Ge_{1.9}Ga_{0.1}$ indicates that the transition is of second order. ΔS_T has been determined from direct and indirect measurements in $Gd_5Si_2Ge_2$. Our results have a much higher precision than the previously reported values in the literature, obtaining a maximum of $-\Delta S_{T,\mathrm{max}} = 13.9$ J/kg·K ($\Delta B = 5$ T) on heating or demagnetizing processes and 15.4 J/kg·K on cooling or magnetizing processes. The MCE of $Gd_5Si_2Ge_2$ is not so giant. Although the MCE of the Ga-doped compound is much lower than that of $Gd_5Si_2Ge_2$, their effective refrigeration capacities are similar. The refrigeration capacity of the doped compound is much smaller than that of Gd, that is not advantageous for its use in magnetic refrigeration.

- Two $LaFe_{13-x}Si_x$ samples with nominal compositions $x = 1.0$ and 1.2 prepared using the melt-spinning technique have been studied. The actual concentration of Si in the ribbon samples was determined with the help of XRD analysis, obtaining values close to $x = 1.3$, that agrees with the minimum value reported in the literature for bulk compounds. Although the real compositions and the transition temperatures of $LaFe_{12}Si_1$ and $LaFe_{11.8}Si_{1.2}$ are almost the same, the observed hysteresis in the former sample is smaller. The application of magnetic field produces different effects on the shape of the heat-capacity anomalies in the two sam-

ples. The MCEs obtained from heat capacity, magnetization and direct measurements are in good agreement with each other in both $LaFe_{12}Si_1$ and $LaFe_{11.8}Si_{1.2}$. The maximum values of the magnetocaloric parameters for magnetic field changes of 2 T and 5 T are $-\Delta S_{T,\max} = 19.6$ J/kg·K and 23.4 J/kg·K, $\Delta T_{S,\max} = 6.4$ K and 9.9 K for $LaFe_{12}Si_1$, and $-\Delta S_{T,\max} = 22.1$ J/kg·K and 27.2 J/kg·K, $\Delta T_{S,\max} = 7.0$ K and 11.6 K for $LaFe_{11.8}Si_{1.2}$.

The concentration of H in the studied $LaFe_{11.57}Si_{1.43}H_y$ ribbons is found to be 1.72, leading to an increase of the transition temperature from 194 K to 334 K. The MCE in $LaFe_{11.57}Si_{1.43}$ is slightly reduced by the hydrogenation. Specifically, for magnetic field changes of 2 T and 5 T, $-\Delta S_{T,\max}$ decreases from 20 J/kg·K to 16 J/kg·K and from 26 J/kg·K to 23 J/kg·K, and $\Delta T_{S,\max}$ changes very slightly from 6.6 K to 6.5 K and from 12.0 K to 11.7 K, respectively. The observed large MCE near room temperature indictates that the hydrided ribbons are promising candidates as working refrigerants in magnetic refrigeration.

- Up to 1.5 at.% and 2 at.% substitutions of Mn by Fe and Co do not destroy the first-order magnetostructural transition occurring in MnAs. The doping with Fe and Co has similar effects on the magnetic and magnetocaloric properties of MnAs. That is, with increasing content of Fe or Co, the transition shifts to lower temperatures, the thermal hysteresis increases, the heat-capacity anomaly decreases and broadens. An unusual virgin behavior is found in the heat capacity at zero field in the as-prepared samples $Mn_{0.985}Fe_{0.015}As$ and $Mn_{0.98}Co_{0.02}As$.

The ΔS_T plots of all the studied $Mn_{1-x}T_xAs$ compounds exhibit spurious spikes on increasing and decreasing fields when determined from isothermal magnetization data measured following protocol 1. For increasing field, the height of the "spike" is significantly reduced by performing the isothermal magnetization measurements following protocol 2. For decreasing field, the "spike" effect does not show when taking into account only the data at low fields (e.g. below 6 T) after applying a higher maximum field (e.g. 9 T).

The "spike" effect does not happen in ΔS_T derived from isofield magnetization data. However, there could be an underestimation of $\left(\frac{\partial M}{\partial T}\right)_B$ in the case of sharp transitions as occur in the $Mn_{1-x}T_xAs$ compounds, leading to an underestimation of $|\Delta S_T|$. The heat-capacity curves at constant magnetic fields produce more precise results of ΔS_T and ΔT_S. Direct measurements give coinciding results with those from heat capacity only when they are carried out following protocols 2 and 3 in the transition region.

Taking into account the corrections of irreversibility in each technique, precise and agreeable ΔS_T values can be obtained from all the three techniques, i.e. magnetic, calorimetric and direct methods. Consequently, giant but not colossal MCE is found in the studied $\mathrm{Mn}_{1-x}\mathrm{T}_x\mathrm{As}$ compounds over a large temperature range near room temperature. The MCEs of the $\mathrm{Mn}_{1-x}\mathrm{T}_x\mathrm{As}$ compounds are comparable to that of MnAs, but occur at lower temperatures.

The phase transition and magnetocaloric properties of the $\mathrm{Mn}_{1-x}\mathrm{T}_x\mathrm{As}$ compounds can be semi-quantitatively illustrated with the Bean-Rodbell model.

- The nature of the transitions occurring in the studied $(\mathrm{Mn,Fe})_2\,\mathrm{P}_{0.75}\mathrm{Ge}_{0.25}$ compounds is first order, due to the presence of small, but clear, thermal hysteresis. The transition temperature and hysteresis are influenced by the Mn:Fe ratio, what also happens by changing the P:Ge ratio [164]. Therefore, improved magnetocaloric materials could be obtained by tailoring the ratios of Mn:Fe and P:Ge. Large MCE is observed in the studied compounds near room temperature. The maxima obtained upon field changes of 2 T and 5 T are $-\Delta S_{T,\mathrm{max}} = 8.6$ J/kg·K and 14.7 J/kg·K and $\Delta T_{S,\mathrm{max}} = 3.1$ K and 6.2 K for $\mathrm{Mn}_{1.26}\mathrm{Fe}_{0.74}\mathrm{P}_{0.75}\mathrm{Ge}_{0.25}$, and $-\Delta S_{T,\mathrm{max}}$ = 15.8 J/kg·K and 21.0 J/kg·K and $\Delta T_{S,\mathrm{max}}$ = 5.2 K and 9.3 K for $\mathrm{Mn}_{1.18}\mathrm{Fe}_{0.82}\mathrm{P}_{0.75}\mathrm{Ge}_{0.25}$. The effective refrigeration capacities for both compounds are comparable to that of Gd.

- The compound $\mathrm{MnCo}_{0.98}\mathrm{Cu}_{0.02}\mathrm{GeB}_{0.02}$ undergoes a first-order magnetostructural transition from the low temperature FM phase with orthorhombic structure to the high temperature PM phase with hexagonal structure. The heat capacity and magnetization of the fresh sample exhibit a virgin behavior that disappears after a thermal cycling. The shape of the heat-capacity anomalies does not change by applying magnetic fields below 5 T. With increasing field, the transition temperature increases slightly. It is evident that the isothermal magnetization data measured following protocol 1 cannot produce the correct entropy change in the transition region. Reliable values of ΔS_T were obtained from both heat-capacity measurement and direct measurement performed following protocol 3. Comparable values of ΔT_S are also determined from heat-capacity and direct measurements. The maximum values are found to be $-\Delta S_{T,\mathrm{max}} = 31.8$ J/kg·K and $\Delta T_{S,\mathrm{max}} = 5.2$ K for a field change from 0 to 5 T. The magnitude of $\Delta S_{T,\mathrm{max}}$ for the MnCoGe-type compounds is comparable to those of other materials exhibiting first-order transitions.

Bibliography

[1] C.B. Zimm, A. Jastrab, A. Sternberg, V. Pecharsky, K. Geschneidner Jr., M. Osborne and I. Anderson, Adv. Cryog. Eng., 43 (1998) 1759.

[2] http://en.wikipedia.org/wiki/Montreal_ protocol.

[3] E. Brück, *Magnetocaloric refrigeration at ambient temperature*, Handbook of Magnetic Materials, ed. K.H.J. Buschow, vol. 17, Amsterdam, (2008) 235-281.

[4] E. Warburg, Ann. Phys. Chem., 13 (1881) 141.

[5] S. Yu. Dan'kov, A.M. Tishin, V.K. Pecharsky and K.A. Gschneidner Jr., Phys. Rev. B, 57 (1998) 3478.

[6] G.V. Brown, J. Appl. Phys., 47 (1976) 3673.

[7] S.A. Nikitin and A.S. Andreenko, Phys. Met. Metallogr., 52(1) (1981) 55.

[8] S.A. Nikitin, A.S. Andreenko, A.M. Tishin, A.M. Arkharov and A.A. Zherdev, Phys. Met. Metallogr., 59(2) (1985) 104.

[9] A. Smaïli and R. Chahine, J. Appl. Phys., 81 (1997) 824.

[10] C.B. Zimm, E.M. Ludeman, M.C. Severson and T.A. Herring, Adv. Cryog. Eng., 37B (1992) 883.

[11] B.J. Korte, V.K. Pecharsky and K.A. Gschneidner Jr., Adv. Cryog. Eng., 43 (1998) 1737.

[12] K.A. Gschneidner Jr., V.K. Pecharsky and S.K. Malik, Adv. Cryog. Eng., 42 (1996) 475.

[13] A.A. Azhar, C.D. Mitescu, W.R. Johanson, C.B. Zimm and J.A. Barclay, J. Appl. Phys., 57 (1985) 3235.

[14] M.I. Ilyn, A.M. Tishin, V.K. Pecharsky, A.O. Pecharsky and K.A. Gschneidner Jr., CEC/ ICMC, Madison, (2001).

[15] V.K. Pecharsky and K.A. Gschneidner Jr., Cryocoolers, 10 (1999) 629.

[16] D. Wang, S. Huang, Z. Han, Z. Su, Y. Wang and Y. Du, Solid State Commun., 131 (2004) 97.

[17] M.P. Annaorazov, S.A. Nikitin, A.L. Tyurin, K.A. Asatryan and A.Kh. Dovletov, J. Appl. Phys., 79 (1996) 1689.

[18] V.K. Pecharsky and K.A. Gschneidner Jr., J. Magn. Magn. Mater., 200 (1999) 44.

[19] V.K. Pecharsky and K.A. Gschneidner Jr., Phys. Rev. Lett., 78 (1997) 4494.

[20] A.O. Pecharsky, K.A. Gschneidner Jr. and V.K. Pecharsky, J. Magn. Magn. Mater., 267 (2003) 60.

[21] V. Provenzano, A.J. Shapiro and R.D. Shull, Nature(London), 429 (2004) 853.

[22] R.D. Shull, V. Provenzano, A.J. Shapiro, A. Fu, M.W. Lufaso, J. Karapetrova, G. Kletetschka and V. Mikula, J. Appl. Phys., 99 (2006) 08K908.

[23] N.P.Thuy, L.T. Tai, N.T. Hien, N.V. Nong, T.Q. Vinh, P.D. Thang, T.P. Nguyen and P. Molinie, Proceedings of the Eighth Asia-Pacific Physics Conference, Tapei, (2000) 354-359.

[24] H. Huang, A.O. Pecharsky, V.K. Pecharsky and K.A. Gschneidner Jr., Adv. Cryog. Eng., 48 (2002) 11.

[25] V.V. Ivtchenko, V.K. Pecharsky and K.A. Gschneidner Jr., Adv. Cryog. Eng., 46 (2000) 405.

[26] N.P. Thuy, Y.Y. Chen, Y.D. Yao, C.R. Wang, S.H. Lin, J.C. Ho, T.P. Nguyen, P.D. Thang, J.C.P. Klaasse, N.T. Hien and L.T. Tai, J. Magn. Magn. Mater., 262 (2003) 432.

[27] L. Pytlik and A. Zieba, J. Magn. Magn. Mater., 51 (1985) 199.

[28] H. Wada and Y. Tanabe, Appl. Phys. Lett., 79 (2001) 3302.

[29] L. Tocado, *Thermomagnetic study of materials with giant magnetocaloric effect*, Ph.D. thesis, prensas Universitarias de Zaragoza, (2008).

[30] L. Tocado, E. Palacios and R. Burriel, J. Therm. Anal. Cal., 84 (2006) 213.

[31] H. Wada, T. Morikawa, K. Taniguchi, T. Shibata, Y. Yamada and Y. Akishige, Physica B, 328 (2003) 114.

[32] A. de Campos, D.L. Rocco, A.M.G. Carvalho, L. Caron, A.A. Coelho, S. Gama, L.M. Silva, F.C.G. Gandra, A.O.D. Santos, L.P. Cardoso, P.J.V. Ranke and N.A. de Oliveira, Nat. Mater., 5 (2006) 802.

[33] F.X. Hu, B.G. Shen, J.R. Sun, Z.H. Cheng, G.H. Rao and X.X. Zhang, Appl. Phys. Lett., 78 (2001) 3675.

[34] S. Fujieda, A. Fujita and K. Fukamichi, Appl. Phys. Lett., 81 (2002) 1276.

[35] A. Fujita, S. Fujieda, K. Fukamichi, H. Mitamura and T. Goto, Phys. Rev. B, 65 (2001) 014410.

[36] A. Fujita, K. Fukamichi, J.T. Wang and Y. Kawazoe, Phys. Rev. B, 68 (2003) 104431.

[37] F.X. Hu, X.L. Qian, J.R. Sun, G.J. Wang, X.X. Zhang, Z.H. Cheng and B.G. Shen, J. Appl. Phys., 92 (2002) 3620.

[38] M. Balli, D. Fruchart and D. Gignoux, J. Phys.: Condens. Matter, 19 (2007) 236230.

[39] A. Fujita, S. Fujieda, Y. Hasegawa and K. Fukamichi, Phys. Rev. B, 67 (2003) 104416.

[40] Y.F. Chen, F. Wang, B.G. Shen, G.J. Wang and J.R. Sun, J. Appl. Phys., 93 (2003) 1323.

[41] F.W. Wang, G.J. Wang, F.X. Hu, A. Kurbakov, B.G. Shen and Z.H. Cheng, J. Phys. Condens. Matter, 15 (2003) 5269.

[42] O. Tegus, E. Brück, K.H.J. Buschow and F.R. de-Boer, Nature(London), 415 (2002) 150.

[43] O. Tegus, *Novel materials for magnetic refrigeration*, Ph.D. Thesis, University of Amsterdam, (2003).

[44] E. Brück, O. Tegus, X.W. Li, F.R. de Boer and K.H.J. Buschow, Physica B: Condens. Matter, 327 (2003) 431.

[45] O. Tegus, E. Brück, L. Zhang, Dagula, K.H.J. Buschow and F.R. de Boer, Physica B, 319 (2002) 174.

[46] A. Yan, K.H. Müller, L. Schultz and O. Gutfleishch, J. Appl. Phys., 99 (2006) 08K903.

[47] Z.Q. Ou, G.F. Wang, L. Song, O. Tegus, E. Brück and K.H.J. Buschow, J. Phys.: Condens. Matter., 18 (2006) 11577.

[48] N.T. Trung, Z.Q. Ou, T.J. Gortenmulder, O. Tegus, K.H.J. Buschow and E. Brück, Appl. Phys. Lett., 94 (2009) 102513.

[49] D.T. Cam Thanh, E. Brück, O. Tegus, J.C.P. Klaasse and K.H.J. Buschow, J. Magn. Magn. Mater., 310 (2007) e1012.

[50] D.T. Cam Thanh, E. Brück, O. Tegus, J.C.P. Klaasse, T.J. Gortenmulder and K.H.J. Buschow, J. Appl. Phys., 99 (2006) 08Q107.

[51] D.T. Cam Thanh, E. Brück, N.T. Trung, J.C.P. Klaasse and K.H.J. Buschow, J. Appl. Phys., 103 (2008) 07B318.

[52] L. Song, G.F. Wang, Z.Q. Ou, O. Haschaolu, O. Tegus, E. Brück and K.H.J. Buschow, J. Alloys. Compds., 474 (2009) 388.

[53] A.M. Tishin and Y.I. Spichkin, *Magnetocaloric effect and its application*, Series in Condensed Matter Physics, IOP publishing, Bristol, Philadelphia, (2003).

[54] K.A. Gschneidner Jr., V.K. Pecharsky and A.O. Tsokol, Rep. Prog. Phys., 68 (2005) 1479.

[55] E. Brück, J. Phys. D: Appl. Phys., 38 (2005) R381.

[56] M.H. Phana and S.C. Yub, J. Magn. Magn. Mater., 308 (2007) 325.

[57] A. Planes, L. Mañosa and M. Acet, J. Phys.: Condens. Matter, 21 (2009) 233201.

[58] http://en.wikipedia.org/wiki/Magnetic _ refrigeration # History.

[59] P. Debye, Ann. Physik, 81 (1926) 1154.

[60] W.F. Giauque, J. Amer. Chem. Soc., 49 (1927) 1864.

[61] W.F. Giauque and D. P. MacDougall, Phys. Rev., 43 (1933) 768.

[62] K.A. Gschneidner Jr. and V.K. Pecharsky, *Rare Earths: Science, Technology and Applications III*, ed R.G. Bautista et al., Warrendale, PA: The Minerals, Metals and Materials Society, (1997) 209.

[63] K.A. Gschneidner Jr. and V.K. Pecharsky, Annu. Rev. Mater. Sci., 30 (2000) 387.

[64] K.A. Gschneidner Jr. and V.K. Pecharsky, *Fundamentals of Advanced Materials for Energy Conversion*, ed D. Chandra and R.G. Bautista, Warrendale, PA: The Minerals, Metals and Materials Society, (2002) 9.

[65] K.A. Gschneidner Jr. and V.K. Pecharsky, International Journal of Refrigeration, 31 (2008) 945.

[66] B. Yu, M. Liu, P.W. Egolf and A. Kitanovski, International Journal of Refrigeration, 33 (2010) 1029.

[67] G.J. Liu, J.R. Sun, J. Shen, B. Gao, H.W. Zhang, F.X. Hu and B.G. Shen, Appl. Phys. Lett., 90 (2007) 032507.

[68] L. Tocado, E. Palacios and R. Burriel, J. Appl. Phys., 105 (2009) 093918.

[69] L. Caron, Z.Q. Ou, T.T. Nguyen, D.T. Cam thanh, O. Tegus and E. Brück, J. Magn. Magn. Mater., 321 (2009) 3559.

[70] K.A. Gschneidner Jr. and V.K. Pecharsky, Mater. Sci. Eng., A287 (2000) 301.

[71] R. Burriel, L. Tocado, E. Palacios, T. Tohei and H. Wada, J. Magn. Magn. Mater., 290-291 (2005) 715.

[72] K.A. Gschneidner Jr., V.K. Pecharsky, A.O. Pecharsky and C.B. Zimm, Mater. Sci. Forum, 315-317 (1999) 69.

[73] C.P. Bean and D.S. Rodbell, Phys. Rev., 126 (1962) 104.

[74] R. Zach, M. Guillot and J. Tobola, J. Appl. Phys., 83 (1998) 7237.

[75] O. Tegus, G.X. Lin, W. Dagula, B. Fuquan, L. Zhang, E. Brück, F.R. de Boer and K.H.J. Buschow, J. Magn. Magn. Mater., 290-291 (2005) 658.

[76] P.J. von Ranke, N.A. de Oliveira and S. Gama, J. Magn. Magn. Mater., 277 (2004) 78.

[77] P.J. von Ranke, N.A. de Oliveira and S. Gama, Phys. Lett. A, 320 (2004) 302.

[78] R.W. Cahn, *Physical metallurgy*, Third edition, Elsevier Science Publishers B.V., (1983).

[79] http://wzar.unizar.es/invest/sai/exafs/exafs.html.

[80] http://www-llb.cea.fr/fullweb/.

[81] http://wzar.unizar.es/invest/sai/mic_ele/dotacion/dotacion.html.

[82] http://www.unizar.es/icma/depart/O8_atd.html.

[83] http://wzar.unizar.es/invest/sai/ins_ele/ins_ele.html.

[84] http://www.qdusa.com/products/mpms.html.

[85] http://www.qdusa.com/products/ppms.html.

[86] http://www.cryogenic.co.uk/products/cf_systems/variable_tempera ture.asp.

[87] F. Pavese and V.M. Malyshev, Adv. Cryog. Eng., 40 (1994) 119.

[88] V.K. Pecharsky, J.O. Moorman and K.A. Gschneidner Jr., Rev. Sci. Instrum., 68 (1997) 4196.

[89] E.F.Westrum Jr., G.T. Furukawa and J.P. McCullough, *Adiabatic low-temperature calorimetry*, London, (1968).

[90] V.K. Pecharsky and K.A. Gschneidner Jr., J. Appl. Phys., 86 (1999) 565.

[91] http://www.lakeshore.com/temp/sen/cgrtdts.html.

[92] A.M.G. Carvalho, A.A. Coelho, S. Gama, P.J. von Ranke and C.S. Alves, J. Appl. Phys., 104 (2008) 063915.

[93] A.M.G. Carvalho, A.A. Coelho, P.J. von Ranke and C.S. Alves, J. Alloys Compd., 509 (2011) 3452.

[94] V.K. Pecharsky and K.A. Gschneidner, Jr., J. Appl. Phys., 86 (1999) 565.

[95] C. Xu, G.D. Li and L.G. Wang, J. Appl. Phys., 99 (2006) 123913.

[96] D.M. Liu, M. Yue, J.X. Zhang, T.M. McQueen, J.W. Lynn, X.L. Wang, Y. Chen, J.Y. Li, R.J. Cava, X.B. Liu, Z. Altounian and Q. Huang, Phys. Rev. B, 79 (2009) 014435.

[97] S. Gama, A.A. Coelho, A. de Campos, A.M.G. Carvalha, F.C.G. Gandra, P.J. von Ranke, N.A. de Oliveira, Phys. Rev. Lett., 93 (2004) 237202.

[98] D.L. Rocco, A. de Campos, A.M.G. Carvalho, L. Caron, A.A. Coelho, S. Gama, F.C.G. Gandra, A.O. dos Santos and L.P. Cardoso, Appl. Phys. Lett., 90 (2007) 242507.

[99] H.W. Zhang, J. Shen, Q.Y. Dong, T.Y. Zhao, Y.X. Li, J.R. Sun and B.G. Shen, J. Magn. Magn. Mater., 320 (2008) 1879.

[100] S. Das, J.S. Amaral and V.S. Amaral, J. Phys.D: Appl. Phys., 43 (2010) 152002.

[101] W.B. Cui, W. Liu and Z.D. Zhang, Appl. Phys. Lett., 96 (2010) 222509.

[102] A. Giguère, M. Foldeaki, B. Ravi Gopal, R. Chahine, T. K. Bose, A. Frydman and J.A. Barclay, Phys. Rev. Lett., 83 (1999) 2262.

[103] M. Balli, D. Fruchart, D. Gignoux and R. Zach, Appl. Phys. Letter., 95 (2009) 072509.

[104] Y. Zhou, R. Chahine and T.K. Bose, IEEE Trans. Magn., 39 (2003) 3358.

[105] J.W. Cable and E.O. Wollan, Phys. Rev., 165 (1968) 733.

[106] S.Yu. Dan'kov, A.M. Tishin, V.K. Pecharsky and K.A. Gschneidner Jr., Rev. Sci. Instrum., 68 (1997) 2432 .

[107] H. Callen, *Thermodynamics and an introduction to thermostatistics*, John Wiley and Sons, (1985).

[108] A. Aharoni, J. Appl. Phys., 83 (1998) 3432.

[109] W. Dagula, O. Tegus, B. Fuquan, L. Zhang, P.Z. Si, M. Zhang, W.S. Zhang, E. Brück, F. R. de Boer and K.H.J. Buschow, IEEE Tran. Magn., 41 (2005) 2778

[110] O. Beckman, L. Lundgren, P. Nordblad, P. Svedlindh, A. Törne, Y. Anderson and S . Rundqvist, Physica Scripta., 25 (1982) 679.

[111] V.K. Pecharsky and K.A. Gschneidner Jr., Appl. Phys. Lett., 70 (1997) 3299.

[112] H.E. Fischer, G.J. Cuello, P. Palleau, D. Feltin, A.C. Barnes, Y.S. Badyal and J.M. Simonson, Appl. Phys. A, 74 (2002) S160.

[113] P. Schobinger-Papamantellos, J. Phys. Chem. Solids, 39 (1978) 197.

[114] E. Palacios, J. A. Rodríguez-Velamazán, G.F. Wang, R. Burriel, G. Cuello and J. Rodríguez-Carvajal, J. Phys.: Condens. Matter, 22 (2010) 446003.

[115] A.O. Pecharsky, K.A. Gschneidner Jr., V.K. Pecharsky and C.E. Schindler, J. Alloys Comps., 338 (2002) 126.

[116] O. Svitelskiy, A. Suslov, D. L. Schlagel, T.A. Lograsso, K.A. Gschneidner Jr. and V.K. Pecharsky, Phys. Rev. B, 74 (2006) 184105.

[117] S. Aksoy, A. Yucel, Y. Elerman, T. Krenke, M. Acet, X. Moya and L. Mañosa, J. Alloys Comps., 460 (2008) 94.

[118] E. Palacios, G.F. Wang, R. Burriel, V. Provenzano and R.D. Shull, J. Phys.: Conf. Ser., 200 (2009) 092011.

[119] K.A. Gschneidner Jr., V.K. Pecharsky, E. Brück, H.G.M. Duijn, and E.M. Levin, Phys. Rev. Lett., 85 (2000) 4190.

[120] S. Fujieda, A. Fujita, K. Fukamichi, Y. Yamaguchi and K. Ohoyama, J. Phys. Soc. Jpn., 77 (2008) 074722.

[121] M.K. Han and G.J. Miller, Inorg. Chem., 47 (2008) 515.

[122] G.H. Wen, R.K. Zheng, X.X. Zhang, W.H. Wang, J.L. Chen and G.H. Wu, J. Appl. Phys., 91 (2002) 8537.

[123] M. Balli, D. Fruchart and D. Gignoux, J. Phys.: Condens. Matter, 19 (2007) 236230.

[124] S. Fujieda, A. Fujita, N. Kawamoto and K. Fukamichi, Appl. Phys. Lett., 89 (2006) 062504.

[125] M. Balli, D. Fruchart, D. Gignoux, M. Rosca and S. Miraglia, J. Magn. Magn. Mater., 313 (2007) 43.

[126] S. Fujieda, A. Fujita and K. Fukamichi, J. Appl. Phys., 102 (2007) 023907.

[127] G.F. Wang, L. Song, F.A. Li, Z.O. Ou, O. Tegus, E. Brück and K.H.J. Buschow, J. Magn. Magn. Mater., 321 (2009) 3548.

[128] J. Shen, Y.X. Li, J.R. Sun and B.G. Shen, Chin. Phys. Soc., 18 (2009) 1674.

[129] O. Gutfleisch, A. Yan and K.H. Müller, J. Appl. Phys., 97 (2005) 10M305.

[130] A.Yan, K.H. Müller and O. Gutfleisch, J. Appl. Phys., 97 (2005) 036102.

[131] J. Lyubina, O. Gutfleisch, M.D. Kuz'min and M. Richter, J. Magn. Magn. Mater., 320 (2008) 2252.

[132] F.X. Hu, J. Gao, X.L. Qian, M. IIyn, A.M. Tishin, J.R. Sun and B.G. Shen, J. Appl. Phys., 97 (2005) 10M303.

[133] K. Mandal, D. Pal, O. Gutfleisch, P. Kerschl and K.H. Müller, J. Appl. Phys., 102 (2007) 053906.

[134] J. Lyubina, K. Nenkov, L. Schultz, and O. Gutfleisch, Phys. Rev. Lett., 101 (2008) 177203.

[135] http://physics.nist.gov/cgi-bin/cuu/Value?asil.

[136] R. Weltera, G. Venturinia and B. Malamana, J. Alloys and Compd., 189 (1992) 49.

[137] F.X. Hu, Max Ilyn, A.M. Tishin, J.R. Sun, G.J. Wang, Y.F. Chen, F. Wang, Z.H. Cheng and B.G. Shen, J. Appl. Phys., 93 (2003) 5503.

[138] S. Fujieda, A. Fujita, K. Fukamichi, Y. Yamazaki and Y. Iijima, Appl. Phys. Lett., 79 (2001) 653.

[139] S.M. Podgornykh and Ye.V. Shcherbakova, Phys. Rev. B, 73 (2006) 184421.

[140] J.L. Zhao, J. Shen, F.X. Hu, Y.X. Li, J.R. Sun and B.G. Shen, J. Appl. Phys., 107 (2010) 113911.

[141] B.G. Shen, J.R. Sun, F.X. Hu, H.W. Zhang and Z.H. Cheng, Adv. Mater., 21 (2009) 4545.

[142] T. Liu, Y.G. Chen., Y.B. Tang, S.F. Xiao, E.Y. Zhang and J.W. Wang, J. Alloy. Compd., 475 (2009) 672.

[143] J. Shen, F. Wang, J.L. Zhao, J.F. Wu, M.Q. Gong, F.X. Hu, Y.X. Li, J.R. Sun and B.G. Shen, J. Appl. Phys., 107 (2010) 09A909.

[144] J. Liu, M. Krautz, K. Skokov, T.G. Woodcock and O. Gutfleisch, Acta Materialia, 59 (2011) 3602.

[145] L. Jia, J.R. Sun, J. Shen, Q.Y. Dong, J.D. Zou, B. Gao, T.Y. Zhao, H.W. Zhang, F.X. Hu and B.G. Shen, J. Appl. Phys., 105 (2009) 07A924.

[146] M. Phejar, V. Paul-Boncour and L. Bessais, Intermetallics, 18 (2010) 2301.

[147] A.K. Pathak, P. Basnyat, I. Dubenko, S. Stadler and N. Ali, J. Appl. Phys., 106 (2009) 063917.

[148] J. Shen, Y.X. Li, J. Zhang, B. Gao, F.X. Hu, H.W. Zhang, Y.Z. Chen, C.B. Rong and J.R. Sun, J. Appl. Phys., 103 (2008) 07B317.

[149] Y.F. Chen, F. Wang, B.G. Shen, F.X. Hu, J.R. Sun, G.J. Wang and Z.H. Cheng, J. Phys.: Condens. Matter, 15 (2003) L161.

[150] M.Z. Ding, Z. Liu, R.J. Chen and A.R. Yan, J. Appl. Phys., 107 (2010) 09A952.

[151] E.C. Passamani, A.Y. Takeuchi, A.L. Alves, A.S. Demuner, E. Favre-Nicolin, C. Larica, J.R. Proveti and A. M. Gomes, J. Appl. Phys., 102 (2007) 093906.

[152] A.K. Pathak, P. Basnyat, I. Dubenko, S. Stadler and N. Ali, J. Magn. Magn. Mater., 322 (2010) 692.

[153] W.B. Cui, W. Liu, X.H. Liu, S. Guo, Z. Han, X.G. Zhao and Z.D. Zhang, Mater. Lett., 63 (2009) 595.

[154] R.H. Wilson and J.S. Kasper, Acta Cryst., 17 (1964) 95.

[155] H. Fjellvåg, A. Kjekshus, A.F. Andresen and A. Zięba, J. Magn. Magn. Mater., 73 (1988) 318.

[156] A. Zięba, Y. Shapira and S. Foner, Phys. Lett. A, 91 (1982) 243.

[157] A. Zieba, K. Selte, A. Kjekshus and A.F. Andresen, Acta Chem. Scand. A, 32 (1978) 173.

[158] C. Guillaud, J. Phys. Radium, 12 (1951) 223.

[159] H.E. Stanley, *Mean field theory of magnetic phase transitions. Introduction to phase transitions and critical phenomena.* Oxford University, (1971).

[160] A.M.G. Carvalho, A.A. Coelho, S. Gama, F.C.G. Gandra, P.J. von Ranke and N.A. de Oliveira, Eur. Phys. J. B, 68 (2009) 67.

[161] R.Zach, M. Guillot and R. Fruchart, J. Magn. Magn. Mater., 89 (1990) 221.

[162] E. Brück, M. Ilyn, A.M. Tishin and O. Tegus, J. Magn. Magn. Mater., 290-291 (2005) 8.

[163] J.L. Shapiro, B.F. Woodfield, R. Stevens, J. Boerio-Goates and M.L. Wilson, J. Chem. Thermodynamics, 31 (1999) 725.

[164] N.T. Trung, *First-order phase transitions and giant magnetocaloric effect*, PhD thesis, Technische Universiteit Delft (2010).

[165] V. Johnson, Inorg. Chem., 14 (1975) 1117.

[166] T. Kanomata, H. Ishigaki, T. Suzuki, H. Yoshida, S. Abe and T. Kaneko, J. Magn. Magn. Mater., 140-144 (1995) 131.

[167] S. Niziol, A. Weselucha, W. Bazela and A. Szytula, Solid State Commun., 39 (1981) 1081.

[168] J.T. Wang, D.S. Wang, C. Chen, O. Nashima, T. Kanomata, H. Mizuseki and Y. Kawazoe, Appl. Phys. Lett., 89 (2006) 262504.

[169] K. Koyama, M. Sakai, T. Kanomata and K. Watanabe, Jpn. J. Appl. Phys., 43 (Part 1) (2004) 8036.

[170] S. Niziol, A. Zieba, R. Zach, M. Baj and L. Dmowski, J. Magn. Magn. Mater., 38 (1983) 205.

[171] S. Anzai and K. Ozawa, Phys. Rev. B, 18 (1978) 2173.

[172] S. Niziol, R. Zach, J.P. Senateur and J. Beille, J. Magn. Magn. Mater., 79 (1989) 333.

[173] Song Lin, O. Tegus, E. Brück, W. Dagula, T.J. Gortenmulder and K.H.J. Buschow, IEEE Trans. Magn., 42 (2006) 3776.

[174] K.G. Sandeman, R. Daou, S. Özcan, J.H. Durrell, N.D. Mathur and D.J. Fray, Phys. Rev. B, 74 (2006) 224436.

[175] W.G. Zhang, O. Tegus, Y.L. Wu, Yirgeltu, H.Y. Yan and L. Song, J. Mater. Sci. Technol., 25 (2009) 781.

[176] J.B. A. Hamer, R. Daou, S. Özcan, N.D. Mathur, D.J. Fray and K.G. Sandeman, J. Magn. Magn. Mater., 321 (2009) 3535.

[177] Y.K. Fang, C.C. Yeh, C.W. Chang, W.C. Chang, M.G. Zhu and W. Li, Scripta Mater., 57 (2007) 453.

[178] N.T. Trung, L. Zhang, L. Caron, K.H.J. Buschow and E. Brück, Appl. Phys. Lett., 96 (2010) 172504.

[179] N.T. Trung, V. Biharie, L. Zhang, L. Caron, K.H.J. Buschow and E. Brück, Appl. Phys. Lett., 96 (2010) 162507.

[180] V.V. Khovaylo, K.P. Skokov, O. Gutfleisch, H. Miki, T. Takagi, T. Kanomata, V.V. Koledov, V.G. Shavrov, G.F. Wang, E. Palacios, J. Bartolomé and R. Burriel, Phys. Rev. B, 81 (2010) 214406.

Acknowledgements

First of all, I would like to express my deep and sincere gratitude to my promoter, Prof. Ramón Burriel, who has given me the opportunity to study in Spain. Ramón, it is my great pleasure to be your student. Thanks a lot for your excellent supervision on this research and great assistance in the preparation of this Thesis. My gratitude also goes to your wife, Juli, who helped me a lot in the PhD life.

I am deeply grateful to my supervisor, Prof. Elías Palacios, who is always very patient and enthusiastic in training me experimental skills. Thanks very much for his valuable guidance and constructive comments during my PhD journey.

I would like to greatly acknowledge the sample suppliers: Prof. S. Gama, Dr. A. A. Coelho, Prof. V. Provenzano, Prof. R.D. Shull, Prof. O. Gutfleisch, Dr. J. Lyubina, Prof. O. Tegus, Prof. E. Brück and Dr. Nguyen Thanh Trung.

I would like to appreciate Dr. Concepción Sánchez and Dr. Ana Belén Arauzo for their kind assistance in X-ray diffraction and magnetization measurements.

I am thankful to Ainhoa Urtizberea, Cristina Saenz de Pipaón and Miguel Castro for their friendly information about the defence.

I would like to give my deep thanks to secretarial staffs, Aurora Espinosa, María Abadías, Marisa Bonilla, Germán Romeo, who helped me a lot during this four years.

I would like to thank all the committee members: Prof. Lluis Mañosa, Prof. Vitor Amaral, Prof. O. Tegus, Prof. Victorino Franco, Dr. Marco Evangelisti.

I gratefully acknowledge the JAE-predoc scholarship from Consejo Superior de Investigaciones Científicas (CSIC).

I would like to thank Prof. Tegus who introduced me to Ramón. Grateful appreciation is given to Prof. Song Lin and his wife Nuo Min who provided great assistance to my trip to Spain.

I owe my loving thanks to my parents, parents-in-law, my wife ZengRu Zhao, my younger brother GuoFeng Wang, my daughter MiaoKe Wang, and my relatives. Without their love, support, encouragement and understanding it would be have been impossible for me to finish this work.